SLAC-R-676

Observation of Nonlinear Compton Scattering*

Theofilos Kotseroglou

Stanford Linear Accelerator Center
Stanford University
Stanford, CA 94309

SLAC-Report-676

Prepared for the Department of Energy
under contract number DE-AC03-76SF00515

Printed in the United States of America. Available from the National Technical Information Service, U.S. Department of Commerce, 5285 Port Royal Road, Springfield, VA 22161.

* Ph.D. thesis, University of Rochester, Rochester, New York.

Observation of
Nonlinear Compton Scattering

by
Theofilos Kotseroglou

Submitted in Partial Fulfillment
of the
Requirements for the Degree
Doctor of Philosophy

Supervised by
Professor A. C. Melissinos
Department of Physics and Astronomy
The College
Arts and Sciences

University of Rochester
Rochester, New York
1996

Acknowledgments

The list of people who educated, supported, guided, and befriended me during my graduate studies is long, and I will do my best to thank them all. The long hours I spent studying with Emile Ettedgui my first year in graduate school will not be forgotten. The help of the SLAC staff was invaluable and so was that of Pat Borelli, Tom Haelen and Larry Kuntz of the U. of Rochester.

Contrary to large High Energy Physics experiments, the members of this relatively small experiment knew and interacted with each other on a daily basis. I wish to thank them all and I devote to them the first Appendix of this thesis. I would like to thank Todd Blalock who first introduced me to laser's principles and Charlie Bamber who taught me his unique method of doing physics experiments. I am thankful to Kostya Shmakov for all the long discussions and the time he devoted to teach me the tools of High Energy Physics. Steve Boege was a great help in this experiment and a good friend. I know I bored Christian Bula with most of my questions which he kindly answered. The guidance of Dave Burke on the data analysis and the use of the electron beam during the runs was critical. Discussions with Clive Field and Kirk McDonald have provided me with a physics insight on this experiment. David Meyerhofer was a great 'vice advisor' whose mysterious powers on the laser system made this experiment work.

My special thanks go to my supervisor and mentor for the last five long years, Adrian Melissinos. He is a great teacher and a source of enthusiasm and encouragement.

Finally, I am grateful to my parents $\upsilon\theta\alpha\lambda\iota'\alpha$ and $K\upsilon\rho\iota\alpha'\kappa o$ for their love and constant support.

This work was supported in part by the U.S. Department of Energy grants DE-FG02-91ER40671, DE-FG02-91ER40685, DE-FG05-91ER40627 and contract DE-AC03-76SF00515.

Abstract

This experiment tests Quantum Electrodynamics in the strong field regime. Nonlinear Compton scattering has been observed during the interaction of a 46.6 GeV electron beam with a 10^{18} W/cm^2 laser beam. The strength of the field achieved was measured by the parameter $\eta = e\mathcal{E}_{rms}/\omega mc = 0.6$. Data were collected with infrared and green laser photons and circularly polarized laser light. The timing stabilization achieved between the picosecond laser and electron pulses has $\sigma_{rms} = 2$ ps.

A strong signal of electrons that absorbed up to 4 infrared photons (or up to 3 green photons) at the same point in space and time, while emitting a single gamma ray, was observed. The energy spectra of the scattered electrons and the nonlinear dependence of the electron yield on the field strength agreed with the simulation over 3 orders of magnitude.

The detector could not resolve the nonlinear Compton scattering from the multiple single Compton scattering which produced rates of scattered electrons of the same order of magnitude. Nevertheless, a simulation has studied this difference and concluded that the scattered electron rates observed could not be accounted for only by multiple ordinary Compton scattering; nonlinear Compton scattering processes are dominant for $n \geq 3$.

Contents

List of Tables

List of Figures

Chapter 1

Theory and Motivation

1.1 Introduction

Quantum Electrodynamics is a theory tested extensively in the weak field regime, where perturbative methods can be employed to make very precise predictions. These methods are less reliable when one extends the study of QED into the strong field regime where the onset of many interesting phenomena that scale nonlinearly with the field intensity is expected [1, 2].

Nonlinear (multiphoton) Compton scattering is one of the processes that should take place in strong electromagnetic fields. Although multiphoton effects have been studied extensively in atomic systems, before this experiment there were only a few attempts at the observation of such effects on free electrons [3, 4]. In this process a free electron absorbs many laser photons, in distinction with the well known Compton scattering where a high energy electron only interacts with one photon, recoils and emits a high energy gamma ray. Multiphoton effects become important in a wave field of frequency ω when the dimensionless invariant parameter

$$\eta = \frac{e\mathcal{E}_{rms}}{\omega mc} \tag{1.1}$$

approaches or exceeds unity. Here e and m are the charge and mass of the electron, c the velocity of light and $\mathcal{E}_{rms}$ the rms electric field of frequency ω. η plays the role of an expansion parameter in the field strength. This is intuitive since weak interactions

of electrons and fields would mean that not only the interaction constant α should be small, but also the field should be weak.

In the non-relativistic regime the electron performs an oscillatory motion under the influence of the Lorentz force from the field. If the maximum amplitude of this motion is x_0 and the field wavelength is λ then it can be shown that

$$\eta = \frac{2\pi x_0}{\lambda} = \frac{v_{osc}}{c} \tag{1.2}$$

The last equation leads to the following interpretation: For η larger than one the maximum amplitude of the oscillation is larger than the wavelength of the field and the dipole approximation does not apply. In this case the electron emits multipole radiation. From the same equation it is also seen that η is equivalent to the electron's velocity.

Instead of increasing the strength of the field, we also get $\eta >> 1$ by decreasing the frequency of the field. For a static magnetic field multiphoton absorption can be used to describe synchrotron radiation [1].

These multiphoton effects also have a semiclassical origin and are present in strong fields where they lead to a sizable 'transverse mass' correction [5] - [10]. This correction increases the mass of the electron (so called 'mass shift') and could be observed experimentally. The parameter η is proportional to the magnitude of the classical vector potential of the wave field, and characterizes the transverse velocity induced on an electron by the wave. When this transverse motion becomes relativistic, higher multipole radiation becomes important [11].

The behavior of an electron in a strong field can be theoretically formulated by using the exact (Volkov) solution of the Dirac equation for a particle in an electromagnetic field [12, 13]. An analytic expression for the probability and intensity of photon emission in these processes has been obtained and is relatively simple for circularly polarized waves, [14] - [16]. This approach of Narozhnyi et al. is used in this experiment in order to compare the theory with the data.

The theory of multiphoton Compton scattering of free electrons from photons was formulated many years ago; but, until recently it lacked experimental testing due to the nonexistence of sources of very intense fields. In this experiment a state of the

art terawatt laser is used to create an electromagnetic intense field at its focus, where relativistic (46.6 GeV) electrons are brought into collision with the laser field to study nonlinear aspects of QED. The scattered electrons were detected, their momentum and energy being measured in a magnetic spectrometer and a silicon calorimeter. In ordinary Compton scattering there is a cutoff minimum energy for these scattered (recoil) electrons while their spectrum, due to multiphoton Compton, extends below this cutoff permitting an identification of the nonlinear process. The number of high energy scattered photons was also measured by a gas-Čerenkov monitor. The energy spectra of the scattered electrons and their nonlinear dependance on the field strength were found to be in agreement with the theoretical prediction. The experiment was done at two laser wavelengths, infrared (IR) and green (GR), and electrons that absorbed up to 4 laser photons in the IR and up to 3 in the GR were observed.

Apart from nonlinear Compton scattering this experiment characterized the produced gamma ray beam to be used in a future light by light experiment where collisions of this beam with laser photons will be studied. The products of this interaction are expected to be electron-positron pairs according to the Breit - Wheeler (B-W) theory [17]. The current experimental setup provided a first look into these positron production processes due to the subsequent interaction of the gamma (produced already by Compton scattering) with the laser photons while still in the focus of the laser. The theory of the B-W process and of the related process of beamstrahlung, [20, 21] is summarized here, while the results of the experiment on these processes are a subject of another thesis [22].

1.2 Electron in a strong field

The field that the electron experiences in this experiment is indeed very strong and close to the critical field of QED defined in Appendix B. The laser intensity, in terms of the energy stored in the field of the laser, is given by

$$I = uc \tag{1.3}$$

The energy of the field can be expressed as

$$u = \frac{1}{2}\epsilon_0 \mathcal{E}^2 + \frac{1}{2}\frac{1}{\mu_0}\mathcal{B}^2 \tag{1.4}$$

where ϵ_0 and μ_0 are the permittivity and permeability of free space and $\mathcal{E}$ and $\mathcal{B}$ are the instantaneous electric and magnetic components of the field. The velocity of light is also given by

$$c = \frac{1}{\sqrt{\epsilon_0 \mu_0}} \tag{1.5}$$

By using the above eq. the intensity becomes

$$I = \sqrt{\frac{\epsilon_0}{\mu_0}}\mathcal{E}^2 = \frac{1}{Z_0}\mathcal{E}^2 \tag{1.6}$$

where $Z_0 = 377\Omega$ is the vacuum impedance. Since $\mathcal{E}$ is the instantaneous field it can be written as

$$\mathcal{E} = \mathcal{E}_0 \cos \omega t \tag{1.7}$$

so that

$$I = \frac{1}{Z_0}\mathcal{E}_0^2 \cos^2 \omega t \tag{1.8}$$

and the average (in time) laser intensity is

$$< I >= \frac{1}{Z_0}\frac{1}{2}\mathcal{E}_0^2 = \frac{1}{Z_0}\mathcal{E}_{rms}^2 \tag{1.9}$$

But the root-mean-square electric field as viewed by the counter-propagating electrons is

$$\mathcal{E}_{e-restframe} = 2\gamma \mathcal{E}_{rms} \tag{1.10}$$

where $\gamma \simeq 10^5$ is the Lorentz boost in this experiment. The electric field as viewed by the electrons that is achieved with laser intensity in the lab equal to 10^{18} Watts/cm^2 is

$$\mathcal{E} = \sqrt{4\gamma^2 Z_0 I_{rms}} = 0.4 \times 10^{16} \mathrm{V/cm} \tag{1.11}$$

An interesting fact is that at this intensity the photon density becomes 10^{27} / cm^3, and the radiation length of this 'photon gas' is about 100 μm, i.e. the photon density is 50 times that of the electron density of lead!

1.2.1 Classical analysis

The steady-state motion of an electron in a plane electromagnetic wave is simple in a frame where the electron is at rest on the average, especially for the case of a circularly polarized wave. Then the electromagnetic field vectors $\vec{\mathcal{E}}$ and $\vec{\mathcal{B}}$ have constant magnitude and rotate at the angular frequency of the wave in the plane perpendicular to the direction of the wave propagation. The electron moves in a circle at angular velocity ω, with its velocity parallel to $\vec{\mathcal{B}}$. Allowing for the possibility of relativistic velocities, $F = ma$ becomes

$$\gamma_\perp m\omega^2 r = \gamma_\perp m\omega v = eE \tag{1.12}$$

where $\gamma_\perp = 1/\sqrt{1-\beta_\perp^2}$ and $\beta_\perp = v/c$. Hence we can write:

$$\gamma_\perp \beta_\perp = \frac{e\mathcal{E}}{m\omega c} \equiv \eta \tag{1.13}$$

leading to $\gamma_\perp = \sqrt{(1+\eta^2)}$. In weak fields the quantity $e\mathcal{E}/m\omega c$ is equal to v_{osc}/c, and can be found in this formalism in plasma physics studies. Due to its transverse oscillation in the field, the electron acquires an 'effective mass'

$$\bar{m}^2 = m^2\gamma_\perp^2 = m^2(1+\eta^2) \tag{1.14}$$

The radius of the electron's orbit is

$$r = \frac{e\mathcal{E}}{\gamma_\perp m\omega^2} = \frac{\eta}{\sqrt{1+\eta^2}}\frac{\lambda}{2\pi} \tag{1.15}$$

where λ is the wavelength of the EM field.

Although from the above treatment it seems that multiphoton phenomena on free electrons can be studied in the focus of an intense laser beam, while the electron is at rest, this is in practice difficult. In a focused beam the intensity has a strong transverse gradient, called the ponderomotive force, which will push the electron away from the optical axis and will expel it from the strong field region. This happens during the stage in time the electron absorbs energy and momentum from the wave, while shifting its mass from m to $\bar{m}$, according to the above. The electron will be able to penetrate the photon beam only with initial velocities such that $\gamma\beta > \eta$, i.e.

multiphoton phenomena in intense laser beams can only be probed by relativistic electrons.

For waves with other than circular polarization we redefine the parameter η as

$$\eta^2 \equiv \frac{e^2 < \mathcal{E}^2 >}{m^2\omega^2c^2} \tag{1.16}$$

where the average is with respect to time, and all the above hold for any polarization of the field.

In terms of the power of the laser pulse and the aperture ratio of the focusing system f/d, η becomes:

$$\eta = \frac{e\mathcal{E}}{m\omega c} = \frac{e\mathcal{E}\lambda}{2\pi m} \simeq \frac{8 \times 10^{-6}\sqrt{P[Watts]}}{(f/d)} \tag{1.17}$$

where the rms peak electric field strength was used as:

$$\mathcal{E}_{rms}[Volts/cm] = \sqrt{Z_0 I} = \frac{8\pi}{(f/d)\lambda[cm]}\sqrt{P[Watts]} \tag{1.18}$$

i.e. η is independent of the laser wavelength for fixed power and focusing strength.

1.2.2 Quantum mechanical description

Although we have motivated the mass shift classically it was first noted in solutions to the Dirac's equation for an electron in a plane electromagnetic wave as in [12] and in [1]. It also arises naturally in studies of nonlinear scattering processes in the presence of a quantized radiation field [23] - [25]. For the rest of this chapter we set $\hbar = c = 1$.

If $A^\mu = (\Phi, \vec{A})$ is the 4-potential of the external EM field, k is the field wavenumber, p is the electron momentum and ψ its wavefunction in the field, then Dirac's equation is written as

$$[\gamma(p - eA) - m)]\psi = 0 \tag{1.19}$$

and by using identities of the Dirac γ matrices it can be transformed into the second order eq.

$$[(p - eA)^2 - m^2 - \frac{1}{2}\imath eF_{\mu\nu}\sigma^{\mu\nu}]\psi = 0 \tag{1.20}$$

that can be solved exactly for a plane wave. $F_{\mu\nu}$ is the EM field tensor and $\sigma^{\mu\nu}$ the matrix related to the γ matrices as:

$$\sigma^{\mu\nu} = \frac{1}{2}(\gamma^\mu\gamma^\nu - \gamma^\nu\gamma^\mu) \tag{1.21}$$

A solution to eq. 1.20 of the form

$$\psi = e^{-ipx}F(\phi) \tag{1.22}$$

was first introduced by Volkov and can be found to be

$$\psi_p = [1 + \frac{e}{2(kp)}(\gamma k)(\gamma A)] \times \frac{u}{\sqrt{2p_0}} \times e^{iS} \tag{1.23}$$

where the exponent S is given by

$$S = -px - \int_0^{\phi=kx} [\frac{e}{(kp)}(pA) - \frac{e^2}{2(kp)}A^2]d\phi \tag{1.24}$$

and from boundary conditions we deduce that u is the bispinor amplitude of the free wave, and can have the normalization $u\bar{u} = 2m$.

Using the Volkov states of the electron in the presence of an EM field, its mass shift in this field can be calculated as follows:

The expectation value of the canonical momentum of the electron $p - eA$ is given by

$$\psi_p^\star(p^\mu - eA^\mu)\psi_p \tag{1.25}$$

and it can be shown that the time average of the canonical momentum, i.e. q^μ, of the electron in the plane wave is

$$q^\mu = p^\mu - \frac{e^2\bar{A}^2}{2(kp)}k^\mu \tag{1.26}$$

The effective mass $\bar{m}$ of the electron is defined by $q^2 = \bar{m}^2$ and so it is given by:

$$\bar{m}^2 = q^2 = m^2 - e^2\bar{A}^2 \tag{1.27}$$

and we may write

$$\bar{m} = m\sqrt{1 - \frac{e^2\bar{A}^2}{m^2}}. \tag{1.28}$$

and after substitution of

$$\eta^2 = -\frac{e^2\bar{A}^2}{m^2}. \tag{1.29}$$

the effective mass of the electron can be written as

$$\bar{m} = m\sqrt{1+\eta^2}. \tag{1.30}$$

In this way the parameter η is introduced to characterize the mass shift of the electron in the field of a plane EM wave.

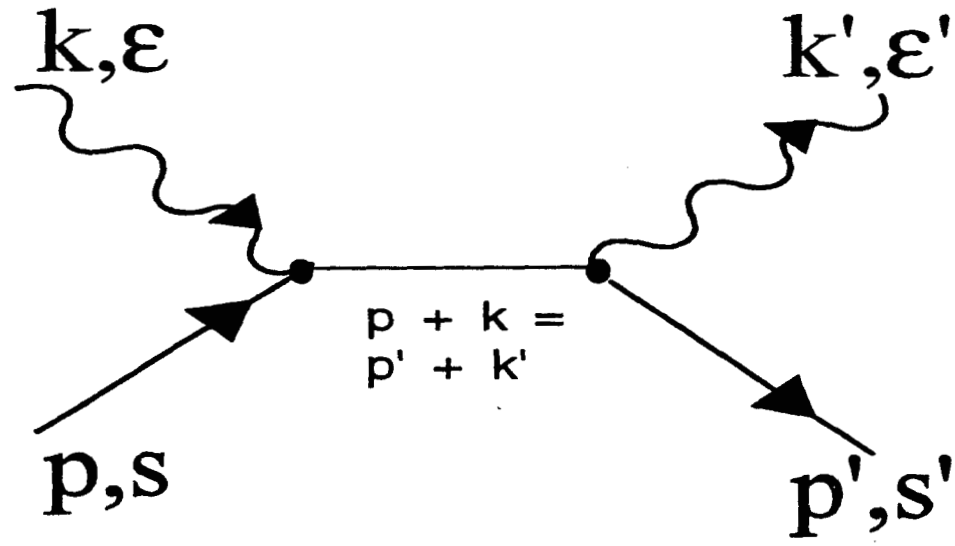

Figure 1.1: Feynman diagram for linear Compton scattering

1.3 Compton scattering

Compton scattering refers to scattering of photons by free electrons and has been treated in many textbooks [1], [26]. An incoming photon with four-momentum k, and polarization vector ϵ is absorbed by an electron with four momentum p and a

second photon with four momentum k' and polarization vector ϵ' is emitted, while the electron recoils with momentum p'. The corresponding Feynman diagram is shown in Figure 1.1 and the conservation of 4-momentum is expressed by the equation:

$$p + k = p' + k' \tag{1.31}$$

Momentum and energy conservation lead to the formula for the energy of the emitted photon:

$$\omega' = \frac{\omega}{1 + \frac{\omega}{m_0}(1 + \cos\theta)} \tag{1.32}$$

where ω, ω' are the energies of the incoming and the outgoing photon respectively, θ is the angle between them in the rest frame of the incoming electron and m_0 is the rest mass of the electron.

The traditional form of the unpolarized cross section for Compton scattering in the electron's rest frame is the Klein - Nishina (KN) equation: [27]

$$\frac{d\sigma}{d\Omega} = \frac{r_0^2}{2}(\frac{\omega'}{\omega})^2(\frac{\omega'}{\omega} + \frac{\omega}{\omega'} - \sin^2\theta) \tag{1.33}$$

where Ω is the solid angle where one observes the emitted photon and the quantity r_0 is the 'classical radius of the electron, a name that originates from the incorrect notion that the rest mass of the electron can be explained in terms of the electrostatic energy of an extended charge sphere. Its value is:

$$r_0 = \alpha\frac{1}{m_0} = \frac{e^2}{\hbar c}\frac{\hbar}{m_0 c} = \frac{e^2}{m_0 c^2} \simeq 2.8 \times 10^{-13}\text{cm} \tag{1.34}$$

In the classical limit ($\omega \to 0$ or $\theta \to 0$) Eq. 1.33 becomes the Thomson cross section:

$$\frac{d\sigma}{d\Omega} = \frac{r_0^2}{2}(1 + \cos^2\theta) \tag{1.35}$$

while in the high-frequency limit $\omega, \omega' >> m_0$, Eq. 1.32 becomes:

$$\omega' \simeq \frac{m_0}{1 - \cos\theta} = \frac{m_0}{2\sin^2\frac{\theta}{2}} \tag{1.36}$$

valid for angles $\theta^2 >> 2m_0/\omega$. In this limit the KN equation becomes:

$$\frac{d\sigma}{d\Omega} = r_0^2\frac{m_0}{\omega}\frac{1}{4\sin^2\frac{\theta}{2}} \tag{1.37}$$

Figure 1.2 is the Compton result between the two limiting cases. Clearly at higher energies of the incoming photon, the angular distribution of emitted photons peaks in the forward (incoming photon) direction.

In this experiment it is more useful to write the differential Compton cross section w.r.t. the outgoing photon energy as in reference [14].

$$\frac{d\sigma}{dy} = \frac{2\pi r_0^2}{x}[(1-y) + \frac{1}{(1-y)} - \frac{4y}{x(1-y)} + \frac{4y^2}{x^2(1-y)^2}] \tag{1.38}$$

where

$$x = \frac{s-m^2}{m^2}$$
$$y = 1 + \frac{u-m^2}{s-m^2} \tag{1.39}$$

The kinematic invariants s, t, u are defined as in [1] using the 4-momentum

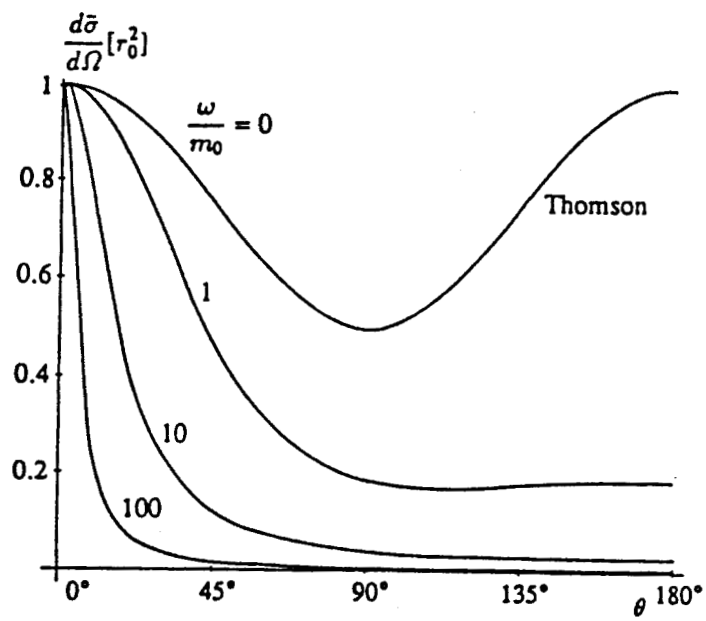

Figure 1.2: Limiting cases of linear Compton scattering cross section as a function of final scattering angle of photons.

conservation law stated above:

$$\begin{aligned} s &= (p+k)^2 = (p'+k')^2 = m^2 + 2pk = m^2 + 2p'k' \\ t &= (p-p')^2 = (k'-k)^2 = 2(m^2 - pp') = -2kk' \\ u &= (p-k')^2 = (p'-k)^2 = m^2 - 2pk' = m^2 - 2p'k \end{aligned} \tag{1.40}$$

and

$$s + t + u = 2m^2 \tag{1.41}$$

Since s and u are invariants, the functions x and y are dimensionless invariants and the last form of the differential cross section for Compton scattering applies to any frame. It can be shown that Eq. 1.38 reduces to the KN expression (Eq. 1.33) [28].

In the laboratory frame one can make some realistic approximations for the functions x and y. There x becomes

$$x = \frac{2\omega(E - p\cos\alpha)}{m^2} \simeq \frac{2\omega E}{m^2}(1 - \cos\alpha) \tag{1.42}$$

where α is the complement of the crossing angle of the electron and the photon and is $\alpha = 163^0$ in this experiment. Also in the lab frame y becomes:

$$y \simeq \frac{\omega'}{E} \tag{1.43}$$

A plot of the differential Compton cross section with the substitution of x and y as above, is shown in Figure 1.3. The total cross section can be found by integrating the differential Compton cross section over all scattered photon energies. Such an integration yields:

$$\sigma_c = \frac{2\pi r_0^2}{x}[(1 - \frac{4}{x} - \frac{8}{x^2})\ln(1+x) + \frac{1}{2} + \frac{8}{x} - \frac{1}{2(1+x)^2}] \tag{1.44}$$

For $E = 46.6$ GeV initial electron energy and $\omega = 1.17$ eV, i.e. infrared laser photons, the total Compton cross section is $\sigma_c = 1.8\times\ 10^{-25}$ cm^2. It becomes $\sigma_c = 3\times\ 10^{-25}$ cm^2 for green laser light.

An analytic calculation of the linear Compton rates for this experiment is possible, if both the laser and the electron beam are treated as cylindrical Gaussians in space. In reality the laser is directed onto the electron beam at an angle of 17^0, which

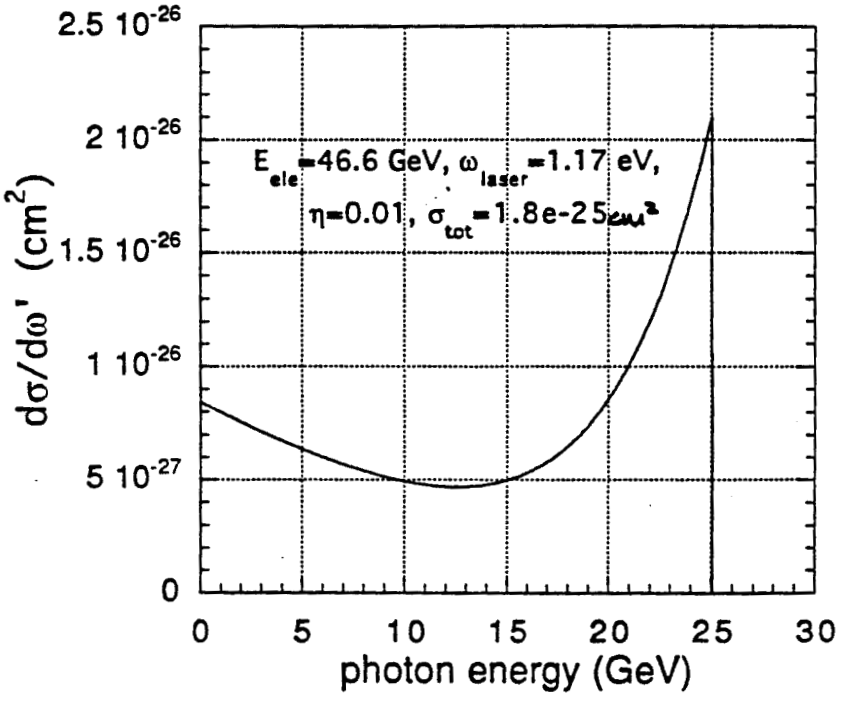

Figure 1.3: Differential linear Compton scattering cross section as a function of scattered photon energy.

complicates the geometry at the scattering region, and is not treated in the analytic calculation. In order to increase the photon density at the interaction point to enhance higher order processes with much smaller cross section than the linear Compton cross section, the laser is focused onto the electron beam. Due to the focusing, the assumption of the cylindrical Gaussian beam in space for the laser pulse is worse for the higher order processes, but is acceptable for the estimate of the linear Compton scattering rates for the following reasons:

The diameter of the laser at its focus in the interaction region is given by:

$$r_f = \frac{\sqrt{2} f_{\#} \lambda}{\pi} \tag{1.45}$$

For infrared laser photons $\lambda = 1.053\ \mu$m. The diameter of the laser beam in the input of the focusing optics, which is an Off Axis Paraboloid (OAP), at the $1/e^2$ point in intensity is 5 cm and the focal length of the OAP is 30 cm, so that $f_{\#} = f/d = 6$

. For these parameters equation 1.45 gives a diameter $r_f = 3$ μm. This diameter projected on the transverse to the electron beam plane due to the 17^0 angle, is much smaller than the electron beam dimensions. The Rayleigh range of the laser is given by:

$$z_R = \frac{4}{\pi} f_{\#}^2 \lambda \tag{1.46}$$

and for the above parameters is equal to $z_R = 0.5$ mm. This also is much smaller than the length of the electron bunch projected on the laser direction. So, indeed, the dimensions of the focal region are much smaller than the electron beam size and for this reason one can assume the laser pulse as a cylindrical Gaussian in space.

With the above assumptions one can write the electron density as

$$n_e(\vec{x},t) = \frac{N_e}{\pi^{3/2}\sigma_{ex}\sigma_{ey}\sigma_{ez}} exp - \{\frac{x^2}{\sigma_{ex}^2} + \frac{y^2}{\sigma_{ey}^2} + \frac{z-ct^2}{\sigma_{ez}^2}\} \tag{1.47}$$

and the photon density as

$$n_\omega(\vec{x},t) = \frac{N_\omega}{\pi^{3/2}\sigma_{\omega x}\sigma_{\omega y}\sigma_{\omega z}} exp - \{\frac{x\cos\theta + z\sin\theta^2}{\sigma_{\omega x}^2} + \frac{y^2}{\sigma_{\omega y}^2} + \frac{z\cos\theta - x\sin\theta + ct^2}{\sigma_{\omega z}^2}\} \tag{1.48}$$

The linear Compton rate is given by integrating over the region of overlap of the two beams at any fixed time and then integrating over time:

$$N_1 = \sigma_c \frac{v_{rel}}{c} \int_{-\infty}^{+\infty} d\vec{x} \cdot cdt \cdot n_e(\vec{x},t) \cdot n_\omega(\vec{x},t) \tag{1.49}$$

where the total Compton cross section is as given previously $\sigma_c = 3 \times 10^{-25}$ cm^2 for green laser photons and $\sigma_c = 1.9 \times 10^{-25}$ cm^2 for infrared. Assuming counter-propagation of the laser and electron beams we get $v_{rel}/c \simeq 2$. For electron beam dimensions of 60 μm $\times$ 60 μm $\times$ 870 μm and infrared laser focused to 70 μm^2 with pulse-length of 2 ps fwhm and energy of 100 mJ the integration yields a linear Compton rate of $N_1 = 1.9 \times 10^6$ gamma rays per shot and at green $N_1 = 7.5 \times 10^5$. During the run-taking-period the parameters of the interaction were varied; the rate was increased 8-fold for the data at the highest laser energy in the IR, and 4-fold in the green. These rates agree with the experimental data as will be shown in chapter 4.

The probability of laser photon - electron interaction per pulse can be estimated as follows: The size of the electron bunch for the particular configuration described above gives a volume of 3.9×10^6 μm^3. The spatial volume of the laser in the green in rms was 2.5 μm × 2.5 μm × 230 μm , i.e. 1.5×10^3 μm^3. Since the number of electrons per bunch is 5×10^9, the number of the electrons interacting each laser pulse from the above estimates is $N_{inter} = 1.9 \times 10^6$. For 100 mJ of green and interaction conditions as stated above the total gamma flux is 7.5×10^5 gammas per pulse. So, electrons that passed through the focus of the laser at peak intensity had close to 40% probability of interacting!

no. of laser photons, n	η=0.0	η=0.2	η=0.5	η=1.0
Infrared laser: ω=1.176 eV				
1	25.3	25.9	27.9	32.8
2	17.4	17.8	19.9	25.3
3	13.2	13.6	15.5	20.6
4	10.7	11.0	12.6	17.4
5	9.0	9.3	10.7	15.0
Green laser: ω=2.353 eV				
1	17.4	17.8	19.9	25.3
2	10.7	11.0	12.6	17.4
3	7.7	8.0	9.7	13.3
4	6.0	6.3	7.3	10.7
5	5.0	5.1	6.0	9.0

Table 1.1: The kinematic edges namely minimal energy of the recoil electrons for IR and green in GeV for 46.6 GeV incident electron energy.

1.4 Nonlinear Compton scattering

In this experiment we studied nonlinear Compton scattering in the interaction of a laser pulse with the electron beam. The electron absorbs n, rather than only one, laser photons to produce a high energy gamma ray:

$$e^- + n\omega_l \longrightarrow e^- + \omega_\gamma \tag{1.50}$$

The diagram for this process is shown in Figure 1.4. If multiphoton Compton scattering takes place in the presence of a strong field, then it can not be described by simple perturbation methods. Furthermore, the four momenta conservation equation can be written for the lab frame as

$$n\omega_\mu + p_\mu = \omega' + p'_\mu \tag{1.51}$$

where ω_μ is the laser photon momentum, p_μ is the electron 4-momentum, and the primes refer to quantities after scattering. A calculation using kinematic arguments

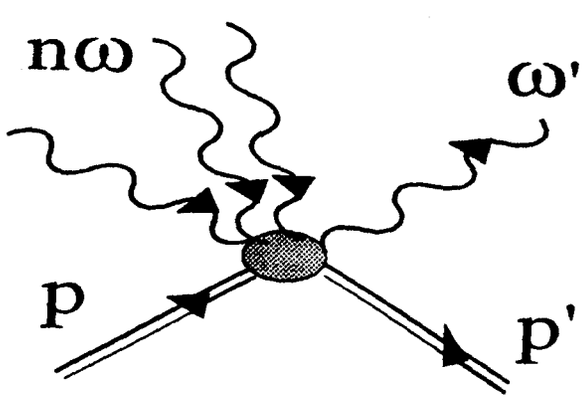

Figure 1.4: Diagram for nonlinear Compton scattering

and equations 1.26 and 1.29 gives the scattered photon's energy:

$$\omega' = \frac{2n\gamma^2\omega(1+\beta\cos\theta)}{2\gamma^2(1-\beta\cos\theta') + (\frac{2n\omega\gamma}{m} + \frac{\eta^2}{1+\beta\cos\theta})(1+\cos\theta\cos\theta' + \sin\theta\sin\theta')} \tag{1.52}$$

Here $\theta = 17^0 = \pi - \alpha$ where α is the angle of the laser direction of propagation with respect to the electron direction of propagation in the laboratory frame; θ' is the angle of the scattered gamma ray direction of propagation with respect to the electron direction of propagation; since the electrons have $\gamma \simeq 10^5$, θ' is very small, the same way as in the linear Compton scattering. The number of laser photons absorbed is denoted by n and η is the parameter defined in the last section. The maximum energy of the scattered gamma rays is given by:

$$\omega'_{max} = \frac{2n\gamma^2\omega(1+\beta\cos\theta)}{1 + \frac{4n\gamma\omega}{m} + \frac{\eta^2}{1+\beta\cos\theta}} \tag{1.53}$$

Equivalently one can detect the scattered electrons, which emerge with energy $E = E_0 - \omega'$ where E_0 is the initial electron energy; therefore $E_{min} = E_0 - \omega'_{max}$. In this experiment $E_0 = 46.6$ GeV and we observed electrons with energies lower than the minimum of the $n = 2$, 3 and 4 kinematic edges. Table 1.1 gives the kinematic edges for our experiment up to 5 absorbed laser photons and with various realistic η values. Since η depends on the laser intensity, which is variable in space and time in the interaction region due to focusing, the integration performed over the volume of the interaction in the experiment smears these edges.

A process comparable in rate with nonlinear scattering, is multiple Compton scattering in which an electron undergoes successive ordinary (linear) Compton scatterings at different points as it traverses the laser focus. The diagram for this process is shown in Figure 1.5. There is also a possibility of linear Compton scattering in the laser focus after the electron has already undergone nonlinear scattering of some order. The contribution of all possible scattering combinations has the visible effect of decreasing the slope of the kinematic edges. This is shown in Figure 1.6 a simulation of recoil electron spectra at realistic laser and electron beam parameters for a sum of these processes. As will be discussed in a later section, the rates for n=2 nonlinear Compton scattering and double ordinary Compton scattering are of the same order

of magnitude in the energy range 20 - 25 GeV. Double Compton scattering depends on the width of the interaction region. In this experiment double Compton scattering presents a serious background, since it can not be resolved from nonlinear Compton scattering when detecting only the recoil electrons. In a future experiment, the gamma spectrum will be measured by converting them in a thin target and studying the resulting pairs with a CCD pair spectrometer [29].

1.4.1 Nonlinear Compton scattering cross section

The nonlinear Compton scattering cross section is easier to calculate for the special case of an electron in a circularly polarized EM field, i.e. circularly polarized laser light:[14]

$$\sigma_{n\omega} = \frac{2\pi r_0^2}{u_1 \eta^2} \int_0^{u_n} \frac{du}{(1+u)^2} [-4J_n^2(z) + \eta^2 (2 + \frac{u^2}{1+u})(J_{n-1}^2(z) + J_{n+1}^2(z) - 2J_n^2(z))] \quad (1.54)$$

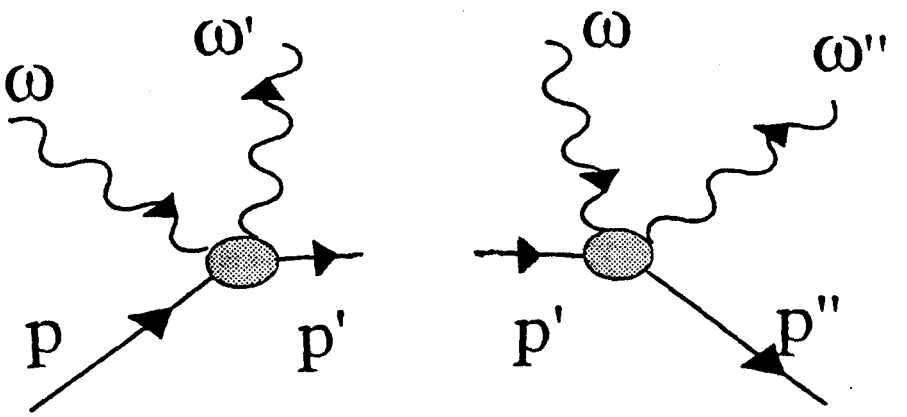

Figure 1.5: Diagram for double linear Compton scattering

where $u = \frac{\omega_\mu \omega'^\mu}{\omega_\mu q'^\mu}$, $u_1 = \frac{2\omega_\mu q^\mu}{\bar{m}^2}$, $u_n = nu_1$ and $z = \frac{2\eta\sqrt{u(u_n-u)}}{u_1\sqrt{1+\eta^2}}$

Since the photons emerge with very small angles $\theta \simeq 1/\gamma$, but also have a broad range of energies, it is more interesting to express the differential scattering cross section as a function of the scattered photon energy, rather than the scattering angle. For this one relates the invariant u to the photon energy by:

$$\frac{du}{(1+u^2)} = \frac{d\omega'}{\gamma m} \tag{1.55}$$

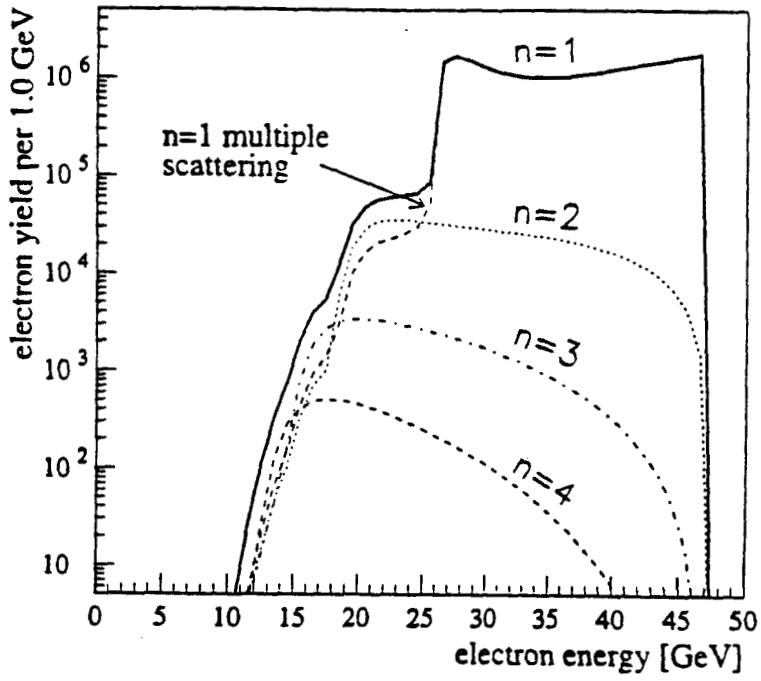

Figure 1.6: Recoil electron rates for linear, nonlinear and multiple Compton scattering for 400 mJ IR laser energy, 70 μm^2 and 2 ps laser parameters and standard electron beam parameters for this experiment. The cross section from Narozhnyi et al. for circularly polarized field was used in the simulation. The solid line is the sum of all possible processes. The n=2, n=3 and n=4 processes are depicted by the dashed lines as pointed in the figure. Single photon linear Compton scattering has a cutoff at about 25 GeV, but due to multiphoton and multiple Compton scattering electrons with smaller energies can be recorded.

in order to get

$$\frac{d\sigma_{n\omega}}{d\omega'} = \frac{2\pi r_0^2}{u_1 \eta^2 \gamma m}[-4J_n^2(z) + \eta^2(2 + \frac{u^2}{1+u})(J_{n-1}^2(z) + J_{n+1}^2(z) - 2J_n^2(z))] \quad (1.56)$$

When $\eta \to 0$ the nonlinear Compton scattering differential cross section given above approximates the linear Compton. The differential cross section with respect to the recoil electron energy can be found by substituting the energy of the scattered gamma in the above equation with the initial electron energy minus the recoil electron energy. Then the scattered electron rate can be found after integrating over the interaction volume as was done for the linear Compton rates. The multiphoton scattering electron rates are shown in Figure 1.6 for 400 mJ of infrared laser focused to $70\mu m^2$ with pulse-length of 2 ps fwhm and with electron beam dimensions of $60\mu m \times 60\mu m \times 870\ \mu m$.

The dependence of the cross section on both parameters η and n reveals the interplay of strong field and multiphoton phenomena. Although theoretically these can be formulated independently, experimentally they are coupled. In this experiment we observed multiphoton processes from free electrons in the presence of a strong field.

1.4.2 Nonlinear and double Compton scattering rates

An analytic calculation of the nonlinear Compton rates can be given following the same assumptions as for the linear rate calculation. It can be shown that the multi-photon Compton scattering rate (P_2), involving only 2 laser photons ($n = 2$), has a relative probability to the ordinary Compton scattering ($n = 1$) rate (P_1) equal to

$$P_2 = 0.8\eta^2 P_1 \quad (1.57)$$

But for circular polarization η is dependent on the laser photon density n_ω as

$$\eta = \frac{e\mathcal{E}}{m\omega c} = \frac{e}{m\omega c}\sqrt{n_\omega \omega} = \frac{e}{mc}\sqrt{\frac{n_\omega}{\omega}} \quad (1.58)$$

or $\eta^2 = An_\omega$ with $A = (\frac{e}{mc})^2 \frac{1}{\omega}$ and $A = 2.2\times\ 10^{-27}$ cm^3 for green wavelength laser pulses. Then taking into account the treatment of the linear Compton rate we conclude that the number of n=2 scatters is:

$$N_2 = 0.8A\sigma_c(\frac{v_{rel}}{c}) \int_{-\infty}^{+\infty} d\vec{x} \cdot cdt \cdot n_e(\vec{x}, t) \cdot n_\omega^2(\vec{x}, t) \quad (1.59)$$

Assuming green laser photons and laser and electron beam dimensions as in the linear rate calculation we estimate that $N_2 \simeq 2 \times 10^4$ for laser energy of 400 mJ.

The competitive to n=2 multiphoton scattering process is the double scattering of the electron off the laser photons, as previously discussed and can be calculated through:

$$N_d = \sigma_c \frac{v_{rel}}{c}^2 \int_{-\infty}^{+\infty} d\vec{x} \cdot cdt \cdot n_\omega(\vec{x}, t) \cdot \int_{-\infty}^{t} cdt' \cdot n_e(\vec{x}', t') \cdot n_\omega(\vec{x}', t') \tag{1.60}$$

Using the same electron and laser parameters as above we estimate the double scatters yield to be of the same order as the n=2 multiphoton scatters yield. This result is compatible with the simulation as shown already in Figure 1.6.

1.5 Critical electric field of QED and multiphoton Breit-Wheeler process

In an electromagnetic field with strength that approaches the critical field, QED phenomena scale nonlinearly with this strength. This critical field is defined as the field in which an electron in one Compton wavelength gains energy equal to its rest mass:

$$\mathcal{E}_{crit} = \frac{m^2 c^3}{e\hbar} = 1.3 \times 10^{16} \text{ V/cm}. \tag{1.61}$$

The corresponding critical magnetic field is

$$\mathcal{B}_{crit} = 4.4 \times 10^{13} \text{ Gauss}. \tag{1.62}$$

By requiring that the rms electric field in the laser focus is equal to the critical field in the electrons' rest frame the laser intensity required in the lab is given by

$$I = \frac{1}{Z_0} \frac{\mathcal{E}_{crit}^2}{4\gamma^2} = 1.4 \times 10^{19} \text{ Watts/cm}^2. \tag{1.63}$$

This intensity can be achieved using the Table Top Terawatt laser (T^3) described in a later Chapter.

Critical electromagnetic fields can be found in nature at the surface of neutron stars [30, 31], or in the rest frame of very high energy cosmic ray electrons entering the

earth's field. In the laboratory apart from this experiment they can also be present in collisions of MeV heavy ions due to the combined Coulomb field from the two nuclei [32].

It is valid to view the interaction of the electrons in the laser field as a two step process: First nonlinear Compton scattering; second Breit-Wheeler pair production. In the Breit-Wheeler process a gamma ray absorbs many laser photons and creates a pair. Pair creation by real photons

$$n\omega_0 + \omega \longrightarrow e^+e^- \tag{1.64}$$

is a cross-channel process from nonlinear Compton scattering, and for circular polarization of both the laser photons and of the high energy photon the cross section is given by: [17, 18]

$$\frac{d\sigma_n}{dy} = \frac{2\pi r_0^2}{x}[\frac{4}{\eta^2}J_n^2(z) + (u-2)(J_{n-1}^2(z) + J_{n+1}^2(z) - 2J_n^2(z))] \tag{1.65}$$

where (for $n\omega_0 << \omega$)

$$x = \frac{4\omega_0\omega}{m^2},\ y = \frac{E_e}{\omega},\ y_{max,min} = \frac{1}{2} \pm \sqrt{\frac{1}{4} - \frac{1+\eta^2}{nx}},\ u = \frac{1}{y(1-y)}$$

and z is defined as in Eq. 1.54.

The thresholds for pair production in this experiment are calculated as follows: When a backscattered photon with energy ω absorbs n laser photons ω_l and produces an e^+e^- pair, the invariant s can be written before and after the interaction:

Before:

$$s = (\omega + n\omega_l)^2 - (\vec{p}_\omega - n\vec{p}_{\omega_l})^2 = 2n(\omega\omega_l + \vec{p}_\omega\vec{p}_{\omega_l}) = 4n\omega\omega_l \tag{1.66}$$

After:

$$s = (2m)^2 \tag{1.67}$$

By also introducing the effect of the mass shift of the electron as discussed before, the expression for the gamma energy required for threshold pair production from n laser photons now becomes:

$$E_n = \frac{m^2(1+\eta^2)}{n\omega_0} \tag{1.68}$$

For example, a gamma ray produced in the interaction of a green laser photon with a 50 GeV electron beam due to linear Compton scattering, has a maximum energy of 36.5 GeV. At this energy at least four more laser photons are required for pair production using Eq. 1.68.

Since we have only one interaction region, it is difficult to distinguish experimentally this process from direct trident production. However under the experimental conditions the trident rate is at least 10 times lower than the two step process. The study of pair production could be extended in the future to explore the structure, if any, in the invariant mass spectrum of the pair. For this purpose one can use the same CCD pair spectrometer that would also investigate the gamma spectrum of the nonlinear Compton scattering, as discussed in a previous section. The measurement of the mass spectrum of the pairs produced in the scattering of light by light (in the low mass region of 1.0 - 2.0 MeV, with a mass resolution of 10 keV) could reveal the existence of a new phase of QED at these high fields [32, 33].

The creation of positrons by direct pair production can be of use at future e^+e^- accelerators [34]. At present positrons are produced with high emittance by scattering electrons on a solid target. Then the positron beam emittance is reduced in damping rings. In our geometry the laser focus can also be considered as a target that produces positrons, but due to the absence of heavy nuclei the positrons created preserve the geometric emittance of the electron beam. Therefore, damping rings are not required and the potential luminosity and cost of the collider will be more favorable.

Finally it has been recognized that linear e^+e^- colliders could also be operated as $\gamma - e$ or $\gamma - \gamma$ colliders [35] - [37]. For such operation the high energy γ beam will be best provided by an intense short-pulse laser as used in this experiment. The present experiment has already demonstrated a conversion efficiency of 40% for the electrons traversing the laser focus into high energy photons.

1.6 Beamstrahlung

An alternate view to consider pair production was given by Chen and Telnov [21]. In future linear colliders, the electron bunches will be tightly focused and during collision

the electrons of one of the colliding bunches will be experiencing the Coulomb field of the other bunch. That will create high energy gammas in a similar fashion that an electron scattered from the field of a nucleus generates bremsstrahlung radiation. These high energy gammas can now interact again with the EM field of the other bunch and produce pairs. These lower energy pairs can cause background problems and constrain the geometry of the detector of the experiment. A detector for positrons was used in the experiment and recorded a weak signal. Since the pair production has a highly nonlinear dependence on the laser intensity, future experiments with increased laser energy will study this process extensively.

From simulations, this kind of 'beamstrahlung pair production' is possible, if the laser intensity is increased to a level where $\Upsilon \simeq 0.3$ as defined in Appendix B. The dependence of the number of pairs per incoming electron to this parameter is [21]:

$$n_p = \frac{4\sqrt{3}}{25\pi}[\frac{\alpha\sigma_z}{\gamma\lambda_c}\Upsilon]^2\Xi(\Upsilon)]\Upsilon << 1 \tag{1.69}$$

where σ_z is the root-mean-square longitudinal length of the laser focal region, α is the fine structure constant, λ_c is the electron Compton wavelength and the function $\Xi(\Upsilon)$ decreases exponentially for $\Upsilon << 1$. The last equation is obtained from the re-scattering of real photons and, therefore, depends quadratically on σ_z since it describes a two-step process. Also the contribution of virtual photons (tridents) is very much suppressed for $\Upsilon << 10$. For $\Upsilon = 0.3$, $\gamma = 10^5$ and $\sigma_z = 100\mu$m

$$n_p \simeq 8 \times 10^{-7} \text{ pairs per incoming electron.} \tag{1.70}$$

In this experiment the number of electrons interacting in every laser shot is 5×10^9. Therefore, the rate of pairs produced should be substantial.

1.7 Summary

As discussed above, the theory of the nonlinear Compton scattering and pair production mechanisms can be investigated in the field of the laser of this experiment. In the following chapter the experimental setup that allowed for such studies of nonlinear QED phenomena is presented. The data and conclusions only from the investigation

of the nonlinear Compton scattering process will be described in the third and fourth chapters, while results for the pair production process are a subject of another thesis [22].

Chapter 2

Apparatus

The experimental ingredients necessary to study multiphoton Compton scattering are two: A high energy electron beam, in order to probe strong electric fields which also become even stronger in the electrons' rest frame due to the relativistic boost and an intense laser in order to achieve the necessary electric fields at its focus.

For the first reason this experiment was performed in the Stanford Linear Accelerator Center, Figure 2.1, located in Stanford, California. This linear accelerator (LINAC) delivers 46.6 GeV electrons with the ability of polarizing them using a photocathode rf gun as their source. Our experiment is located at a newly constructed line, the Final Focus Test Beam (FFTB). This facility is a prototype used to address some of the challenges of the construction of the Next Linear Collider (NLC) and especially to study the focusing of high energy electron beams in spot sizes that are ten times smaller than the wavelength of visible light.

For the second reason the laser is a solid state laser that can reach terawatt intensities, with satisfactory high repetition rates. It is a Table Top Terawatt (T^3) laser since it can fit on the top of four optical tables. It delivers the laser pulses at the interaction point with high timing and spatial stability due to an elaborate optical transport system. A timing system to tune the synchronization of the laser with the electron beam at the ps level is employed by locking the laser to the accelerator rf using both an electronic feedback on the laser pulse timing and an optical delay to scan this timing.

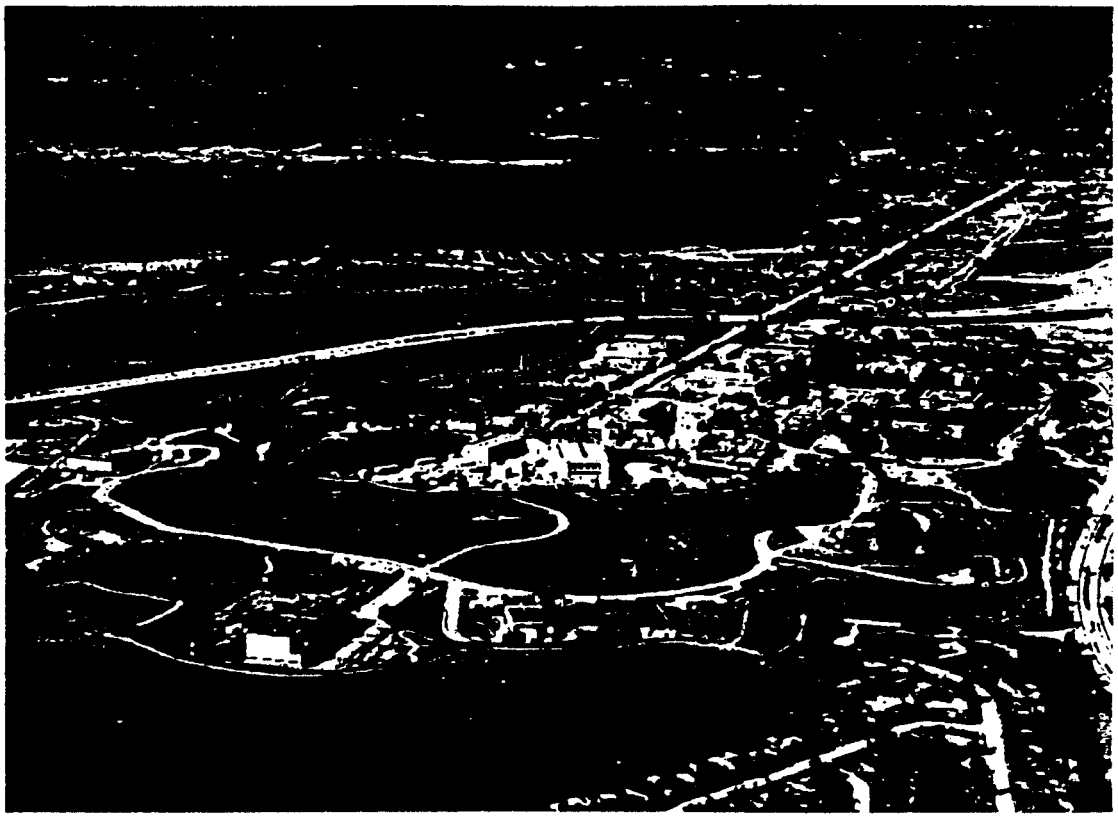

Figure 2.1: The Stanford 2 mile Linear Accelerator (SLAC)

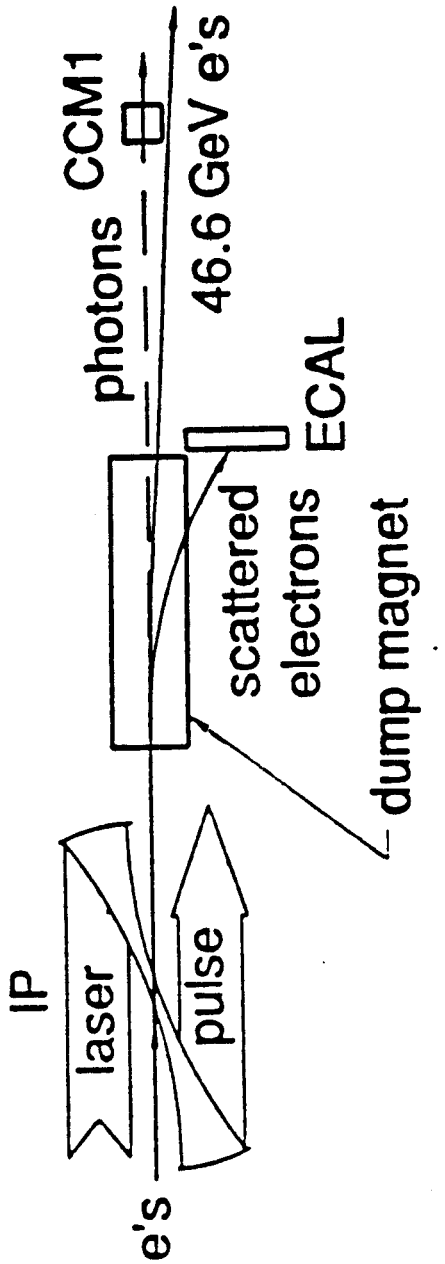

Figure 2.2: Schematic of the experimental setup: The laser pulses interact with the electrons in the interaction point (IP). The scattered electrons are bent by the dump magnets into the electron calorimeter (ECAL). The scattered photons are detected by the Cherenkov counter (CCM1)

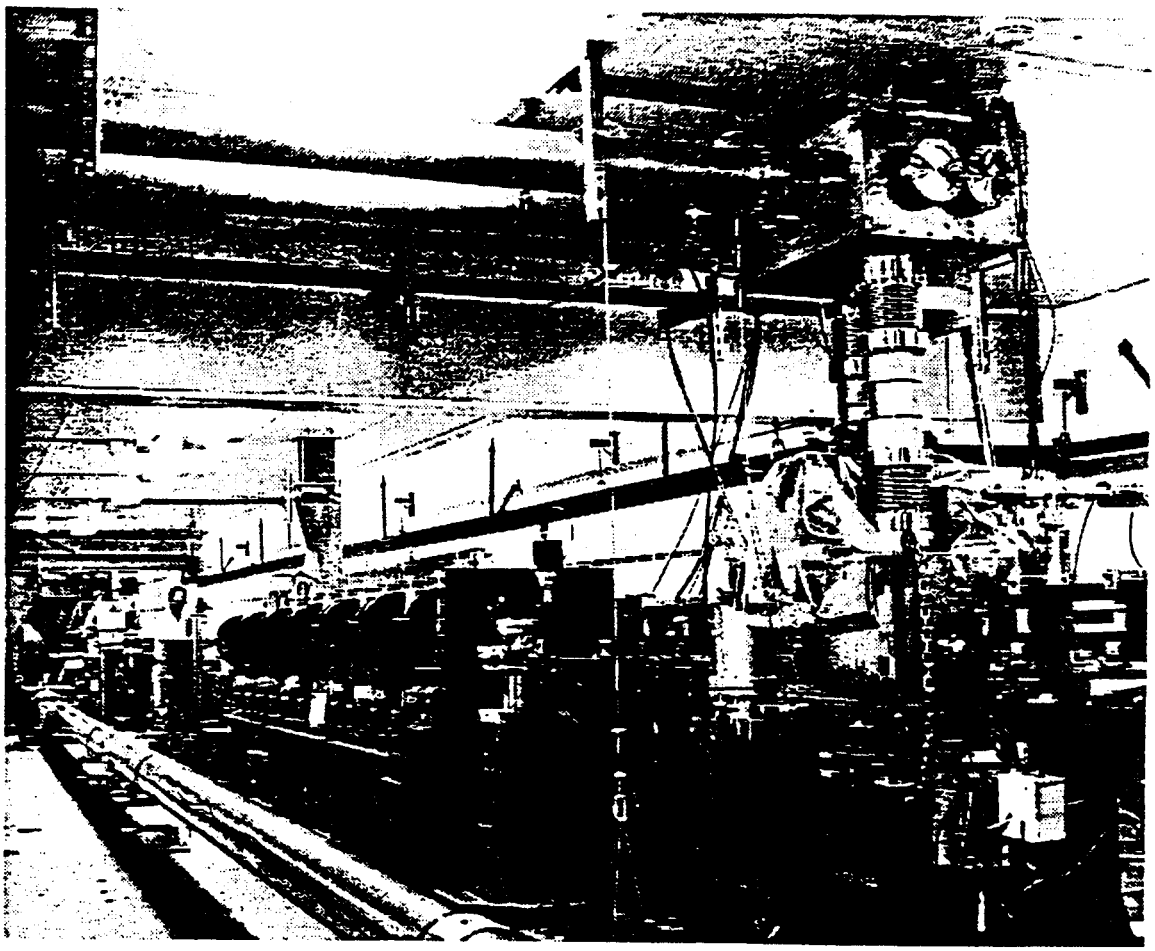

Figure 2.3: Picture of the experimental setup in the FFTB tunnel

The main detectors of the experiment are a calorimeter that collects the multi-photon Compton scattered electrons and a monitor that detects the forward scattered total photon flux. A PC based data acquisition system efficiently collects and analyzes the data that are presented in subsequent chapters. Figure 2.2 gives an overview of the experimental setup and Figure 2.3 is a picture inside the electron beam tunnel, looking downstream with respect to the electron motion.

2.1 Electron beam

The FFTB setup is particularly suitable for this experiment due to: (a) the 46.6 GeV energy of the electrons, (b) the low emittance of the electron beam, and (c) its tunability (regarding spot sizes, low backgrounds, and electron charge per bunch). Moreover, the existing equipment, such as the dump magnets of the electron beam, were useful for the electron spectrometer. Table 2.1 gives some of the electron beam parameters.

Although the interaction point is located 12 m downstream of the final focus, we were able to tune the beam to small bunch sizes of the order of $40\mu m \times 40\mu m \times .8mm$ in $\sigma_x \times \sigma_y \times \sigma_z$ where z is along the electron beam path. This can be seen in Table

Parameter	FFTB
Beam Energy (GeV)	46.6
Emittance $\gamma\epsilon_y(rad-m)$	3×10^{-6}
Focusing $\beta_y^*(\mu m)$	100
Demagnification	380
Beam Height $\sigma_y(nm)$	60
Aspect Ratio	15
Bunch Length $\sigma_z(\mu m)$	500
Bandwidth $\delta p/p(\%)$	± 0.3
Bunch Population (10^9)	5 - 20

Table 2.1: Parameters of the Final Focus Test Beam

Run no.	$\sigma_x(\mu m)$	$\sigma_y(\mu m)$	$\sigma_z(\mu m)$	nominal e^- config.
12101 - 12223	60	80	650	1
12224 - 12287	60	80	1080	2
12292 - 12304	85	40	870	3
12305 - 12358	67	32	870	4
12359 - 12435	47	85	1080	5
12436 - 12470	127	40	870	6
12471 - 12503	40	43	870	7

Table 2.2: The dimensions of the electron bunch, during the running period of March '95

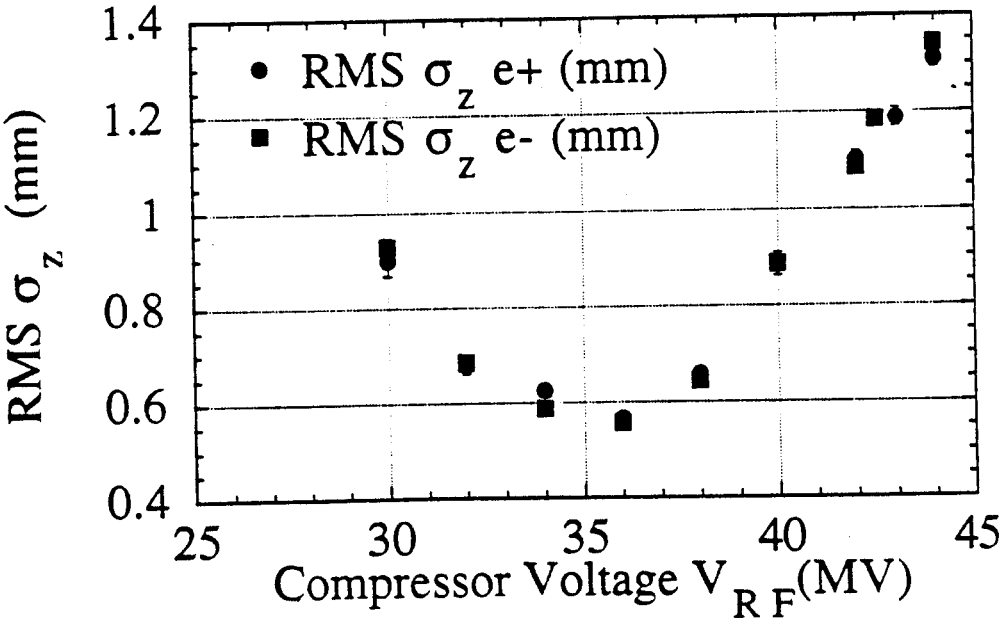

Figure 2.4: Length of the electron bunch as a function of the bunch compressor settings

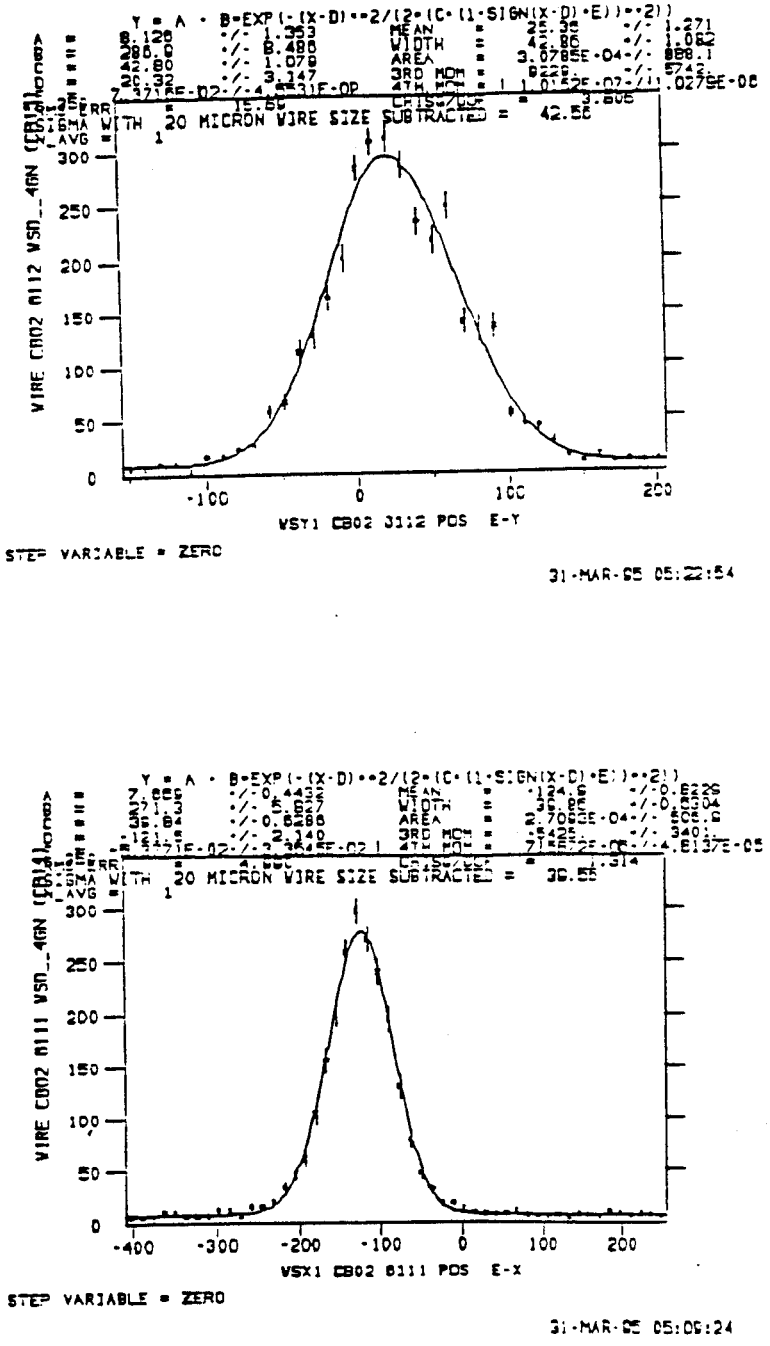

Figure 2.5: The dimensions of the electron beam in IP, using a wire scan: $\sigma_x = 39.55$ μm and $\sigma_y = 42.56$ μm

2.2 where the electron size is shown for some of the runs of this experiment. The horizontal and vertical dimensions were measured by scanning the electron beam over the wire in the interaction point (IP). The longitudinal dimension of the bunch is tunable by varying the energy compressor settings and was measured using the calibration of Figure 2.4 from [39]. The effect of timing jitter in the synchronization of the 1.5 ps laser pulses with the electron bunches is smaller for longer electron bunches. For this reason, the electron beam bunch length was increased to 3.6 ps (rms) for the nonlinear Compton scattering experiment. Figure 2.5 is a wire scan of the electron beam at the interaction point for a typical run configuration. The beam configuration was changed when we searched for positrons in order to have the smallest possible spot in IP and the lowest backgrounds. We must note that beam backgrounds can be due to scattering from the electron pipe, collimators etc., but mostly originate in the collimators of the electron beam, upstream of the IP, and propagate with the beam to the interaction point; therefore, are difficult to eliminate.

The electron beam parameters recorded in a typical run are the charge distribution, the energy spread of the beam relative to the 46.6 GeV central energy and the position and angles of the beam as measured by beam position monitors (BPMs) located close to the IP. The beam charge and energy is plotted in Figure 2.6. The shape of the energy distribution is typical for a linear accelerator [40]. Apart from the double peaking of some of these parameters, which is due to the various tuning configurations of the electron beam in the IP, they are very stable and within the tolerances of the experiment.

Although the repetition rate of the electron beam can be as high as 30 Hz, the experiment is limited by the laser repetition rate which is 0.5 Hz in normal operating conditions. For this reason, and for collecting electron beam background data when the laser is not firing, we operate the electron beam at 10 Hz. At the detector calibration runs we have increased the beam rate as high as 120 Hz. Some data were taken with a new mode of LINAC operation in which pulses of as few as 10^7 electrons were transmitted at 1 Hz for 9 seconds, alternated with 30 Hz pulses of 5×10^9 electrons for 1 second, while the LINAC feedback system was operational.

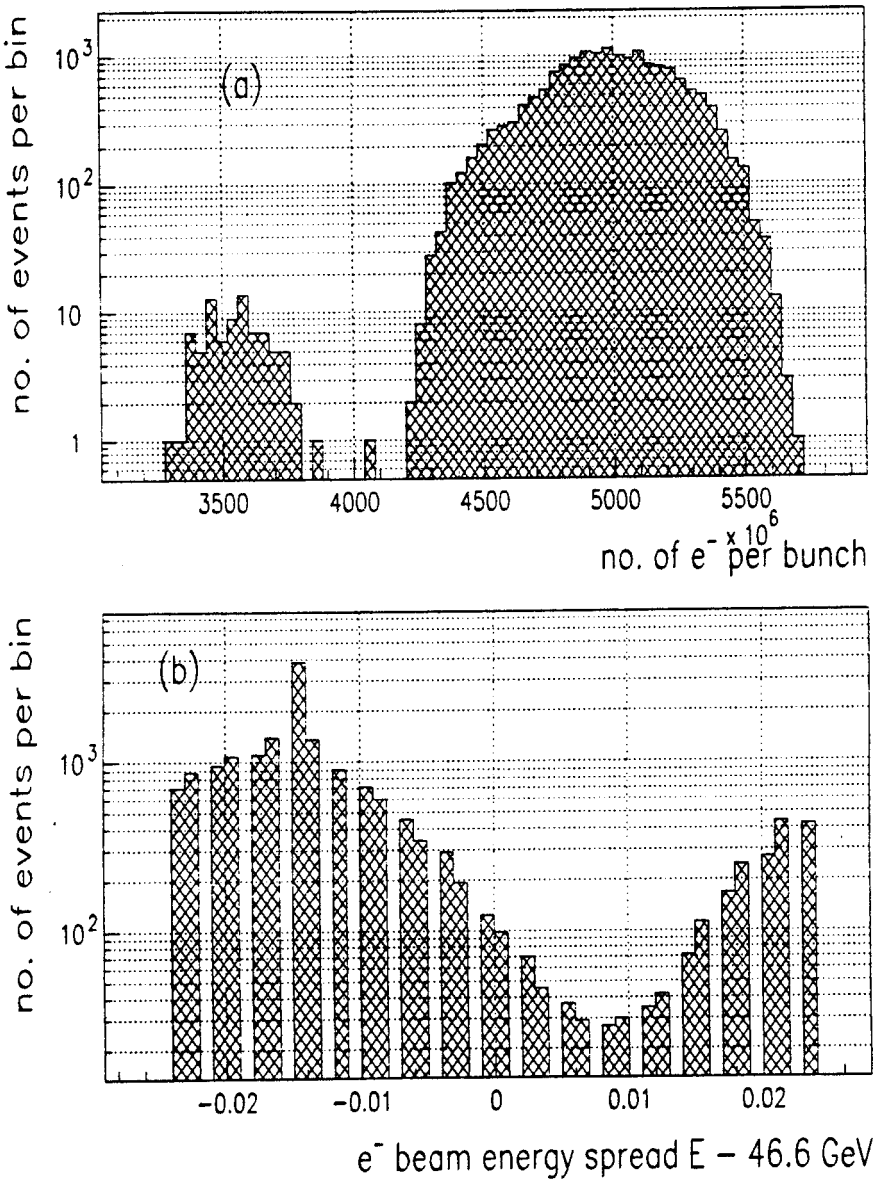

Figure 2.6: Electron beam parameters for the IR runs: (a) Beam charge, (b)Beam energy relative to 46.6 GeV.

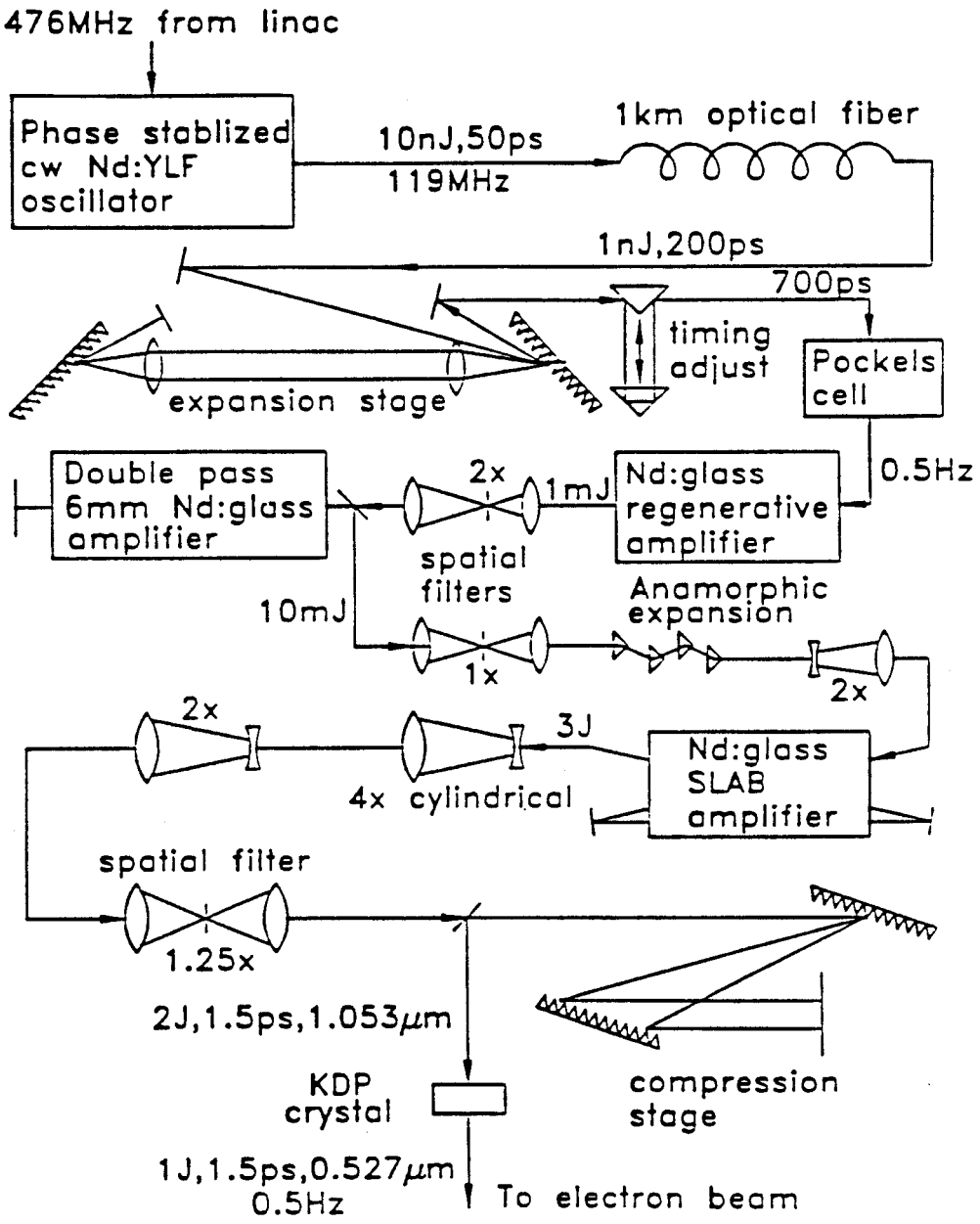

Figure 2.7: The laser system schematic

2.2 Laser

The laser is a 0.5 Hz repetition rate, table top terawatt (T^3) laser, that operates at 1.053 μm wavelength (IR) or after efficient ($\sim$ 45 %) frequency doubling at 0.527 μm (green)[43]. While it has delivered 2.4 J in the IR at the interaction point, during the nonlinear Compton studies described here the maximum energy achieved was 800 mJ of IR and 320 mJ of green. The laser has been focused to a minimum of 1.4 times the diffraction limited area. The smallest pulse-length achieved during the running period was 1.5 ps FWHM. With an average power of 1 Watt, intensities above 10^{18} W/cm^2 at the laser focus have been produced. The laser is based on the Chirped Pulse Amplification (CPA) technique ([44, 45]) and it consists of a mode-locked Nd:YLF oscillator, a Nd:glass regenerative amplifier, a two pass Nd:glass rod amplifier and finally a flashlamp-pumped Nd:glass slab amplifier. A schematic of the laser system is shown in Figure 2.7.

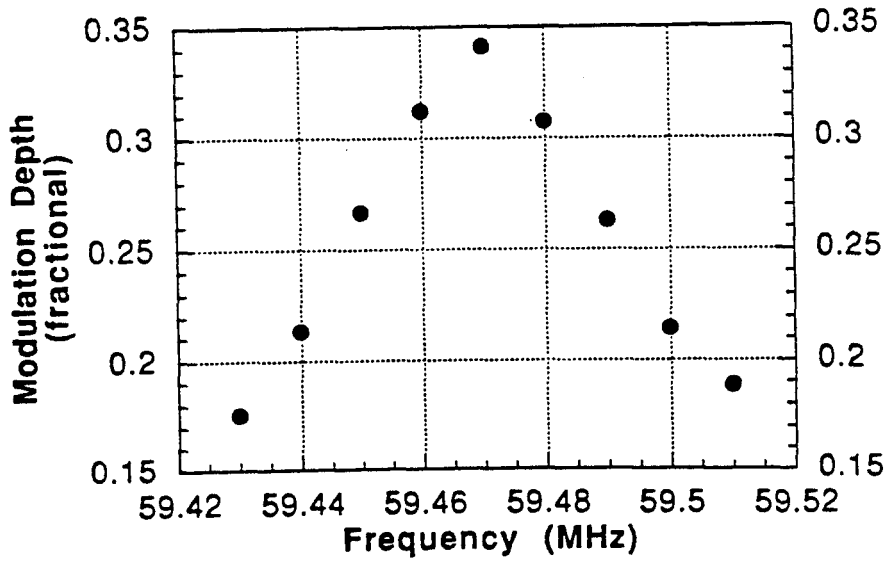

Figure 2.8: Resonance frequency and quality factor Q estimate of the ML crystal

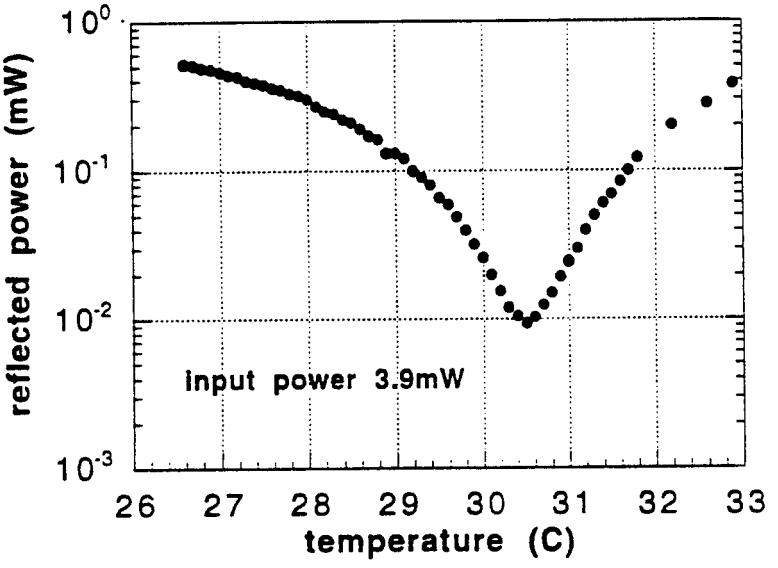

Figure 2.9: Temperature dependence of the resonance frequency of the ML crystal

In order to collide a laser pulse with an electron bunch the front end of the laser, i.e. the oscillator, must be locked to the accelerator rf. For that purpose we transport the 476 MHz reference signal from the accelerator master clock into the laser room, with a system described in a later section. After frequency dividing, this signal is used to drive the acoustooptic mode-locker of the cw-pumped oscillator at 59.5 MHz, while the phase of the laser pulses with respect to the reference is maintained by a phase-locked loop.

The low-Q mode-locker [46] is driven from the reference 59.5 MHz signal after amplification from a power amplifier to 4W. The Q was measured to be $Q \simeq 1400$. with the following setup: A synthesizer operating at frequencies around 59.5 MHz was amplified to 4W and used to drive the ML. A He-Ne laser was aligned through the center of the ML and a fast photodiode was positioned to detect the He-Ne laser light after the ML on the 0th order Bragg reflection. The signal from the diode was send to a spectrum analyzer and to a 400 MHz oscilloscope. The frequency of the synthesizer was varied and Figure 2.8 gives the fractional modulation depth of the He-Ne light. From the last Figure we see that at FWHM of fractional modulation $\Delta f = (59.515 - 59.430)MHz = 85kHz$ and the peak is centered at 59.47 MHz. Then the quality factor of the ML is:

$$Q = \frac{2 * f_0}{\Delta f} = 1400 \tag{2.1}$$

The optimum temperature of the ML is measured to be 30.5 C^0 after a study where the power in the ML was kept at 4W, while the temperature was varied and the reflected power from a forward coupler using a power meter was monitored, Figure 2.9.

The oscillator produces a 119 MHz train of 50 ps pulses at a wavelength of 1053.5 nm. The oscillator pulse train goes through a Faraday rotator to ensure minimal reflection backwards into the cavity, and then through two wave-plates that can be adjusted to vary the polarization and power into an optical fiber. The optical fiber is 1 km long, single mode with a 9 μm core [47]. In the fiber the pulses undergo a stretching in time and also a chirping in frequency due to the effects of self phase modulation (SPM) and group velocity dispersion (GVD) [48]. The pulses out of the

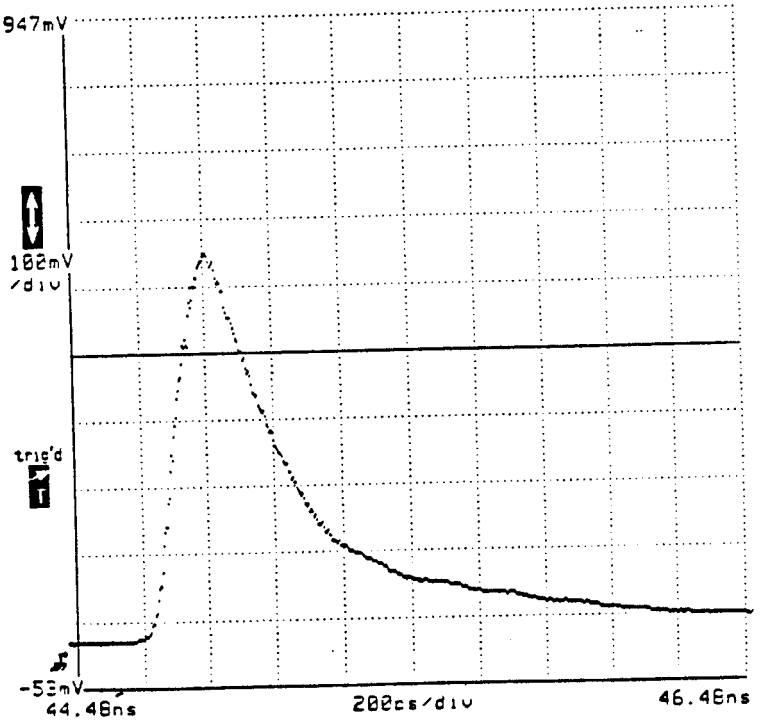

Figure 2.10: The oscillator pulse after dispersion in the optical fiber

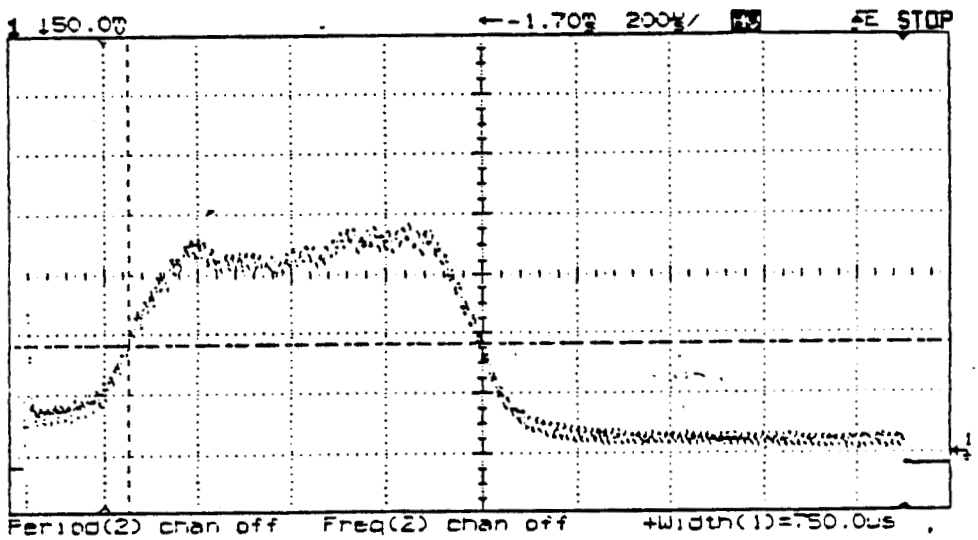

Figure 2.11: The bandwidth of the oscillator pulses after dispersion in the optical fiber is 27$\AA$ using the grating spectrometer calibration of 7.6 Åper division

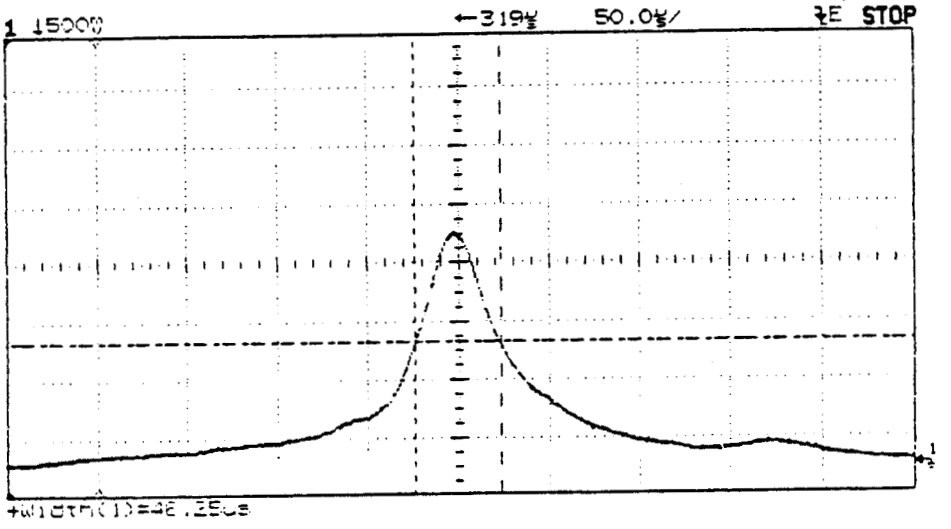

Figure 2.12: CW autocorrelator trace of oscillator pulse after is being dispersed in the fiber and then compressed with a grating pair. Taking into account the calibration of the autocorrelator this measurement corresponds to 1.2 ps FWHM laser pulse-length

optical fiber are detected by a large bandwidth photodiode (20 GHz), and recorded on a sampling scope. Typically they have a pulse-width of 250 ps as shown in Figure 2.10. The bandwidth of these pulses is 27 $\AA$ at the FWHM point, centered around 1054 nm, as measured by a grating spectrometer in Figure 2.11.

The grating spectrometer consists of a narrow vertical slit to allow only a fraction of the laser pulse for spectral analysis, a lens to match the distance to the detector and a grating with 1000 lines/mm and its grooves positioned vertically. The detector is a reticon [49] with only horizontal resolution and is 14 mm long. The spectrometer is calibrated with a red laser diode as follows: The grating equation is

$$\sin\theta_i + \sin\theta_0 = n\frac{\lambda}{D} \tag{2.2}$$

where $\theta_i = 23^0$ and $\theta_0 = 80^0$ are the input and output angles of the laser on the grating measured from the perpendicular to the grating axis, n is the order of dispersion, λ = 1.05 μm and D is the grating groove spacing. The angular spread of the dispersion after the grating is given after differentiation of Eq. 2.2 and substitution:

$$d\theta_0 = \frac{d\lambda}{D}\frac{1}{\cos\theta_0} = 5.99 \times 10^{-2} rad. \tag{2.3}$$

This angular spread translates to a spread horizontally on the face of the reticon. located at distance l = 33 cm away, equal to $\delta x = d\theta_0 l$ = 20 mm. Since the reticon is 14 mm, it can detect a total of 70 $\AA$. On the other hand, the total length of the reticon corresponds to 1.85 ms on the oscilloscope . Thus a calibration of 3.8 $\AA$/100 μs for the spectrometer applies to Figure 2.11.

The pulse after the fiber is also partially collected by a 2.5 GHz photodiode that provides one input to the Time Stabilizer phase locked loop, as described in detail at the timing system section. A cw autocorrelator monitors pulses compressed by a small grating stage, in order to ensure the compressibility of these pulses before they are transmitted through the rest of the laser chain. Figure 2.12 shows a measurement of 1.2 ps laser pulse-length taking into account the calibration of the cw autocorrelator.

The pulse exiting the fiber is further dispersed by an expansion grating pair. Pulse-widths recorded by a streak camera [50] after the expansion stage as seen in Figure 2.13, show that the pulse in time follows the shape of the pulse in frequency domain

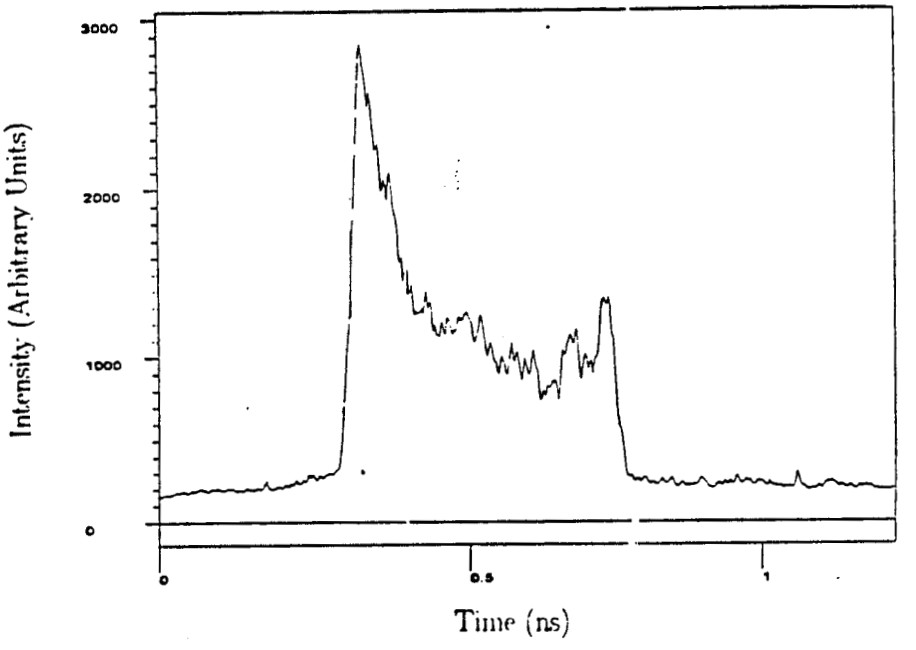

Figure 2.13: Laser pulse-width after the expansion stage

recorded by the grating spectrometer. Furthermore, the chirping of the expansion can be measured by studying the total width of the pulse in time as a function of the FWHM of the bandwidth. From this linear correlation we estimate that the pulses are chirped approximately 700 ps across a 28 $\mathring{A}$ bandwidth:

$$\frac{\Delta t}{\Delta \lambda} = 22 \frac{ps}{\mathring{A}} \tag{2.4}$$

which is compatible within error with the standard theoretical treatment [51, 52], and the geometry of the expansion stage setup.

The energy of a laser pulse at this stage of the system is about a nanojoule and after it travels through a prism on a mechanical stage (which is the optical delay line for the fine adjustment of the timing overlap of the laser pulse with the electrons) is ready to be injected in the regenerative amplifier. A single pulse is selected out of

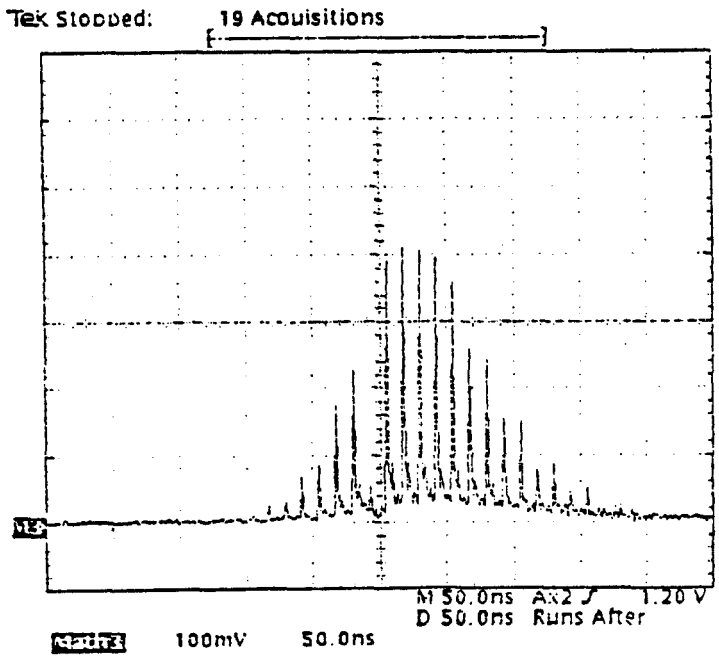

Figure 2.14: Regenerative amplifier pulse train. The missing pulse has been selected by a Pockels cell and continues to the rest of the laser system

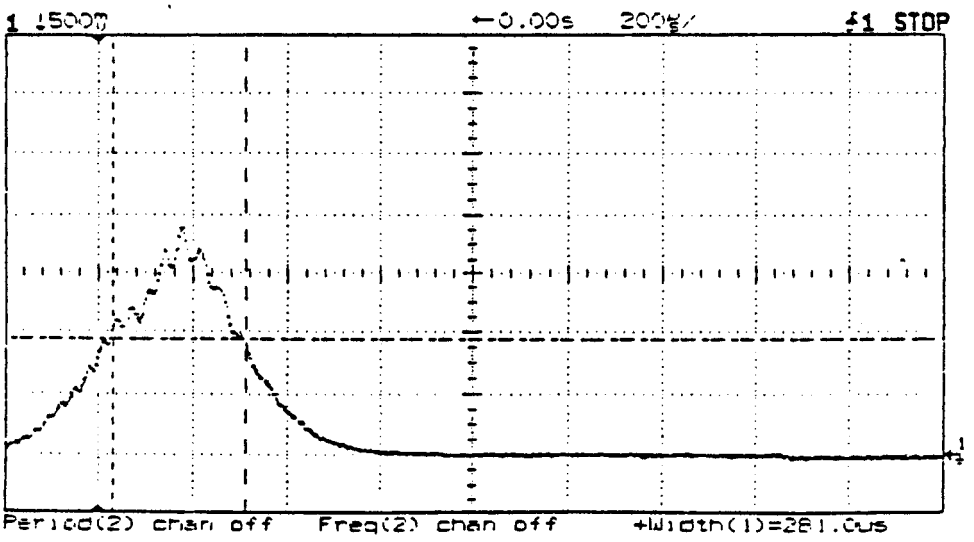

Figure 2.15: The bandwidth of the pulse after the regenerative amplifier reveals the effect of gain narrowing

the 119 MHz pulse train by a Pockels cell and seeded into a Q-switched, end-mirror-dumped regenerative amplifier. The amplifier medium is a 6-mm diameter Nd:glass rod [54]. The pulse train out of the amplifier is shown in Figure 2.14. One more Pockels cell is used to select one of these pulses, with energy about 1 mJ, pulse-width of 700 ps and repetition rate of 0.5 Hz. Although the regenerative amplifier is operational at even larger repetition rates, the rest of the amplifier chain presents limitations in this repetition rate. These limitations come from thermal effects that create stresses on the amplifier's active medium and for this reason define a preferred direction for the laser polarization. If the input to the amplifier polarization does not coincide with the preferred axis, depolarization effects occur that destroy the laser pulse wavefront. For this purpose the repetition rate must be low in order to allow for sufficient cooling. Another consideration at this part of the laser system is gain narrowing in the regenerative amplifier [58]. This effect reduces the spectrum to a Gaussian with bandwidth of approximately 12 Å, as seen in Figure 2.15 which is measured using the grating spectrometer on a single pulse out of the regenerative amplifier. The bandwidth necessary to produce 1.0 ps pulses after compression at the end of the laser system is 16 Å, and due to gain narrowing to 12 Å, we can only achieve 1.3 ps after compression which is consistent with the experimental data.

An air spatial filter up-collimates and spatially cleans the pulse before it is amplified by a double-pass, 6 mm diameter and 160 mm long amplifier [54]. Due to depolarization effects on this amplifier, the maximum energy per pulse achieved is 10 mJ. Burn-marks of the amplifier when is operated at a high voltage setting of 1900 V clearly show the 'Maltese cross' due to depolarization effects as seen in many textbooks [58]. For this reason the highest voltage setting is set empirically where depolarization effects are absent.

A 1 m long vacuum spatial filter with equal focal length lenses cleans the spatial profile of the beam, which had picked up intensity variations from scattering by optical defects or particles in the air or on the optics upstream in the laser system. In the focus of the first lens, an image of the 'source' is produced with all the imperfections in the optical path de-focused in an annulus centered on the optical axis with radius

$$D_n = \frac{F\lambda}{dn}$$

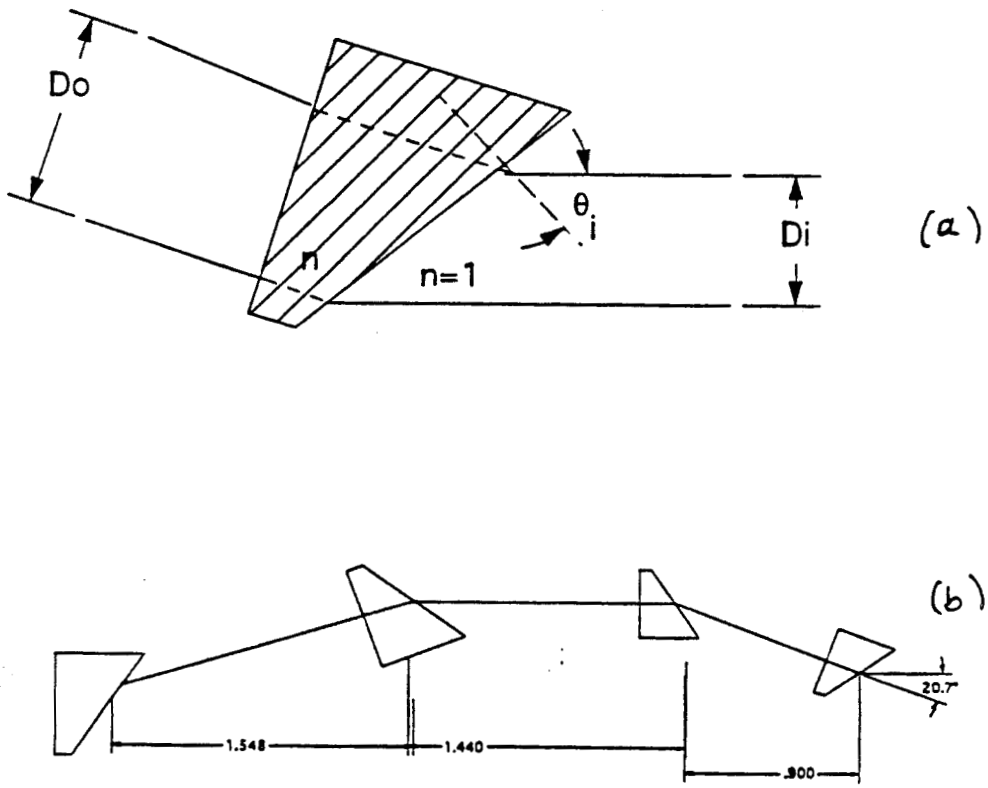

Figure 2.16: Anamorphic expansion setup

where F=50 cm is the focal length of the lens, λ = 1053 nm the IR wavelength and d_n is the wavelength of the noise of the beam intensity, which ideally has a Gaussian profile. If the radius of this ideal profile at the $1/e^2$ point is α, then a pinhole at the focus with diameter

$$D = \frac{F\lambda}{\alpha}$$

blocks all noise with spatial wavelengths smaller than 2α; therefore, the outgoing beam has a profile very close to the ideal and 99% of the initial intensity remains. In this experiment $\alpha_{max} \simeq 3$ mm as defined by the aperture of the 2-pass amplifier, which gives a pinhole diameter of 170 μm. As we found during the course of the experiment we could use larger diameter pinholes, since the input beam to the spatial filter has a radius less than 1.5 mm. Currently a 400 μm diamond pinhole is used due to the high intensities produced in the focus of the laser and its mount allows scans vertically and along the laser pulse direction. The pressure in the spatial filter is 10^{-6} Torr, in order to avoid ionization of air molecules in the focus of the first lens.

The beam exiting the spatial filter is anamorphically expanded with aspect ratio 4:1 using prisms as shown in Figure 2.16. This is done in order to extract as much energy as possible from the last amplifier that has a slab geometry. The anamorphic prism expansion makes use of the Brewster law to give a magnification factor equal to the refractive index for each prism: From simple geometry the refracted and incident angles are related to the dimensions of the input and output beam diameter as

$$M = \frac{D_o}{D_i} = \frac{\cos\theta_r}{\cos\theta_i}$$

with M being the magnification from a single prism. From Snell's law we get:

$$\theta_r = \sin^{-1}(\frac{\sin\theta_i}{n})$$

with n the refraction index of the prism material. Also since the input face of the prism is aligned to the Brewster's angle we get:

$$\tan\theta_B = n$$

and so

$$\sin^2\theta = \frac{n^2}{n^2+1}$$

and the magnification factor then becomes indeed $M = n$. For fused silica $n = 1.41$ and a series of 4 prisms gives an aspect ratio of $(1.41)^4$:1, close to the desired 4:1. A Galilean expander further expands the beam by a factor of two.

The last amplifier of the laser system is a Nd:glass [57] slab amplifier. A characteristic of the slab geometry is the Brewster angle input and output faces. This geometry [55, 56] has the advantage of excellent phase front transmission, while retaining high gain and repetition rate in a compact unit. This is due to more efficient cooling compared to a rod of large diameter. The slab geometry eliminates depolarization effects

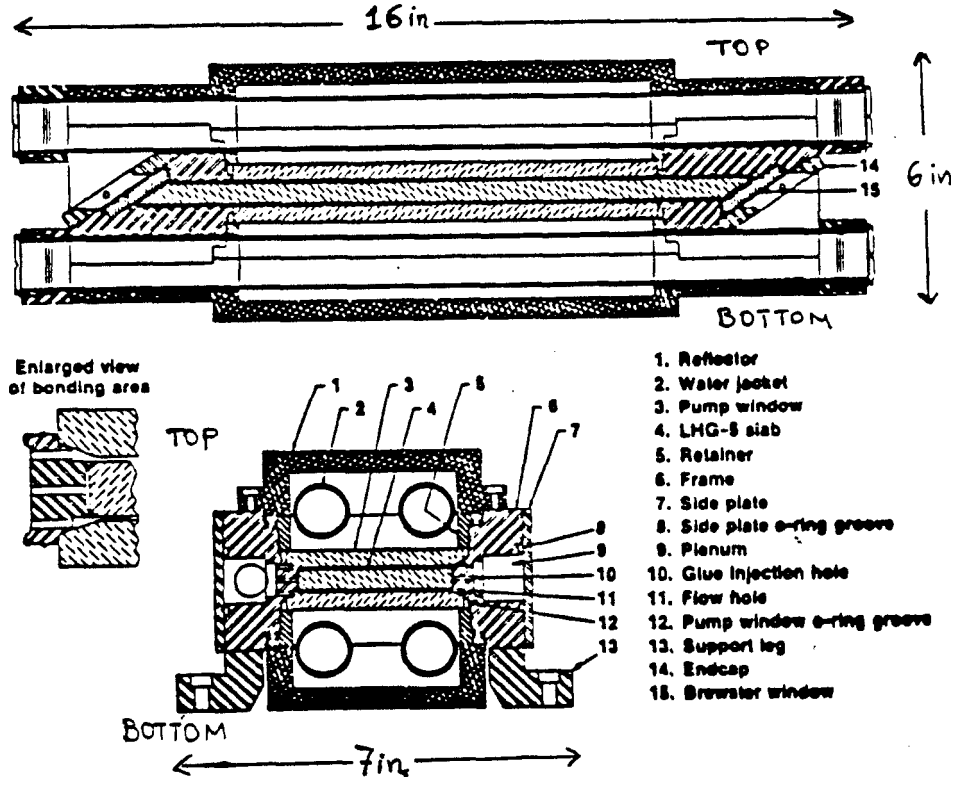

Figure 2.17: The slab amplifier frame

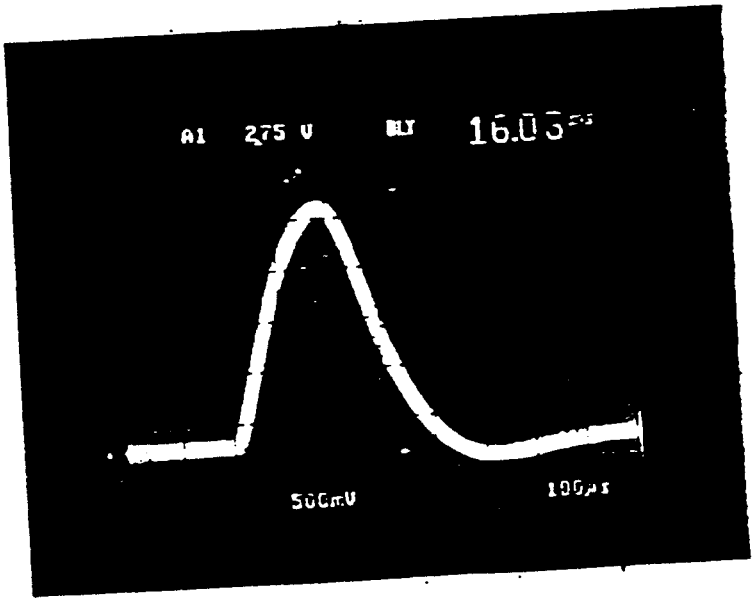

Figure 2.18: The current supplied to one of the slab lamps by its PFN

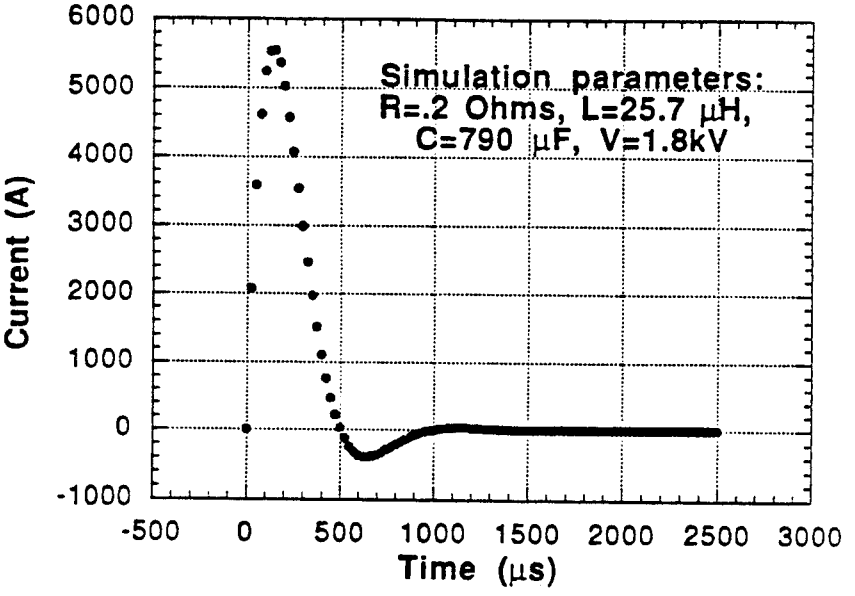

Figure 2.19: Simulation of the current of one of the slab amplifier lamps

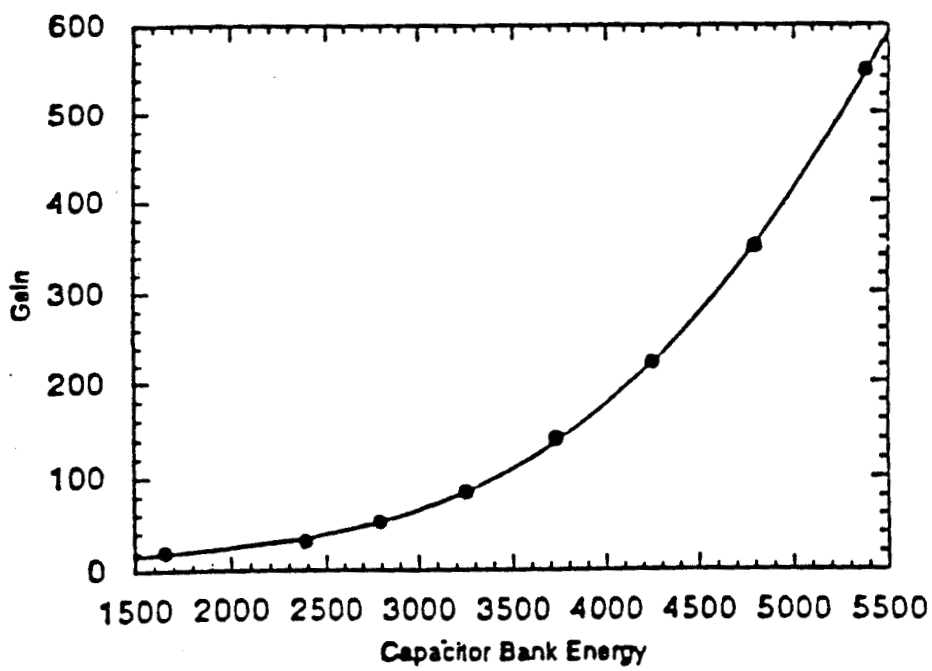

Figure 2.20: The slab amplifier gain

if the electric field is perpendicular to the large surface of the slab. In our case the clear aperture is 1.1 cm × 6.5 cm, so that large beams can be used, reducing peak intensity and related nonlinear effects. The large aperture allows us to use 3 passes into the amplifier in a bow-tie configuration. Using the Brewster angle input window, in each pass the beam internally reflects 12 times from the surfaces of the slab, and so increasing the optical path in the active medium. Of these, 8 bounces are in the 20.3 cm pumped length. A simplified drawing of the amplifier frame, which is made of stainless steel, is shown in Figure 2.17. Small signal gain of the triple pass slab has been measured to be of the order of 600 for 6 kJ of flashlamp energy, as is shown in Figure 2.20. The choice of Nd:glass over crystal materials as Nd:YLF and Nd:YAG is justified due to its availability in high optical quality and large sizes and its capability of storing very high energy densities before reaching the limit of super-fluorescence.

The slab active medium is 'pumped' by four lamps that discharge a high voltage which at peak laser power provides approximately 6 kJ of energy. This discharge lasts about 200 μs due to each lamp's current pulse shaping circuit called Pulse Forming Network (PFN). Figure 2.18 shows the current as a function of time as measured by a coil current probe for one of the lamps. The general nonlinear differential equation that gives the current of the PFN and lamp system is [59] :

$$L\frac{dI}{dt} + RI \pm K_0|I|^{\frac{1}{2}} + \frac{1}{C}\int_0^t I d\tau = V_0 \tag{2.5}$$

Where L is the inductance, R the resistance, C the capacitance, I the instantaneous current and V_0 is the initial voltage stored in the capacitors. The lamp itself is nonlinear and K_0 depends on characteristics of the lamp such as gas pressure and dimensions. Approximate parameters for the PFN components of each lamp are a 790 μF capacitor bank, an inductor of 19 μH, a resistor of 0.2 Ω, including the cable to the lamp. The above nonlinear equation can be very well approximated for our system with a critically damped LCR circuit with the current given by the following equation:

$$I = \frac{V_0}{\sqrt{\omega^2 - \alpha^2}L} e^{-\alpha t} \sin\left(\sqrt{\omega^2 - \alpha^2}t\right) \tag{2.6}$$

with $\alpha = \mathrm{R/2L}$ and $\omega = (\sqrt{LC})^{-1}$. The simulation of the current shown in Figure 2.19 is based on the last equation and well approximates the shape and time dependence

of the discharge.

Since the beam exiting the slab amplifier is elliptic we re-circularize it by two cylindrical lenses, which also up-collimate the beam to a size of a 3 cm in diameter at the $1/e^2$ intensity point. The first of the cylindrical lenses is made of fused silica which has a high damage threshold, while the second is made out of BK7 with lower damage threshold. The beam size has increased and hence its energy density has decreased on the second cylindrical lens and so one can afford using there a more inexpensive material like BK7. The alignment of the cylindrical lenses is critical to the wavefront quality downstream in the laser system and especially to the astigmatism introduced in the beam.

Following the cylindrical lenses a wave-plate rotates the polarization from vertical (imposed by the geometry of the slab), into horizontal to match the groove orientation of the grating compressor. Immediately after the wave-plate a Galilean expansion stage brings the beam into a diameter of about 4.5 cm. This Galilean expander was aligned with a test interferometer for better wavefront quality. Then the laser pulses are cleaned again by another vacuum spatial filter. It is 2.7 m long and also up-collimates the laser beam to a maximum of 7.5 cm in diameter. The spatial filter's vacuum is maintained at 10^{-6} Torr. A burn at full power of the slab amplifier before and after this filter indeed shows that the high frequency spatial noise is reduced by the filter.

The laser pulse is then directed through the compression stage, which consists of two 1760 lines/mm, gold-coated 160 mm $\times$ 220 mm holographic gratings [60] used in the near Littrow, double pass configuration with a separation distance of 164 cm [52]. They compress the laser pulse to 1.5 ps. A grating scan where the compressed laser pulse-length was measured with a streak camera is shown in Figure 2.21. The grating distance is set at the minimum laser pulse-length point. This distance is different for various oscillator bandwidth settings which results in variations of the compressed laser pulse-length, therefore every effort was made to keep this bandwidth fixed during the running period.

After compression we have the possibility to double the frequency of the laser. For this purpose we use a 4 mm or a 8 mm thick Type II KDP crystal [63], with

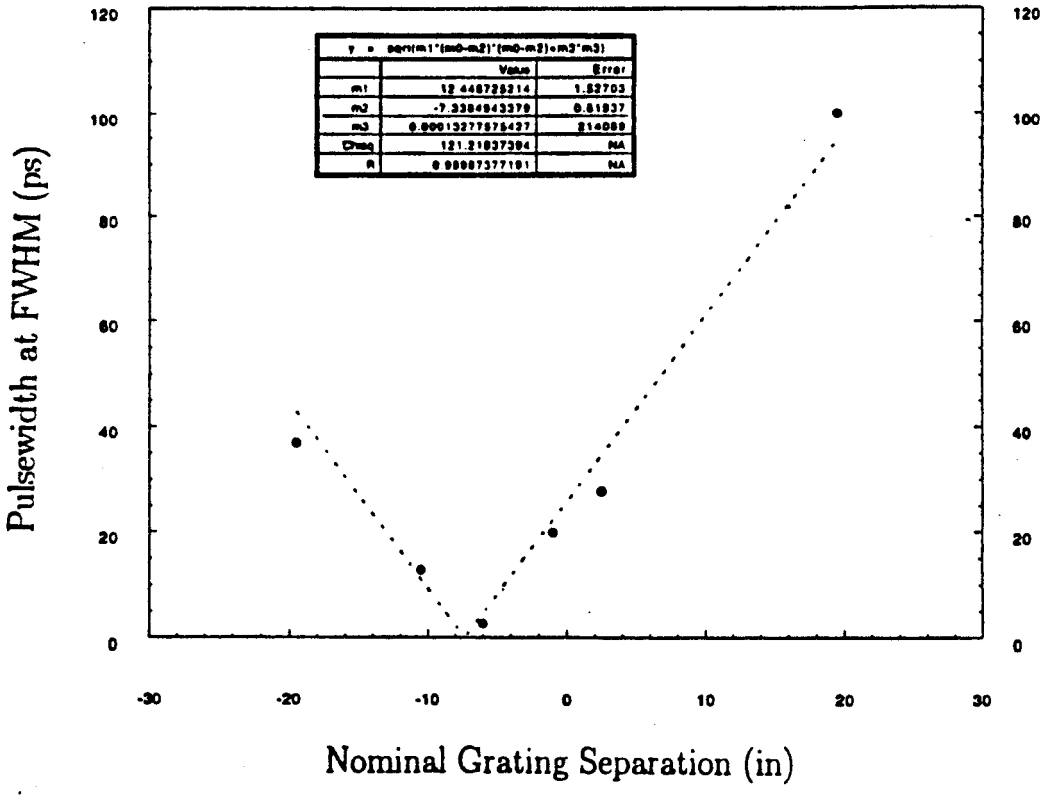

Figure 2.21: The compressed laser pulse-length as a function of compression grating separation

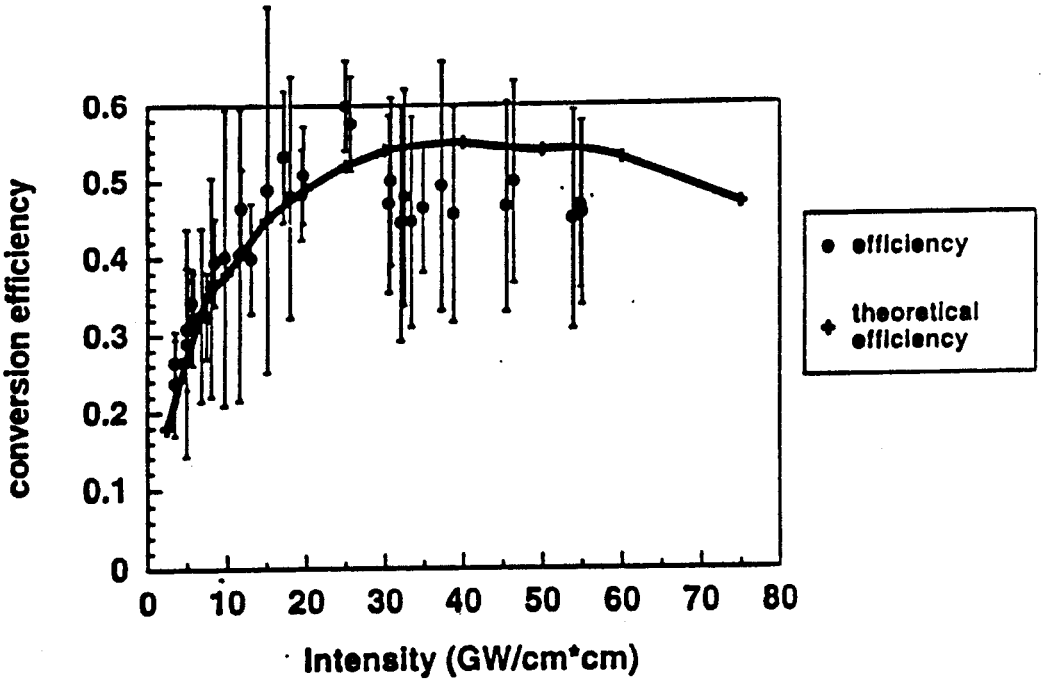

Figure 2.22: Frequency doubling with a 8mm Type II KDP crystal

the thicker crystal used at lower intensities (< 30 GW/cm^2). A doubling curve is shown in Figure 2.22 for the 8mm crystal. The 45% efficiency compares well with the theoretically predicted 50% [61, 62].

For the data analyzed here the laser was circularly polarized, using a Liquid Crystal Polarizer (LCP). Since the energy densities of the laser are high at this point of the laser system, the LCP has a Sol - Gel coating. This coating though, is very sensitive to temperature and humidity conditions in the room and easy to destroy from minor scratches.

Finally the laser pulse is then transported to the interaction point and then returned to the laser room in order to measure its energy, pulse-width and focal area. The laser energy is measured both by a leakage monitor behind one of the mirrors before the transport line and behind a flat in the diagnostic line after the transport. Figure 2.23 shows a histogram of the IR laser energy for a 1700 shot run with an

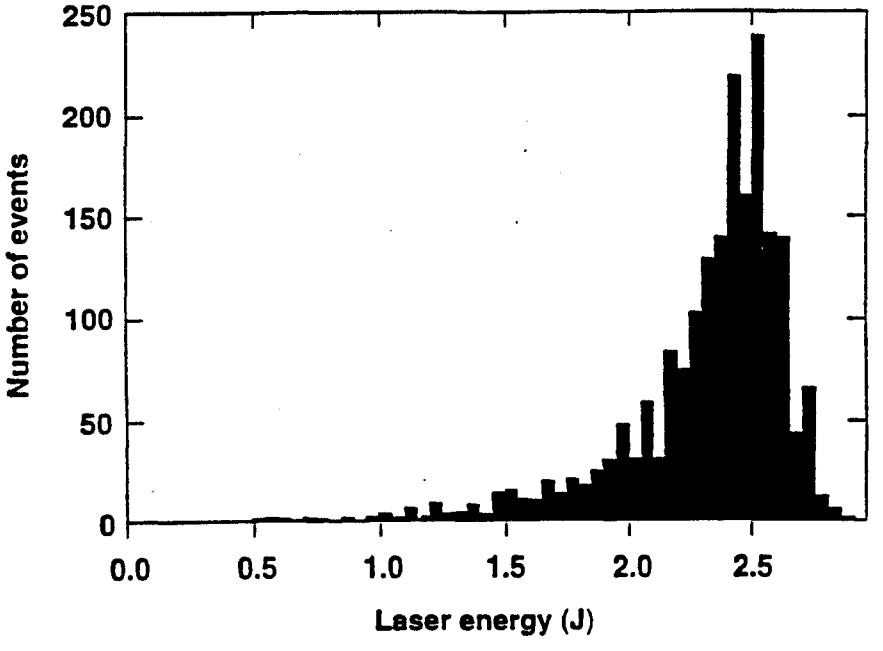

Figure 2.23: The laser energy in a 1700 event run at 1.053 μm wavelength

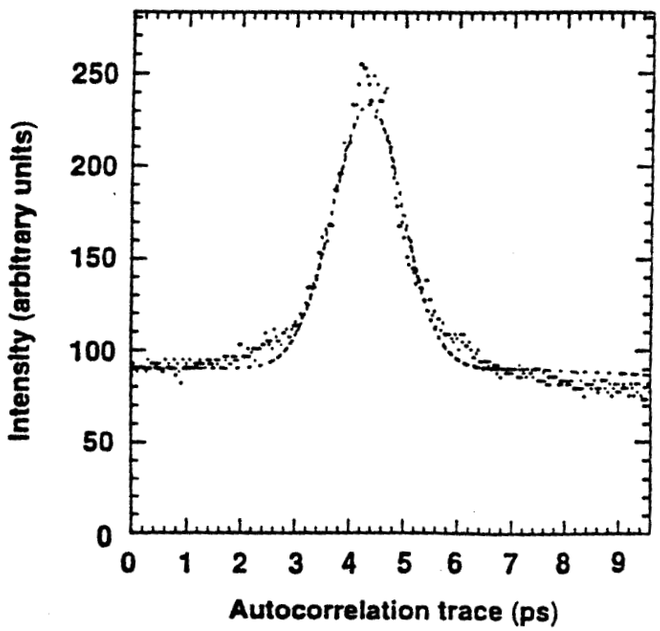

Figure 2.24: Single shot autocorrelator trace of an IR pulse

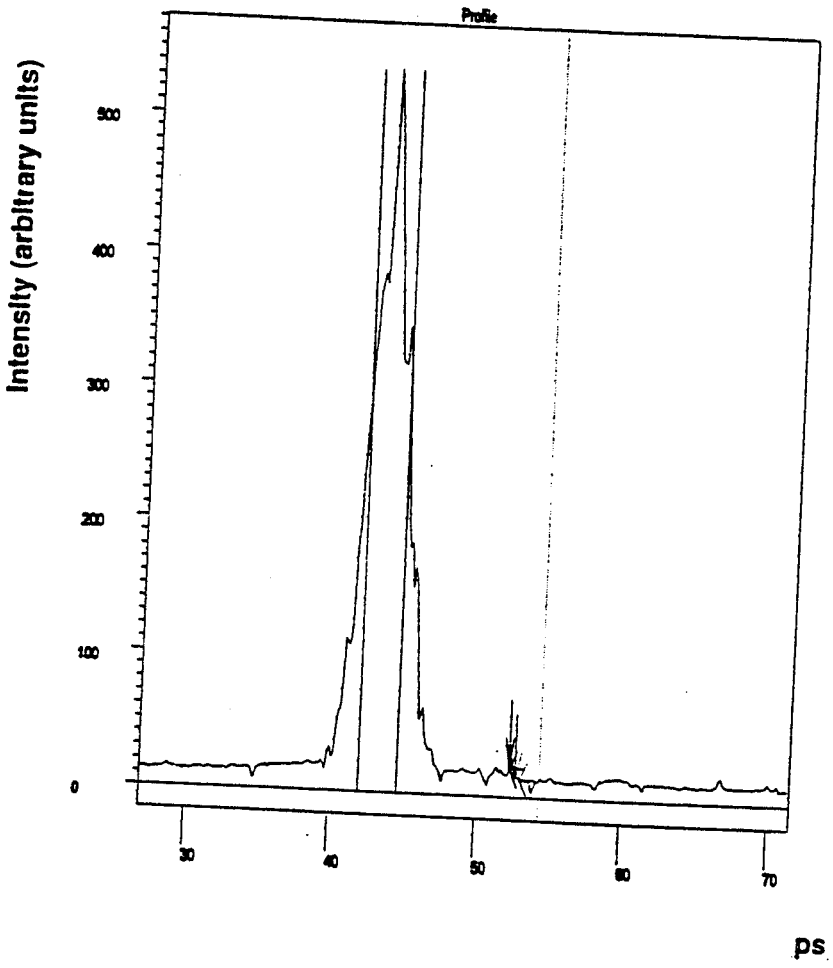

Figure 2.25: Streak camera pulse-width of a green pulse

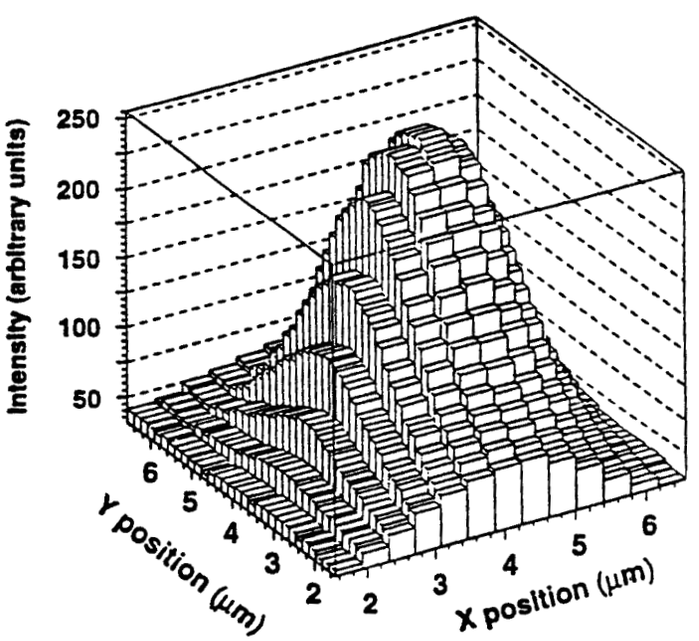

Figure 2.26: A typical focal spot in the interaction point as measured by the ETP technique

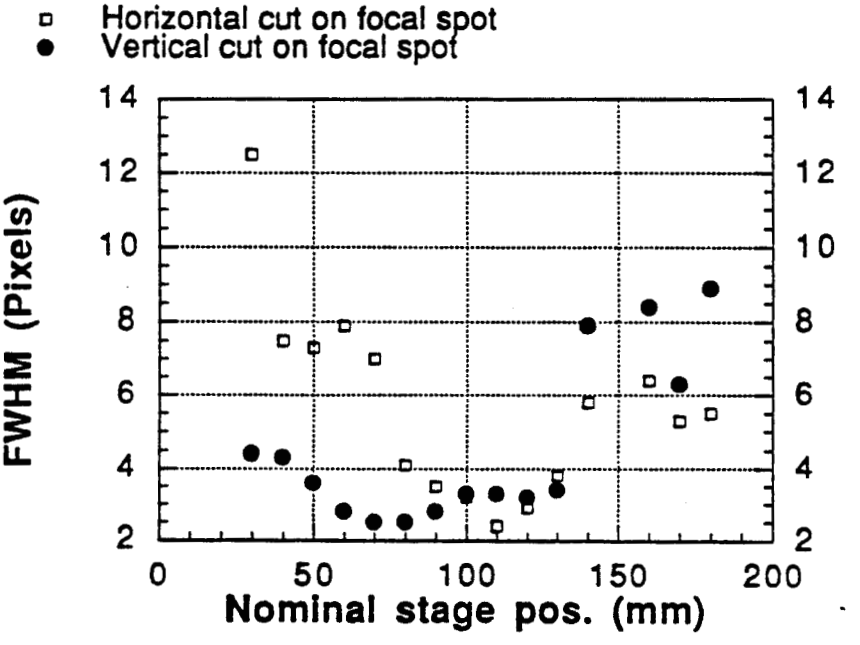

Figure 2.27: The different positions of the focus of the horizontal and vertical axis of the laser spot are an indication of astigmatism in the laser chain.

average energy of 2.4 ± 0.4 J at the input to the transport line.

The IR pulse-width is measured with a single shot autocorrelator in the diagnostic line. For a 500 mJ, IR laser pulse we measured 1.5 ps FWHM as in Figure 2.24. A streak camera was also available during the run and gave similar values for pulse-width measurements. In the green a single shot autocorrelator was not available during the run, so the green pulses were measured by the streak camera. A typical streak camera profile for a green pulse is shown in Figure 2.25.

The focal spot at the interaction point is measured indirectly by using the Equivalent Target Plane (ETP) technique after the return of the laser beam into the laser room. For this purpose the beam is refocused after the transport with a 4m focal length lens, reflected off four flats which attenuate the beam energy by 10^6 and by using neutral density filters is further attenuated. The focus is imaged with a 5 × microscope objective onto a CCD camera. For 500 mJ IR laser pulses, the focal spot has 4 μm radius at the 1/e point in intensity and so has a 50 μm^2 area. Degradation of the focal spot was observed at energies above 1 J. For the frequency doubled pulses the area decreases to about 20 μm^2. A typical focal spot measurement of the laser at the interaction point is shown in Figure 2.26. The diffraction limit of the radius of the focal spot is given by

$$w_{dif} = 2\frac{\lambda f_{\#}}{\pi} \tag{2.7}$$

and we define the diffraction limited area as

$$A_{dif} = 2\pi w_{dif}^2 \tag{2.8}$$

So we achieved 1.4 times diffraction limited pulses in the IR and 3 times in the green.

The ETP technique proved also valuable in monitoring the astigmatism introduced in the laser system. When the CCD is scanned over a range around the focal point then in case of astigmatism the horizontal and vertical dimensions focus in separate places. This is shown in Figure 2.27. Normally the cylindrical lenses are the largest source of astigmatism and their alignment is tuned by minimizing the separation of the minimum waists of the two axis.

The peak focused laser intensity was obtained for IR pulses of energy U = 1.2 J, focal area A=80 μm^2 and pulse-width Δt = 1.5 ps, for which $I = 10^{18}$ W/cm^2

corresponding to a laboratory field of 20 GV/cm. At these conditions the strong field QED parameter η becomes $\eta = 0.6$ and the critical field parameter Υ becomes $\Upsilon = 0.4$.

2.3 Laser transport system and interaction point

The laser pulse is brought into collision with the electron bunch after being transported 12 m from the laser room optical tables to the electron beam in the FFTB

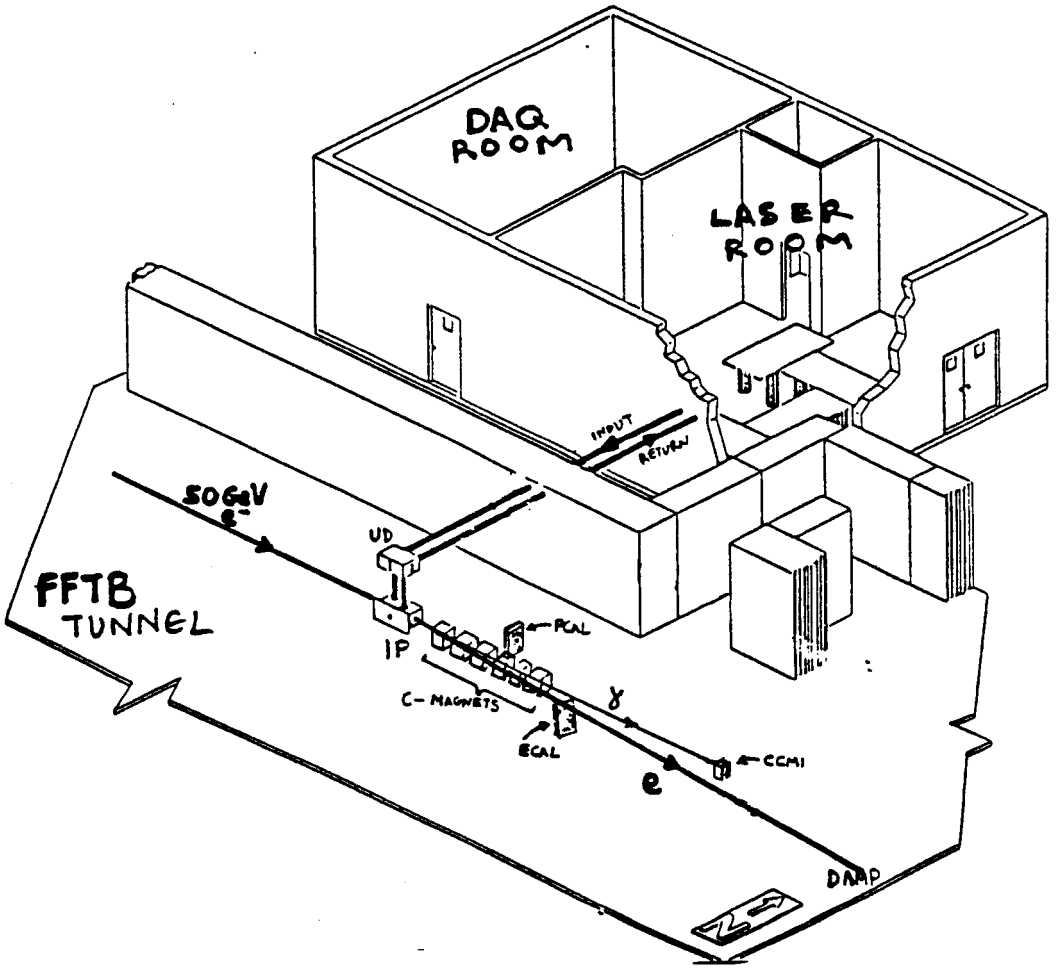

Figure 2.28: The optical transport system

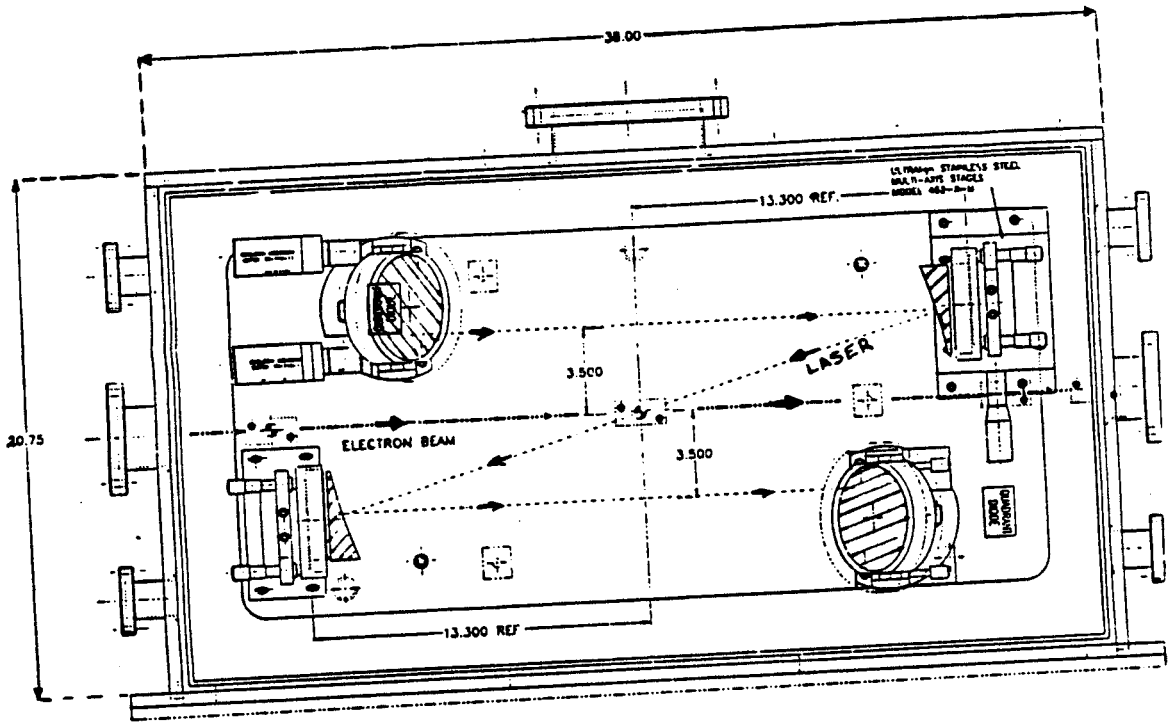

Figure 2.29: The interaction point box; dimensions are in inches

tunnel as shown in Figure 2.28. The laser pulse is raised to a height of 2.5 m using a periscope inside the laser room, then passes through a glass window coated for anti-reflection at the appropriate wavelength (green or IR) and a 10 m long tube under medium vacuum which was better than 10^{-3} Torr. Just above the electron beam pipe the laser pulse is deflected downwards using a mirror on stepper motors, that can be adjusted from a controller in the laser room. The mirror is located in the upper deflection (UD) box which also includes the return mirror. The pulse then travels downwards through one more window that separates the medium vacuum region of the transport with the high vacuum region in the electron pipe, and enters the interaction point (IP) box which is shown in Figure 2.29. There it is reflected horizontally by a 45^0 mirror, is focused by an Off Axis Paraboloid (OAP) mirror with 30 cm focal length onto the incoming electron beam; the laser beam is re-collimated by a similar OAP after the interaction and is sent horizontally into another mirror that reflects the laser pulse upwards into the UD box. All the optics inside the IP box are mounted on an invar plate to reduce optical path changes due to temperature variation. The electron direction of motion and the laser path have a 17^0 angle between them.

The IP box was placed on a magnet mover which can position the IP in the horizontal (x) and vertical (y) directions and can also introduce a roll in the xy plane but it does not provide a motion along the electron beam path (z). The three motors used for the IP mover are interfaced into the SLAC Control Program (SCP) and were used to scan the laser focus with respect to the electron beam, since the laser path is fixed with respect to the IP box. The limits on the range of the IP box motion, in the 3 axis, are coupled due to the magnet mover hardware and this is shown in Figure 2.30. The UD box and the IP box are decoupled by bellows to avoid stresses on the IP box and to allow its free motion. Some stability issues are of concern since the IP box is on top of a column sitting on the FFTB concrete floor. Long term drifts of the order of μm have been measured that are due to diurnal thermal expansion of the tunnel. From the UD box the laser pulse is sent into the room with a system similar to the input transport and in the same vacuum.

The window located in the entrance to the optical transport as well as the one that separates the medium vacuum of the transport line from the high vacuum of the

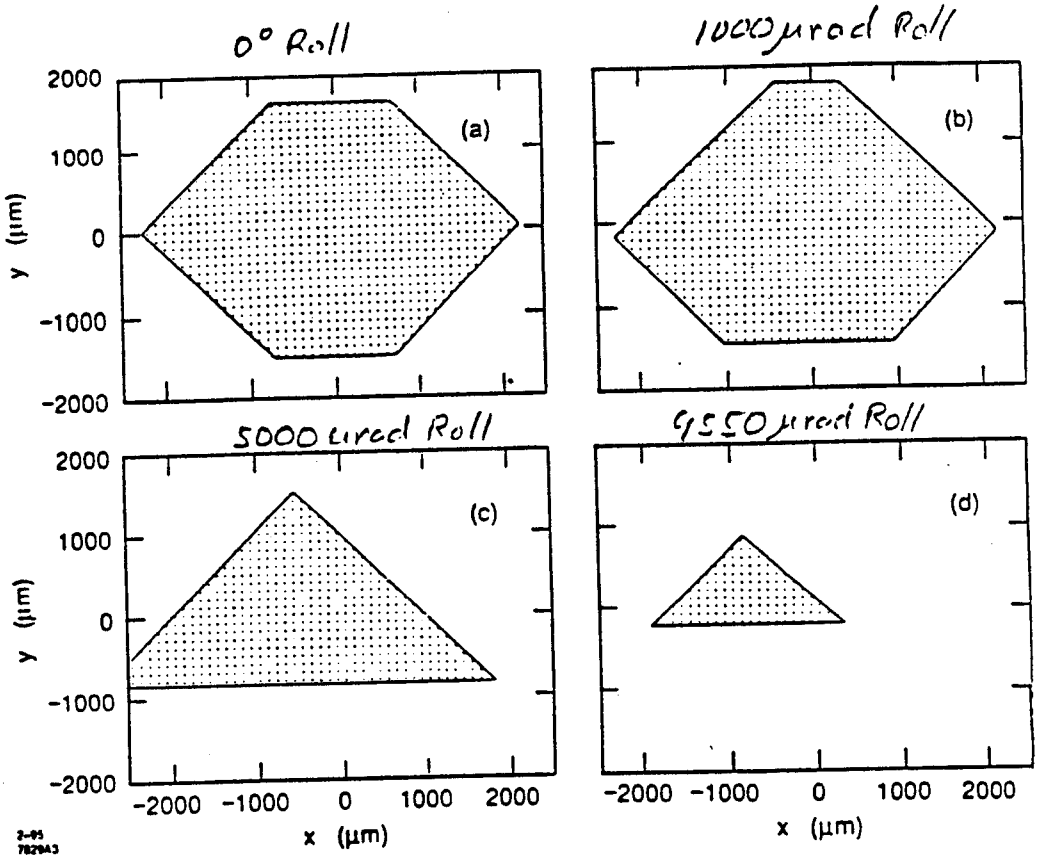

Figure 2.30: Coupling of the 2 direction motion of the IP magnet mover

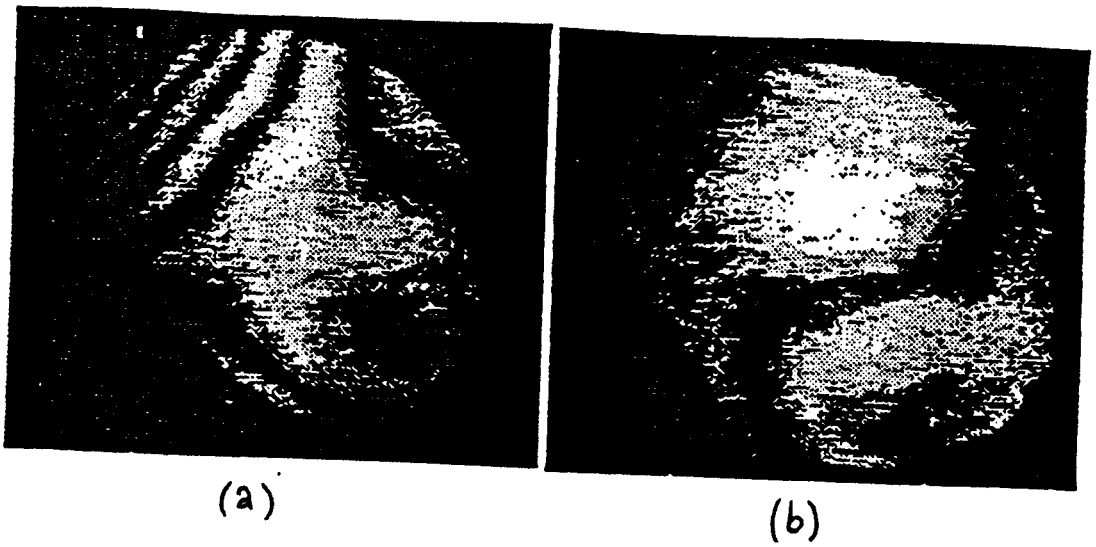

Figure 2.31: Two interferograms of the optical transport interferometer: (a) the optical transport is slightly misaligned and (b) well aligned

IP box could contribute to an increase in the B-integral effect and to a deterioration on the wavefront of the laser pulse. From [64] the B-integral is given by :

$$B = \frac{2\pi}{\lambda}\int_0^h n_2(z)I(z)dz \longrightarrow 2\pi\frac{h}{\lambda}n_2 I \tag{2.9}$$

where the approximation is valid for constant laser intensity and n_2 is the 2nd order index of diffraction. The laser beam diameter at the $1/e^2$ point of the intensity is estimated to 5 cm at the input to the optical transport and for 1 J energy and 1.5 ps pulse-length we get an intensity of $I = 3 \times 10^{10}$ W/cm^2. By substituting $n_2 = 3\times 10^{-16}$ cm^2/W, $\lambda = 1053$ nm and total path-length in the 2 windows h = 5 cm we get that $B = 3$ which is the critical value at which wavefront distortion is tolerable [64]. The two return windows have the same thickness as the input ones and contribute in the deterioration of the wavefront in the returned beam.

Good wavefront quality of the beam returning to the laser room is an indication that the alignment of the OAP pair is correct and that the pointing of the beam incident on the first OAP coincides with the OAP axis. If the wavefront quality is better than $\lambda/4$ over the entire beam, the spot at the IP is diffraction limited. Rather than trying to measure the beam quality of the IR pulsed beam we use a co-propagating cw frequency stabilized He-Ne beam with a large enough diameter ($\simeq$7.5 cm). A beamsplitter co-injects part of the He-Ne laser beam into the transport and after its return from the IP interferes it with the part kept in the laser room, in a configuration of a Mach - Zehnder interferometer. Figure 2.31 shows two interferograms, one when the transport system is slightly misaligned and one when is well aligned. The alignment of the optical transport can deteriorate in a 24 hour period and depends mostly on ambient temperature variations, transport vacuum losses, and IP motion.

The transport system was modeled by an optical ray tracing, and Gaussian beam propagation software package COMP [42] that allowed us to set limits on the misalignment of the laser pointing and orientation of the OAPs. There are 5 degrees of freedom over which the OAPs must be aligned: 3 displacements so that the focal points will coincide and 2 rotations to set the optical axis parallel to the OAP axis. The tolerances in position in the x, y, z directions are 3 μm, 3μm and 10 μm respectively. The tolerance on the incident beam rotation about the horizontal axis is 5

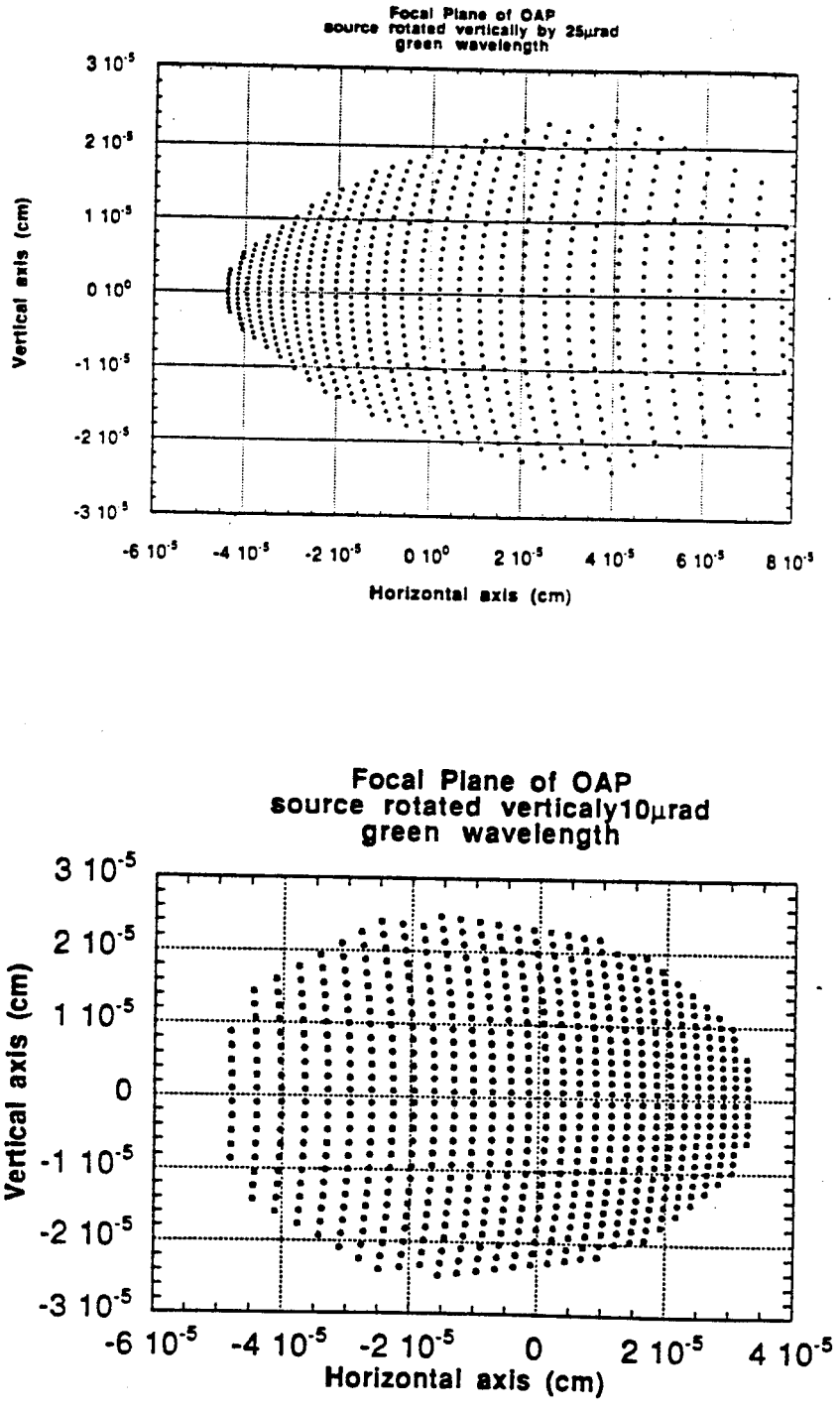

Figure 2.32: Simulation of the IP focus with and without misaligned OAP

μrad and about the vertical axis is 15 μrad. The most precise method for aligning the elements of the system within these tolerances is by using the interferometer as a diagnostic. Figure 2.32 shows the aberrations in the focal plane of the OAP with a well aligned and a slightly misaligned optical transport as simulated by COMP.

2.4 Spatial overlap of the laser pulse with the electron beam

For collisions to occur the focus of the laser must be in the path of the electron beam. For this purpose a 3-axis stepper motor mounted on the IP box above the interaction point and remotely controlled from the laser room, can drive a 'flag' into the interaction point. The flag consists of a fluorescent screen, a 3 wire cross hair and

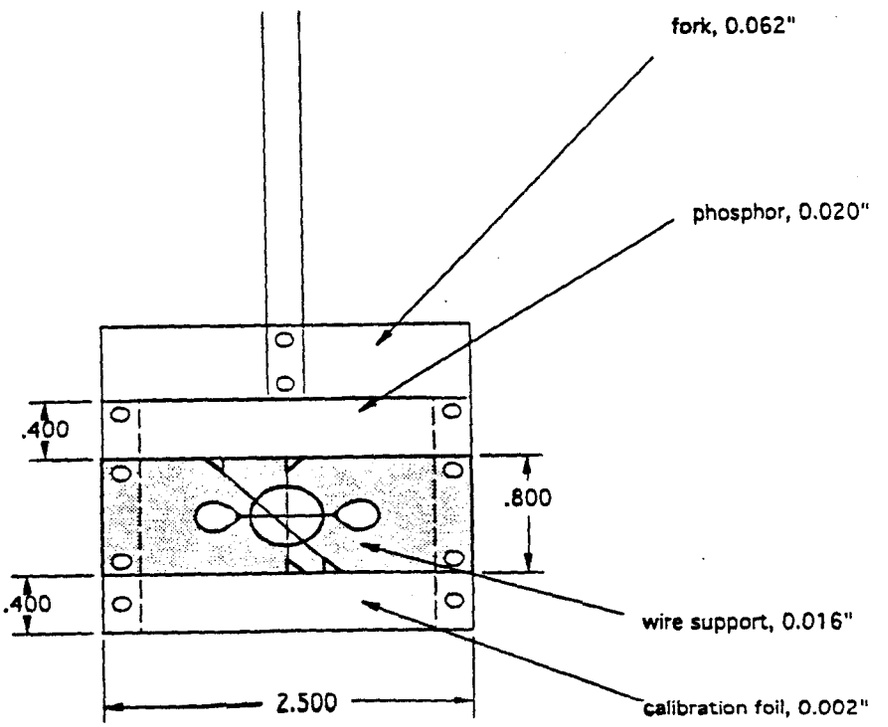

Figure 2.33: The IP flag with the calibration foil, the cross hair and the fluorescent screen

an Al foil, Figure 2.33. When the fluorescent part intercepts the electron beam, a CCD camera, which is mounted on the side, outside of the IP box, gives the position of the electron beam. The He -Ne laser, which is co-injected with the main laser pulse, is also visible to the camera. By moving the flag in z, i.e. in the electron direction, the laser focus is scanned and the flag can be set visually at the focus. Next the electron beam is steered to overlap with the laser. The IP box mover was used for final alignment.

The spatial overlap is fine tuned using the cross-hair of the flag. Since the wire of the cross-hair has a diameter of 20 μm, it can be easily damaged by the Terawatt laser, therefore, the red He-Ne laser is used for this alignment. When the wire is scanned through the laser focus, the equivalent of a razor scan is observed in the laser room, i.e. when the wire is exactly at the focus, the He-Ne beam has totally disappeared. With that method the focus of the laser, located at the same point as the

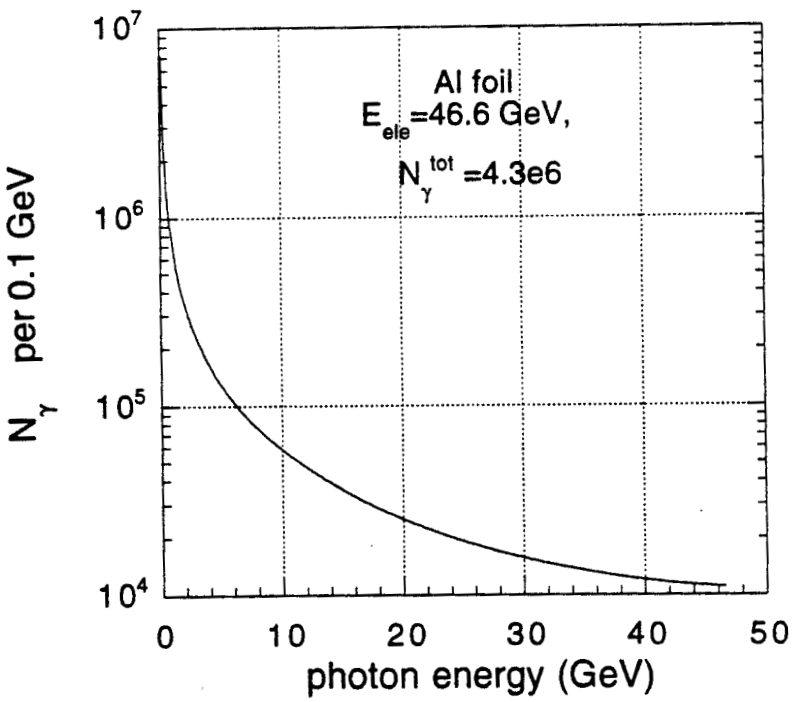

Figure 2.34: The calculated rate of bremsstrahlung gammas produced by the the Al foil in IP

focus of the co-injected He-Ne light, can be found with accuracy. Then the electron beam is scanned over the wire and is set accurately on the wire, by the method of wire scanning: Due to bremsstrahlung of the beam electrons with the wire, gamma rays are generated and are collected by the downstream gamma monitor. This is also used as the linear Compton monitor of the experiment and will be described in the detector section. The number of gammas is proportional to the transverse electron density of the beam at the wire position, so by scanning the electron beam over it, one can achieve a very good alignment. The flag is removed from the interaction point and the IR laser unblocked. This procedure is repeated whenever the electron beam configuration is modified.

The purpose of the aluminum foil mounted on the flag is to calibrate the gamma flux monitor. The bremsstrahlung differential cross section in the extreme relativistic case is given by:

$$\frac{d\sigma}{dk} = \frac{4Z^2 r_0^2}{137}\frac{dk}{k}[(1+(\frac{E}{E_0})^2 - \frac{2}{3}\frac{E}{E_0})(\ln(183Z^{-\frac{1}{3}}) - \sqrt{(Z)}) + \frac{1}{9}\frac{E}{E_0}] \qquad (2.10)$$

where E_0 and E are the initial and final electron energies in units of electron rest mass, k is the energy of the emitted photon also in units of electron rest mass, Z is the atomic number of the target material and r_0 is the classical electron radius. Due to energy conservation one can substitute in equation 2.10

$$\frac{E}{E_0} = (1 - \frac{k}{E_0}) \qquad (2.11)$$

By integration of equation 2.10 over the emitted photons (and using a low energy cutoff so that the integral will not diverge) one can calculate the total cross section σ_{tot} for bremsstrahlung for Al with Z=12. Then the total number of bremsstrahlung gammas is

$$N_\gamma = \sigma_{tot}\rho_0 dN_e \qquad (2.12)$$

where $\rho_0 = 6.03 \times 10^{22}$ cm^{-3} is the density of target (Al) nuclei, $d = 50$ μm the thickness of the foil and $N_e = 5 \times 10^9$ is the number of initial electrons. Figure 2.34 shows the differential and the total number of gammas from the above calculation which is used in the calibration of the linear rate monitor.

2.5 Synchronization of the laser pulse with the electron beam

One of the primary technical challenges for the experiment is the synchronization of the laser pulse with the electron beam in order to achieve collisions at the interaction point. Since the laser pulse has a pulse-width as short as 1.5 ps FWHM, and the electron bunches can have a longitudinal rms of 1.0 ps, it is necessary to control the relative timing of the two counter-crossing pulses at the 1 ps level. The strategy used to time the beams is shown in Figure 2.35. A sub-multiple of the master accelerator frequency drives the mode-locker of the laser oscillator that sets the time for the laser pulse launching. An electronic feedback locks the phase of the oscillator pulses to the accelerator rf. The delay of the rf driving signal of the ML is adjusted and the laser pulse fine timing is found by scanning with an optical delay line. At the same time the products of the laser-electron interaction are monitored, i.e. the linearly Compton scattered gammas into the gamma monitor or the more sensitive signal of the nonlinearly scattered electrons into the electron calorimeter (ECAL). When the interaction yield is plotted versus the timing delay, the best overlap timing is at the peak of this plot.

2.5.1 Experimental setup for laser - electron timing

The accelerator master oscillator located in the injector area, i.e 3 km from the laser room, provides 20 Watts of rf power at 476 MHz. A fiducial of 360 Hz is also superimposed on the 476 MHz signal in order to define the klystron firing timing. This signal is transmitted via the Main Drive Line (MDL) [65] in a rigid coax cable that runs the length of SLAC's klystron gallery and is the source for both the RF drive and reference signals for all klystrons and rf devices in the LINAC. The internal frequency of 476 MHz is multiplied by 6 at each sub-booster to produce the rf for S-band systems, as shown in the schematic of Figure 2.36. The performance of the accelerator is sensitive to any drifts in the phase of the rf provided by the MDL, so a feedback loop is employed to compensate for any changes in the electrical length of the

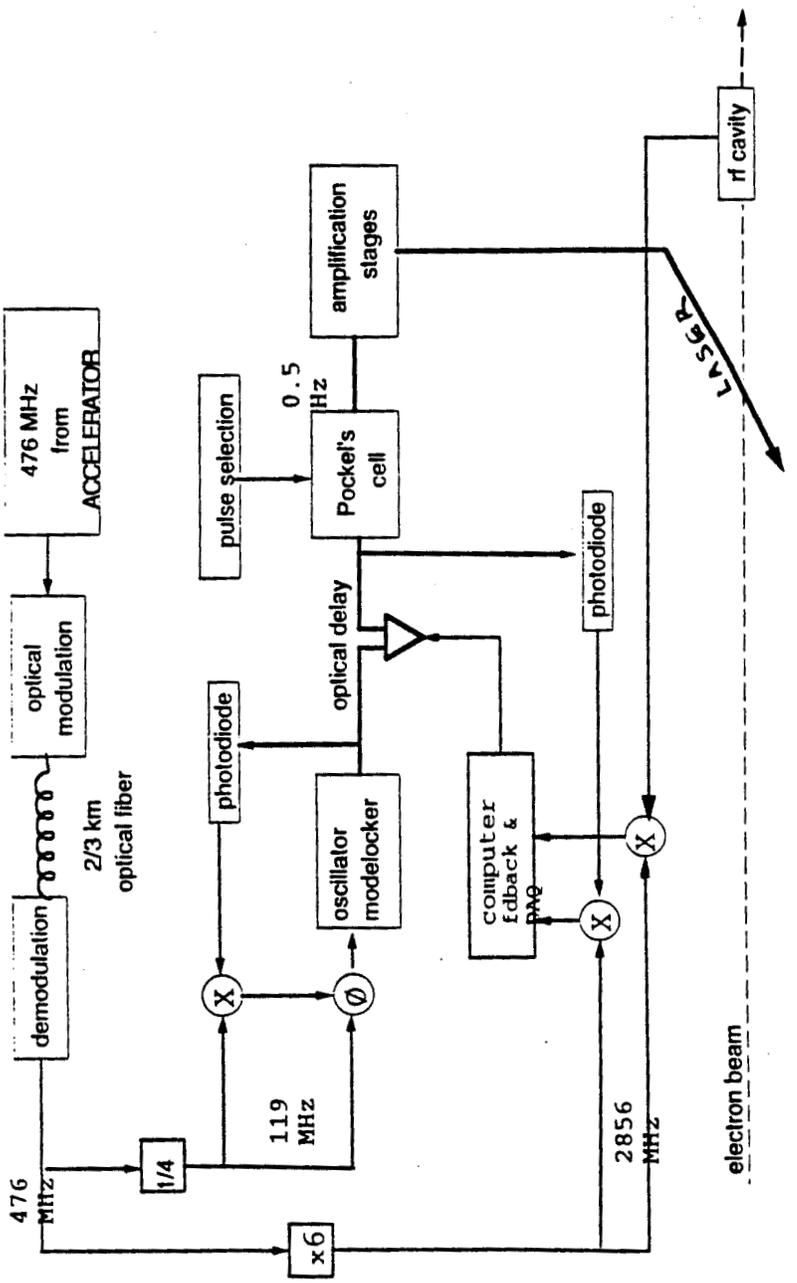

Figure 2.35: Overview of the timing system for the synchronization of the laser pulses with the electron beam

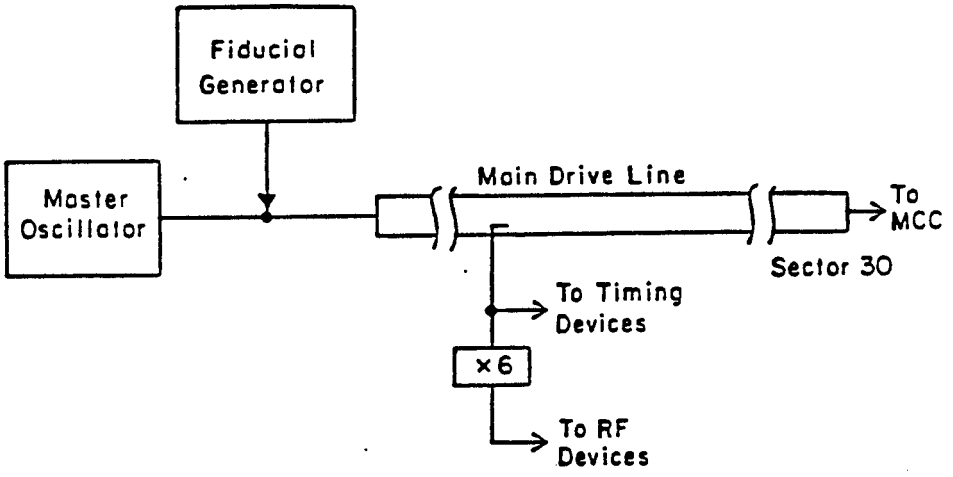

Figure 2.36: The SLAC Main Drive Line

MDL. This loop is controlled by the software tools that support all slow feedback loops in the SLC, and is a feed-forward loop, i.e. the environmental effects which change the phase stability of the MDL are not controllable and can only be compensated for. The measurement of the phase length of the MDL is done with a single interferometer by introducing a modulated reflection of the rf at the end of the LINAC (sector 30), allowing instrumentation in the front end (sector 0) to compare the phase of the reflected rf with that of the source. Thus, the accelerator rf signal which is used to synchronize the laser with the electrons, contains, apart from the main 476 MHz signal, a sideband of 750 Hz (originating from the interferometer), and sidebands of the harmonics of 360 Hz (originating from the fiducial).

The 476 MHz reference signal is amplified by a low noise rf amplifier and is then fed into a Fiber-optic Transmitter (F/T) [66]. The rf modulates the current into a

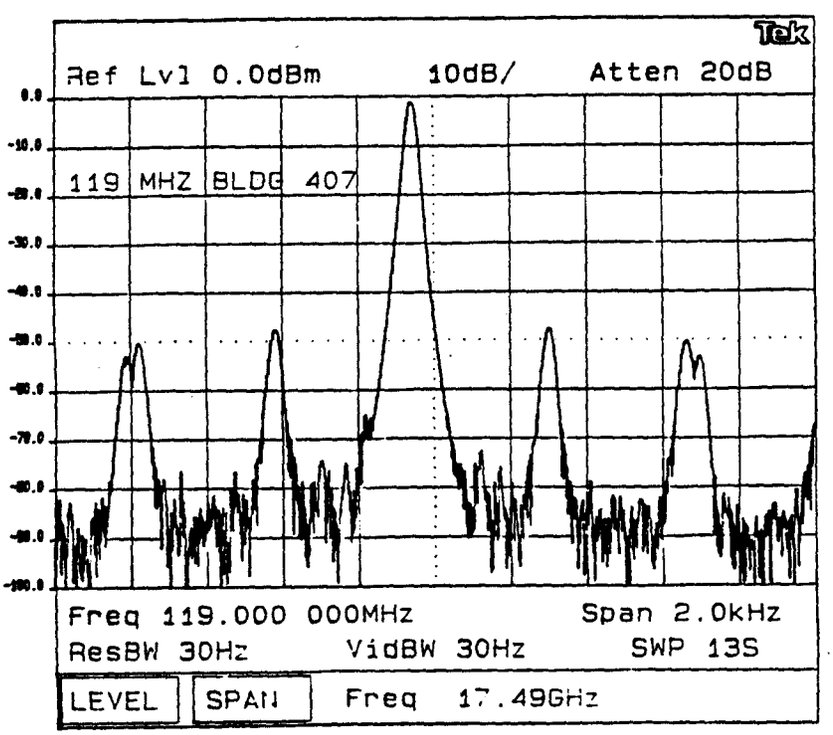

Figure 2.37: Power spectrum of the laser reference 119 MHz rf

distributed feedback laser diode (DFB), which in turn produces an intensity modulated optical signal at 1300 nm wavelength that is coupled into an optical fiber and transported 600 m to the laser room. The fiber solution was preferred over an rf cable due to the low losses, low dispersion and small length variations resulting from ambient temperature changes. In the laser room the optical signal is collected by the Fiber-optic Receiver, which utilizes a high speed photodiode to convert it into the 476 MHz reference. The transmitter/receiver setup is interfaced and monitored by SCP.

The 476 MHz output of the F/O Receiver is then amplified and used to drive the Fiducial Output module (FIDO), which contains circuits that extract the fiducial pulse (T-zero) from the reference signal and others that produce the 4th sub-harmonic at 119 MHz. The output of the FIDO consists normally of a 119 MHz sine wave with a missing half cycle to indicate the T-zero. In our case, an externally supplied circuit inhibits the fiducial pulse, so that a cleaner 119 MHz signal is produced. Figure 2.37 is the spectrum of the 119 MHz signal where the sidebands of 360 and 750 Hz described before can be seen.

The 119 MHz is then sent to the timing stabilizer (TS) module [53]. A simplified block diagram of this module is shown in Figure 2.38. The output of this module is a 59.5 MHz signal in phase with the reference, that after amplification to 4W drives the laser oscillator mode-locker. A 2 GHz bandwidth photodiode collects the oscillator 119 MHz pulse after it has undergone the chirping and expansion through the fiber and after compression from the diagnostic grating compression stage, which is also used by the cw autocorrelator. The diode signal is then phase compared in the TS module with the reference 119 MHz, which was already subdivided and filtered. The output signal of the phase comparator drives the phase shifter circuit that in turn changes the phase of the rf sent to the mode-locker in order to keep the laser pulses in phase with the reference rf. The positioning of the photodiode is critical, since the two signals that are phase compared must be close to their zero crossing in the time domain. Also it collects the laser pulse train after it has traveled into the 1km fiber in order to compensate for changes in the optical path-length due to temperature variations. Finally it is placed after the compression gratings since there the FWHM

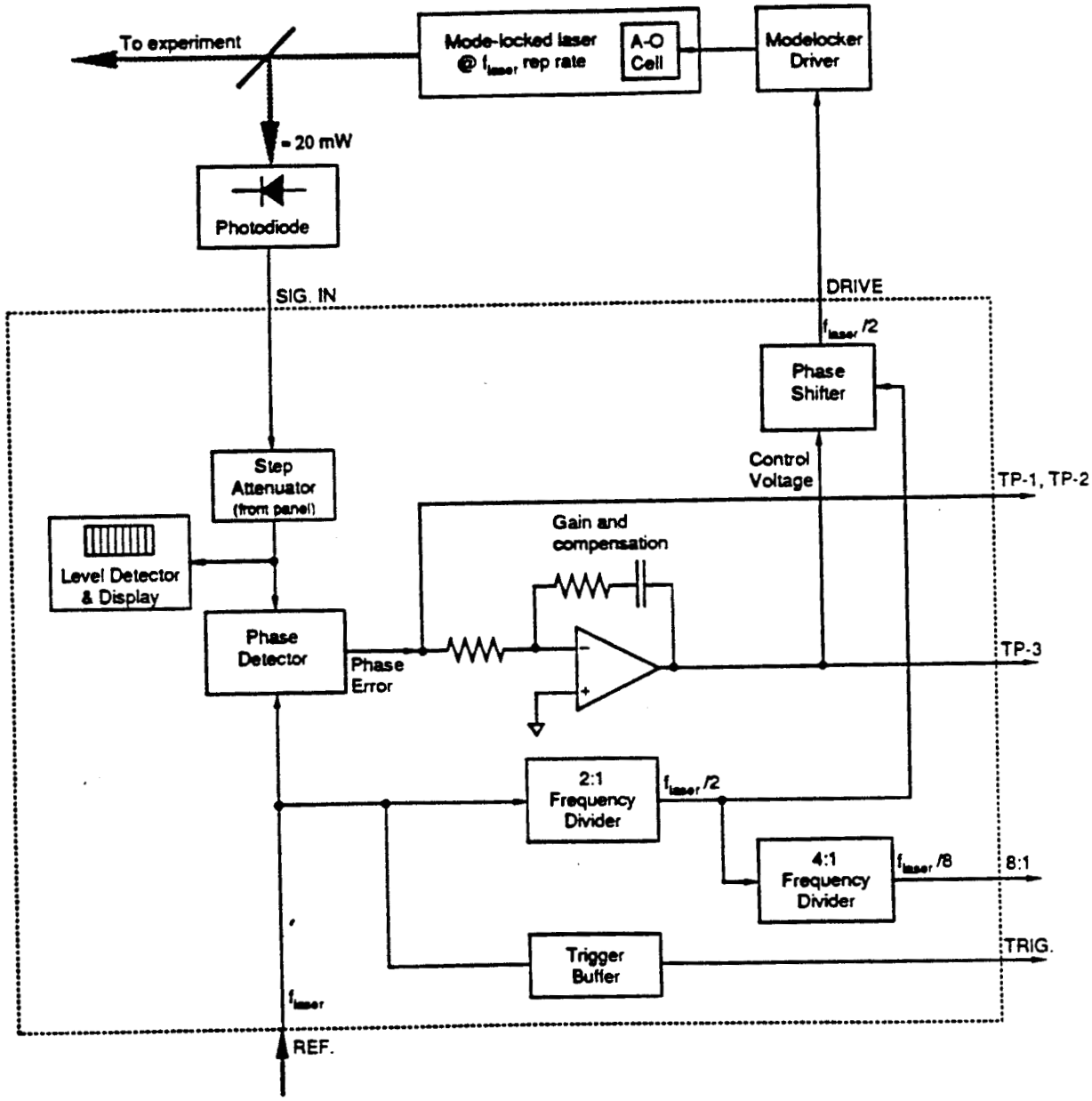

Figure 2.38: Timing Stabilizer block diagram [53]

of its pulse is less than 2 ps and for this reason the timing information from the rising slope of the pulse is more accurate than if it were 200 ps, which is the case just after the 1km fiber.

The setup described above locks the oscillator pulse train to the accelerator master clock. One of these laser pulses is chosen every 2 seconds in order to collide with one of the electron bunches using the following scheme:

The laser triggering is based on the software-defined triggers of SLC which are synchronized also with the master accelerator clock. These triggers can be tuned in both repetition rate and delay from a starting time T_0, which coincides with the injection of the electron beam. Currently the laser trigger starts as a 10 Hz trigger and its delay is adjusted with a Pulse Delay Unit (PDU), interfaced with SCP. The finest timing step of a PDU is 8 ns.

The PDU signal is frequency divided to 0.5 Hz, split and then fed into two commercial delay units [68] that can be timed in picosecond steps. One of them is used to trigger the lamps of the laser amplifiers and is irrelevant for timing purposes since the lamp flash lasts for approximately 200 μs. The other delay unit triggers the 3 Pockels cells of the laser system. The last Pockels cell in the path of the laser defines the switch-out time of the regenerative amplifier pulse train and sets the timing of the laser pulse that will collide with the electron beam. The timing of the other two Pockels cells is then adjusted relative to the switch-out Pockels cell in order to achieve good amplification in the regenerative amplifier and good single pulse contrast.

After the regenerative amplifier the laser pulse travels on the optical table through the rest of the laser chain and finally enters the input periscope in order to travel to the IP through the optical transport line. The laser pulse leakage from the first mirror of the periscope is detected in a photodiode, which is permanently positioned behind the mirror. The signal from this diode is the timing reference laser pulse (TRLP) (assuming no path length changes take place in the optical transport) and is compared with an electron beam based signal.

The electron beam based signal is provided by a 'ringing cavity' installed in the electron beam line, 2 feet downstream of the interaction point. A schematic of this cavity, that has a resonant mode at 2856 MHz and quality factor Q = 1300, is shown

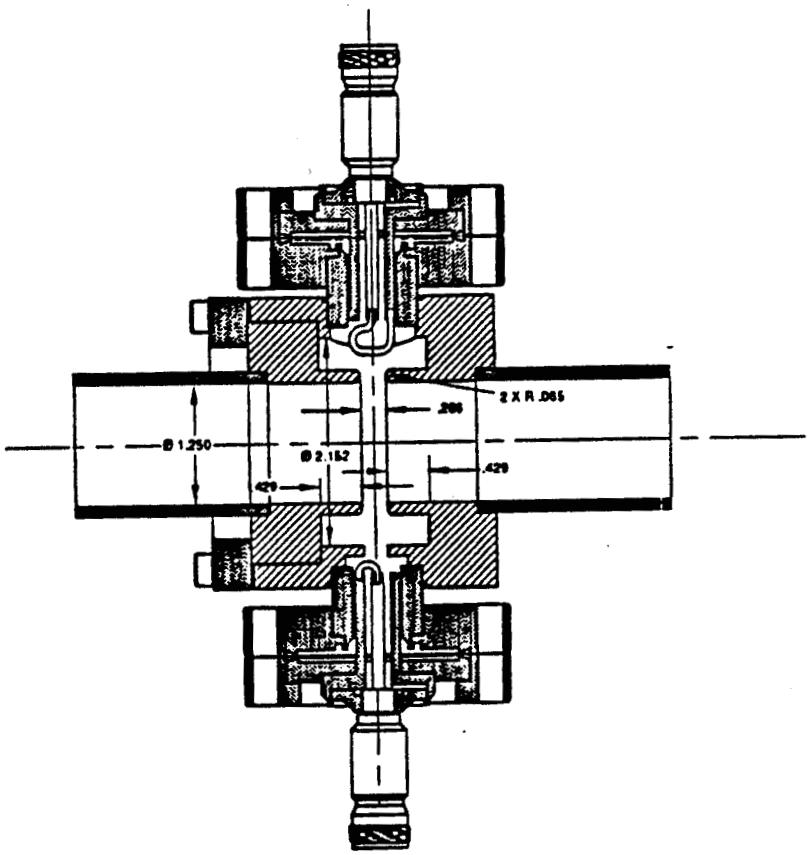

Figure 2.39: Schematic of the ringing cavity

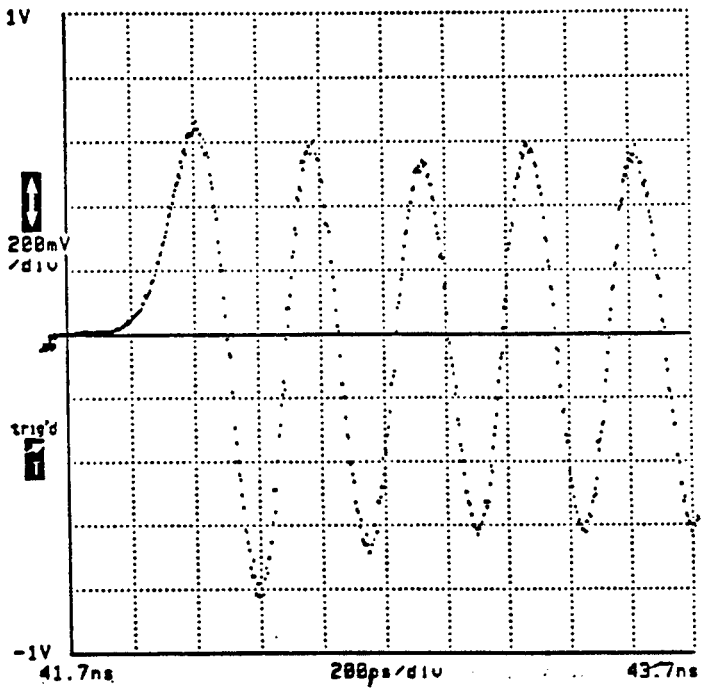

Figure 2.40: The response of the ringing cavity when an electron bunch tavels through

in Figure 2.39. It is made of copper and it normally operates at a temperature of 116^0 Fahrenheit. Figure 2.40 shows the response of the cavity after an electron bunch passed through it. The cables of the ringing cavity signal and the photodiode patch cables are measured using Time Delay Reflectometry (TDR), while the optical transport length is measured by sending the laser pulse into the IP and measuring with 2 photodiodes the relative delay of the input and return signals. Then the TRLP signal is compared in a 400 MHz oscilloscope with the cavity signal and a coarse timing of the laser - electron pulse is achieved by stepping the laser trigger delay using the PDU in 8 ns steps. When needed the phase of the reference rf before the timing stabilizer is adjusted by using a cable delay box with ns steps. The timing using this method can be set to $\pm$ 0.5 ns.

As discussed in the laser section the oscillator pulses before the regenerative amplifier will enter the variable optical delay line, which is used to fine adjust their timing with respect to the electron beam. The timing is achieved by positioning the stage with μm precision either manually or through an HPIB interface of the stage driver with a PC. Since the stage is 25 cm long it can cover the range of $\pm$ 0.5 ns. A PC broadcasts through Ethernet the stage position and receives commands for stage motion from the Data Acquisition System of the experiment. Thus we could perform a real time scan of the laser pulse timing and online correlate the optical delay with the yield of the products of the laser - electron interaction. The relative timing of the laser to the electron beam was established by fitting the signal as a function of optical delay. Figure 3.2 shows a timing scan as seen by the gamma counter.

2.5.2 Studies of timing jitter and long term drift

Both timing jitter and longer term drift are evident at the picosecond timing scale required in this experiment, and they were studied with several diagnostics and ultimately through their effect on the data. Measurements of timing jitter were done both in the time and in the frequency domain, resulting in $\sigma_{rms} = 2$ ps. Three methods were used for measuring the timing jitter and drift of the laser pulses with respect to the accelerator rf. First timing jitter is measured from the power spectrum of the

laser oscillator pulse train as it is revealed by sidebands off a high harmonic of the main 119 MHz frequency. Secondly, it can be measured directly in an oscilloscope as the time jitter of the rising slope of one of the laser oscillator pulses. Thirdly, a phase noise measurement is employed by comparing a high harmonic of the oscillator train with a high harmonic of the accelerator reference rf in a mixer. If the two signals compared are of the same frequency, the DC output of the mixer is proportional to the phase drift between the two signals. Finally the electron beam timing jitter and drift is also measured with respect to the accelerator rf using also a phase comparison technique. From the above measurements we measured the jitter of the laser pulse with respect to the electron bunch itself and compared to the results from the data. These methods are described in detail in the following paragraphs.

In the spectrum of the 476 MHz rf reference in sector 30 all the sidebands can translate into phase noise for any system that utilizes this signal. An estimate of the phase noise or equivalently of the time jitter from an analysis of the power spectrum can be obtained as follows [69]:

The spectrum of a microwave signal of frequency ω_0 is a series of the harmonics of ω_0, at frequencies $n\omega_0$, plus a series of amplitude noise sidebands $S_N(\omega - n\omega_0)$ and phase noise sidebands $n^2\omega_0^2 S_N(\omega - n\omega_0)$. At harmonics of sufficiently low order the amplitude noise sidebands dominate, while the phase noise sidebands have power proportional to n^2 and predominate for harmonics at higher order. The relative power of the sidebands of a high nth harmonic to the power of the nth harmonic itself determines the spectral density $S_J(\omega)$ of the timing jitter of the signal. Then the rms time jitter is given by

$$\sigma_J = \sqrt{< J^2(t) >} = \sqrt{\frac{1}{\pi}\int_{\omega_{low}}^{\omega_{high}} S_J(\omega)d\omega} \tag{2.13}$$

where all the sidebands from frequency ω_{low} close to the nth harmonic up to frequency ω_{high} away from the nth harmonic have been included in the measurement. The low limit is specified by the resolution of the spectrum analyzer used for the measurement and can vary from 50 - 200 Hz, while the high limit is practically taken as 25 kHz. In reality, though, frequencies above 2 kHz contribute little to the timing jitter integral.

We calculate $S_J(\omega)$ using standard methods from the theory of microwave oscillators [71] whose phase stability when operating in some frequency ω is usually specified by parameter $L_n(\omega)$. This is the total single-sideband phase noise spectral density of the nth harmonic of ω. In practice one defines $L_n(\Delta\omega)$ as the ratio of the power at frequency $n\omega_0$ to the power at frequency $\Delta\omega$ away from the $n\omega_0$, in 1Hz integration bandwidth. Since most of the spectra are easier given in decibels this ratio becomes a difference and following the terminology in the microwave literature one specifies from Figure 2.37 that $L(\omega)$ = -50 dB at ω = 360 Hz recorded using a 30 Hz bandwidth of the spectrum analyzer. Then an integration of the $L_n(\Delta\omega)$ over $\Delta\omega$ from ω_{low} to ω_{high}, gives σ_J.

From the above discussion it is obvious that instead of the power spectrum at 119 MHz of Figure 2.37 it is better to measure time jitter from a high harmonic of this signal. Since the ringing cavity has a resonance at 2856 MHz, the 24th harmonic of the reference is chosen and the time jitter calculated with the above method: The power spectrum is segmented in 50 Hz bins from ω_{low} = 100 Hz up to ω_{high} = 1.5 kHz. For each bin the difference of the power to the peak power at the reference frequency is found by also taking into account the resolution bandwidth of the spectrum analyzer. Then by an integration over all the bins and from eq. 2.13 the timing jitter is calculated to have σ_{rms} = 2.0 ps. This is an upper estimate since we have not taken a high enough harmonic and most probably there still remains some amplitude noise in this spectrum.

In the time domain a measurement was performed with a sampling scope [72]. The laser pulse was monitored with a fast photodiode with 20 GHz bandwidth [73] and its output was the signal into the sampling scope. The oscilloscope is triggered by the reference 119 MHz rf signal. The diode was positioned both before and after the laser pulsewidth diagnostic compression grating setup with no particular change in the measured time jitter result. The resolution limit of the time domain technique is set by the jitter of the external triggering module of the scope, which was measured by generating trigger and signal from the 119 MHz using a power splitter and delaying the signal by 34 ns to compensate for the internal scope delay. This measurement gave a time jitter of σ_{rms}^{scope} = 3.5 ps.

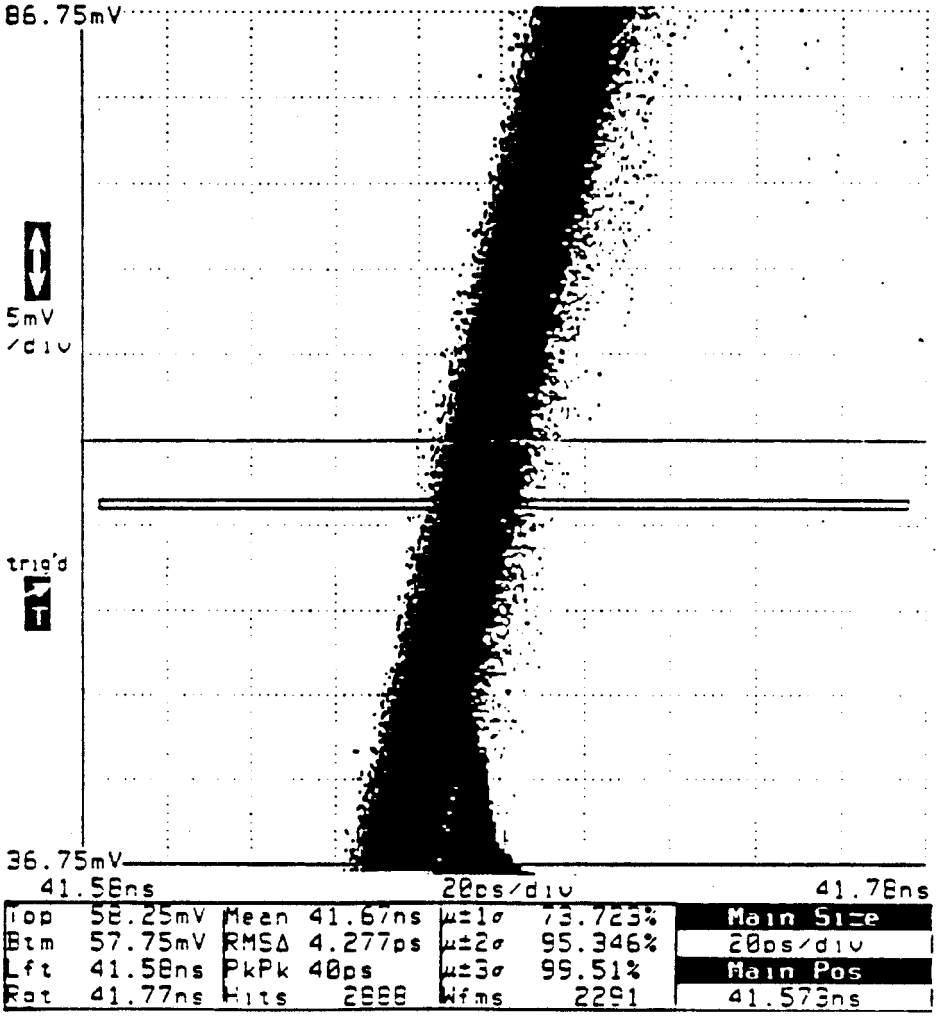

Figure 2.41: Timing jitter measured in time domain

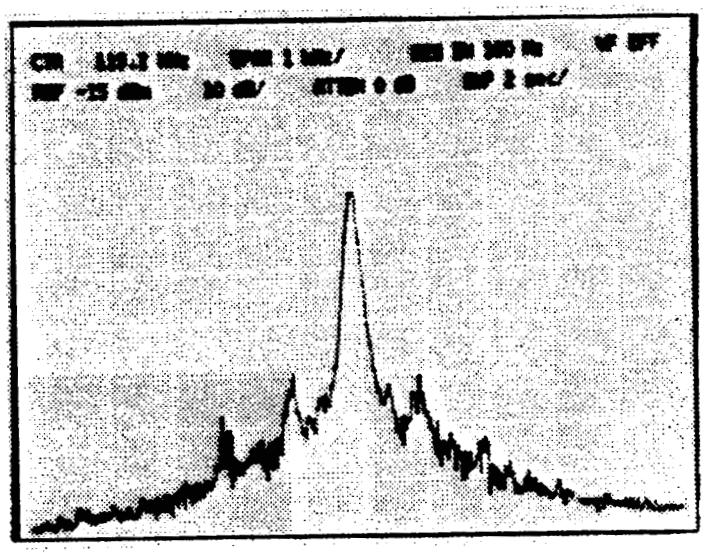

Figure 2.42: Power spectrum of the laser oscillator pulse train

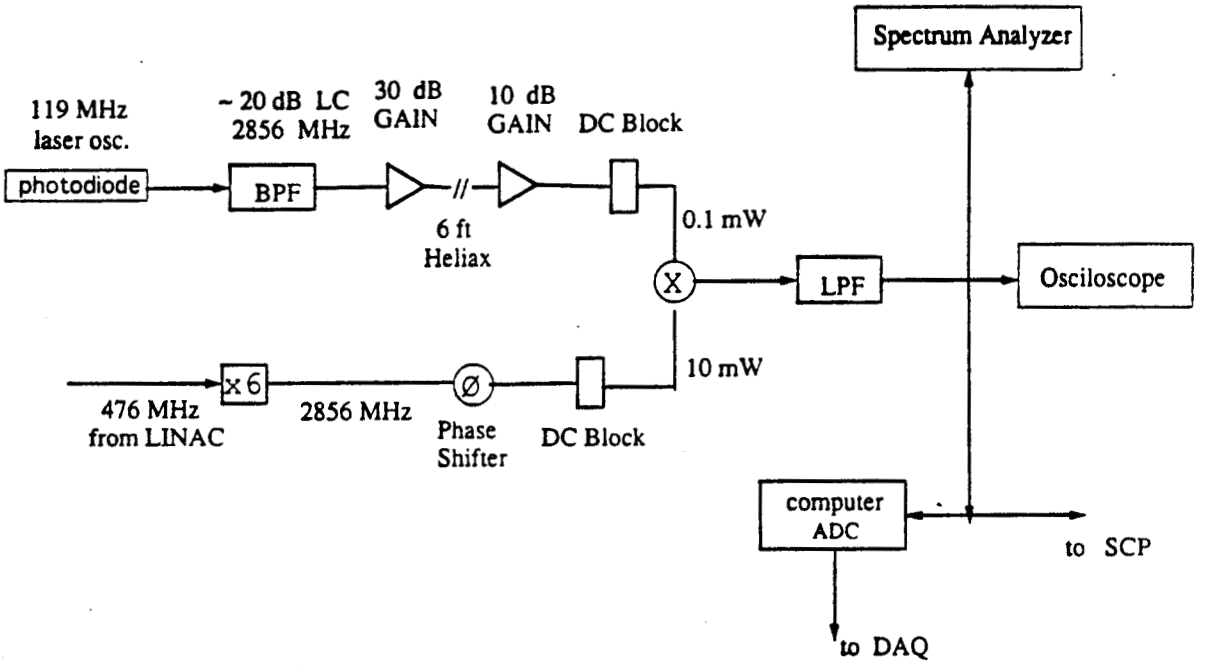

Figure 2.43: Block diagram of the laser pulses phase noise measurement setup

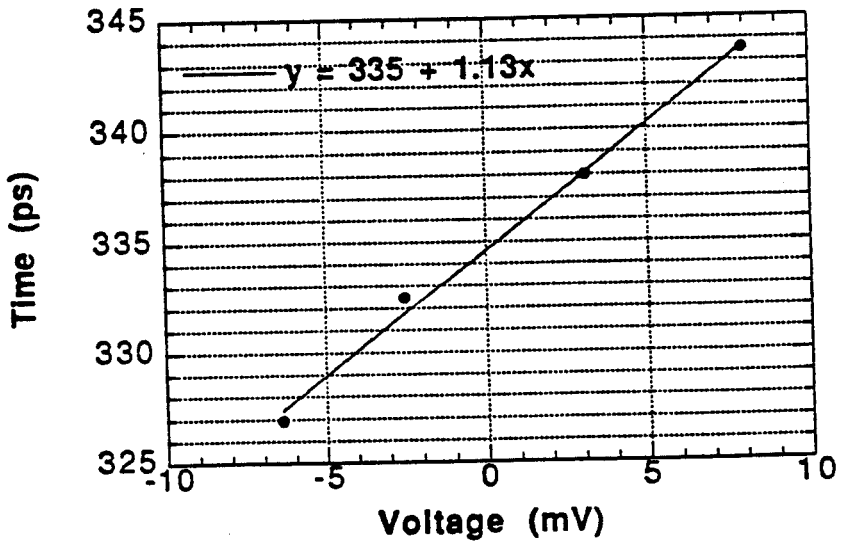

Figure 2.44: Calibration of the phase noise measurement setup taken by phase shifting one of the arms of the mixer with respect to the other.

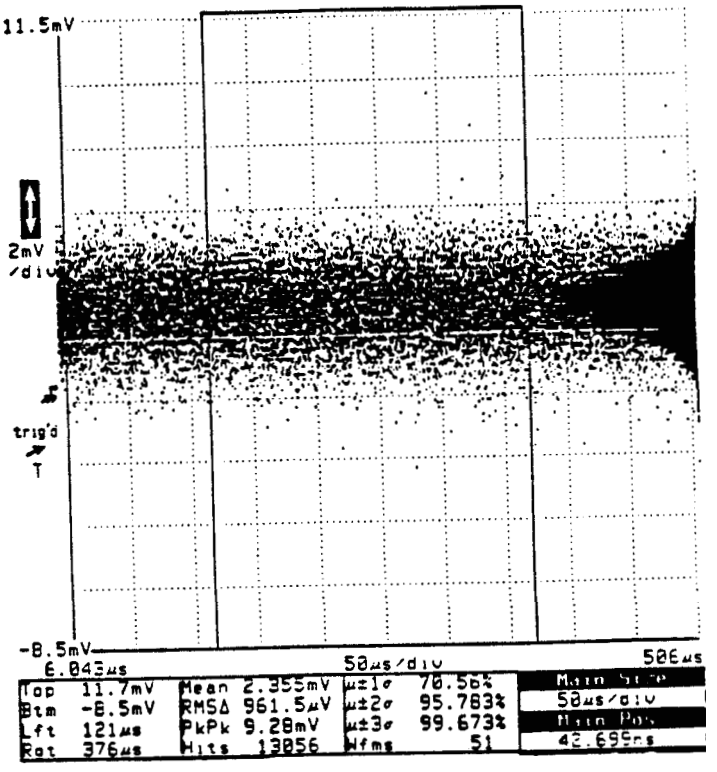

Figure 2.45: Phase noise of the laser oscillator pulses with respect to the reference rf as measured by the phase comparison technique

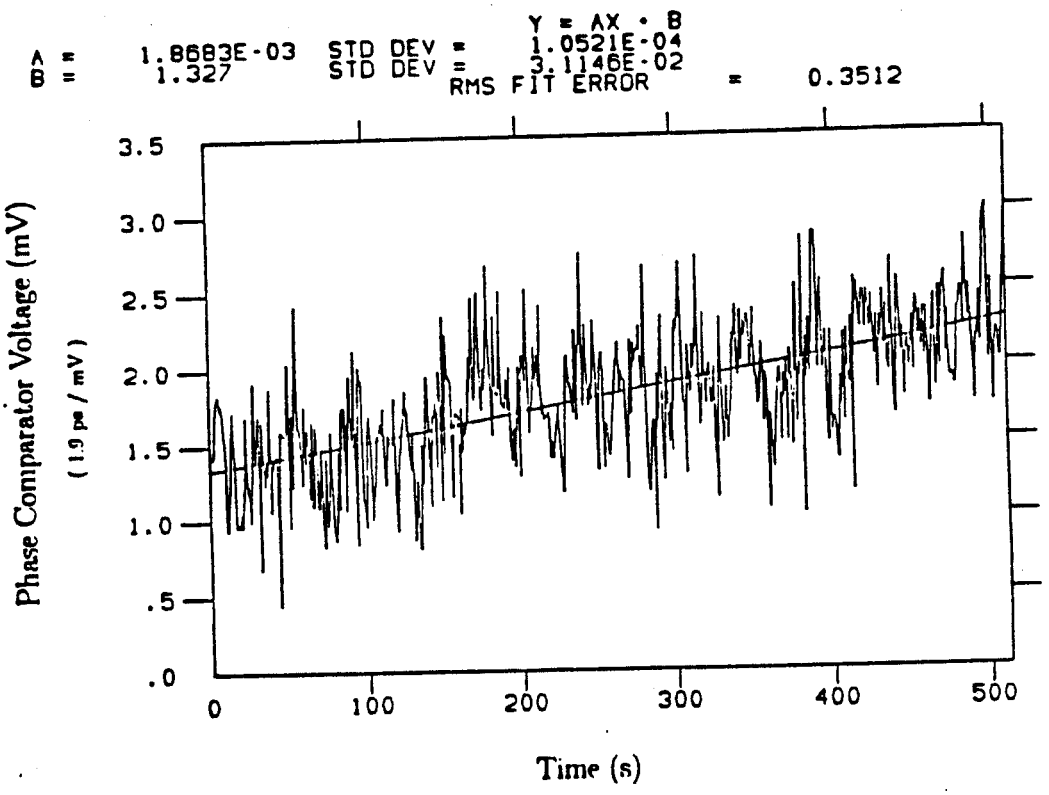

Figure 2.46: Jitter and long term timing drift of the laser pulses with the accelerator reference rf measured by phase comparison

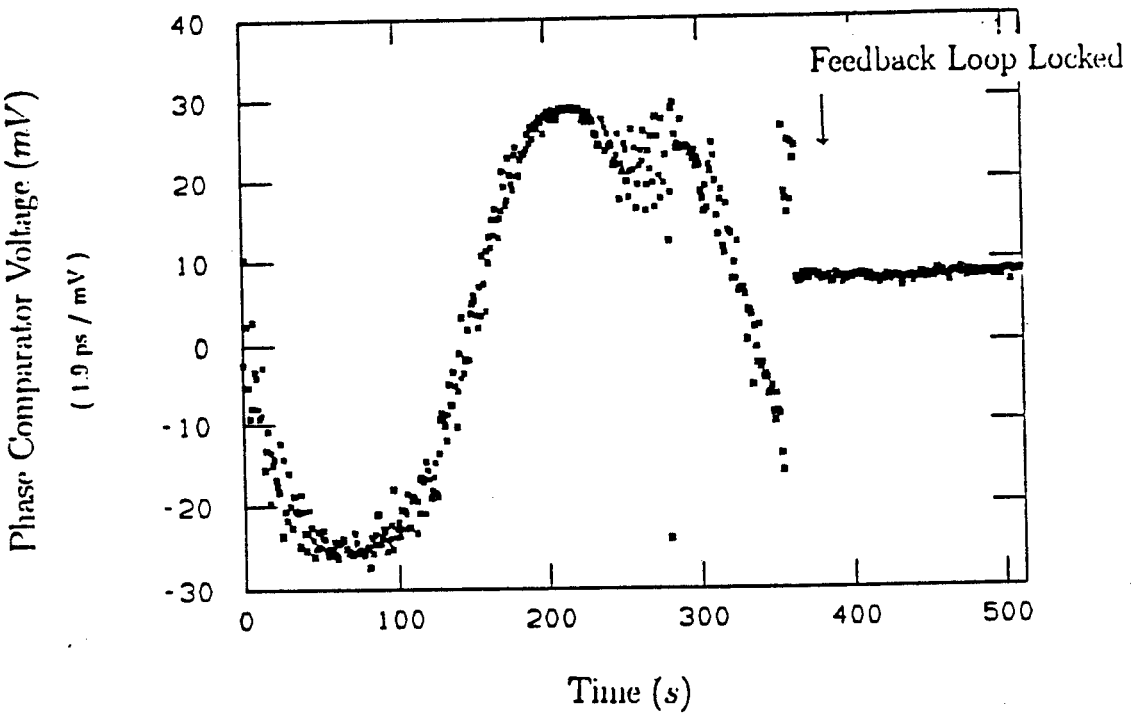

Figure 2.47: Timing drift when deactivating the timing stabilizer feedback loop

An individual laser pulse of the 119 MHz pulse train which was shown in Figure 2.10 can be studied in order to measure its time jitter. To avoid amplitude noise effects one would like to study the low part of the rising edge of this pulse or even its zero crossing with the time axis when a low pass filter is introduced in the signal. Both techniques gave equivalent results. Figure 2.41 shows the leading edge of a laser pulse and gives a nominal (before resolution subtraction time jitter of $\sigma_{rms}^{total} = 4.3$ ps). After quadrature subtraction of the scope limit we are left with the real time jitter of the laser pulses with respect to the accelerator rf:

$$\sigma_{rms} = 2.0ps \tag{2.14}$$

The time jitter induced by the FIDO module can also be measured by comparing the 119 MHz output signal with a fraction of the 476 MHz input in the sampling scope; it was found to be within the scope limit.

The output of the 20 GHz diode was used as an input to a spectrum analyzer [78] and the power spectrum of the laser pulses was measured directly. The main 119 MHz frequency is shown in Figure 2.42. A time jitter measurement from the 24th harmonic spectrum gives a $\sigma_{rms} = 2.5$ ps, which again is an upper limit.

A further diagnostic of the timing stability of the system is a phase comparison of the laser pulse train and the drive rf. This is done at the LINAC frequency of 2856 MHz. The 476 MHz output of the optical fiber is multiplied by 6 and fed to an arm of a double balanced mixer (DBM). The other input to the mixer is the 24th harmonic of the laser pulse train detected by the diode and selected by a 2856 MHz Bessel filter and subsequently amplified by 60 db, being input before the mixer. Then the output of the mixer is filtered for DC with a low-pass 50 MHz filter in order to avoid leakage of both the main 119 MHz frequency and its sub-harmonic 59.5 MHz through the mixer and fed into the sampling scope. Figure 2.43 is a block diagram of this setup. The theory of DBMs [79] suggests that when two signals of identical frequency but of different phase are applied to the inputs of a balanced mixer, the output at the IF port will be DC voltage proportional to the phase difference. The calibration of the mixer used in this setup is shown in Figure 2.44 and corresponds to 1.1 mV/ps. The limit in the sensitivity of the measurement can be found by introducing the reference

signal in both the RF and LO ports of the mixer, and zeroing the mixer output with the phase shifter.

A typical output signal of the phase comparison of the laser and rf reference signals is shown in Figure 2.45. From the width of the trace, after subtracting in quadrature the measurement limit, we deduce that the timing jitter has

$$\sigma = 1.2ps$$

For longer time scales the output of the mixer is sampled by an ADC card in a PC and shows variations of the order of few ps during 30 min of data collection as shown in Figure 2.46. In contrast, when the timing stabilizer loop is deactivated, drifts of order 100 ps in a time scale of minutes are evident as seen in Figure 2.47.

The stability of the electron beam with respect to the reference rf is checked using the ringing cavity. The 2856 MHz signal is transported to the laser room, amplified by 30 db and phase compared with the 476 MHz driving frequency (already multiplied by 6). The system records a phase jitter measurement based on approximately 100 consecutive electron beam bunches and is interfaced with SCP. The rms jitter recorded by the cavity is about 0.3 degrees in S-band, while when the electron beam is absent a pedestal RMS noise of 0.1 degrees is observed. Variations on a time scale of 30 minutes are less than 2 ps rms, while diurnal effects that change the length of the LINAC do change the electron timing on a time-scale of hours. Figure 2.48 shows the phase noise of the electrons with the reference to the laser rf together with the ambient barometric pressure over the period of 6 days, and the 'phase ramp' which is used by the accelerator operators to vary the phase of the electron beam manually in case the MDL feedback is inadequate or needs to be opposed. This adjustment has an instantaneous effect in the laser-electron timing.

Since this experiment utilizes the accelerator and the laser technology, it inherits all the possible noise sources from both. As a result, the frequencies of the timing jitter sources span the range from the low to the high acoustic frequencies, which makes it difficult to isolate and correct. In addition, there are also long term timing drift sources that affect the data collecting process of this experiment.

The accelerator contributes to the timing jitter with frequencies at 360 and 750

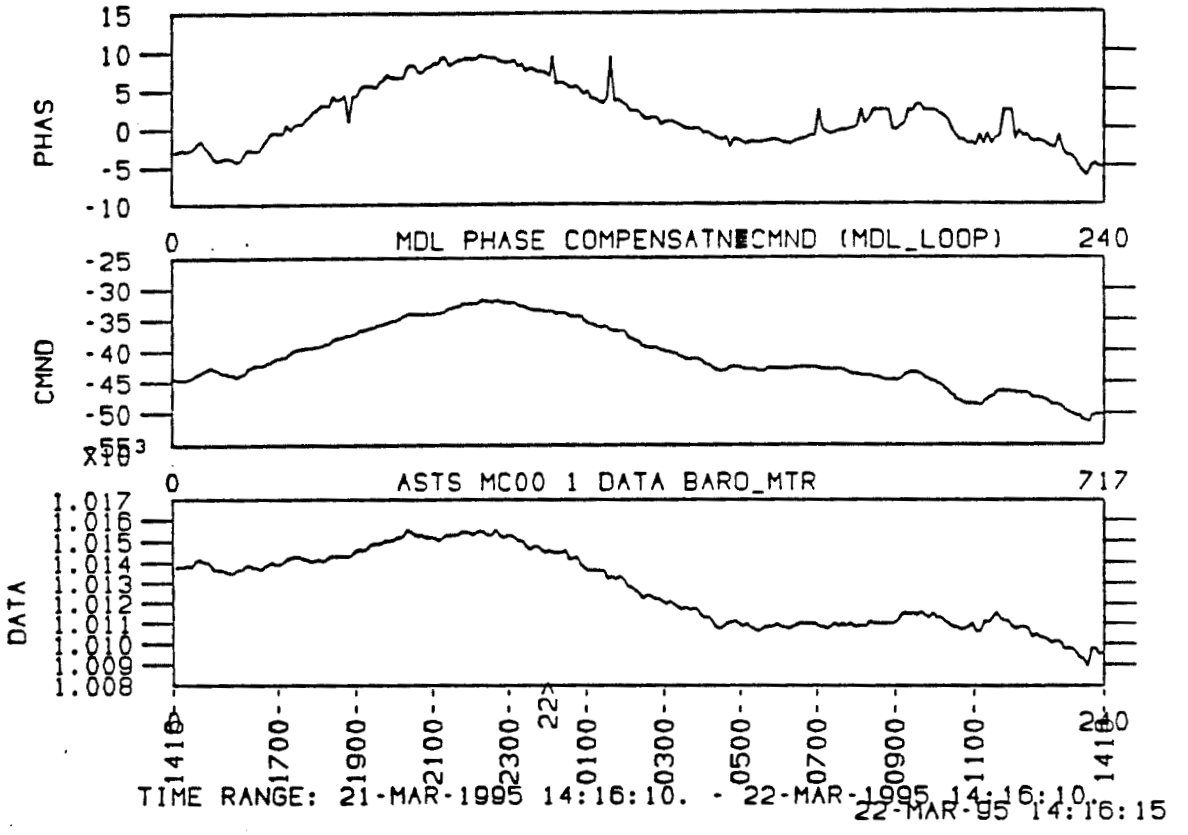

Figure 2.48: Correlation of the electron beam phase drift with respect to the reference rf signal, as measured by the ringing cavity, with the 'operators' phase knob' and the ambient barometric pressure

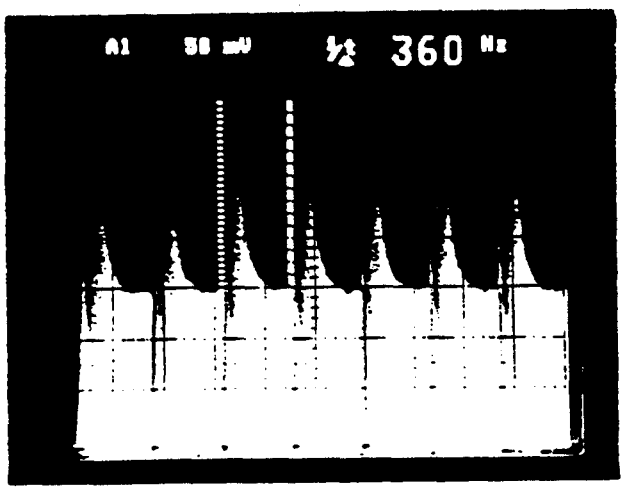

Figure 2.49: Signal of the fast photodiode that monitors the leakage from the curved oscillator cavity mirror. The 360 Hz Fiducial Leakage detunes the ML and creates the instability shown as Spikes

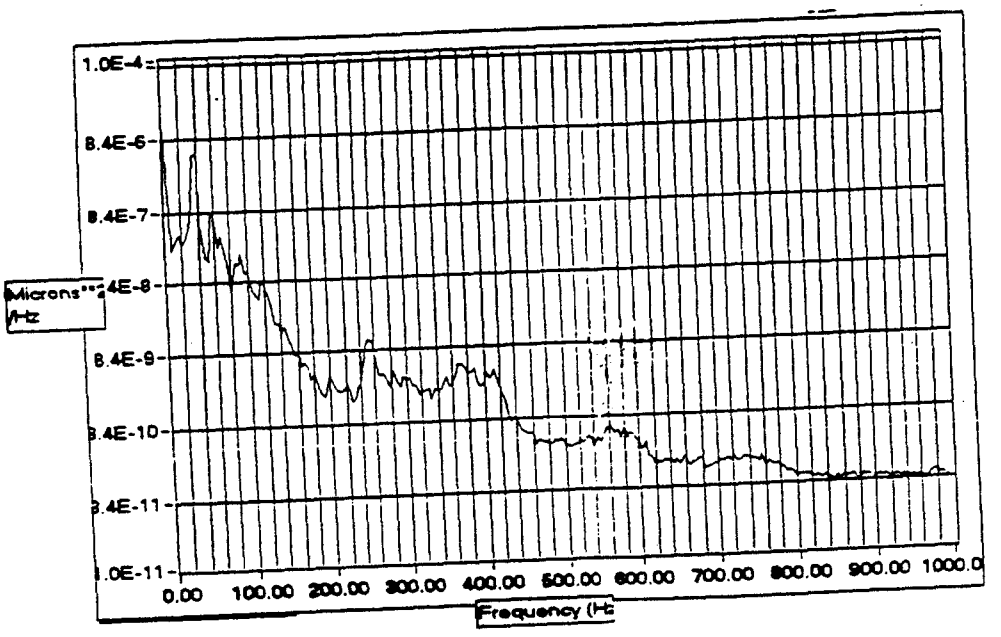

Figure 2.50: Mechanical stability of the oscillator invar plate: Lamps and ML water on

Hz and their harmonics. As mentioned above one possible source of timing jitter is the 360 Hz of the fiducial pulse which shows as a sideband in a power spectrum of the reference rf. Its effect on the oscillator pulse train is immediately noticed on the photodiode that monitors the leakage from the curved oscillator cavity mirror as seen on Figure 2.49. Although the timing stabilizer module filters the input 119 MHz, the 360 Hz is a sideband on the carrier and usual bandpass passive filters have a much broader acceptance [79]. The solution for this problem is to inhibit the fiducial generating circuit inside the FIDO module. The 750 Hz which results from the electron interferometer, can only be inhibited with expensive Phased Locked Loops (PLLs) and it was not corrected for in this experiment. The main 750 Hz sideband on the 24th harmonic of the reference signal has a substantial amplitude and contributes to the phase noise, while its harmonics are steeply falling in amplitude.

Most of the jitter on the laser pulses stems not from the reference signal but from individual components and collective effects of the laser itself. For similar mode locked oscillators these effects are discussed in [69, 74, 75, 76].

Since the oscillator cavity optical path length defines the frequency of the laser pulse train, possible variations on it are a source of timing jitter. This path length varies due to mechanical vibration of the cavity mirrors or refractive index changes of the Nd:YLF rod, the Brewster polarizer or the ML. Thermal changes in the cavity length which would show as long term drift, are unimportant, since the cavity is on top an invar plate which has a small thermal expansion coefficient. A slight detuning of the cavity length increases the noise floor of the power spectrum. This shows that in the frequency domain, the cavity length variations affect the laser pulse train in a broad range of frequencies from as low as a few Hz, the resolution of the spectrum analyzer, and as high as 5 kHz.

The mechanical stability of the oscillator invar plate was checked with an accelerometer. A quiet noise floor of 3.2×10^{-10} $\mu m^2/Hz$ was detected when all the equipment in the laser room was turned off. It increases in specific frequencies when the water re-circulator to the oscillator lamp or the chiller to the ML heat sink are on, as shown in Figure 2.50. Possible vibrations created by the ML chiller are detected at 100, 200, its harmonic at 400 and at 550 Hz, while the lamp's cooling system increases

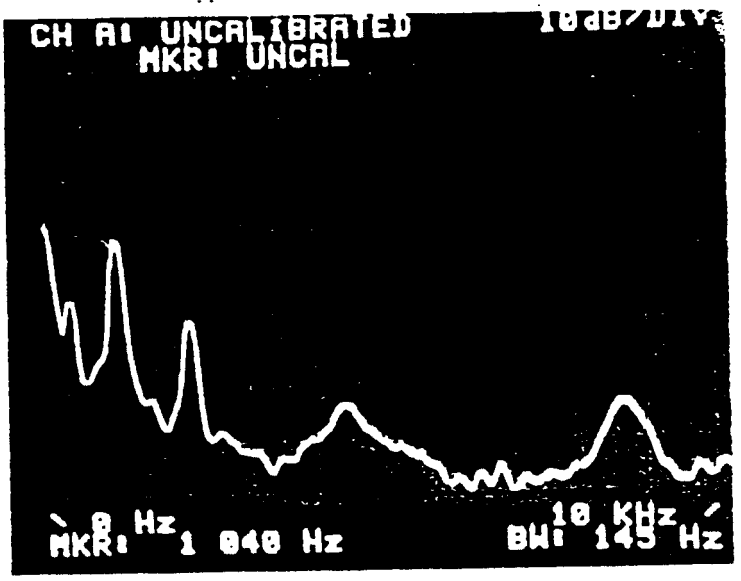

Figure 2.51: The Low Frequency Spectrum of the Laser Pulse Train

10-fold the noise floor in the frequency range of 100 to 500 Hz. The mechanical vibration from the water to the lamps was eliminated by using a flexible hose system that decoupled the laser head from the rest of the system, while the ML chiller was positioned on rubber mats.

A low frequency spectrum analyzer [80] records the rms average of 16 traces from the 20 GHz diode on a 10 kHz span in Figure 2.51. These spectra identify noise sources in other frequencies and especially at 60 Hz, 360 Hz, 1.05 kHz and its 2nd harmonic at 2.1 kHz, and higher frequencies. All these frequencies are discernible as sidebands of the 24th harmonic of the 119 MHz pulse train frequency, which establishes their contribution to the phase noise in the experiment.

Apart from mechanical noise a possible source of timing jitter is the oscillator power supply that results in amplitude fluctuations in the flashlamps. This amplitude noise could couple into phase noise due to the presence of Raman gain in the Nd:YLF which produces an intensity dependent shift of the laser frequency [77]. The 60 and 360 Hz peaks in the power spectrum are identified as this source for noise. The larger source of noise is the 1 kHz sideband, which is only speculated to be originating in the TS circuit feedback loop response.

Longer term drift due to the thermal expansion of the CPA fiber was not detected since the TS diode was positioned both before and after the fiber resulting in similar drifts of 0.5 ps /min. This kind of drift is within the specifications of the TS [70]. A slow change in the polarization of the light after the fiber was detected which results in intensity variation of the light in the time-stabilizer diode diode due to its sensitivity only in S polarization. This change possibly drives the feedback loop with less than the optimal level and so affects its performance. Relaxation of the optics mounts on the optical tables and mainly of the end mirrors of the oscillator cavity can also result in a long term drift. The thermal stability of the ML is critical to its performance and subsequently to the timing jitter of the oscillator pulses, as described in the laser setup, even though the temperature changes of its water recirculator were maintained to approximately 1^0 C. The main reason of long term instability in the timing is the electron beam path length changes due to ambient temperature variations, as observed in Figure 2.48, and due to the IP box motion

which translates into timing drift of the two beams with respect to each other.

In conclusion, there were two main sources for timing jitter: the 750 Hz noise from the electron interferometer and the 1kHz noise, which is only speculated to be the TS phase shifting electronic board. The main source for drift is the TS resulting in 0.5 ps/min timing drift and the electron accelerator length resulting in 2 ps/hour timing drift. During running periods of this experiment, we try to correct for drift by stopping the data taking process and re-timing the laser with the electrons using time scans. The timing jitter was obvious in the data as described in Appendix D and could not be corrected better than $\sigma_{rms} = 1.5$ ps.

2.6 Detectors

At the interaction point the high energy electron beam absorbs one or more laser photons and loses energy while emitting a high energy gamma ray in the forward direction, due to either linear or nonlinear Compton scattering. If the laser field is strong enough in the electrons' rest frame to exceed the critical QED field then electron-positron pairs are expected as well. All the products of the interaction are moving in the forward direction (at an angle $1/\gamma$), but a magnetic spectrometer based on the electron permanent dump magnets deflects the electrons and positrons on opposite directions onto two similar calorimeters. An electromagnetic shower sampling [83] calorimeter (ECAL) [81] detects the backscattered electrons. The gamma ray flux, dominated by the linear Compton scattered gammas, is detected by a photon counter (CCM1) located on the gamma line, downstream of the IP.

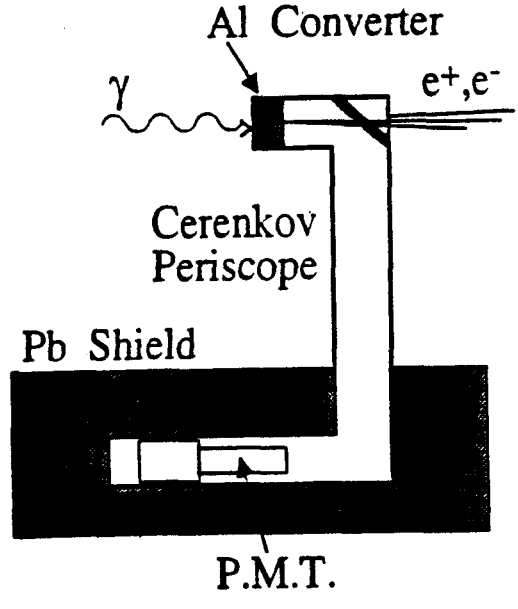

Figure 2.52: A schematic of the forward gamma counter (CCM1)

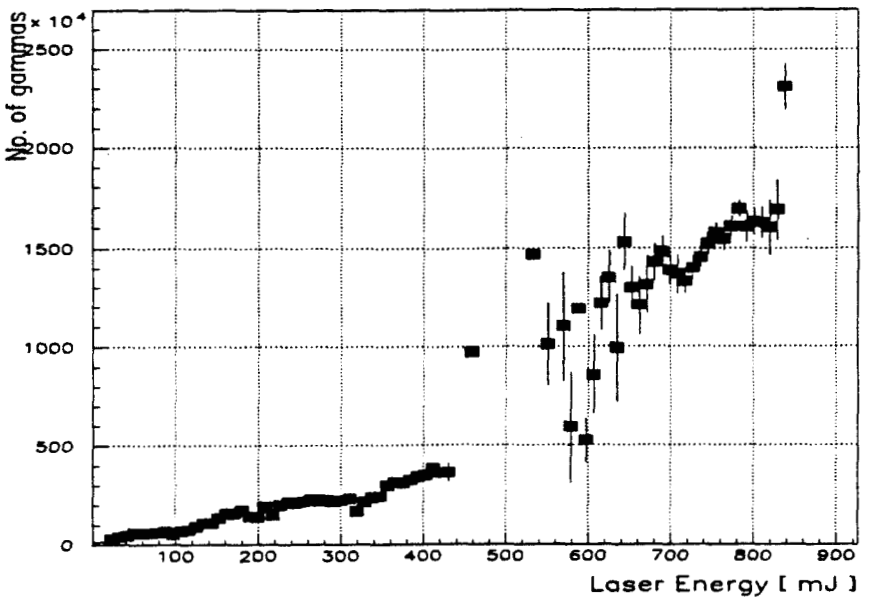

Figure 2.53: The Correlation of the gamma rate with the Laser Energy for IR runs proves the linearity of the monitor. The two distinct slopes correlate well with the change in the electron beam parameters.

2.6.1 Forward gamma monitor

The detector that measures the linear gamma rate and is used to normalize the nonlinear scattered electron rate is similar to the ones used in the SLC wire scanning setup. Figure 2.52 illustrates the counter design. A shower converter, in this case 0.2 radiation lengths of Al from an electron beam flange located in front of the detector, precedes a length of 25 mm of air. The gammas convert into pairs and in turn emit Cherenkov radiation in air. A 45^0 mirror made of polished aluminum directs the Cherenkov light downwards towards another similar mirror which in turn deflects it into a photo-multiplier tube with the total light path being 1 m. The cross section of the initial light channel is 25 mm $\times$ 25 mm and this is increased after each additional 90° reflection to retain rays within 7° of the axis. This design places the PMT far from the electron beam line to reduce backgrounds and allow for shielding by lead.

The walls of the Cherenkov section and the first few cm of the light pipe are painted flat black. Beyond that the walls are made highly reflective by applying aluminized Mylar. The PMT was chosen for its ability to deliver large peak currents, and the voltage division was selected to optimize this for gains of order 10^4 while the tube operates at 1500 to 1800 V. A filter, made out of Al with a regular pattern of 36 holes, can be inserted remotely in the light path. This induces an attenuation of a factor of 10 and is available in order to prevent the PMT space charge saturation which can occur with small spots. The whole gamma counter is on rails and can be remotely taken out of the path of the gamma rays. The PMT reading is sent to an ADC counter on a CAMAC crate, and from there to both the SCP control program and to the data acquisition system of the experiment.

A calibration of the gamma counter is done by inserting the IP Al foil as shown in a previous section. The calibration is based on the assumption that the CCM1 acceptance is the same for bremsstrahlung and linear Compton gammas. Furthermore, the total gamma flux from bremsstrahlung with that foil is calculated to be about equal to that of linear Comptons. Then one can conclude that although the spectra of the two processes are different the calibration based on the bremsstrahlung rate is valid.

Figure 2.53 shows the linearity of the counter with the laser energy during a typical run. The two distinct slopes in this figure correspond to two electron beam configurations with different electron beam horizontal dimensions. Since the laser is colliding with the electron beam in the horizontal plane more gammas are produced if the electron beam extends further horizontally. The gamma rays that the counter detects are primarily from linear Compton scattering and, therefore, should scale linearly with laser energy as long as the geometry of the interaction region, e.g. electron beam configuration, is not changing.

2.6.2 Magnetic spectrometer

The magnetic spectrometer is located downstream of the IP consisting of 6 permanent magnets that also direct the un-scattered electron beam to the electron dump. A

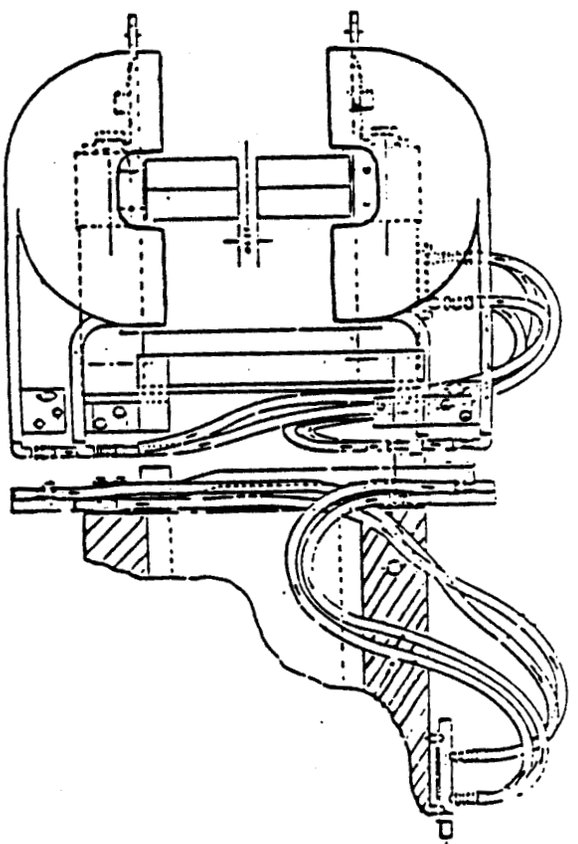

Figure 2.54: A schematic of one of the permanent magnets

scaled schematic of one of these magnets is shown in Figure 2.54. The field map of one of the magnets is shown in Figure 2.55. A particle tracking code was developed and the results are shown in Figure 2.56 where also the position of the two calorimeters and their acceptance is drawn. The electron calorimeter (ECAL) is positioned downstream of the 6th magnet, under the electron beam-pipe and is on a remotely controlled stage that increases its effective acceptance to a range of 5 - 30 GeV. The positron calorimeter is positioned on top of the chamber after the 4th magnet in order to detect positrons with energies in the range 16 - 5 GeV [22].

2.6.3 Electron calorimeter

The electron sampling calorimeter (ECAL) is made of layers of absorber (tungsten) and detector (silicon) with total of 23 layers as in Figure 2.57 [81]. The tungsten layer has 1 radiation length of thickness. Each of the silicon layers is segmented into 12 rows and 4 columns of 1.6 cm × 1.6 cm active area pads. Every 4 rows are separated by 1 mm of inactive silicon. Some of the calorimeter design parameters are shown in Table 2.3. Since the electron calorimeter is centered with respect to the electron beam-line we expect the signal to be measured by the two middle columns (inner pads), while the two outer columns (outer pads) give an estimate of the various backgrounds as will be discussed in the data analysis section. The longitudinal layers of ECAL are wired into four segments in a pattern suggested by an EGS simulation

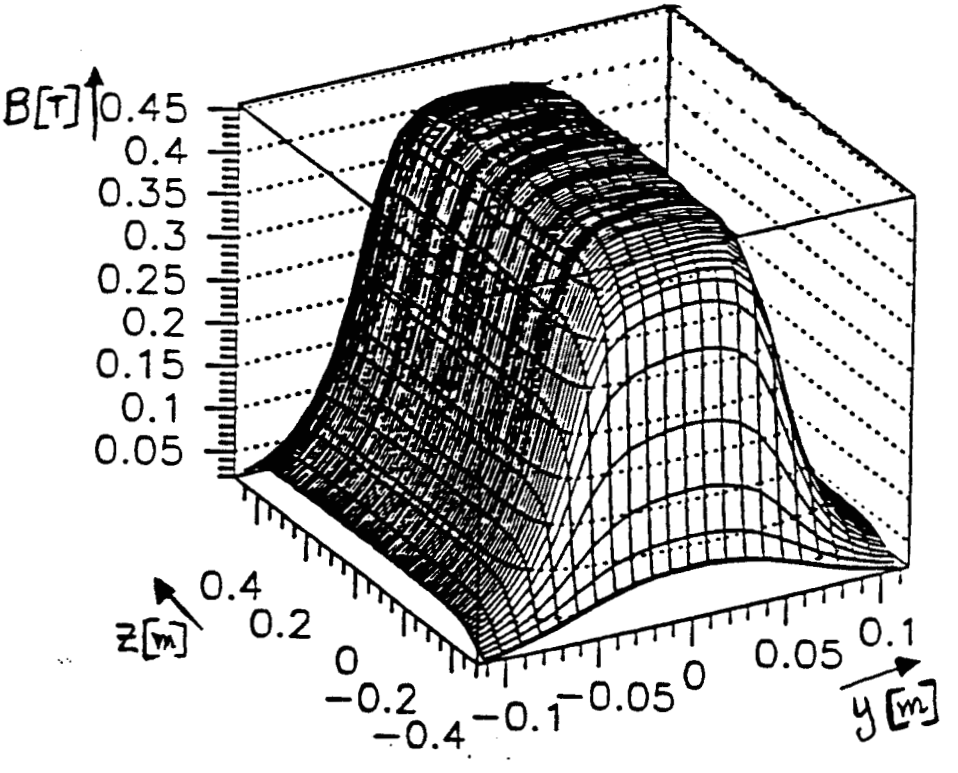

Figure 2.55: Field map of one of the permanent magnets

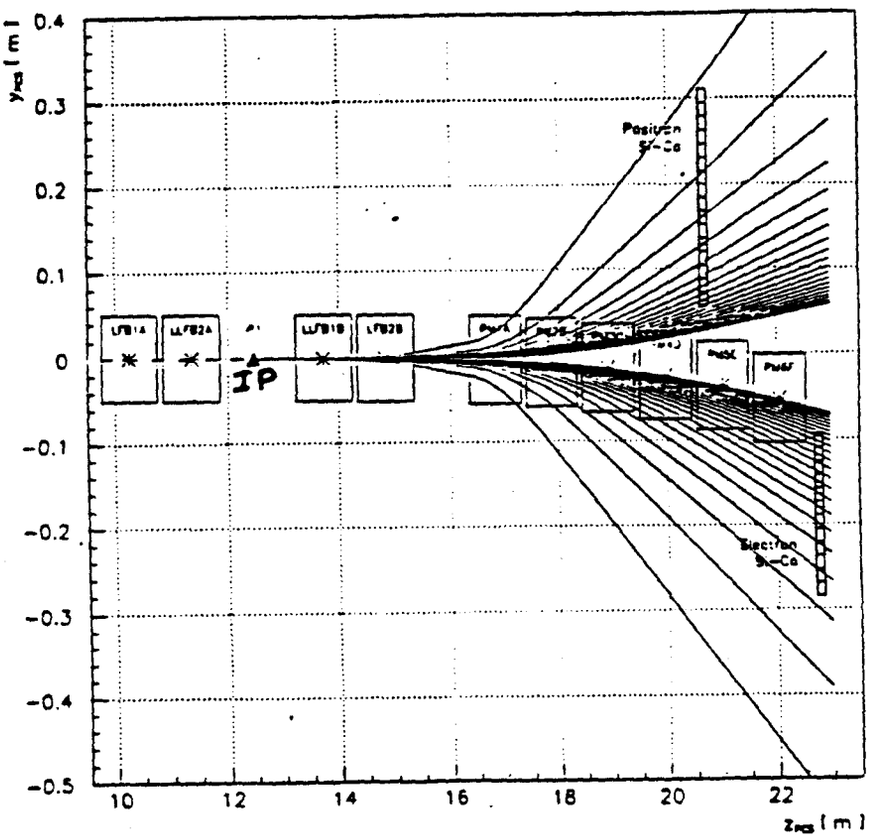

Figure 2.56: Electron and positron trajectories after the interaction point

(a particle propagation simulation code for detectors)[84] to balance the signal in the first three segments and use the last segment to estimate possible backgrounds. This configuration also creates a smaller load on the data acquisition system.

The readout of the calorimeter is done with electronics that had been used at experiment E706 of Fermilab. The Redundant Analog Bus Based Information Transfer (RABBIT) system reads the charge collected by the silicon pads and amplifies it using modules designed also for the E706 Liquid Argon Calorimeter (LACAMP modules). The whole system is interfaced with a PC that is part of the data acquisition system

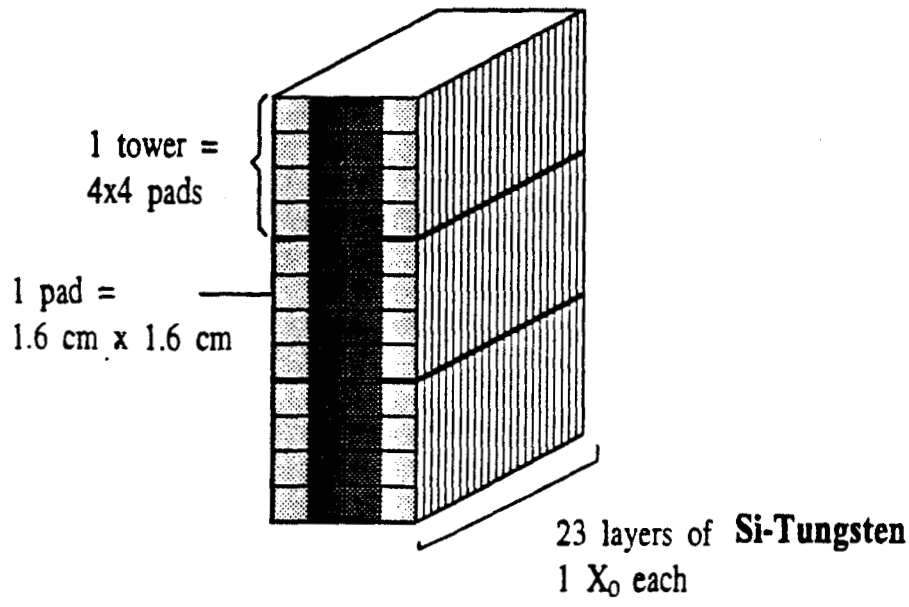

Figure 2.57: Schematic of the electron calorimeter

described in a later section.

The fraction of the total incident energy which is deposited in the silicon is given by [82]:

$$\frac{E_s}{E} \simeq \frac{\frac{dE}{dx}|_s d_s}{\frac{dE}{dx}|_w d_w + \frac{dE}{dx}|_s d_s} \tag{2.15}$$

where $\frac{dE}{dx}|_i d_i$ is the minimum ionizing loss in the medium i and d_i is its depth. So from the parameters given in Table 2.3 we calculate that $E_s/E \simeq 0.1\%$ which confirms the 'sampling fraction' of the same Table. The amount of energy needed to create one electron-hole pair in silicon is 3.6 eV and since holes drift 3 times slower than electrons, the total charge seen by the integrating electronics is approximately 3×10^6 electrons per GeV of incident energy. This signal corresponds to 490 fC and due to the range of electron momenta we would like to explore (5 - 30 GeV/c) we have a limited dynamic range of the electron rate detected by the single amplifier and ADC card. The saturation limit of the ECAL electronics was 10 TeV.

Parameters	**ECAL**
no. of layers	23
wafer size	6.4 cm × 6.4 cm
pad size	1.6 cm × 1.6 cm
height	19.5 cm
width	6.4 cm
inactive area	0.15 cm
sampling fraction	1.1 %
silicon area	2820 cm^2
acceptance	$\simeq$ 5 - 30 GeV
long. segm.	4
channels	192

Table 2.3: Characteristic parameters of the electron calorimeter (ECAL)

ECAL was calibrated in parasitic running of the FFTB to the SLC program in which LINAC-halo electrons of energies between 5 and 25 GeV were transmitted by the FFTB when tuned to a lower energy. The number of such electrons varied between 1 and 100 per pulse, which provided an excellent calibration of the ECAL over a wide dynamic range. Figure 2.58 shows the ECAL response to a beam of 19 GeV electrons. The resolution of the calorimeter can be found from these data to be

$$\frac{\Delta E}{E} = \frac{25\%}{\sqrt{E}}$$

Also in calibration runs the longitudinal profile of the shower in the calorimeter is shown to agree with EGS simulations. The transverse profile of the shower showed very small leakage $\simeq$ 1% from the inner pads to the outer pads.

2.7 Triggers and data acquisition system

The triggers for the experiment were provided by a single PDU which, as described before, is tunable both in time delay and in repetition rate and is synchronized with

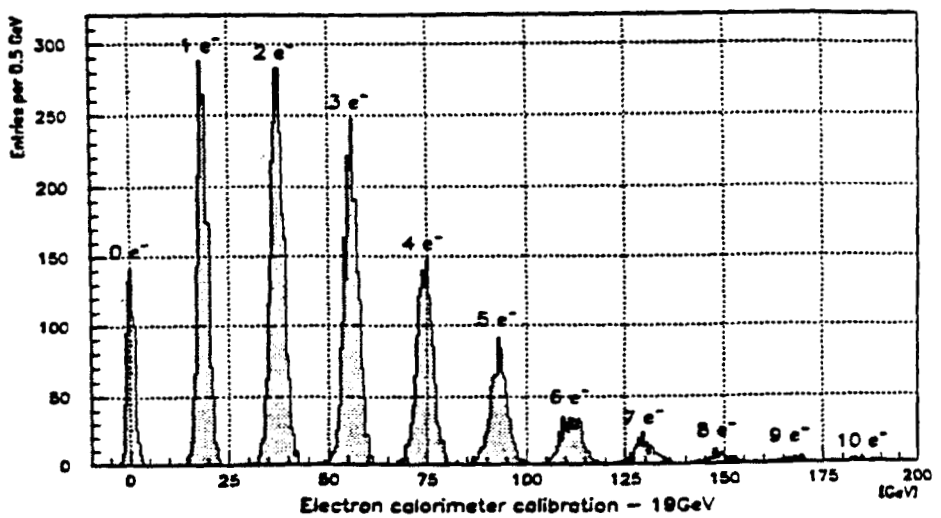

Figure 2.58: ECAL response to 19 GeV electrons in calibration mode

the fiducial of the accelerator rf. A 10 Hz rate is used as the primary trigger for the experiment. This frequency is divided to 0.5 Hz to provide the laser trigger and to 3 Hz to create 3 trigger pulses in between the laser firing for the DAQ system. The main purpose is to collect data in the following cases:

(a) The laser fires and the electron beam is present at the interaction point. This is the trigger for measuring the signal events.

(b) The laser does not fire but the electron beam is still present. This provides the electron beam background measurement.

(c) Neither the laser nor the electron beam are present in the IP, allowing electronic pedestal measurements.

(d) The laser fires but the electron beam is not present at the IP to look for laser associated electronic noise. No noise was detected during the running period.

A 3-bit trigger is used in the DAQ in order to accommodate the above possibilities. A schematic of the trigger electronics is shown in Figure 2.59.

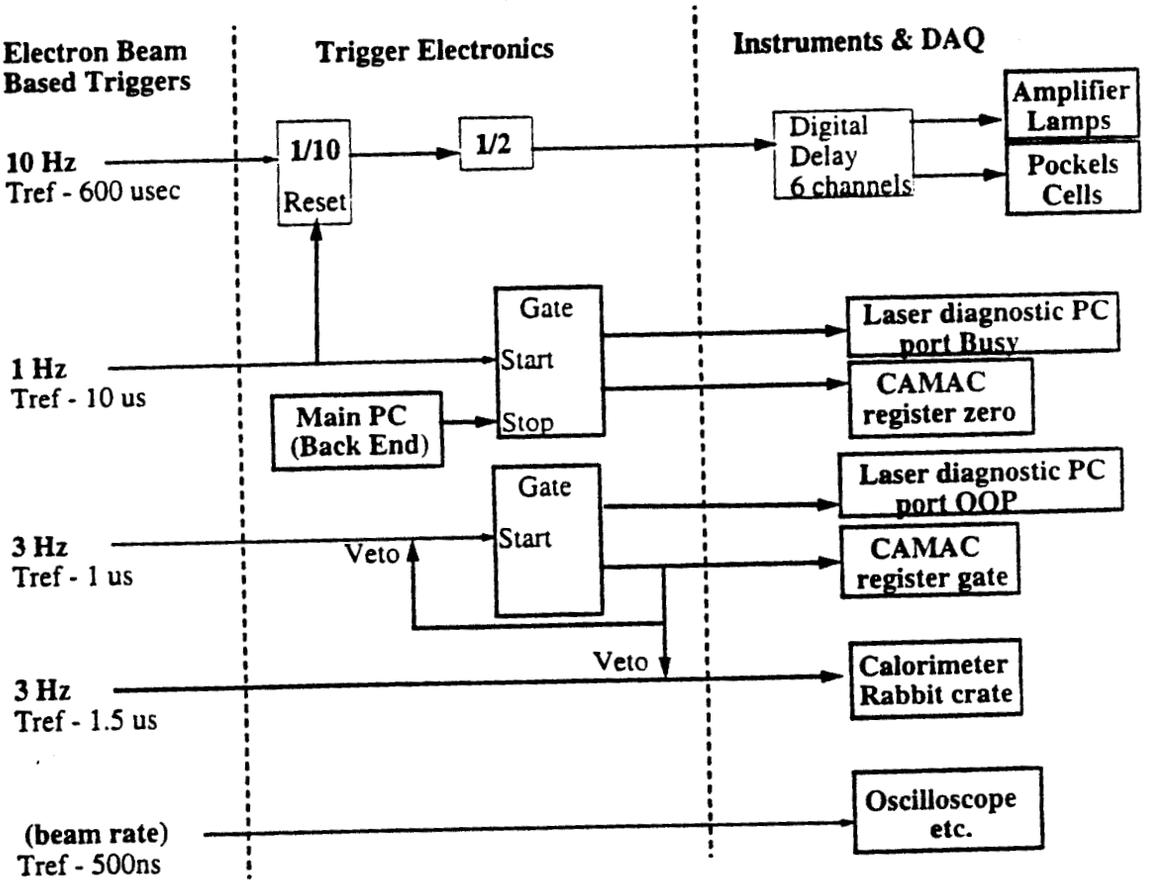

Figure 2.59: The Triggers for the experiment

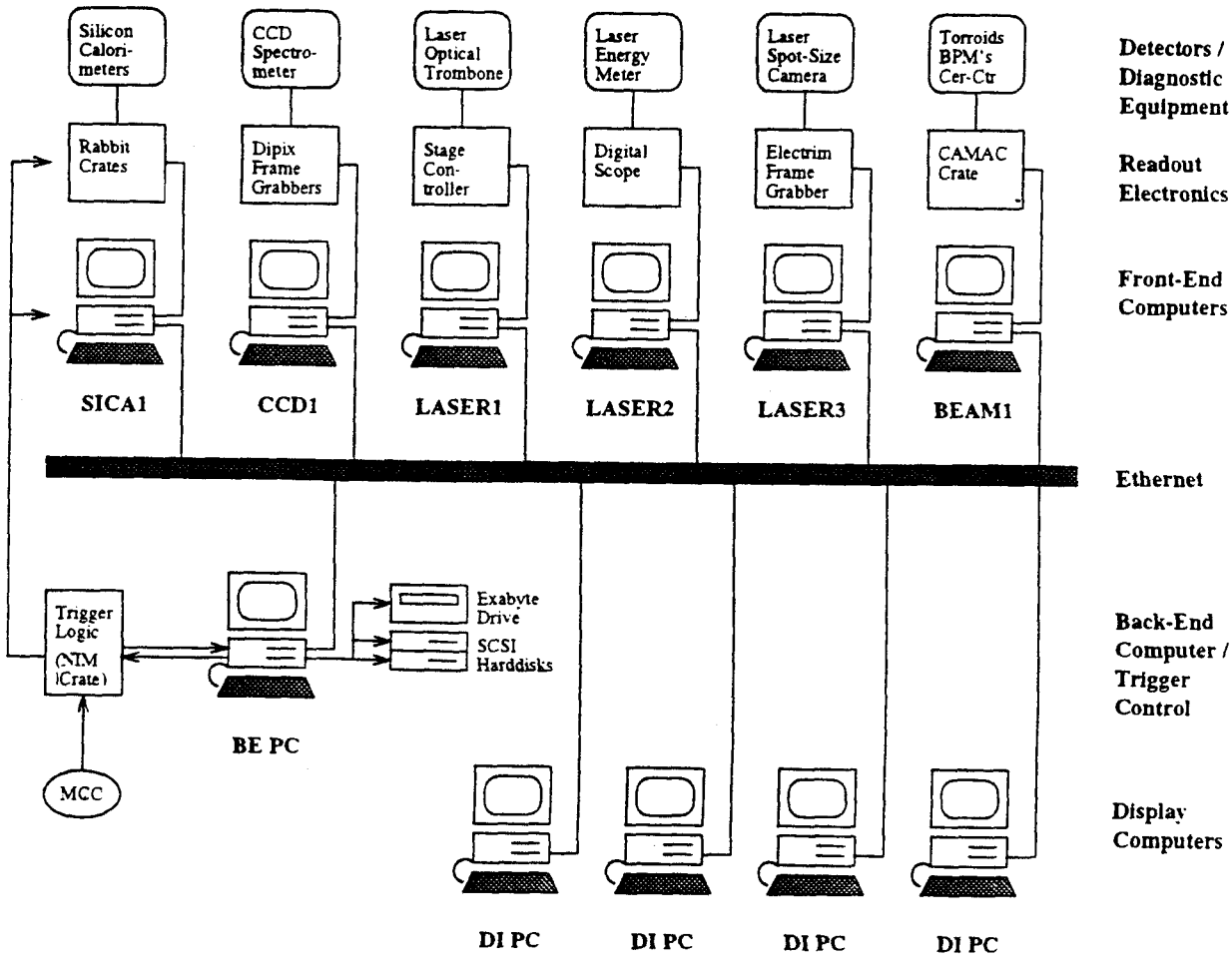

Figure 2.60: The Data Acquisition System

The data acquisition system [87] was capable of recording all the relevant laser and electron parameters and the signal from the detectors, moving the IP box both in the vertical and horizontal plane, scanning the optical delay, and stepping the electron calorimeter in the vertical direction. Due to the relatively low data rate it was possible to base the DAQ system on PC's interconnected via a local Ethernet network as shown in Figure 2.60. The 'Front-End' PC's are interfaced to detector electronics and the diagnostic equipment of the laser and electron beam parameters. The 'Back-End' PC collects the data from the FE's and creates the event block. The event blocks are stored on disk and broadcasted over the Ethernet to SLAC mainframes, at the end of a shift, every 8 hours. A number of 'Display' PC's were used to monitor the data online. This system is modular and can easily adapted to new detector configurations, while at the same time it is built with off-the-shelf components and thus is inexpensive.

The event size is approximately 1 kByte for the calorimeter data, 200 Bytes for the laser parameters and a similar number for the electron beam parameters. For this reason the total storage area in the Main PC was two 2 GByte hard disks allowing for approximately 10 days of non-stop running at a 3Hz readout rate.

The data structure is the following: One data file is recorded for each run that lasts from some minutes to one hour depending of its kind (see data analysis section). Each file consists first of the Run Header which contains a summary of the run parameters and averages of some measured data. Then the data file records the Start-Of-Run Data which gives the structure of each event. And after that each event buffer follows. The structure of the event buffer is similar to that of the run file, i.e. has first the Event Header and then the equipment buffers follow. Finally each equipment buffer contains the header and the equipment data.

A PC based program is used for the off-line analysis that utilizes the PAW graphics and analysis package [88]. It generates large two dimensional arrays (n-tuples) which columns contain the parameters of each event. The analysis was done by applying cuts or selection criteria on the n-tuples and utilizing PAW's arithmetic and boolean operators and mathematical functions. This analysis of the data is described in the following chapter.

Chapter 3

Data analysis

3.1 Introduction

3.1.1 Data collection strategy

Experiment E144 collected data in three periods: March '94, September 94 and May 95 with the data taking periods lasting 1 to 2 weeks. In addition, the calorimeters were calibrated in 2 separate runs, using the FFTB test beam. Also a part of the first running period was devoted to a measurement of the polarization of the electron beam with results described in Appendix E. The data analysis presented here regards only the March '95 data when the experimental conditions were optimum and all the relevant parameters were recorded.

In each data taking period the goals of the experiment were multiple and the run strategy was as follows: Most of the time was devoted to measuring the recoil electron spectrum from nonlinear Compton scattering with n=2, 3 and 4 photons absorbed by the incoming electrons. This study was done for linear and circular polarizations of the laser pulse in order to further check the existing theory; only results obtained with circular polarization will be described here. Data were taken using both infrared (1054 nm) and green (527 nm) wavelengths. For each laser wavelength the energy of the laser was varied from 10 mJ up to 800 J in the infrared (IR) and up to 350 mJ in the green, in discrete steps by setting the gain on the laser amplifiers. For each gain

setting the vertical position of ECAL was adjusted in order to study various sections of the recoil electron spectrum. The linear monitor CCM1 recorded the number of scattered gammas in the range of 10^4 to 10^7 gammas per laser shot depending on the laser intensity. The dynamic range of CCM1 was enhanced with the use of filters in front of the PMT or changes in the PMT high voltage setting. The linear rate was used off-line to normalize the number of nonlinear Compton scattered electrons measured by ECAL.

The data collection process was limited for two reasons: First the spectrum to be measured is dropping very fast in higher order scattering processes; secondly, the electromagnetic shower propagation in the calorimeter and the various backgrounds limit the calorimeter's dynamic range.

The drop of the electron rate beyond the linear Compton edge is very fast even in a logarithmic scale as can be seen in Figure 1.6. As explained in the last chapter the gains of the amplifier boards could not cover such a broad dynamic range that could record both the n=1 linear Compton rate and the n=2 multiphoton Compton rate. So the gains were only tuned for the lower rates of the nonlinear part of the spectrum. That is the reason why the gamma monitor is important since it measures the linear rate in every shot. Furthermore, even the n=2 rate is at least an order of magnitude higher than the n=3 rate. This presents the following problem: If ECAL is positioned with its top rows in the n=2 spectrum and its lower rows in the higher order processes spectrum, then electromagnetic shower spreading from the top rows, that collect a large number of recoil electrons, increases the energy detected in the lower rows of ECAL. This makes it difficult to reconstruct the real signal from the observed one in the lower rows. For this reason only the top four rows of ECAL are useful at each ECAL position.

Even with only the top four rows of ECAL well reconstructed we still cannot measure clearly the drop of the spectrum from one order to the the next higher order. This happens because each row of the calorimeter spans a momentum range ('bite') of about 2.5 GeV for electrons with energy of approximately 20 GeV down to 1.5 GeV for 10 GeV electrons. Since the kinematic edges of the higher order processes are separated by approximately 2 GeV also, a measurement of the steep falling edges

of the recoiled electron spectrum is smeared due to the ECAL row width.

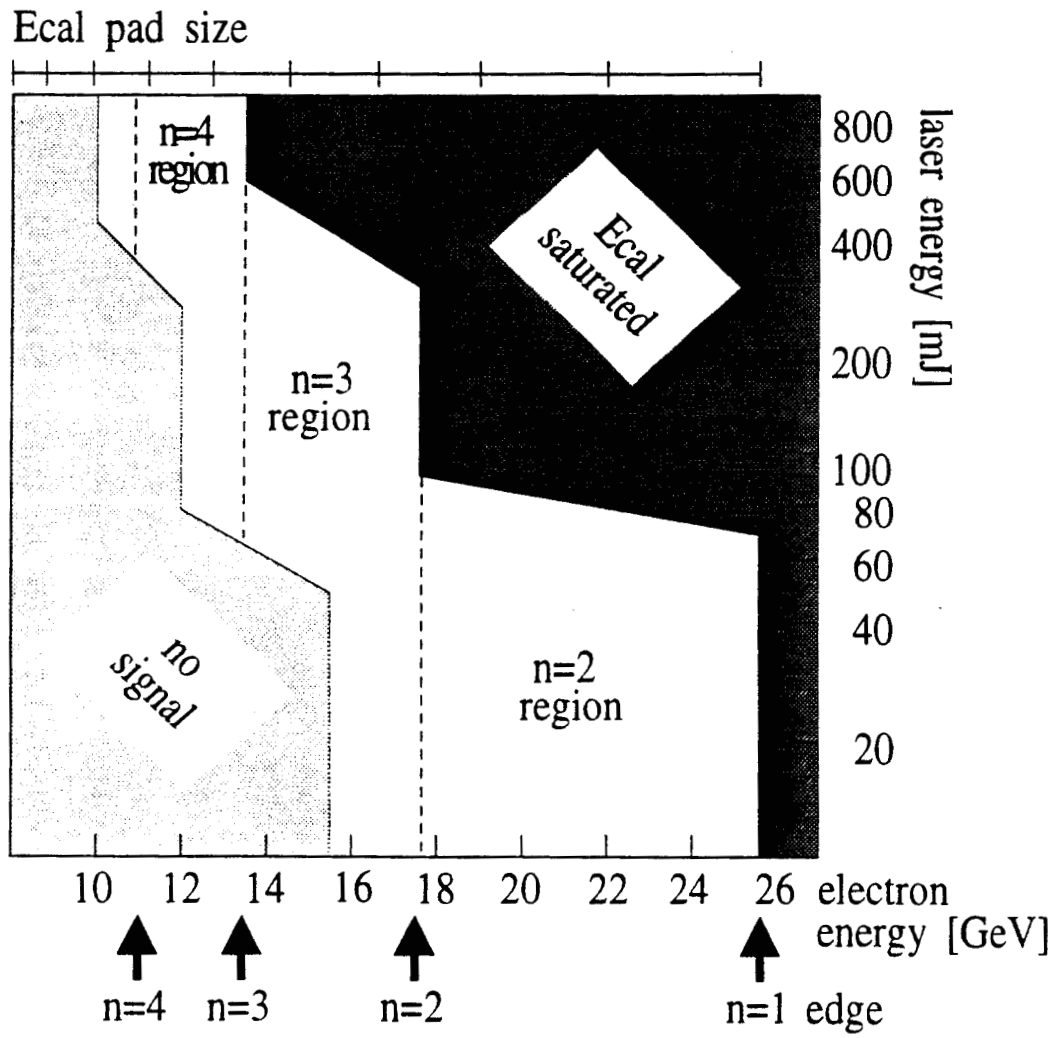

Figure 3.1: Overview of the laser intensity and scattered electron momentum map studied in IR nonlinear Compton scattering

For high laser energies up to 10^7 linear scatters are produced per collision and these can create an immense background, when hitting the electron beam pipe or other obstructions even behind the ECAL position. At even higher laser energies, the nonlinear rate of some order is high enough to produce a large background that inhibits the measurement of the part of the spectrum corresponding to the next scattering order. So one needs to lower the position of ECAL as increasing the laser

energy in order to map the higher order nonlinear Compton processes.

For all the above reasons the dynamic range of ECAL is approximately two orders of magnitude and the limitations in the range of field intensity and electron momentum stemming from this fact are best shown in Figure 3.1.

3.1.2 Description of run types

To overcome the dynamic range problems of the calorimeter and to achieve the maximum recoil electron yield by tuning the spatial and timing overlap of the two beams various running modes were employed. The modes depend on whether the timing stage, the x and y positions of the IP box, the position of ECAL, or a combination of the above, were varied during the data taking period. These modes will be referred to as run types and can be summarized as follows:

(a) The 'X position scans' (XS), where the x position (horizontal) of the IP1 box is varied, in order to scan the focus of the laser over the electron beam and measure the horizontal size of the electron beam.

(b) The 'Y position scans' (YS), similar as the XS's but on the vertical axis.

(c) The 'Timing scans' (TS), where the position of the optical stage was varied. This allowed us to set the synchronization of the laser pulse with the electron beam. Due to a long term drift observed in the timing of the two beams, a TS was repeated between runs collecting nonlinear data, i.e. about every hour. Although the main monitor in TS is the gamma rate, ECAL is much more sensitive to the timing of the pulses, since the nonlinearly recoiled electron yield is highly dependent on the focus characteristics. Figure 3.2 shows the rate of gammas during a TS.

(d) The 'Data Runs' (DR), where the data are collected with the ECAL position, timing setting and IP box position fixed. In a DR we collected up to 2000 events and the statistics are very high. The drawback of this kind of running is the drift of the timing during the run that lessens the quality of the data, and needs to be corrected off-line by the overlap factor (defined in Appendix D).

(e) The 'ECAL scans' (ES), where the position of ECAL is scanned in mm steps collecting 10 events in each step. Although these scans have low statistics, are extremely

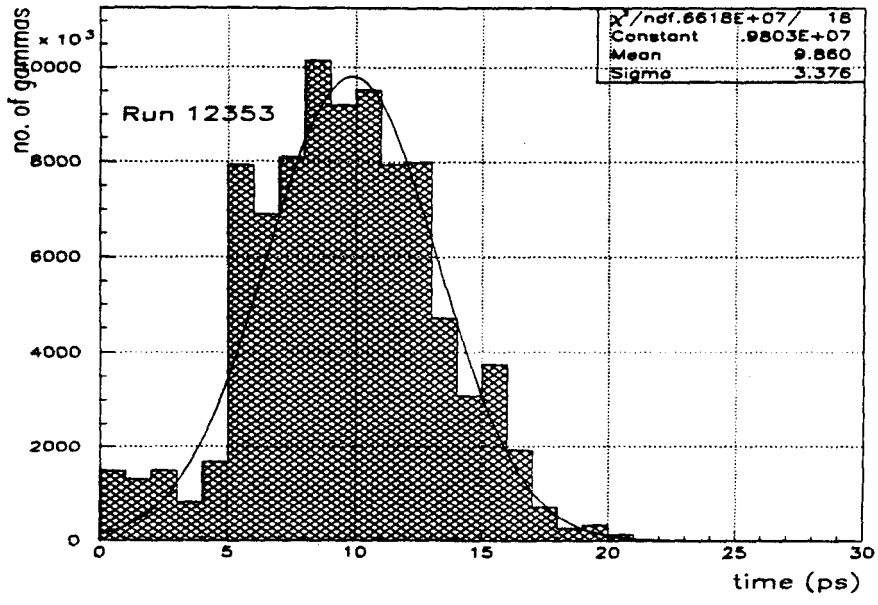

Figure 3.2: Time scan

useful when scanning a kinematic edge, since they enhance the calorimeter's dynamic range.

(f) The raster scans of both the IP x position and the relative timing of the two beams, 'XT scans' (XT), as shown in Figure 3.3. In this mode we measure the energy deposited in ECAL (positioned below the linear Compton edge) and in the gamma monitor for a 2-dimensional grid in x-t space of the interaction, where dx is the spatial offset in x-direction of the laser focus with respect to the center line of the e^- bunch and dt is the temporal offset of the laser pulse center with respect to the e^- bunch center. This way we not only get the rates at $dx = dt = 0$ as in a DR, but we also measure the $n = 1$ related background in ECAL. Due to the timing jitter between the laser pulse and the electron beam we used an 11×11 space-time grid and 10 laser pulses at each point. The drawbacks of this run type are the low statistics and the long time needed to complete a run, especially during the setting of a new box position.

3.2 Nonlinear Compton scattering with circularly polarized infrared laser.

Most of the data was collected at a laser wavelength of 1.053 μm , and circular polarization as can be seen in Appendix C. Combining data runs and ECAL scans we collected 18000 laser ON events at various laser energies and ECAL positions. After the appropriate cuts we are left with 7000 Laser ON events. The distribution of

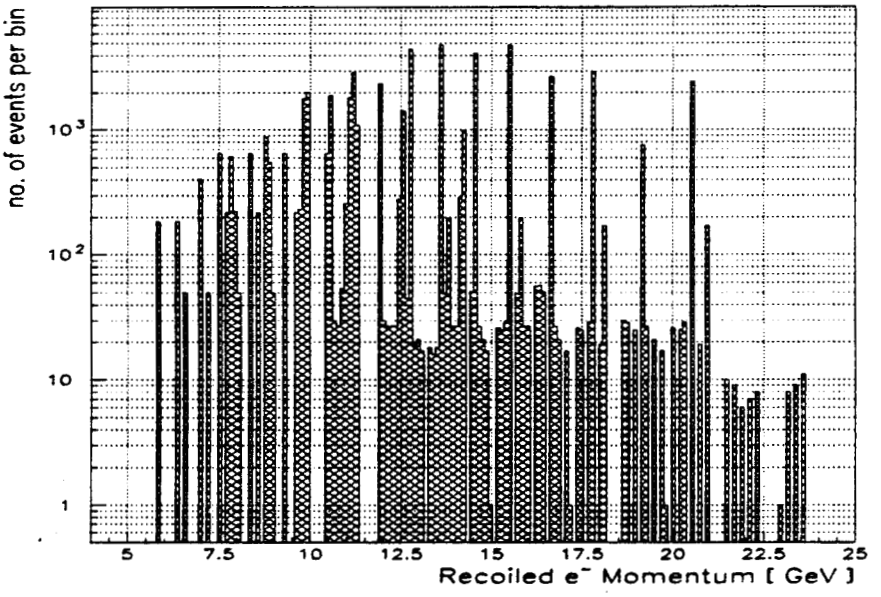

Figure 3.4: The event distribution over the scattered electron momentum range for data taken with IR, circularly polarized laser

the events over the momentum bins is shown in Figure 3.4. Figure 3.5 is a plot of the range of the electron momentum and laser energy covered by the experiment and reflects the overview map of Figure 3.1 on the data.

In this chapter the distributions for the parameters recorded at each event, their analysis and correlations amongst them and the cuts emerging from this analysis will be described. The energy of the events that survive the cuts is studied for each row

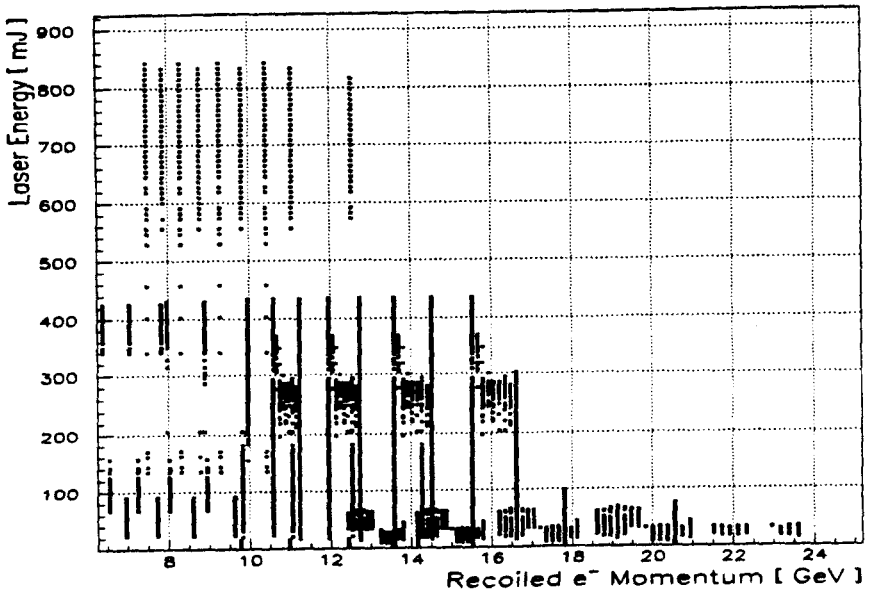

Figure 3.5: The laser energy - electron momentum map for data taken with IR, circularly polarized laser

and segment of ECAL as well as the number of gammas from CCM1. This motivates the creation of a useful quantity to compare with the theoretical results that will be introduced and studied in the next chapter.

3.2.1 Measurement of electron beam parameters

The electron beam was discussed in the experimental setup and some of its parameters were measured. The distribution of the beam charge during the runs with IR, circularly polarized laser is shown in Figure 3.6. The few very low beam charge events possibly occured when the electron beam was not delivered at the interaction point. These are excluded by admitting only events that have less than 3σ deviation from the mean charge of the run from which they belong. The same cut can be applied to beam position and angles, shown in Figure 3.7, as measured by the BPMs upstream

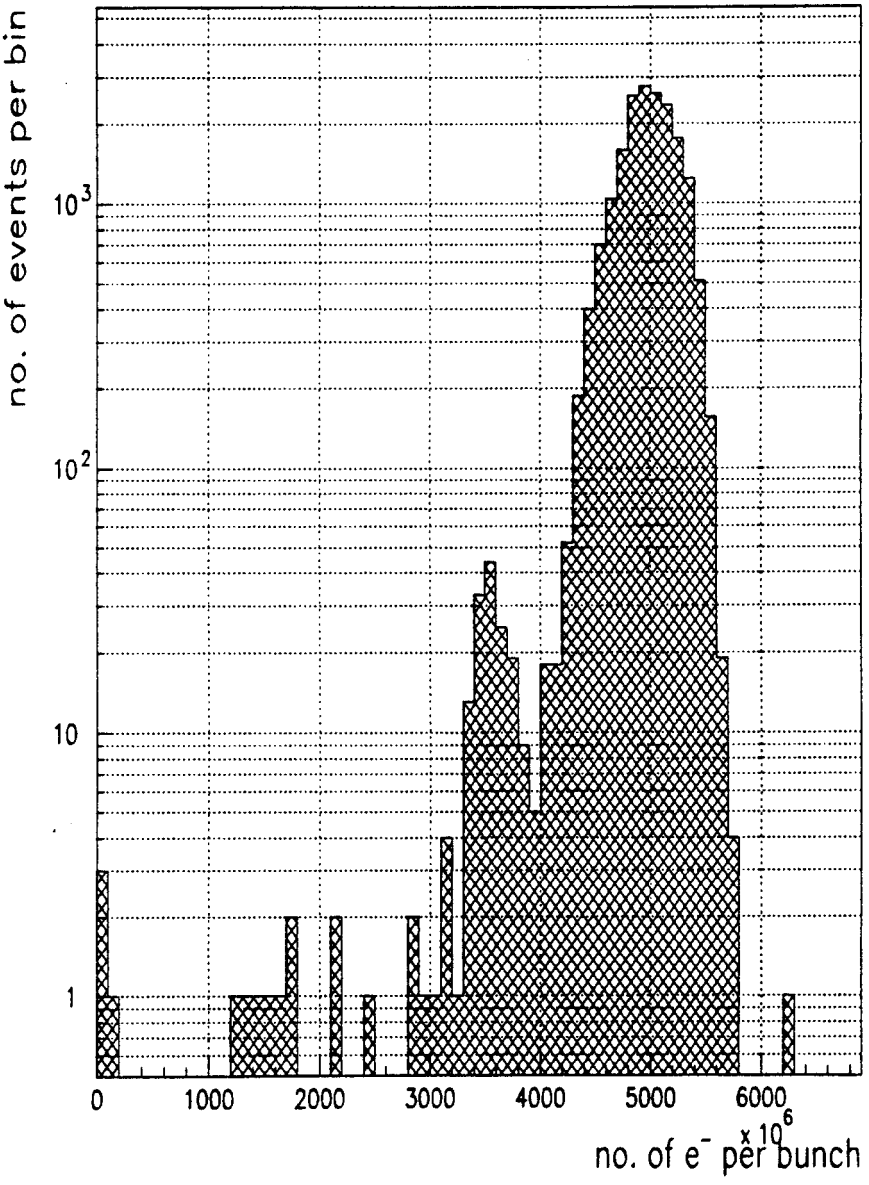

Figure 3.6: The electron beam charge before any cuts for the data taken with IR laser light

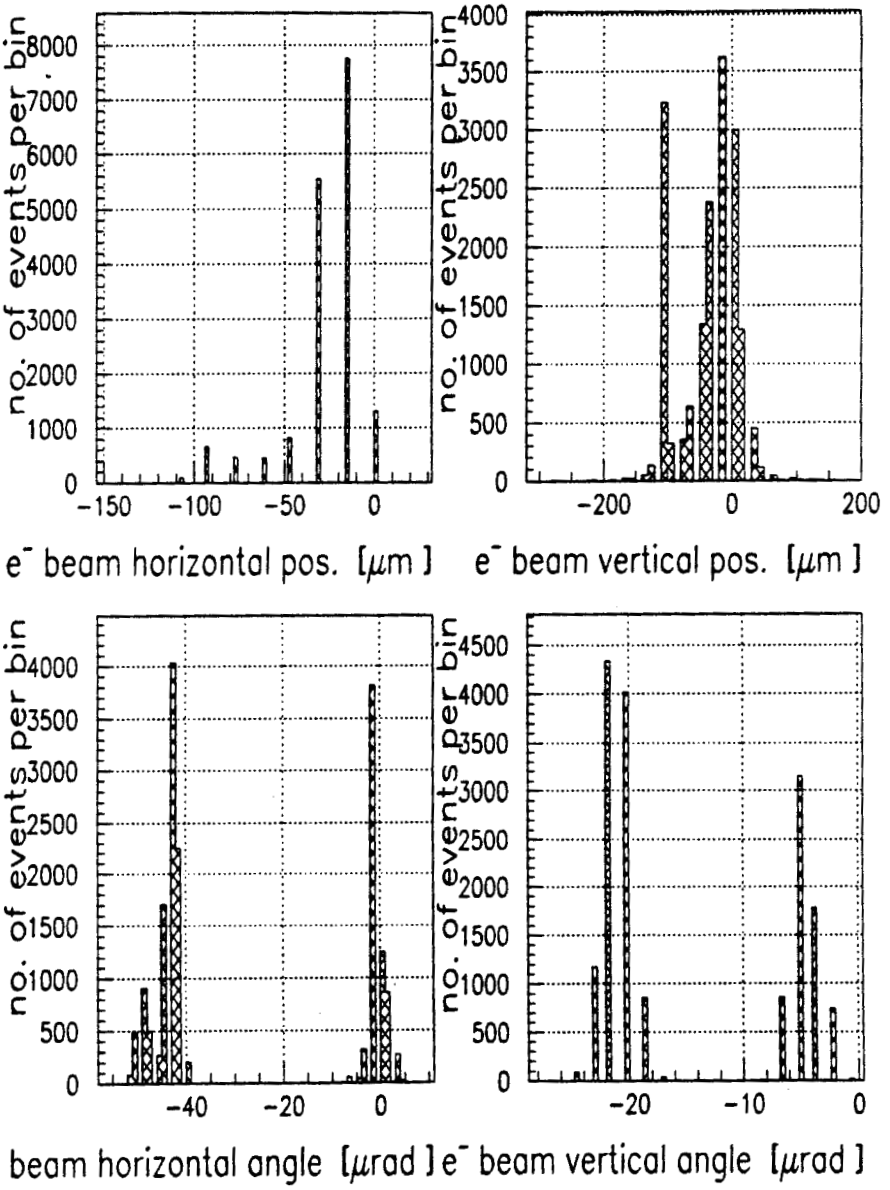

Figure 3.7: The electron beam angle and position at the interaction point for the IR circular runs

and downstream of the interaction point. The energy distribution of the electron beam after a 3 rms cut was shown in Figure 2.6.

The size of the electron beam was also measured directly by wire scanning as described in the apparatus section and also by performing x and y scans of the IP box. The complete measurement of the beam sizes over the course of IR running is given in Table 2.2.

3.2.2 Measurement of laser parameters, η and Υ

The laser energy during the infrared running was recorded in almost every shot and its distribution over the total IR, circular running period is shown in Figure 3.8. The laser amplifier settings were changed so that the laser energy varies in discrete steps from run to run. Nonetheless, for each energy setting there is a spread in the energy distribution, that in most of the runs is of the order of 10%; some events that 'drift ' in laser energy are also observed within each run. Figure 3.8 shows the laser energy distribution over all runs and this distribution for only one low energy run (12192). Although this drift is undesirable from the laser stability point of view, it produced events that uniformly spread the range of 1mJ to 800 mJ. The quality of the events that drift far from the mean laser energy of their run is questionable. For that purpose a loose cut on the ratio of the event's laser energy over the mean energy (RLENE) of the run is employed. The range admitted after cuts is given by: 0.5< RLENE <1.5

The trace of the single shot laser autocorrelator was also recorded in every shot, together with an estimate of its FWHM mostly for online information. A more accurate fit of the autocorrelator pulse-width was performed off-line and Figure 3.8 shows the distribution of the pulse-widths with a valid fit, over the total infrared, circular polarization running period. An equivalent to a χ^2 distribution for this fit is shown in Figure 3.9. The smaller this parameter the better the fit, so we defined an absolute cut for the data so that the reduced pulse-width $\chi^2 < 1.5$. A correlation of laser pulse-width with laser energy is shown in Figure 3.10.

The laser area was recorded as well. The image of the CCD camera that performed the measurement of the focal area in the IP using the Equivalent Target Plane (ETP)

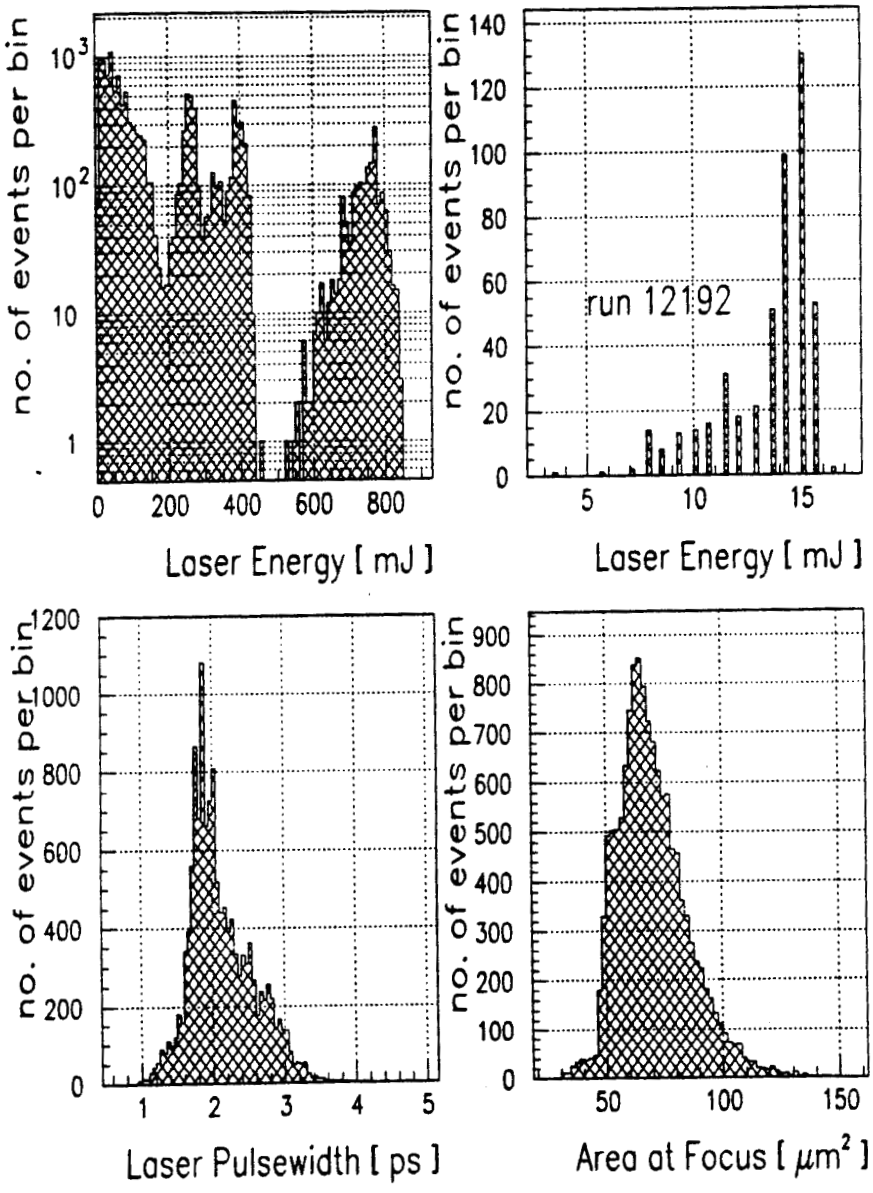

Figure 3.8: Laser parameters for the IR circular runs:(a) the overall energy distribution, (b) energy for run 12192 only, (c) the overall laser pulse-width and (d) the overall laser focal area distribution at the interaction point

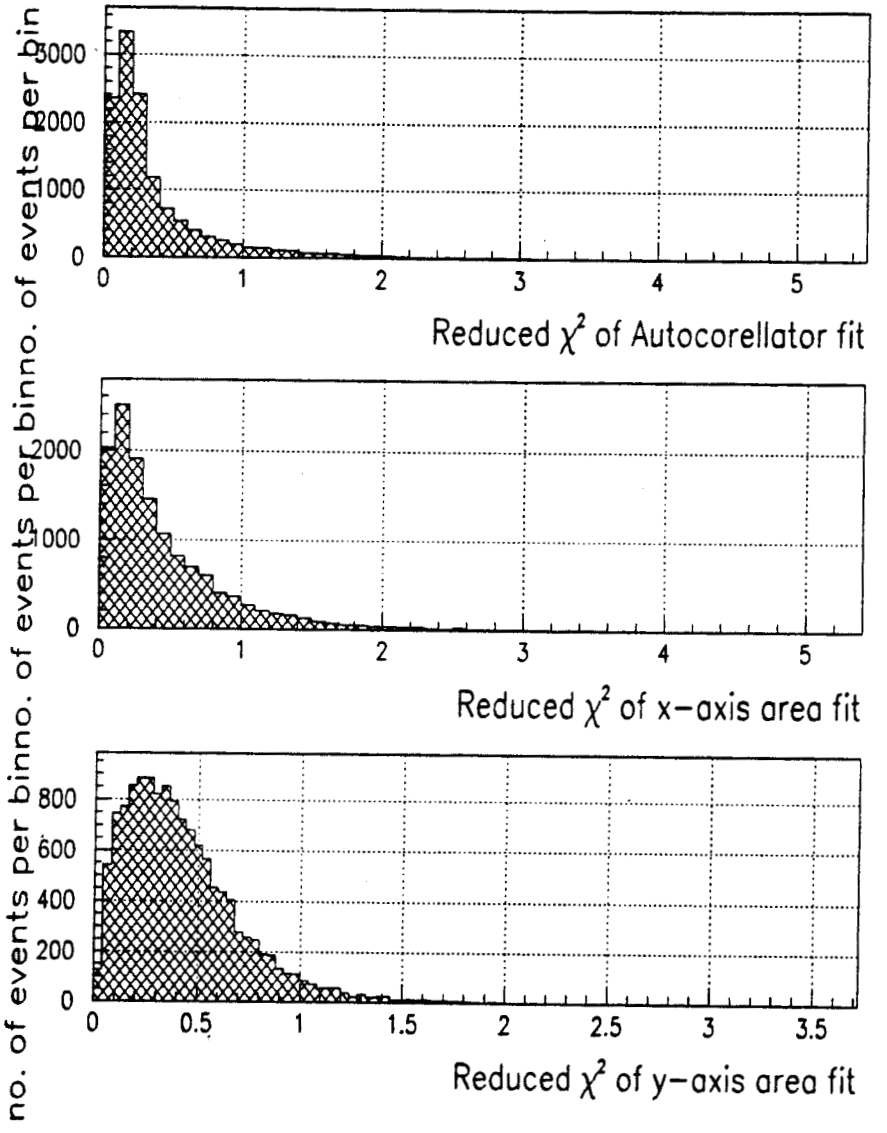

Figure 3.9: Reduced χ^2 of the fit to the laser pulse-width measured pulse by pulse by the IR autocorrelator and of the fit along the x and y axis of the laser area measured by the CCD, for circularly polarized IR runs

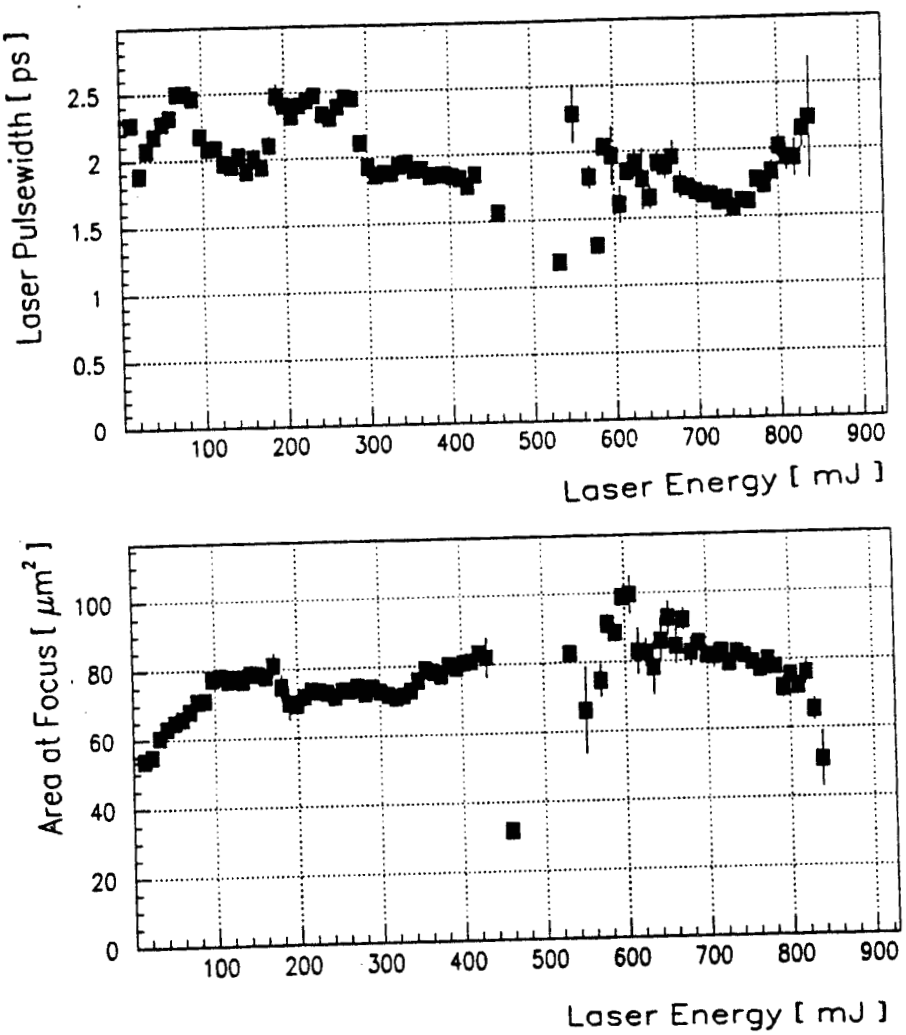

Figure 3.10: The Correlation of Laser Pulse-width and Focal Area with Laser Energy for IR runs

technique was recorded in every shot and fit off-line. The algorithm used locates the peak intensity area of the CCD, then sums two rows in the vertical and two in the horizontal diameter of the CCD, fits the sums with Gaussians plus a background and finally estimates the area of the focus from the standard deviation of the Gaussian. The χ^2 of the area fit and of the individual axis are shown in Figure 3.9. An absolute cut of the reduced focal area $\chi^2 < 1.5$ was used in the construction of the Data Summary N-tuple (DSN). The distribution of the laser area over the course of the infrared laser running is shown in Figure 3.8. The diffraction limit in area for 1.054 μm wavelength and effective f-number 6 is 26 μm^2, so the data show a variation of 2 - 5 times diffraction limited area over all events, which is expected for a T^3 laser. No clear dependence of the area on the laser energy as shown in Figure 3.10, although one could expect a deterioration of the focal spot at high laser energies (due to thermal effects in the last two laser amplifiers, that could affect the quality of the laser pulse wavefront).

From the knowledge of the laser parameters in every shot, we can calculate the parameter η of the strong field produced by the laser on the electrons. The distribution of η over the total IR, circular running is shown in Figure 3.11. The maximum η achieved was approximately 0.6. By definition η^2 is proportional to the laser intensity, and its correlation with the laser parameters is shown in Figure 3.11. Also the critical field parameter Υ was measured to be $\Upsilon = 0.4$. From the range of the values of the two parameters we can conclude that this experiment operates in the regime of QED were $\eta \simeq \Upsilon \simeq 0.5$ and therefore the study of both nonlinear Compton scattering and pair production effects is possible.

3.2.3 Cuts on laser and beam parameters and data binning

The cuts applied on the data are consistent with the above discussion of the laser and electron beam parameters measured in this experiment. These cuts are stated in Table 3.1. The saturated ECAL channels excluded from the cuts are recorded during ECAL scans where the detector approached the linear Compton edge. The cut on the overlap factor is empirically deduced from Figure D.3, but necessary to ensure a valid

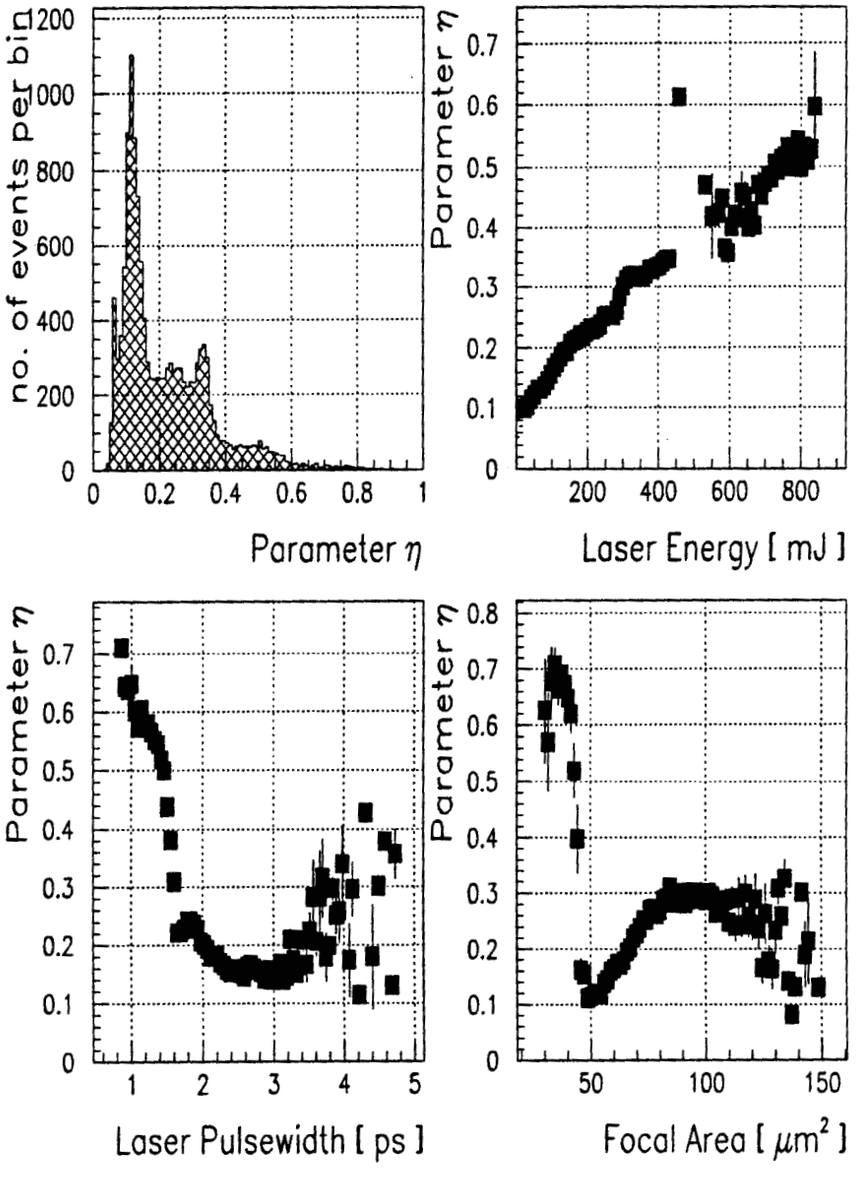

Figure 3.11: The η achieved at the Interaction Point for IR runs and its Correlation with Laser Parameters

energy (mJ)	pulse-width (ps)	area (μm^2)	e^- beam config.	overlap	η	events left
15	2.2 - 2.7	48 - 56	1	0.6	0.07	128
27	1.6 - 1.9	45 - 60	1	0.6	0.11	215
35	1.7 - 2.3	50 - 70	1+2	0.6	0.11	155
43	1.8 - 2.3	50 - 70	1+2	0.6	0.12	487
51	1.7 - 2.2	50 - 70	1	0.6	0.13	141
65	1.7 - 2.3	55 - 75	1	0.6	0.15	73
85	1.7 - 2.3	55 - 75	1	0.6	0.16	51
105	1.6 - 2.0	60 - 90	1+2	0.6	0.18	121
130	1.6 - 2.0	60 - 90	2	0.6	0.20	184
260	1.8 - 2.2	50 - 90	2	0.6	0.27	463
400	1.6 - 2.1	60 - 100	2	0.6	0.34	862
750	1.2 - 2.0	60 - 100	4	0.6	0.45	149

Table 3.2: The Laser parameter bins chosen for analysis, together with an estimate of η and the respective electron beam configurations for the IR circularly polarized runs

3.2.4 Linear rate monitor

The dependence of the linear rate monitor (CCM1) on laser energy is shown in Figure 2.53 for the total IR, circularly polarized laser data. The correlation, although linear, reveals two distinct slopes which are due to the change of the electron beam parameters during the running period. The number of gammas is especially sensitive to the horizontal spread of the electron beam; for larger σ_x of the electron beam the laser pulse interacts with more electrons. This can be seen by comparison of Figures 3.12 and 3.13 where the change in electron beam angle coincides in run number with the increased gamma flux.

The smaller variations in the number of gammas within each of the two slopes in Figure 2.53 are due to slight changes in the calibration of the gamma counter over the various run settings. This is due to filter insertion and tuning of the high voltage on the PMT of the detector in order to increase its dynamic range.

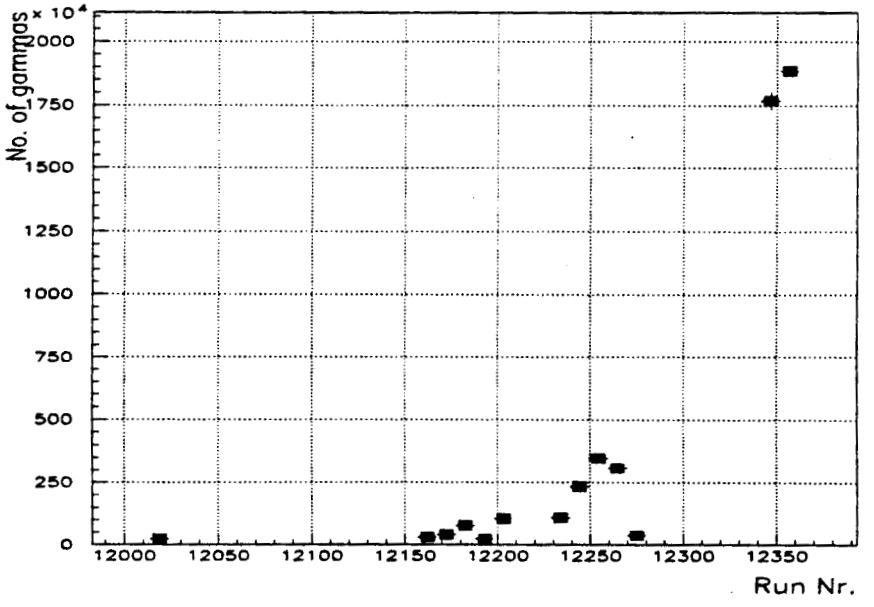

Figure 3.12: Number of gammas plotted for all the IR runs

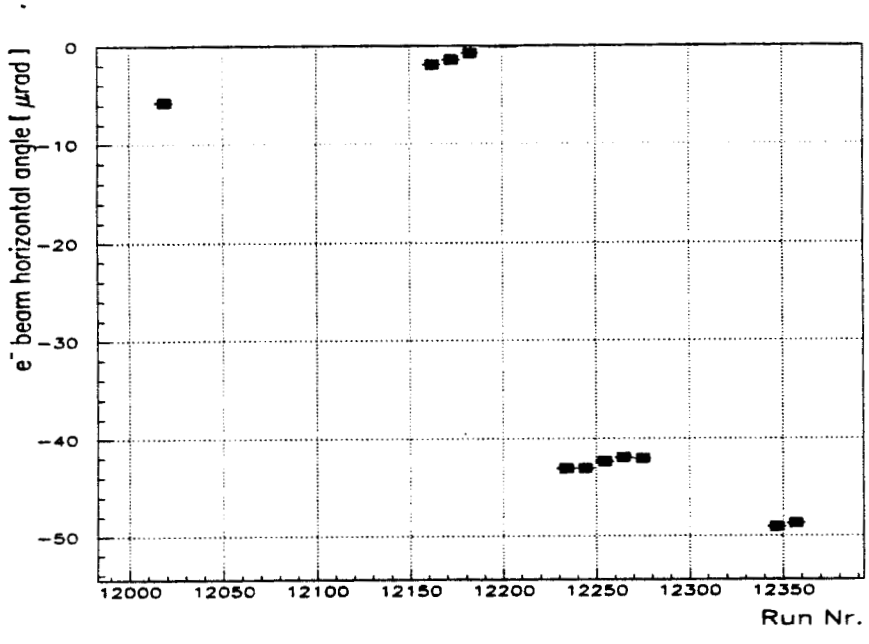

Figure 3.13: Electron beam x angle plotted for all the IR runs

The effect of the timing drift of the laser pulse with the electron beam leads to less gammas than expected. This overlap effect can be best seen in the distribution of the ratio of the linear rate over the laser energy for a given run as in Figure D.2, or in Figure D.3, which shows the ratio of the number of gammas produced over the number of gammas simulated, for each event, over the course of the experiment using IR, circularly polarized laser light. This Overlap Factor (O.F.) as defined in Appendix D, in jitter measurements from the data, peaks at 1 for maximum overlap and has a well determined behavior for the bad overlap events.

3.2.5 Electronic noise and electron beam related backgrounds in ECAL

The noise of the electronic boards was eliminated to the level of 1% and clearly had a smaller effect than the lateral shower, the back-splash or top fore-splash and the

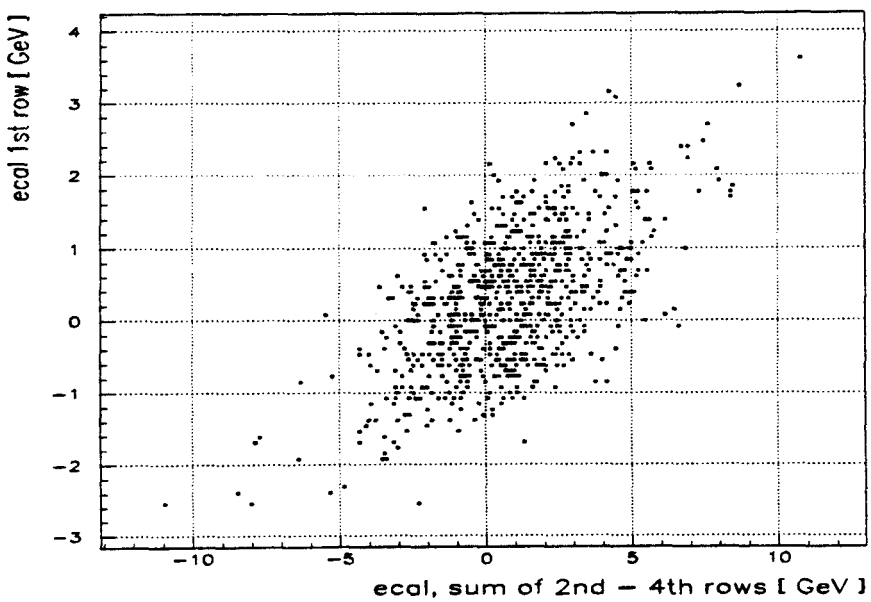

Figure 3.14: Electronic noise in ECAL

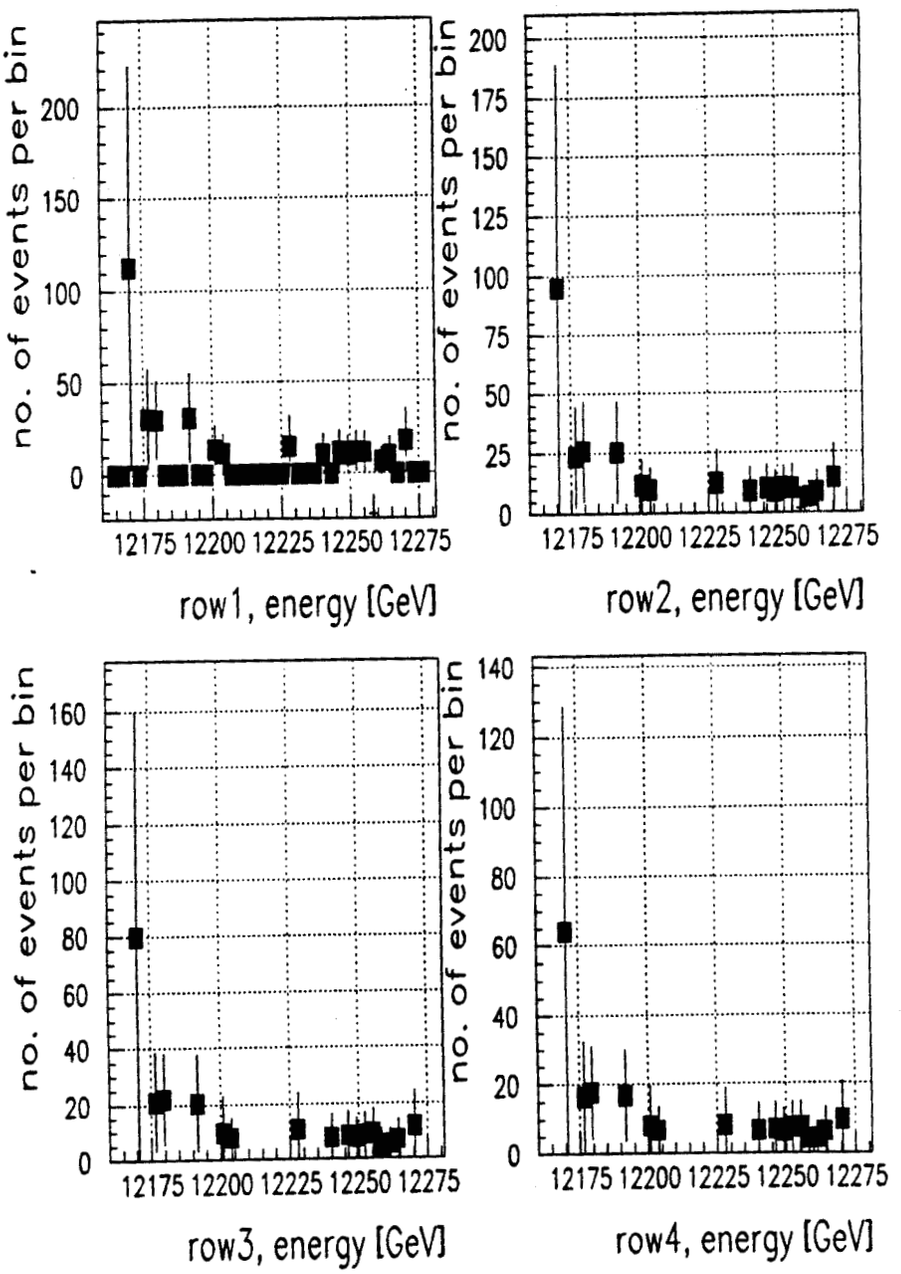

Figure 3.15: Electron beam background for IR runs

electron beam backgrounds. It can be estimated by parameterizing the correlation of the signal in one row with the signal in all other rows. with only pedestal triggers and is shown in Figure 3.14. The round distribution of this data around zero is a good indication of the low electronic noise.

Although the beam is very stable in position and has relatively low backgrounds, this experiment requires a measurement of a few recoil electrons in the steeply falling part of the spectrum of nonlinear Compton scattering. For that reason special care was taken to reduce the electron beam related backgrounds, that mostly originate from collisions of the electron beam or its synchrotron radiation with the beam pipe upstream of the interaction point. The electron beam was tuned occasionally for better backgrounds on the calorimeter. In addition the electron calorimeter's position was lowered in order to avoid saturation from nonlinear Compton recoil electrons at higher laser energies. This had the effect of lowering the electron beam related background in ECAL since it was moved further away from the beam pipe. The combination of these two effects can be seen in Figure 3.15, where the energy in ECAL is plotted for the total IR running period for beam background events, i.e. when the laser was not fired (twice between consecutive laser shots).

The electron beam related background is almost constant within each run and is subtracted on average from the ECAL raw signal.

3.2.6 Laser related backgrounds in ECAL

The most serious background of all is the one associated with the linearly scattered electrons produced by the laser-electron interaction. These interact with the vacuum chamber of the magnetic spectrometer before they reach ECAL, but also propagate behind the detection point were ECAL is located, and mostly interact with the beam pipe walls producing an extensive shower of electrons and gammas and pair produced electrons from these gammas. All these products propagate in every direction, increasing the background signal in the ECAL. Figure 3.16 is a simulation using EGS of the shower from a flange behind the ECAL. Since this background is produced only

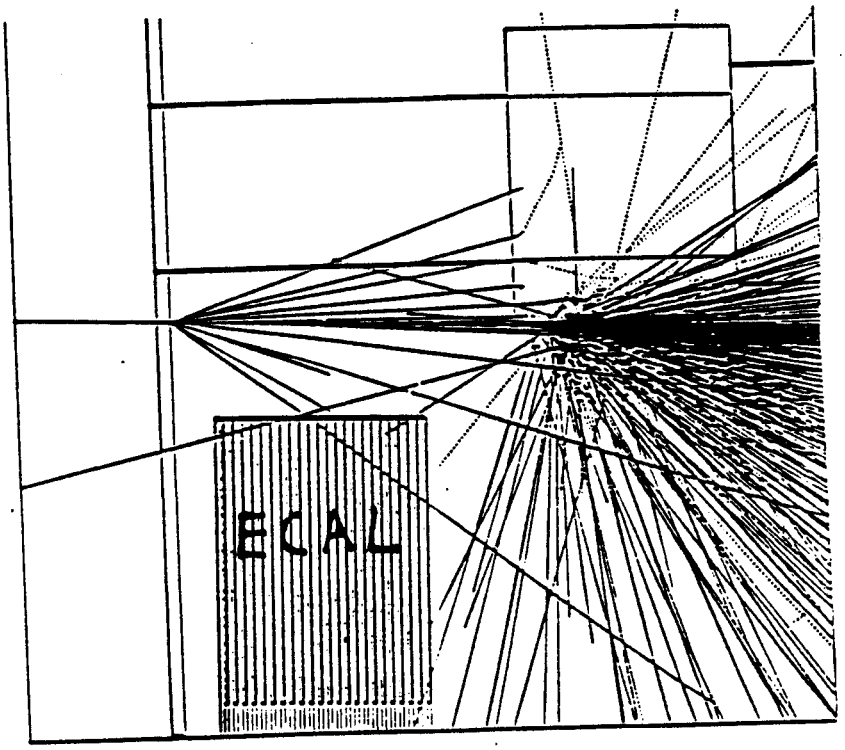

Figure 3.16: EGS simulation of the background due to the flange behind ECAL

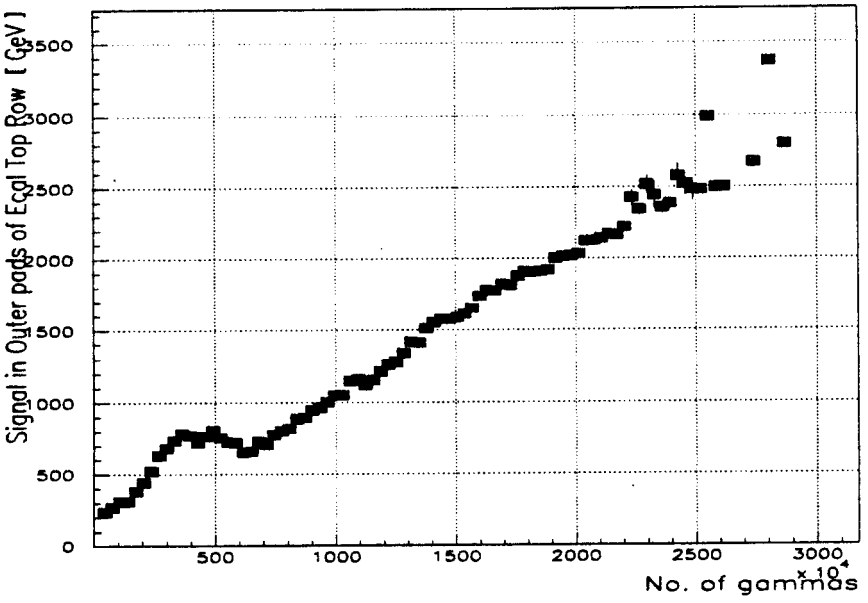

Figure 3.17: The ECAL outer pads as a function of the linear monitor rate

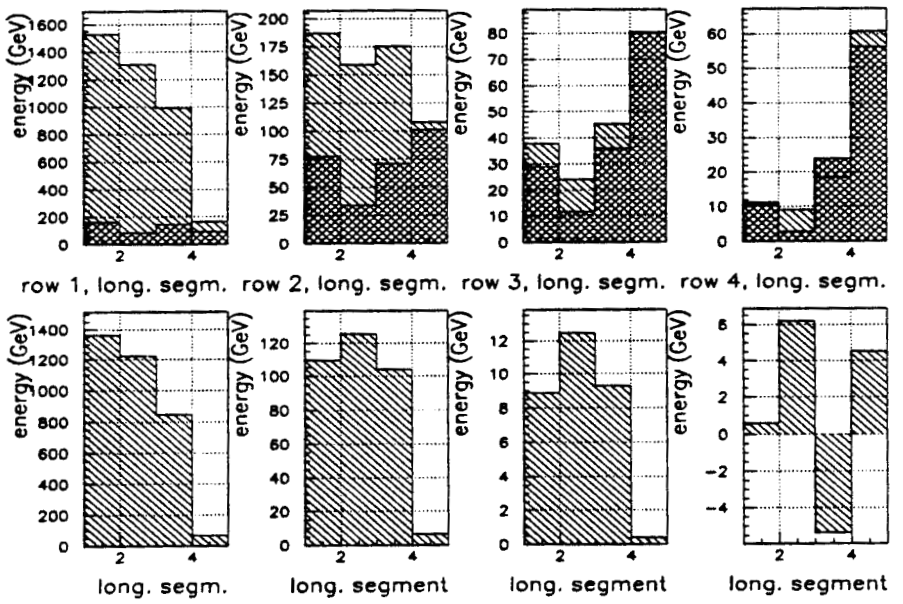

Figure 3.18: The ECAL energy distribution over the four longitudinal segments for run 12180 which is a typical IR laser run. In the top row of the figure, the center pads (single hatch) and the outer pads (double hatch) of ECAL are plotted. The bottom row of the figure shows the energy distribution in ECAL after the subtraction of the outer pads from the inner pads for each row and segment.

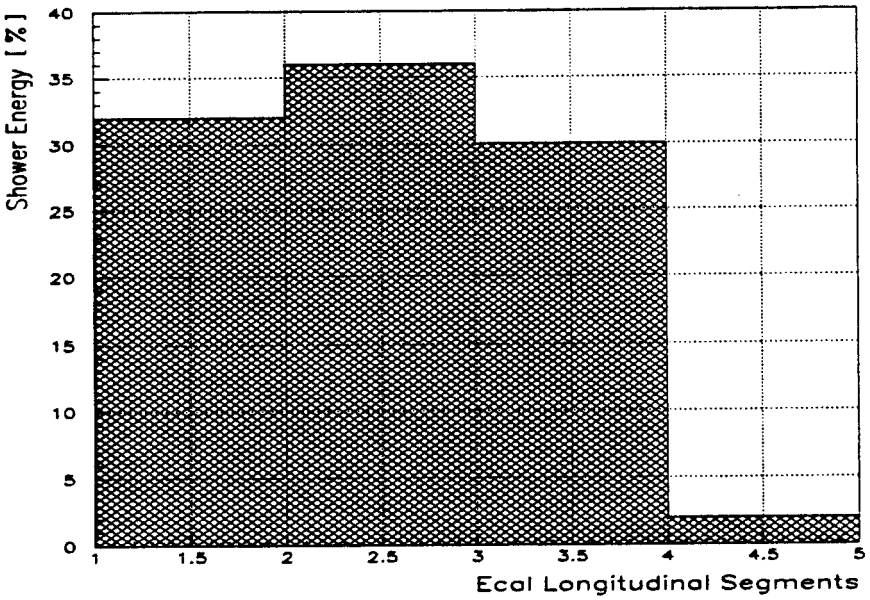

Figure 3.19: The EGS predicted shower distribution over the ECAL longitudinal segments

when the laser fires, it can not be subtracted immediately. Apart from this 'back-splash ', there is also a background that affects the front phase of ECAL (fore-splash) especially when ECAL is on a high vertical position close to the electron beam pipe.

One way to estimate the linear rate background is to correlate the rate from the linear monitors with the outer pads of the ECAL which do not see any real signal due to the forward directionality of the nonlinear scatters. On the contrary, the background events are produced in a larger area and spread over a larger angle easily reaching the outer pads of ECAL. Figure 3.17 is a plot of the signal in the outer pads of the first row of ECAL as a function of the rate in the CCM1 for all the IR runs. The good linear dependence of these two parameters in all runs validates the method used to correct for the linear rate background.

Another handle used to eliminate the back-splash is the signal in the last longitudinal segment of ECAL (back-segment). The energy distribution of the four ECAL

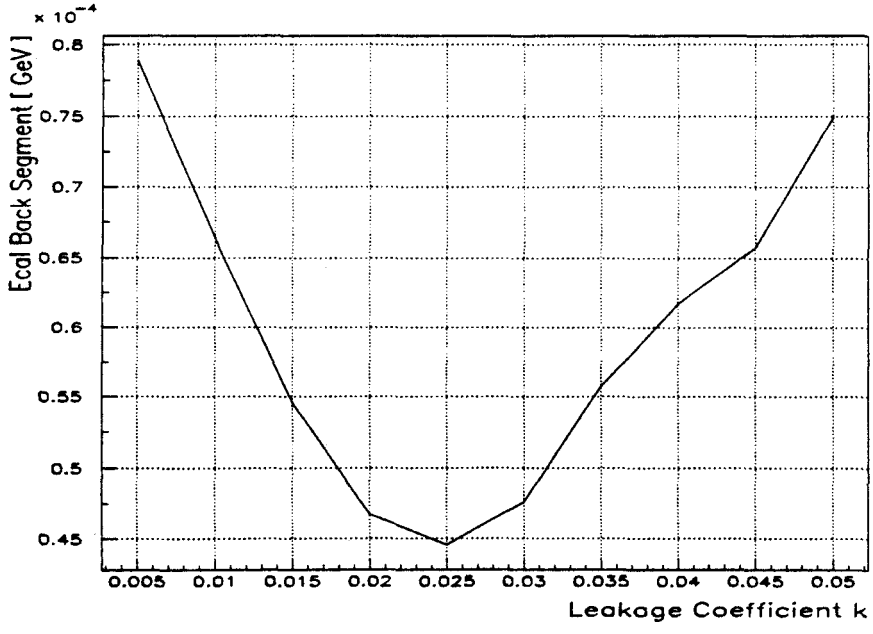

Figure 3.20: Dependence of the rms of the ECAL back-segment energy distribution on the coefficient k that gives the percent shower leakage of the signal into this segment

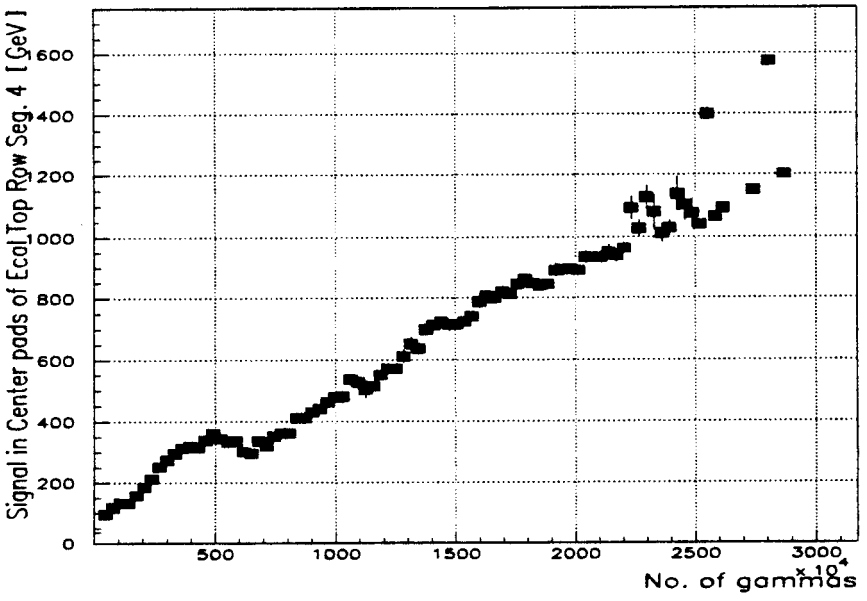

Figure 3.21: Correlation of the back-segment of ECAL with the linear monitor rate

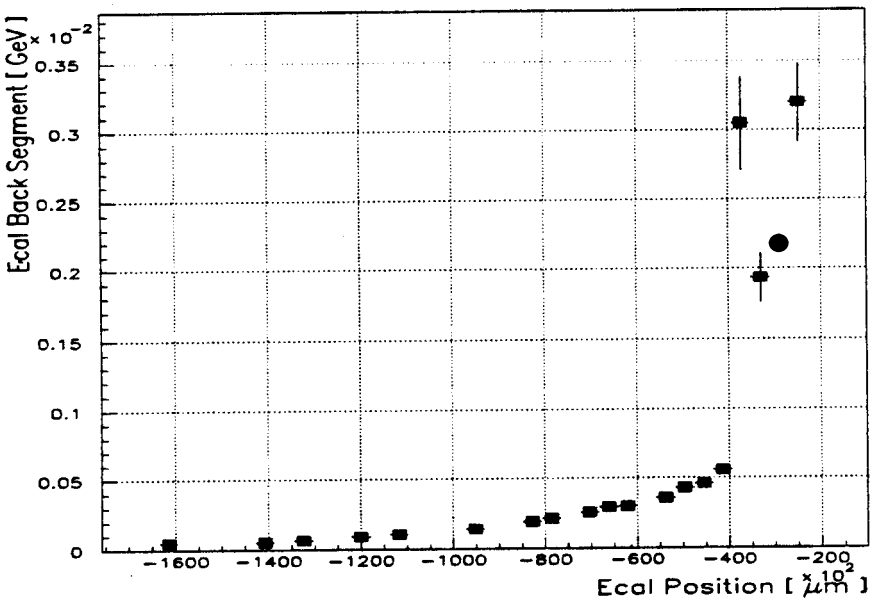

Figure 3.22: Correlation of the energy deposited in the back-segment of ECAL, after leakage correction, with the ECAL position

segments is similar for most of the runs, and can be seen in Figure 3.18 for a particular run. A comparison of the last figure with the predicted by EGS energy distribution over the ECAL four segments, as in Figure 3.19, shows that most of the back-segment signal is indeed background due to the laser firing. Indeed, wiring of the back-segment was chosen to produced an estimate of this background. That the data on the leakage of the true signal from the first 3 segments into the fourth segment agree with the EGS simulation is shown as follows:

The signal leakage into the back-segment can be written as:

$$\Delta E = k * (E_{s1} + E_{s2} + E_{s3}) \tag{3.1}$$

where the coefficient k is simulated by EGS to be 2%, and E_{sj} is the energy of the center pads of the top 4 rows accumulated in the j-th segment of ECAL. The energy distribution of the back-segment can be studied by subtracting from it a variable leakage and then normalize it by the linear rate given by CCM1. Since the leakage contributes also to the spread of this distribution due to the fluctuations in the energy of the shower, we can find the coefficient k that minimizes the rms of this distribution, as in Figure 3.20. The k_{min} is 3.5 % for this specific run and can vary to 1.8% for other runs, which is very close to 2% simulated by EGS. After subtracting the leakage, a correlation of the energy in the back-segment with the linear rate monitors is easily confirmed by Figure 3.21. The correlation of the back-splash with the vertical position of ECAL is crucial for the reconstruction of the signal and can be shown in Figure 3.22.

In this experiment even the nonlinear rates become so high at high laser energies that create a large back-splash in ECAL. When ECAL is moved in a low position that completely avoids the linear rate back-splash we observe a high background in the back-segment at high laser energies. Also, the top row of the third longitudinal segment of ECAL shows an increased energy which originates from nonlinear scatters hitting the top of ECAL. This is due to the angle of the direction of propagation of the nonlinear scatters, since they are bent by the magnets before ECAL. This background is hard to eliminate especially since the signal at these low positions, i.e. low recoil electron momenta, is weak.

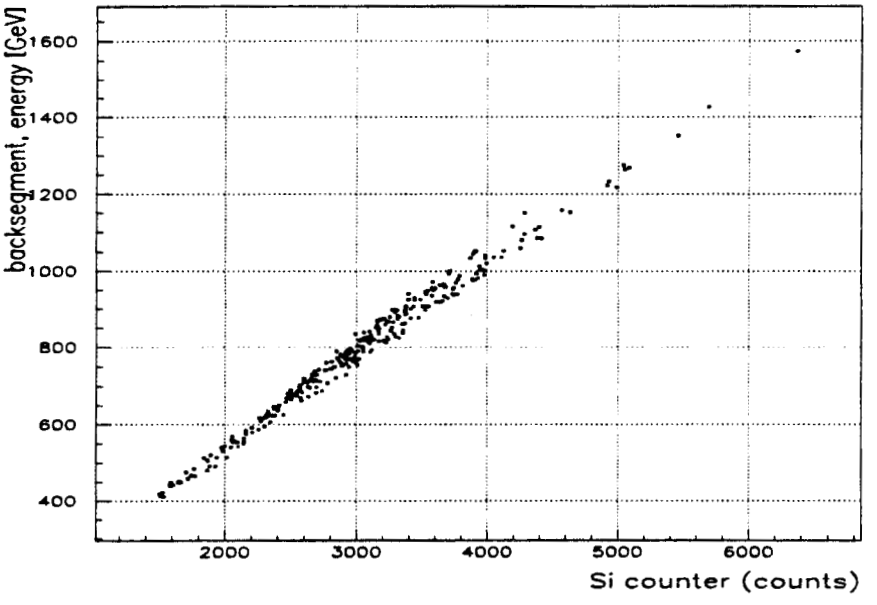

Figure 3.23: Correlation of the silicon counter signal (fore-splash) with the energy deposited in the ECAL back-segment (back-splash)

An estimate of a probable 'fore-splash' in ECAL can be given by the signal of the silicon counters mounted on the front of ECAL. Since their thickness is small they are as sensitive to high energy particles as to low energy particles. A correlation of their signal with the back-splash is shown in Figure 3.23, which confirms that there is a general 'gaseous' behavior of the background, since backgrounds that originate from the front and the back of ECAL are well correlated.

3.2.7 Electromagnetic shower propagation in ECAL

The electron calorimeter as described in the last chapter is a sampling calorimeter, where the absorber is the layers of tungsten and the detector the layers of silicon. When an electron impinges at the face of ECAL, it will interact with an atom in the first absorber layer after one mean free path on average [83]. The reaction products, which are again electrons or an electron and a photon, repeat similar interactions,

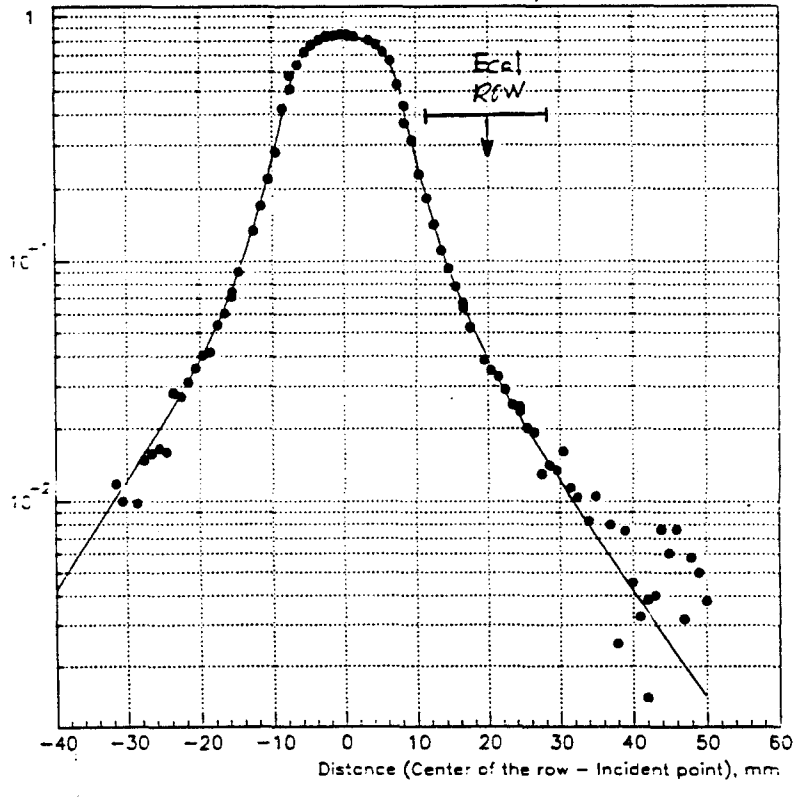

Figure 3.24: Shower transverse profile in ECAL

thus increasing the number of secondary electrons. At a certain depth after many interactions, the average energy of secondary particles becomes low enough to stop further multiplication; at this depth the maxima of the shower are located. At this stage and later the ionization loss and Compton scattering are important for the electrons and photons, respectively. Then the shower decays slowly through these processes. Figure 3.19 showed the longitudinal shower propagation in ECAL with its maximum in the second longitudinal segment. The transverse shower propagation creates a problem for this experiment: The number of electrons that impinge on some ECAL row, create a shower and a small fraction propagates in the lateral direction and enters an adjacent row. Due to the steeply falling rates of the primary electrons with the vertical position on ECAL, this number of electrons is often comparable to the real signal on this row.

For this reason, the shower propagation in the lateral direction was studied both in calibration runs using the test beam of the FFTB and in the nonlinear Compton scattering data. The shower was found to be falling exponentially with the vertical distance from the hit point. The peak and tails of the shower had different falling slopes and were modeled with two different exponentials. Finally, the signal at some distance y, in mm, from the incident point is given by:

$$w = w_1 \frac{1}{2\beta_1} e^{-\frac{|y|}{\beta_1}} + w_2 \frac{1}{2\beta_2} e^{-\frac{|y|}{\beta_2}} \tag{3.2}$$

where $w_1 = 0.7$, $w_2 = 0.3$, $\beta_1 = 2.7$ mm and $\beta_2 = 9.5$ mm, and w_1, w_2 where found empirically, while β_1 and β_2 were found by a GEANT [85] simulation. Figure 3.24 is a fit to calibration data using the above model [86].

3.2.8 ECAL signal reconstruction and energy distribution

The effect of all the backgrounds and showering among the ECAL rows can be modeled empirically and the signals in ECAL can be reconstructed in order to reveal the true signal from the steeply falling spectrum of nonlinear Compton scattered electrons. Two methods were developed for that purpose.

In the first approach [89], the response of the calorimeter to an electron beam incident at a vertical position y (approximated with a delta function) is written as a

vector $X_j(y)$, where j labels the readout channels of ECAL. This is done by taking into account the shower functions $X_j(\delta_y)$, and assuming that the shower response is independent of the ECAL position Y. Then the splash coefficients V_j, where j again denotes the readout channel, were found from fitting the xt-scans away from the nonlinear signal, and correlating them with the Y position of ECAL.

The readout of ECAL under a spectrum $f(y)$ is

$$X_j[f] = \int dy f(y) X_j(y)$$

and the reconstructed signal is

$$R_i[f] = \int dy f(y) R_{ij} X_j(y)$$

where i labels the reconstructed signals. The function $g_i(y) = R_{ij}X_j(y)$ is then the aperture function of the reconstructed signal. We get an estimate of the coefficients R_{ij} by adjusting them, such that $g_i(y)$ is zero for y outside the region of the ECAL pad and is one inside. In that way we do not need to assume any function $f(y)$. The R_{ij} are determined by minimizing χ^2:

$$\chi^2 = \sum_i \sum_k \frac{(R_{ij}X_{jk} - D_{ik})^2}{\sigma_{ik}^2} + \frac{(R_{ij}V_j)^2}{\sigma'^2}$$

where k is the index over the discrete values used for y_k, $X_{ik} = X_i(y_k)$, $D_{ik} = g_i^{desired}(y_k)$ and σ_{ik} and σ' are the tolerances for the deviation of the achieved and desired aperture function.

Minimization of the χ^2 produces the coefficients R_{ij} used to adjust the signal in every ECAL channel. This improved the dynamic range of ECAL and made it possible to observe the kinematic edges of n=2, n=3 and n=4 nonlinear Compton processes.

A second way [90] of reconstructing the ECAL signals is dependent on the shape of the spectrum. An exponential shape $f(y)$ for the distribution of energy within an ECAL row, was assumed. Taking into account the shower spreading among rows, and the parameterization of the back-splash with the vertical position of ECAL, the transformation of the total incident energy to the observed readout was found. This method produced results equivalent to the first one.

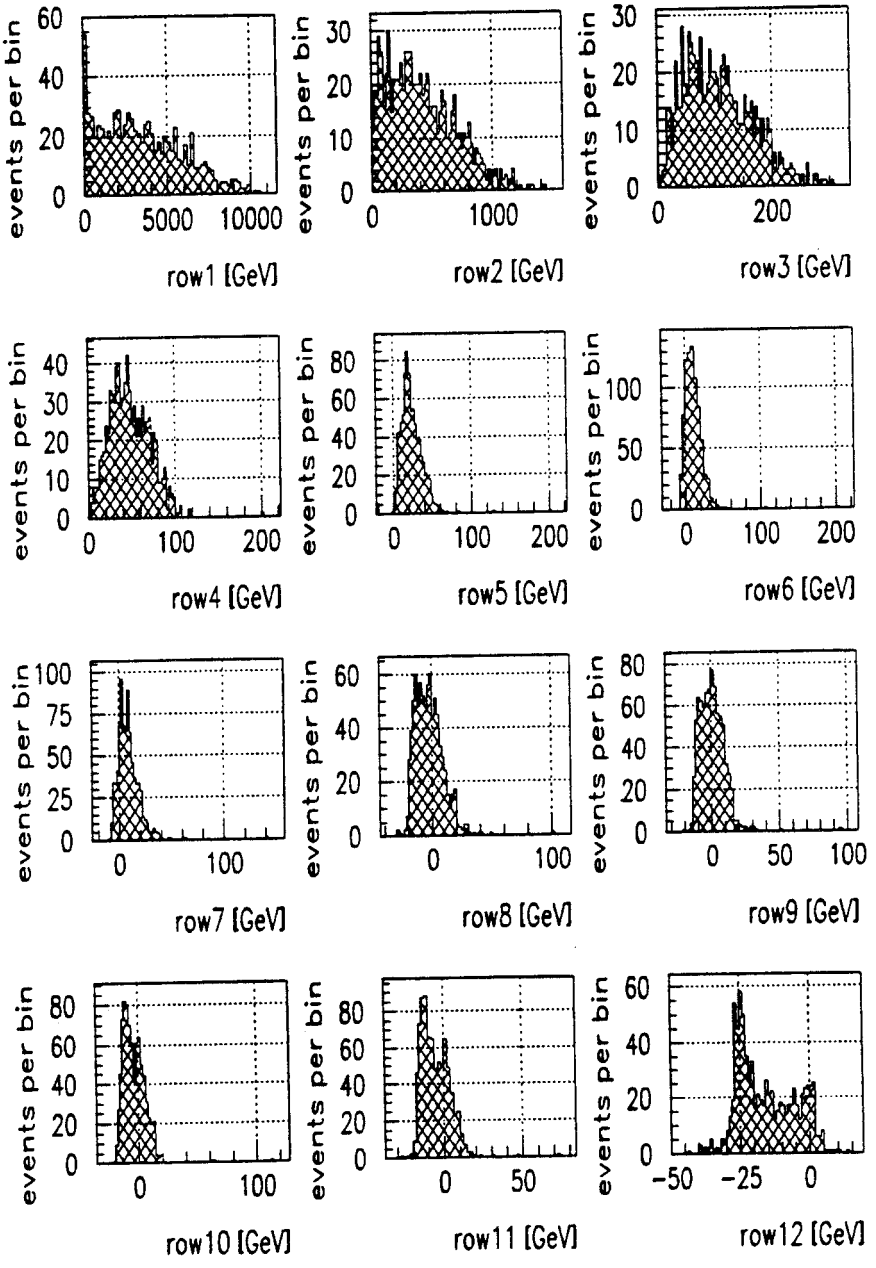

Figure 3.25: Raw data, Center pads ECAL energy distribution run 12180, all rows

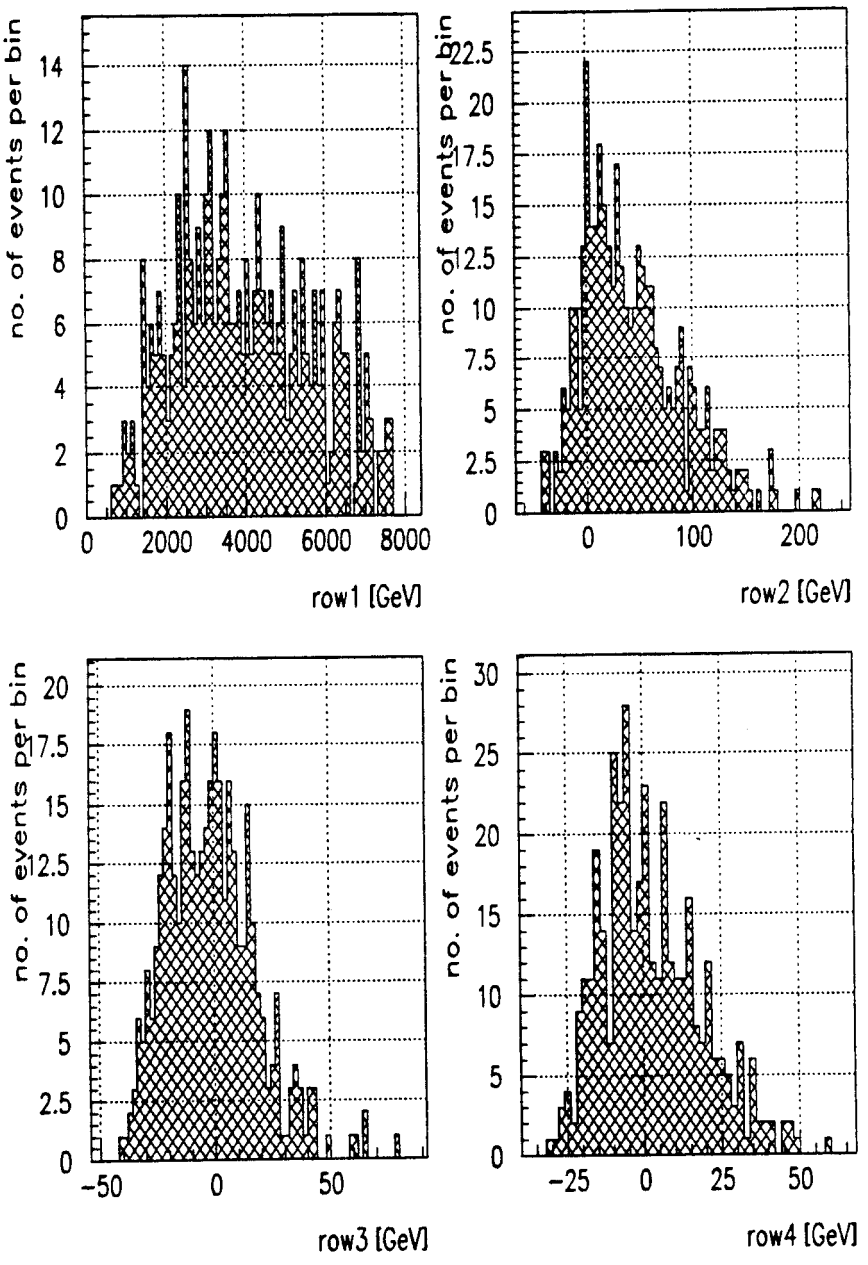

Figure 3.26: Reconstructed data, after cuts, Center pads ECAL energy distribution run 12180, top 4 rows

The raw energy distributions of the ECAL signal as taken from the center columns (center pads, CP) of the electron calorimeter for all 12 rows, for run 12180 is shown in Figure 3.25. After the application of the data reconstruction techniques the top 4 rows of these distributions for events surviving the cuts are plotted again in Figure 3.26. Similar distributions are recorded and reconstructed for all the other runs with the mean energy varying as a function of laser intensity and ECAL position.

Although the scattered electron rate in energies lower than the linear Compton scattering cutoff correlates nonlinearly with both the linear rate and the laser intensity given by the parameter η^2, it is difficult to observe this behavior directly on the energy distribution detected by ECAL. First of all, it is difficult to observe this within a run, since the laser energy varies only over a small range and the jitter in the other laser parameters and timing contributes in large variation in the laser - electron interaction volume. Also, although we combine all runs in the data analysis resulting this way in a larger laser intensity scaling, ECAL at the same time is moved into various ranges of electron energies to avoid saturation and other effects discussed before. So even though such a direct nonlinear correlation of ECAL energy with laser intensity, i.e. quadratic at the n=2, cubic at n=3 etc., would have simplified the data analysis, it is not possible. Another approach leading to a measured quantity that would have such correlations has been followed, resulting in the observations of the next chapter.

3.3 Nonlinear Compton scattering with circularly polarized green laser light.

The data collected for laser wavelength 0.527 μm , and circular polarization can be seen in Appendix C. Combining data runs and ECAL scans we collected 16000 laser ON events with various laser energies and ECAL positions. After the appropriate cuts we are left with 5000 Laser ON events. The range of the ECAL position scanned and its equivalent recoil electron momentum range are given in Figure 3.27. The distribution of the events over the momentum bins is shown in Figure 3.28. Figure 3.29 is a plot of the electron momentum - laser energy phase space covered by this

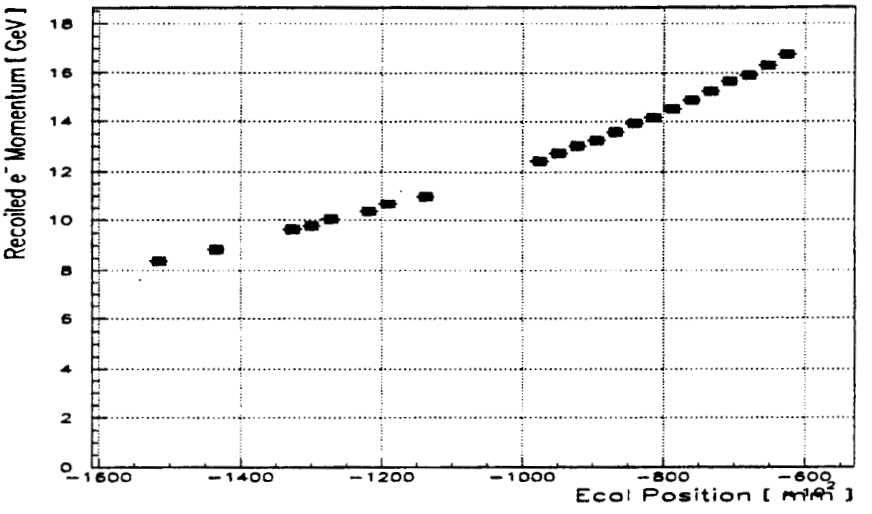

Figure 3.27: The ECAL position, as measured at the top of ECAL, and the equivalent momentum range for all the green circular data runs and ECAL scans

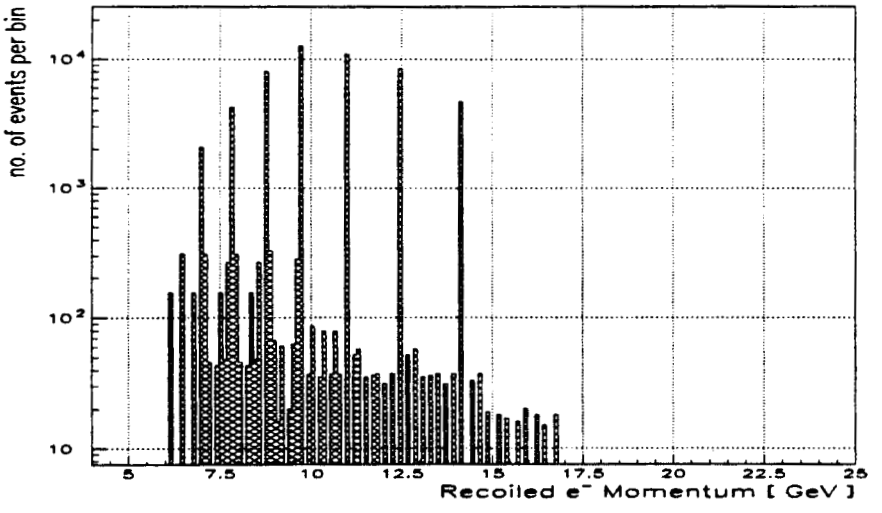

Figure 3.28: The green event distribution over the momentum range

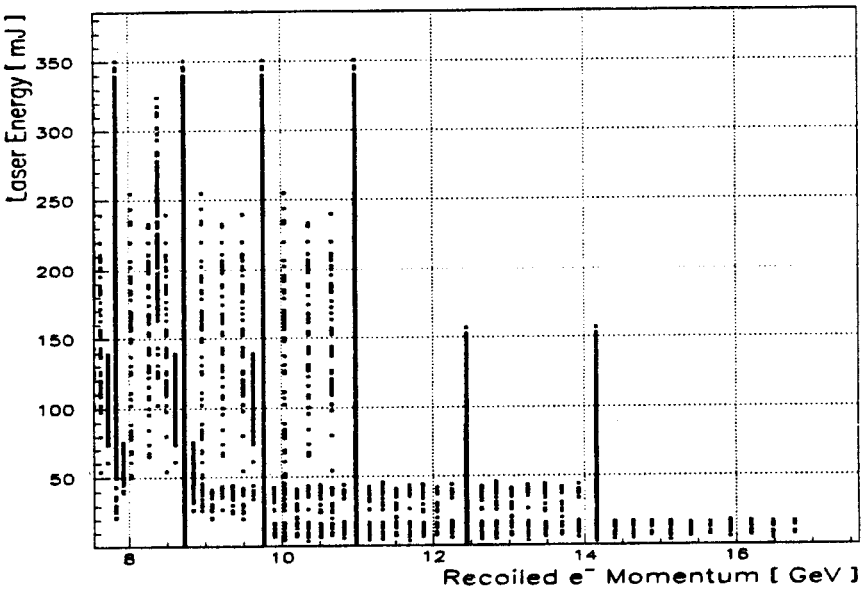

Figure 3.29: The laser energy - electron momentum map of the green circular data

part of the experiment and reflects an attempt giving an overview map for the green laser as done previously for the IR. The analysis of the data taken at green laser light follows the exact steps with the IR, with some exceptions as noted in the following subsections.

3.3.1 Electron beam and laser parameter measurements

The distribution of the beam charge during the runs with green, circularly polarized laser is shown in Figure 3.30, where again a 3σ cut from the average charge at each run was applied. The sizes of the electron beam during the green circular runs were shown in section 2.1. The angles and positions of the beam are more stable than in the IR runs as seen in Figure 3.31.

The laser energy during the green running was recorded in almost every shot and its overall distribution is shown in Figure 3.32. A cut on the ratio of the event's laser

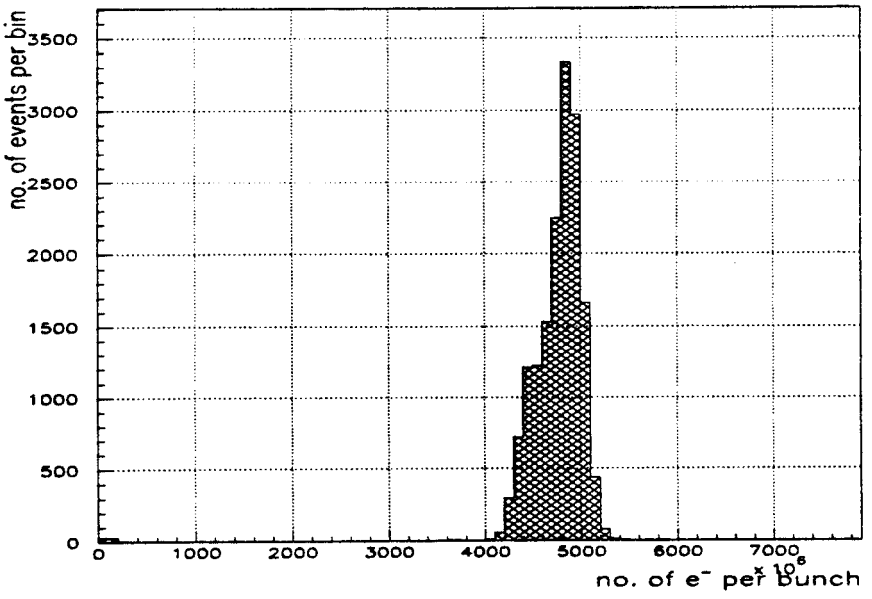

Figure 3.30: Electron beam charge of the green circular runs

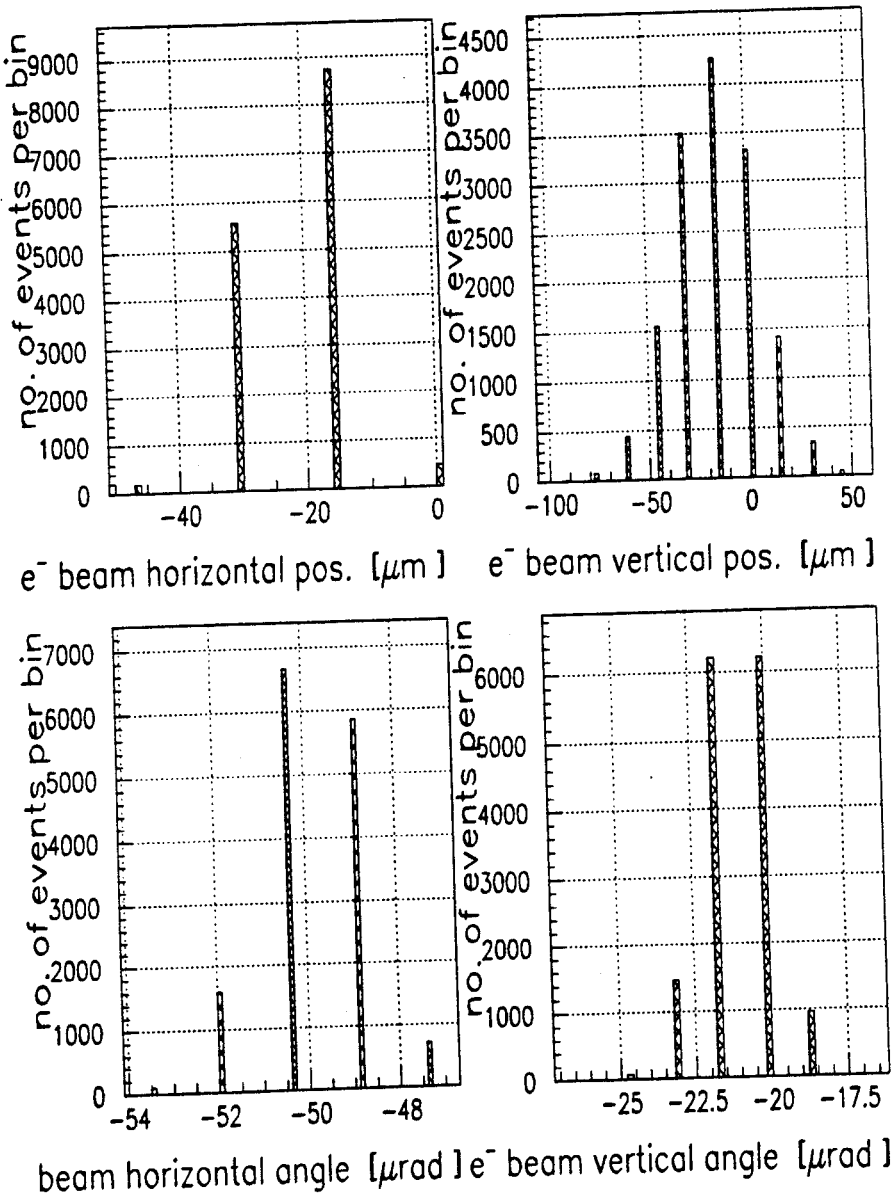

Figure 3.31: Electron beam angle and position at the interaction point for green runs

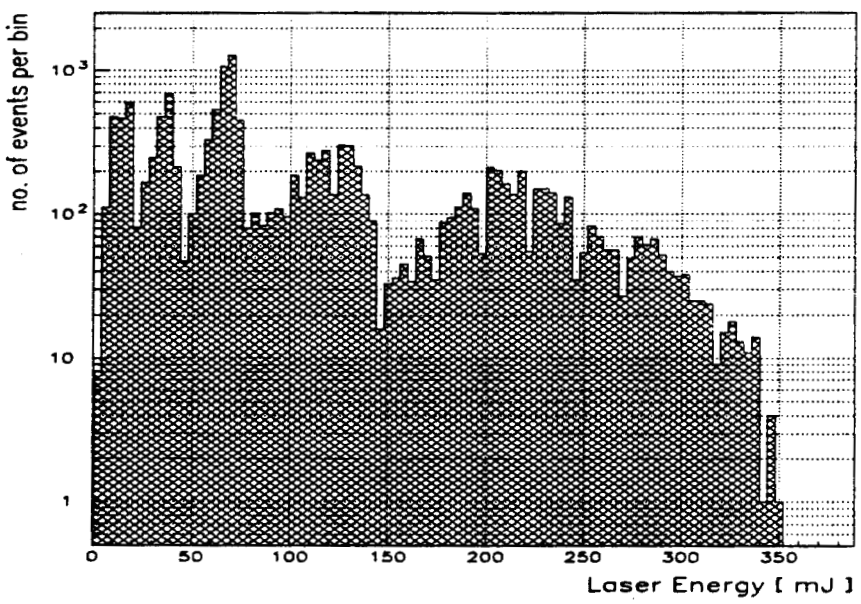

Figure 3.32: Laser energy for the green circular runs

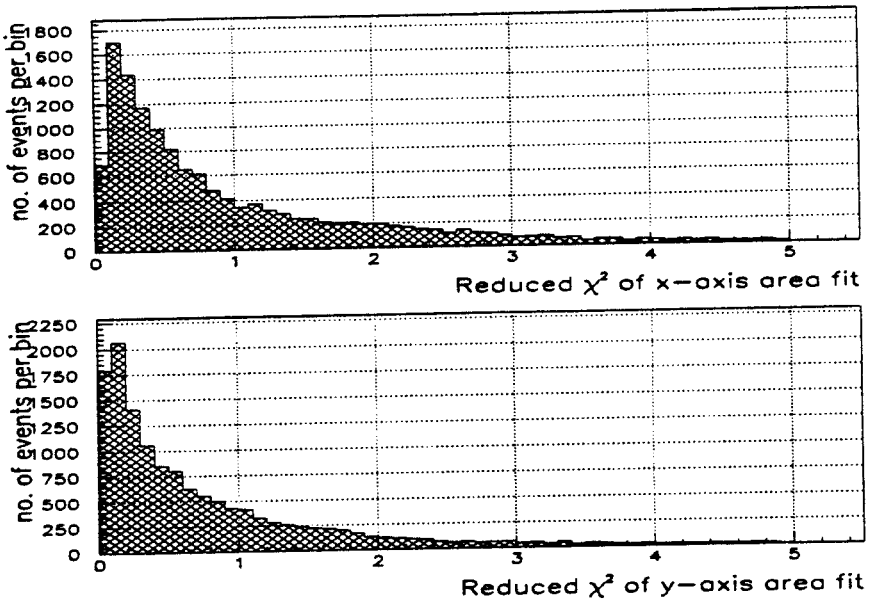

Figure 3.33: Reduced χ^2 of the laser area for green runs

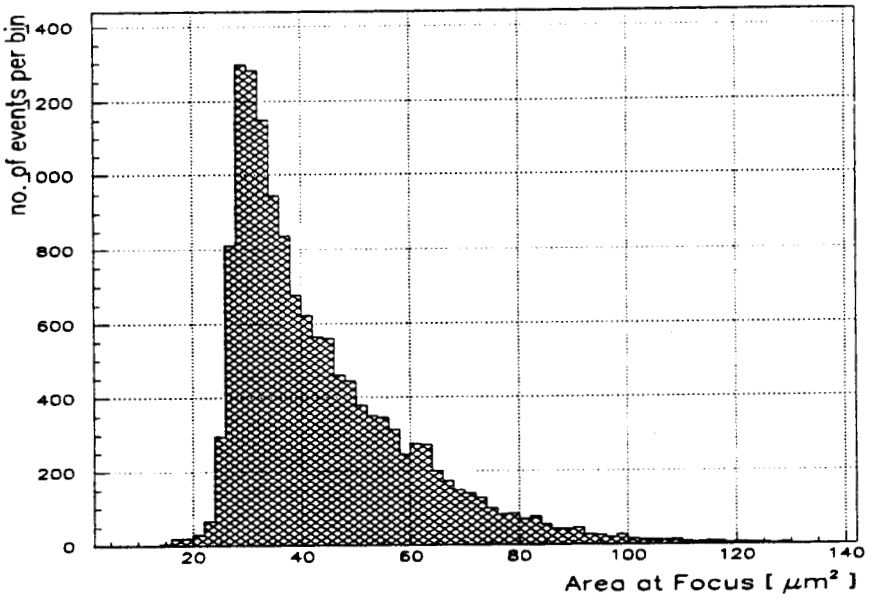

Figure 3.34: The laser focal spot at the IP for green runs

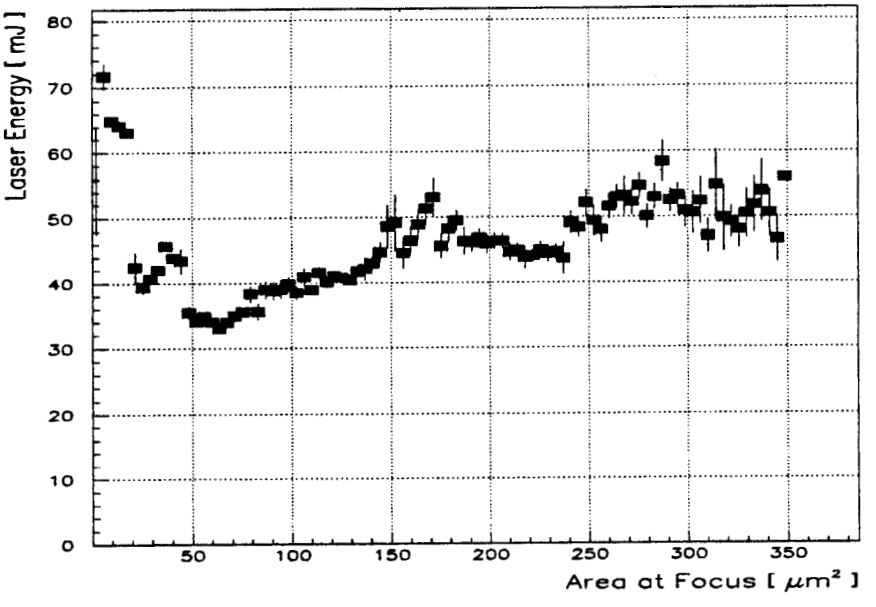

Figure 3.35: Correlation of laser focal area with laser energy for green runs

energy over the mean energy (RLENE) of the run is employed in the range: $0.5 <$ RLENE < 1.5.

The treatment of the green runs differs from that of the infrared runs due to the lack of a green autocorrelator. The pulse-width was recorded by a streak camera placed at the return laser beam after the optical transport. This may overestimate the laser pulse-width in the interaction point due to the additional windows in the optical path. The streak camera recorded pulse-widths of 1.9 ps and higher. One of this streaks was shown in Figure 2.25. Although a slight trend of increasing pulse-width with increasing laser energy appears, the streaks also show a systematic error towards larger pulse-widths for some of the data taken due to the increased level of light intensity on the streak camera CCD. Although the resolution of the streak camera is specified as 750 fs [50], it was not recently calibrated and a deterioration is suspected. Furthermore, a theoretical calculation of frequency doubling of an IR pulse of 1.8 ps (the average laser pulse-width in IR) using the specific doubling crystal geometry estimates a decrease in pulse-width. For these reasons a constant pulse-width of 1.9 ps was assumed for the data analysis of the green runs.

The χ^2 of the focal area fit and of the individual spot axis are shown in Figure 3.33. A cut at $\chi^2 <1.5$ was applied on the data. The distribution of the laser focal spot area over the course of the green laser running is shown in Figure 3.34. The diffraction limit in area for $0.527\mu m$ wavelength and effective f-number 6 of the focusing optic is $7\mu m^2$, so the data show a variation of 2 - 5 times diffraction limited focal spot area over all events. Figure 3.35 does not show a clear dependence of the area on the laser energy.

The distribution of η for the green runs is shown in Figure 3.36. The maximum η achieved was 0.3. Its correlation with the laser parameters is shown in Figure 3.37.

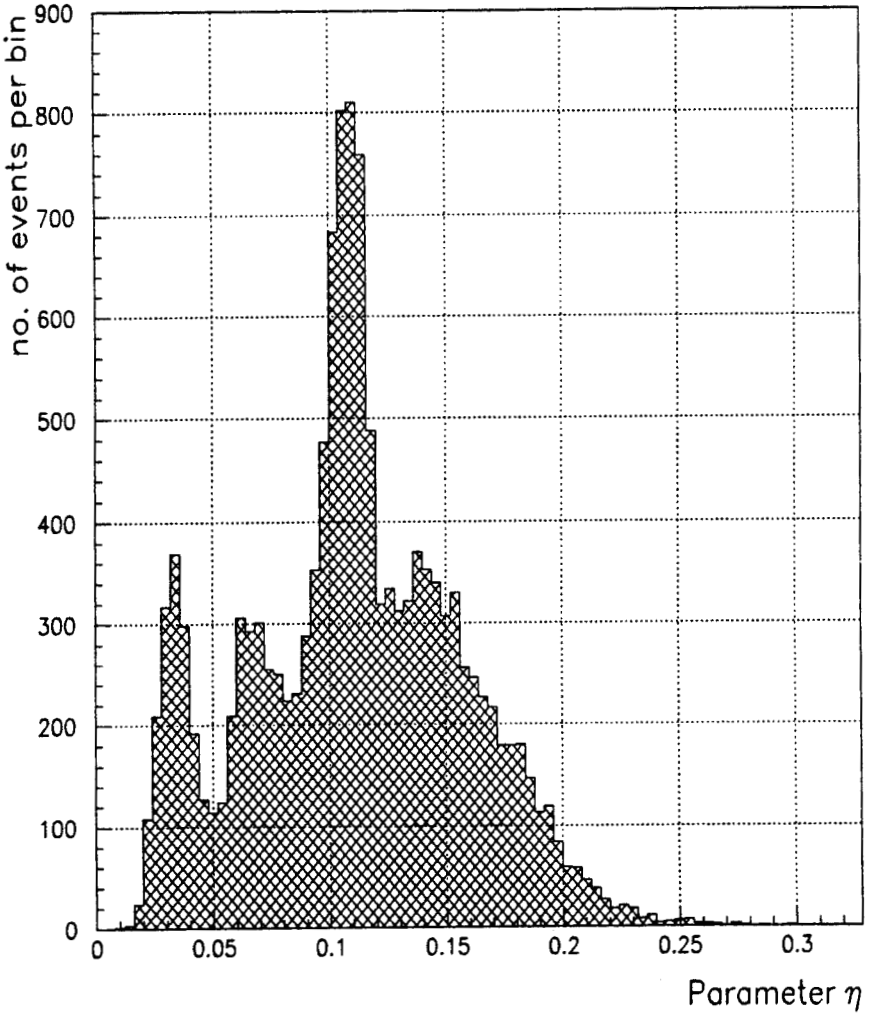

Figure 3.36: The η achieved at the IP for green runs

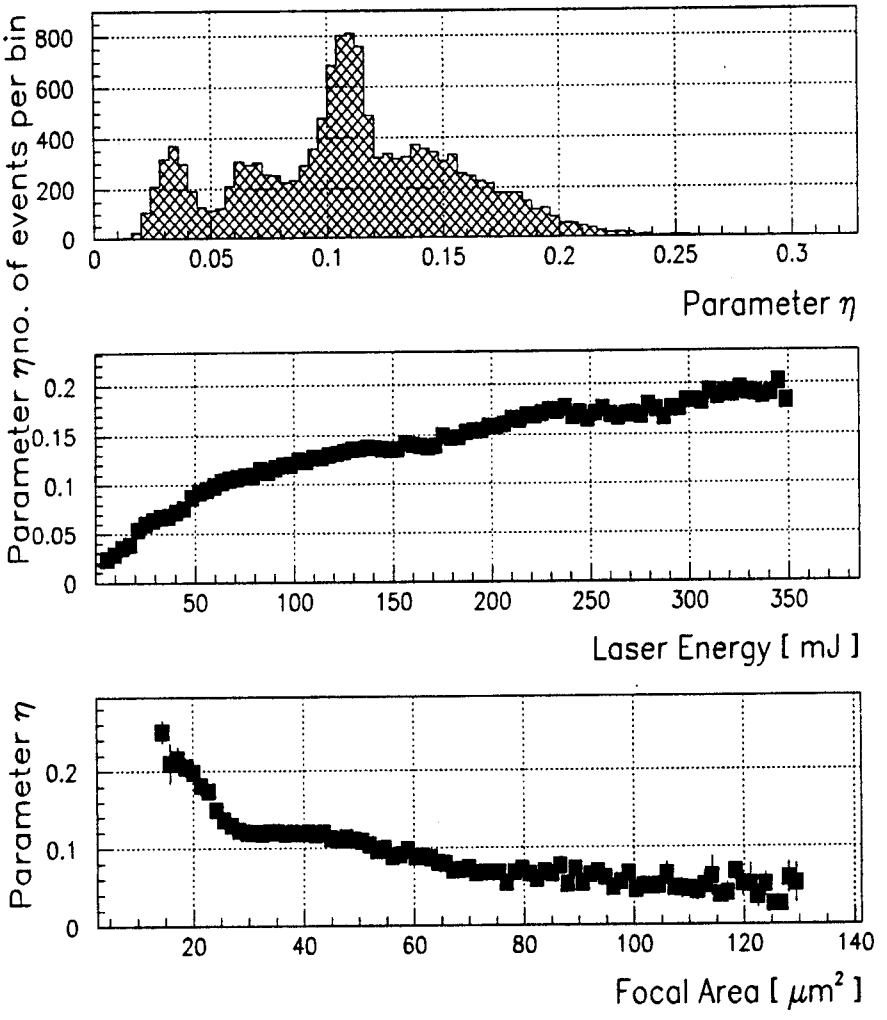

Figure 3.37: Correlation of η with laser parameters for green runs

3.3.2 Cuts on the laser and beam parameters and data binning

The cuts applied on the data are given in Table 3.3, where the names of the variables are consistent with the ones in the IR.

An appropriate binning on the map of laser parameters and recoil electron momentum for the events that survive the cuts was applied in the green data. These bins on the laser parameters together with the corresponding beam configurations and an estimate of the parameter η are shown in Table 3.4.

One can also define adjacent bins of momentum of 0.5 GeV each and construct a matrix having as entries the reconstructed ECAL signal at each momentum bin, for a specific laser bin.

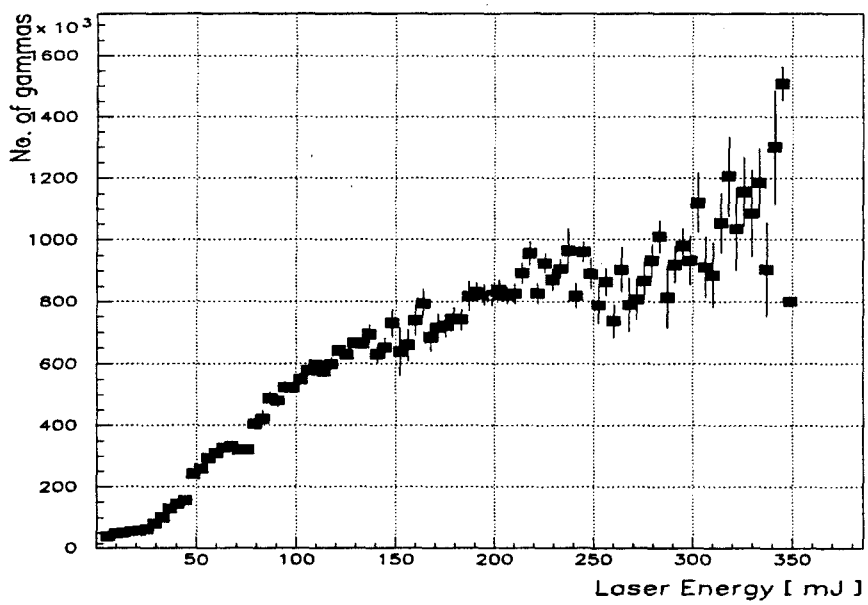

Figure 3.38: Correlation of the linear rate with laser energy for green runs

Cut parameter	Range	Events Remained after cuts
laser energy / run average. (RLENE)	0.5 - 1.5	15832
laser area / run average. (RLARE)	0.5 - 1.5	12720
electron beam charge cut (BFLA)	0	15745
no. of saturated channels (NSEC)	0	16271
overlap factor (NCCM1/NGMC)	0.5 - 1.5	7383
Events before cuts		16322
Events after all cuts		5342

Table 3.3: Cuts on laser parameters, electron beam parameters, the overlap factor and the number of saturated ECAL channels for green runs

3.3.3 Detector studies in the green laser runs

The linearity of the gamma rate with the laser energy is shown in Figure 3.38 for the green runs. The electron beam related background in ECAL is even lower for the green laser runs than the one presented for the IR. This is due to a protective plate inserted on top of ECAL and due to the energy range of the electrons scattered off green laser photons: Because of the shift of the kinematic edges of the nonlinear process into lower energies for green photons, the calorimeter needs to be positioned even further from the electron beam pipe (lower). The electron beam background is again subtracted on average from the ECAL raw signal similarly to the IR analysis. The linear correlation of the outer pads of ECAL with the gamma monitors holds also for green and the reconstruction of ECAL signal due to back-splash is the same as discussed in the IR section.

energy (mJ)	anal. width (ps)	area (μm^2)	e^- config.	overlap	η	events left
8	1.5	40 - 90	5	0.6	0.02	174
14	1.5	40 - 80	5	0.6	0.03	116
32	1.5	25 - 55	5	0.6	0.06	267
57	1.5	26 - 36	5	0.6	0.09	700
85	1.5	29 - 35	5	0.6	0.10	73
100	1.5	26 - 37	5	0.6	0.11	425
180	1.5	20 - 60	5	0.6	0.12	383
230	1.5	35 - 65	5	0.6	0.11	62

Table 3.4: Laser parameter bins chosen for analysis, together with an estimate of η and the respective electron beam configurations for the green circularly polarized runs

Chapter 4

Results

4.1 Introduction

4.1.1 Normalized recoil electron rates.

From the energy distribution of the ECAL rows discussed in chapter 3 one can infer the number of electrons collected pulse by pulse for some recoil electron momentum by dividing the energy by this same momentum:

$$N = \frac{E(p)}{p} \tag{4.1}$$

Since there is a momentum bite dp associated with each ECAL row, p is the average momentum for this ECAL row. A more physical result is the number of electrons per momentum interval (bite):

$$R = \frac{dN}{dp} \tag{4.2}$$

To use this quantity for the study of events having different laser intensities one needs to normalize it by that laser intensity. Even better one can normalize it by the number of linear gammas, so that it will also account of the effect of bad overlap among events. Therefore we have defined the normalized yield:

$$\frac{1}{N_\gamma} \cdot \frac{dN}{dp}$$

We can write the linear rate in terms of the number of beam electrons N_e, laser photons N_ω, the area of the electron-laser interaction A_e, the overlap factor OF and the total Compton scattering cross section σ_0 as follows:

$$N_\gamma = \frac{N_e N_\omega}{A_e} \cdot (OF)\sigma_0 \tag{4.3}$$

The recoil electron rate per momentum interval is therefore

$$\frac{dN}{dp} = \frac{dN}{d\sigma} \cdot \frac{d\sigma}{dp} = \frac{N_e N_\omega}{A_e} \cdot (OF)\frac{d\sigma}{dp} = \frac{N_\gamma}{\sigma_0} \cdot \frac{d\sigma}{dp} \tag{4.4}$$

where

$$\frac{1}{\sigma_0}\frac{d\sigma}{dp}$$

is the differential nonlinear Compton Scattering normalized by the total Compton scattering cross section and equals to the normalized recoil electron yield:

$$\frac{1}{\sigma_0}\frac{d\sigma}{dp} \simeq \frac{1}{N_\gamma} \cdot \frac{dN}{dp} \tag{4.5}$$

The final result of the analysis is the normalized electron yield studied as a function of electron momentum for various laser energies (or intensities) and as a function of laser energy for fixed momenta. This reveals the spectrum with the kinematic edges discussed in chapter 1 and the nonlinear dependence of the process on the laser intensity. The normalized yield is useful because the time jitter between the electron and the laser beam contributes to the variations of the nonlinear yield in a way that can not be calculated by electron and laser measurements only. So although as an average we calculate the correct number of gammas, in an event by event analysis (such is the one presented here) we need to normalize the nonlinear rate with the linear rate which reflects not only the change in the beam parameters but also the timing jitter.

Furthermore, while generally in high energy physics experiments the final result is the differential cross section of the process studied, in this experiment this can not be done. The reason is that the cross section of the nonlinear Compton scattering process of order n scales as

$$\eta^{(2n-1)}$$

i.e it varies with laser intensity. But since the laser is focused in the interaction point the intensity of the field varies both in space and in time. In the following section we will see that the simulation integrates over this space time volume in order to calculate the rate of the process. A cross section that varies in space and time in the interaction region is ill defined and for this reason it is not used in this experiment.

4.1.2 Numerical simulation of nonlinear Compton scattering

Some results of an analytic calculation of the nonlinear Compton rates were given in the first chapter, and the assumptions made there approximate the experimental conditions. Nevertheless, a simulation was developed for this experiment [91] that can calculate recoil electron yields for any laser intensity over a range of recoil electron momentum. It is a numerical integration of the rates given in [14] over a space-time grid around the focus of the laser in the interaction point, taking into account the geometry of the scattering. The crossing angle between the laser pulse with the electron beam is 17^0 and is one of the complications entering the analytic calculation, but can be successfully simulated. The numeric integration also takes into account the laser focusing angle and its Gaussian characteristics, while the analytic calculation could only assume cylindrical Gaussians for both beams.

Furthermore, the attenuation of the electron beam density as the electrons enter the laser field is calculated using the Klein-Nishina approximation. The primary process products of the laser - electron interaction are either the linear Compton scatters (the rate for this process is also estimated using the Klein-Nishina formula) or the nonlinear Compton scatters; the latter rate is calculated using the cross section of the nonlinear Compton scattering. The secondary processes are stemming from the further interaction of the recoil electrons and gammas emitted in the primary process. One of the secondary processes is pair creation from the interaction of a primary gamma (created by the dominant linear Compton scattering); this is calculated using the Breit-Wheeler cross section. Another secondary process calculated by the simulation is the nonlinear Compton scattering due to the electrons that recoil from the first interaction. Gammas can also be produced by a secondary interaction of the

linearly or nonlinearly primarily scattered electrons, which is also taken into account in the numerical integration.

4.2 Nonlinear Compton scattering results for infrared, circularly polarized laser light

4.2.1 Energy spectra of recoil electrons

The results shown here will be the normalized electron rate as a function of the electron energy for a given laser energy range, and as a function of the laser intensity for various electron energy ranges. These data will be shown using two approaches in a natural order as followed during the data analysis.

The first approach called the 'unreconstructed ' (UR) method uses the raw data and regards as real signal the energy deposited in the center-pads after subtracting a portion of the outer pad signal and the electron beam background. In this way the laser associated background which is the main contribution to the outer pad energy is subtracted from the signal. This does not account for showering phenomena in the calorimeter, so there is still leakage of energy from one pad to the other that contributes to our so called 'signal'. Instead of reconstructing further our signal using the methods described in the last chapter, we apply a shower spreading algorithm to the simulation output, that takes into account the shower coefficients in ECAL described previously. This algorithm reads the momentum - position map, constructs the ECAL energy as a function of position, applies the showering on the energy then calculates the number of electrons for each momentum bin and finally gives an output of normalized electron yield as a function of momentum. Since the spreading varies even at the same momentum bin depending on the position of ECAL, the spreading algorithm also moves the ECAL position in steps of mm, and calculates the yield in each momentum bin for each ECAL position. To compare with the data that are integrated over 0.5 GeV bins for presentation purposes (apart from the natural integration of the ECAL row acceptance), we average the yield over a number of mm after correction of shower spreading. Since this method of inputing the shower of the

ECAL energy in the simulation is not done event by event, an average of the laser and electron beam parameters is used; this is the limitation for this method for comparing the data with the simulation.

This method produced the plots in Figures 4.1 to 4.3 for the electron yield as a function of momentum and Figure 4.4 for the dependence of the yield on the laser energy. The nonlinear rates of the data that are dominated by scattering at nth order will scale with the laser intensity as I^n and after normalization by the number of gammas we expect an I^{n-1} scaling. At the UR representation a simulation can only be used with average parameters for laser area and pulse-width. For this reason a plot of normalized yield as a function of laser energy contains the same information as with laser intensity and the same power law will be true. The simulation deviates from a straight line due to the shower spreading.

This kind of presentation (UR) gives us confidence that the direct raw signal is first of all not corrupted and second agrees very well with the simulation when considering the resolution of the calorimeter. Although the kinematic edges are not as easily discernible as in the reconstructed data (shown in a later section) it is still easy to see the drop in yield at the n=2 to n=3 transition. The errors on the data are the sigma of the distribution of the yield for each momentum bin, all rows and events included. No horizontal error is shown for the simulation since it is already smeared over the ECAL momentum acceptance.

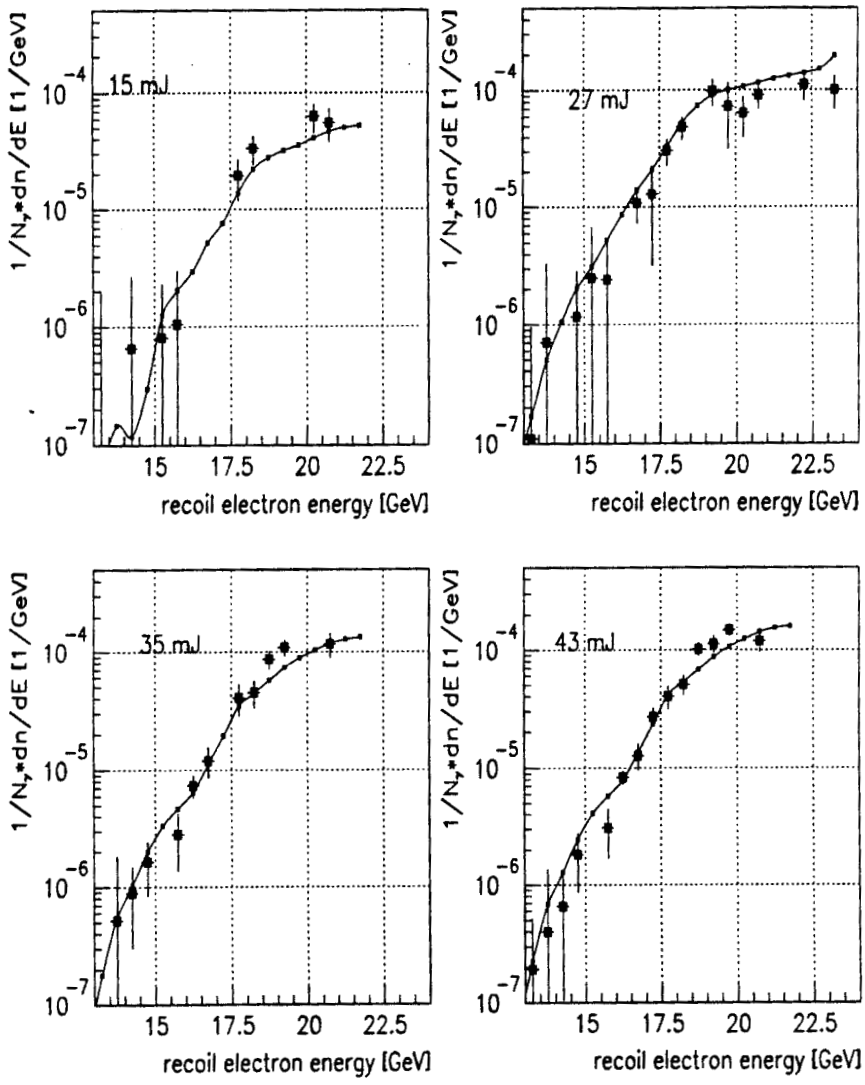

Figure 4.1: Recoil electron yield (unreconstructed) vs momentum for fixed IR laser energy. The large, dark squares are the data points while the line connects the simulation points (small dark dots). The errors on the data represent the statistical error of the electron yield distribution for each laser energy - electron momentum bin.

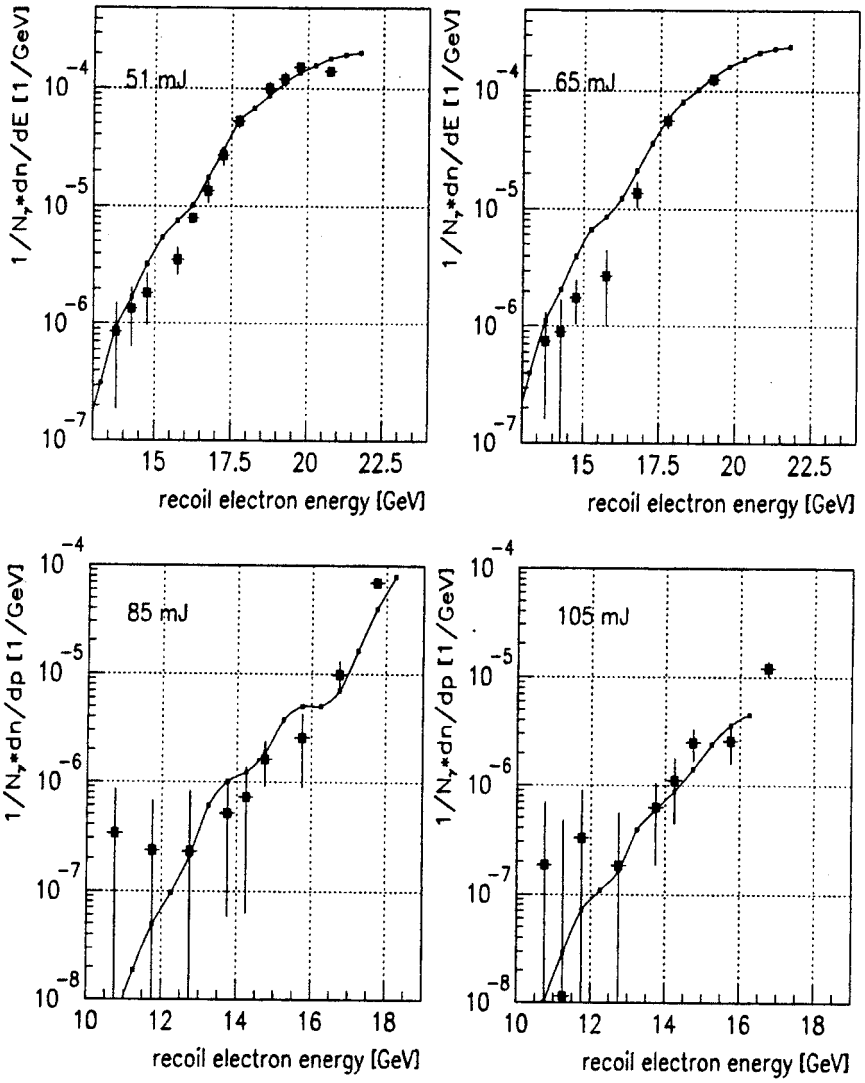

Figure 4.2: Recoil electron yield (unreconstructed) vs momentum for fixed IR laser energy (cont'). The large, dark squares are the data points while the line connects the simulation points (small dark dots). The errors on the data represent the statistical error of the electron yield distribution for each laser energy - electron momentum bin.

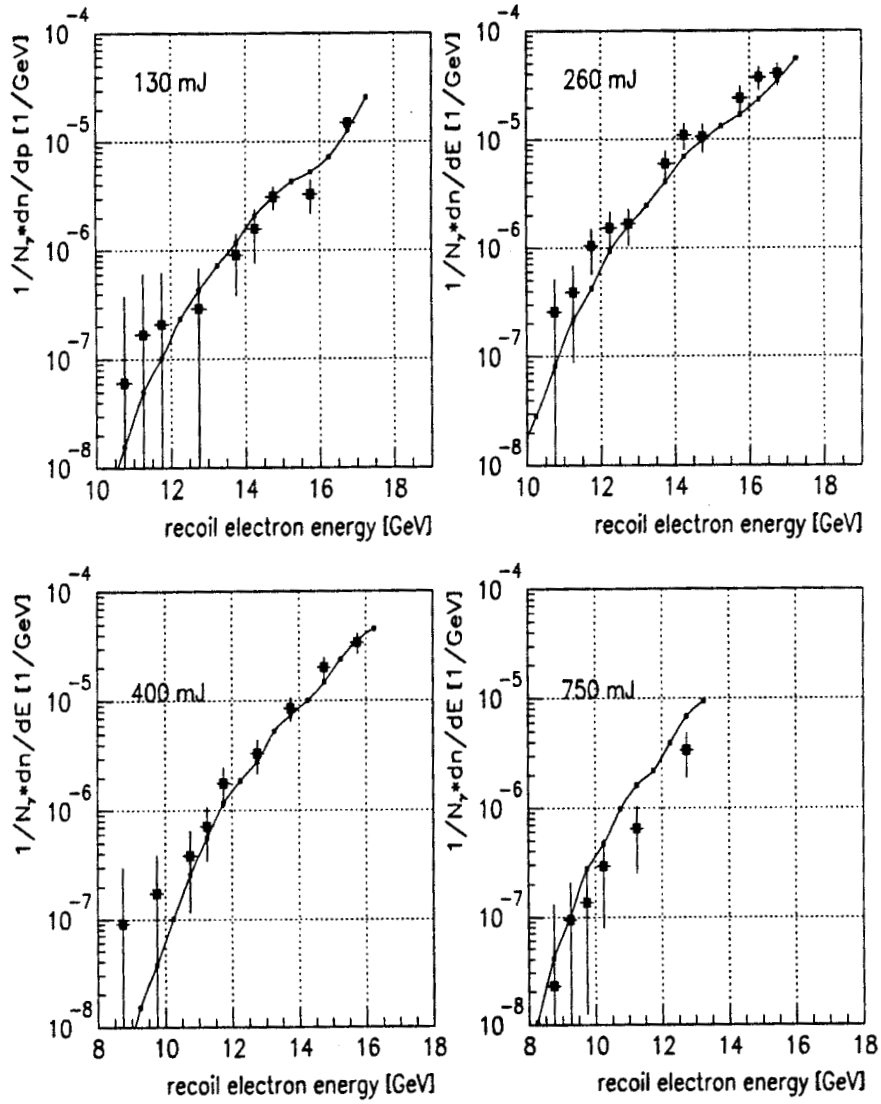

Figure 4.3: Recoil electron yield (unreconstructed) vs momentum for fixed IR laser energy (cont'). The large, dark squares are the data points while the line connects the simulation points (small dark dots). The errors on the data represent the statistical error of the electron yield distribution for each laser energy - electron momentum bin.

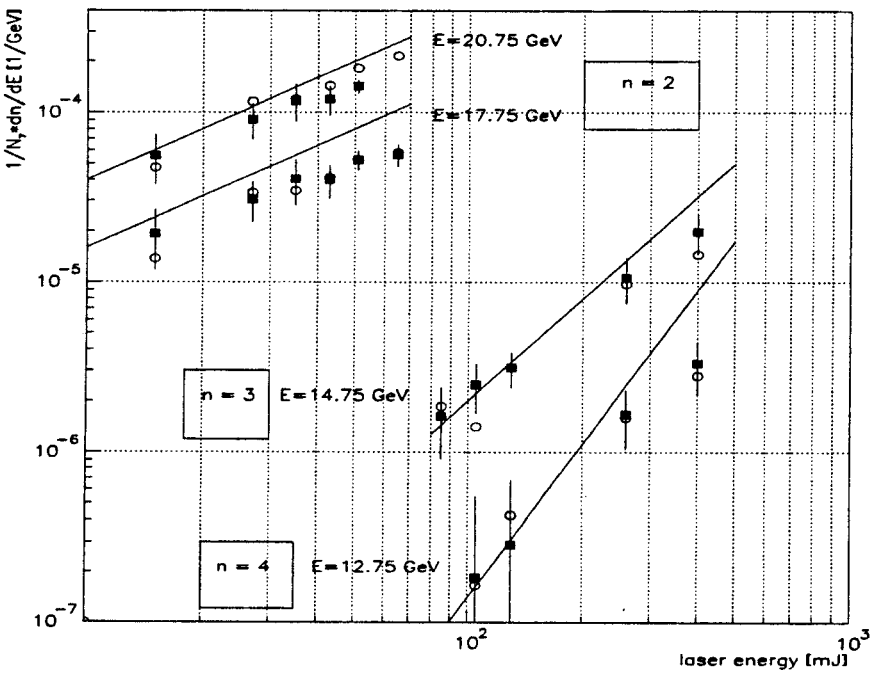

Figure 4.4: Recoil electron yield (unreconstructed) vs laser energy for representative momentum bands, IR. The dark squares are the data and the open circles the simulation. The straight lines represent the theoretical power low expected for each order of the nonlinear Compton scattering. The error bars reflect the statistical uncertainty on the data.

In the second approach the electron yield was calculated by 'reconstructing' the energy deposited in the calorimeter. The data are now compared with the yield predicted by the simulation, using the event by event parameters of the data. For this reason the simulation results are shown as isolated points with a 1-1 correspondence with the data. This simulation includes both nonlinear Compton scattering and multiple ordinary Compton scattering. In most of the data it is easy to discern the kinematic edge of the n=2 to n=3 transition. Due to the high rates of linear electrons we could not map the n=1 kinematic edge. For n=4 and higher the edges are not any more clear since they are packed closer together from the physics of these processes and due to the limited dynamic range of ECAL and the limitations of the reconstruction algorithms in uncovering these edges. Instead, we see a slower drop in the spectrum. (Note that the vertical axis is a logarithmic scale which reduces the visual impact of a step in the presented form, but is necessary in order to view several orders of magnitude of data simultaneously).

The error bars shown on the data points present the statistical uncertainty in the number of scattered electrons and the systematic uncertainty in the correction for backgrounds in the calorimeter due to the two reconstruction methods. These errors were measured as follows:

For a bin in laser energy and electron momentum we have

$$y_i \equiv \frac{1}{N_\gamma} \frac{dN(i)}{dp(i)} \tag{4.6}$$

where y_i is the normalized electron yield in the i-th row. We still distinguish between events that come from different rows (since each momentum bin contains data from several ECAL positions) because otherwise a weighted error estimate for the events diverges, i.e. single events in this momentum bin but coming from low ECAL rows can have electron yields far from the mean of the distribution that would completely dominate the error. By weighting all events according to their rows we approach the real error of the data. The event weights are given by:

$$\omega_i = \frac{1}{\sigma_i^2} \tag{4.7}$$

with $\sigma_i^2 = < y_i^2 > - < y_i >^2$. The electron yield is

$$< y >= \frac{\sum\limits_{allevents} y_i \omega_i}{\sum\limits_{allevents} \omega_i} \tag{4.8}$$

The error on $< y >$ from the statistical variations is σ_{distr} is given by

$$\sigma_{distr}^2 = \frac{< y^2 > - < y >^2}{n_{equiv}} \tag{4.9}$$

where

$$n_{equiv} = \frac{(\sum \omega_i)^2}{\sum \omega_i^2}$$

is the equivalent number of events when each event is weighted by ω_i.

The difference between the two reconstruction methods is included in the error estimate by forming the sigma of the average of the two distributions (which is the quantity plotted) produced by the two methods i.e.

$$\sigma_{recon}^2 = (\frac{< y >_1 - < y >_2}{2})^2 \tag{4.10}$$

Finally the total error σ is calculated as the quadratic sum of the above two errors:

$$\sigma^2 = \sigma_{distr}^2 + \sigma_{recon}^2 \tag{4.11}$$

The horizontal error bar on the simulation denotes our uncertainty in measuring the momentum due to the ECAL pad width (note that the momentum bite varies from 2.8 GeV at 20 GeV to 1.5 GeV at 10 GeV). Figures 4.5 - 4.9 show the data and the simulation as discussed above for circularly polarized IR laser for fixed laser energies.

The systematic error for the linear rate measurement from CCM1 is taken to be 10% and is not included in the plots but is relatively small compared to all other errors. Also significant is the uncertainty in the quoted peak laser energy which is also of the 10% order. Since the simulation takes into account the interaction geometry it also depends on the laser spot size and the laser pulse-width and therefore carries an uncertainty stemming from the measurement errors of these parameters. Since in the IR all three laser parameters were measured in each pulse the uncertainty for the laser intensity can be estimated at the 30% level.

In the results plotted the solid circles are the data points with horizontal and vertical error bars as described above. The open boxes are the simulation where the vertical and horizontal heights are the magnitude of the error bars. The horizontal bar is the same as for the data points corresponding to the width of the ECAL rows. The vertical bar is the statistical uncertainty since each point is an average over many events as was done for the data points. In this representation the simulation can not be approximated with a line since it corresponds to data laser and beam parameters and the data collected do not span the whole laser energy - electron momentum range.

The reconstructed data for the IR are presented in 19 laser energy bins and 20 momentum bins. This is a finer binning in laser energy (we still apply a 0.5 GeV momentum binning) than the one presented in the data analysis and used for the unreconstructed data. This is possible in the reconstructed data due to the better error treatment.

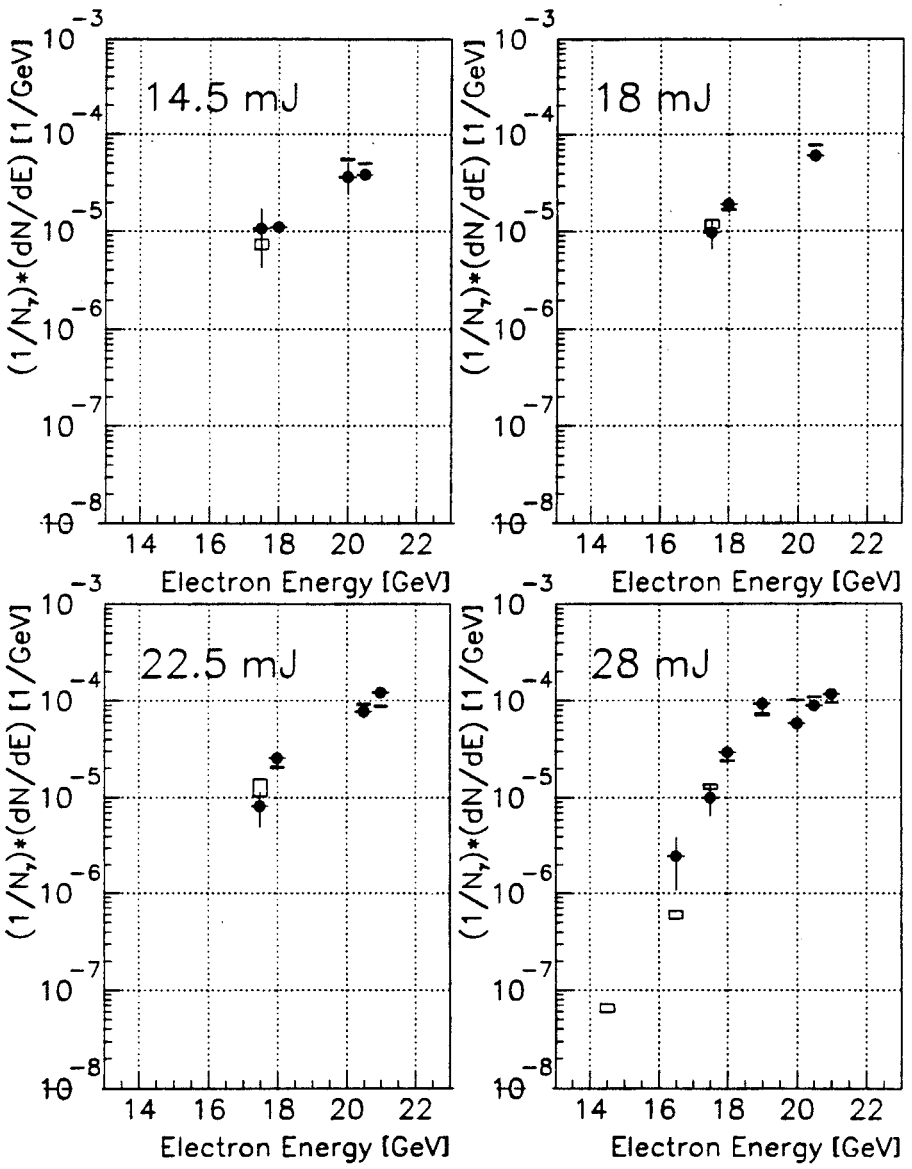

Figure 4.5: Recoil electron yield (reconstructed) vs momentum for fixed IR laser energy. The data are represented with solid circles with horizontal error bars corresponding to the ECAL row width and vertical error bars corresponding to statistical uncertainties and systematic due to the two methods used for signal reconstruction. The open boxes are the simulation where the vertical and horizontal heights are the magnitude of the error bars.

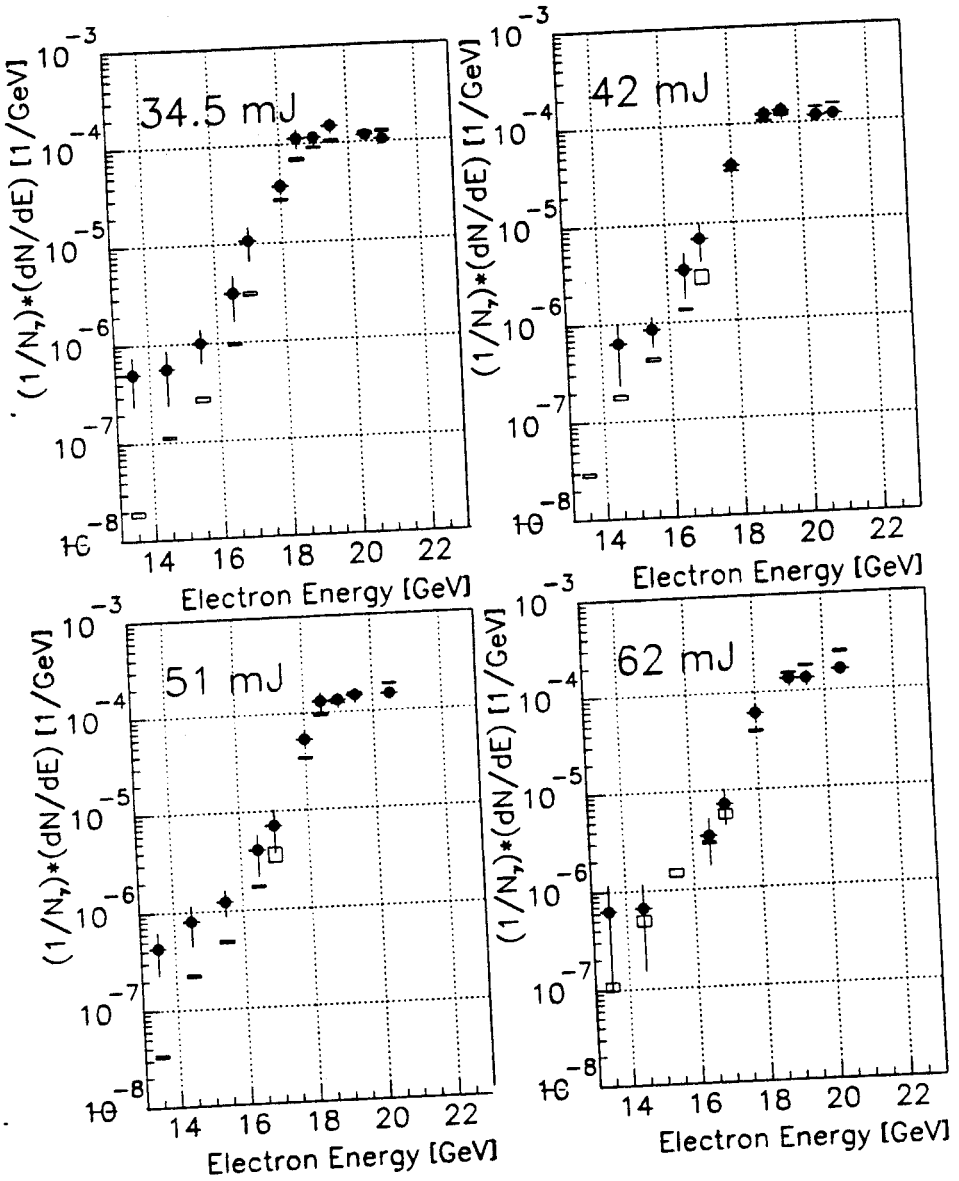

Figure 4.6: Recoil electron yield (reconstructed) vs momentum for fixed IR laser energy (cont'). The data are represented with solid circles with horizontal error bars corresponding to the ECAL row width and vertical error bars corresponding to statistical uncertainties and systematic due to the two methods used for signal reconstruction. The open boxes are the simulation where the vertical and horizontal heights are the magnitude of the error bars.

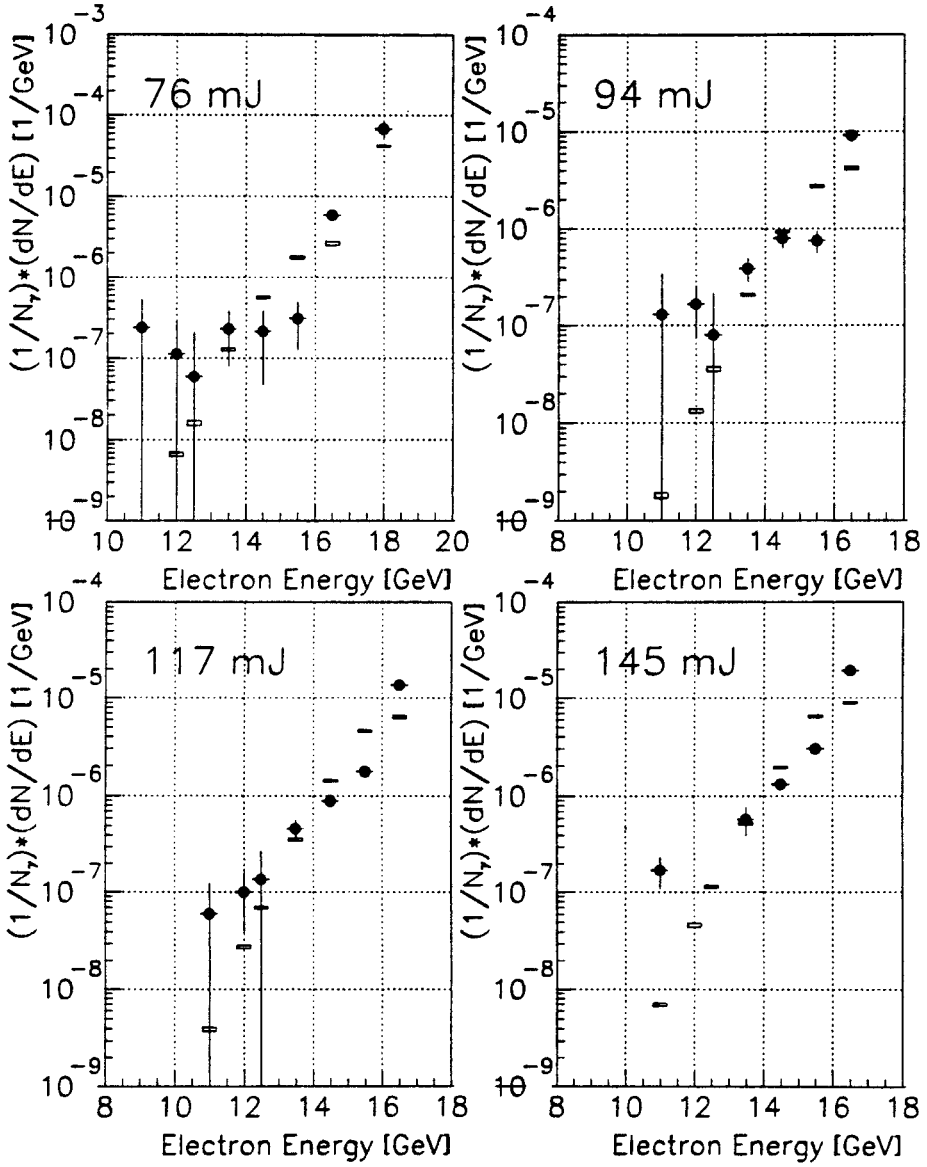

Figure 4.7: Recoil electron yield (reconstructed) vs momentum for fixed IR laser energy (cont'). The data are represented with solid circles with horizontal error bars corresponding to the ECAL row width and vertical error bars corresponding to statistical uncertainties and systematic due to the two methods used for signal reconstruction. The open boxes are the simulation where the vertical and horizontal heights are the magnitude of the error bars.

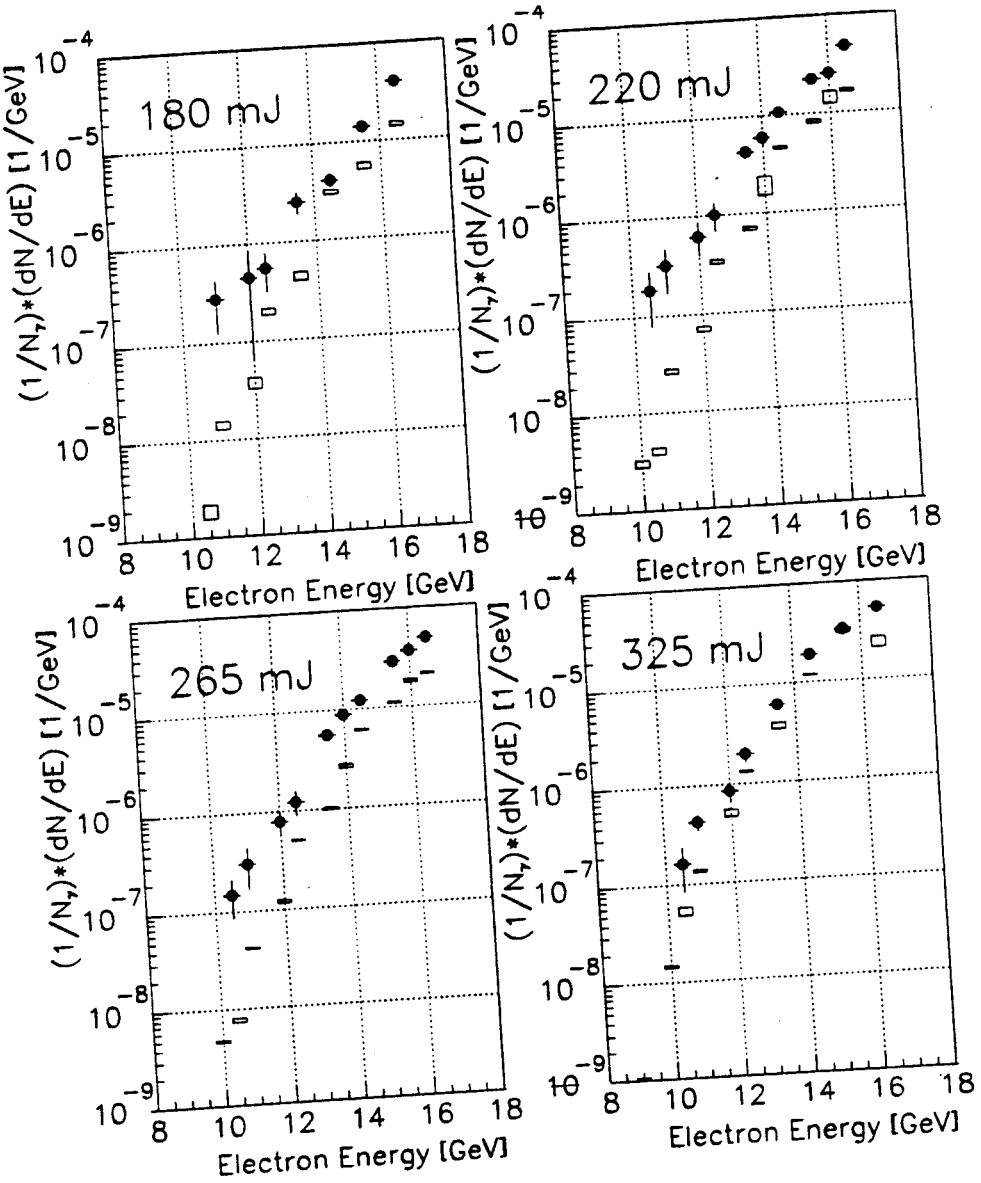

Figure 4.8: Recoil electron yield (reconstructed) vs momentum for fixed IR laser energy (cont'). The data are represented with solid circles with horizontal error bars corresponding to the ECAL row width and vertical error bars corresponding to statistical uncertainties and systematic due to the two methods used for signal reconstruction. The open boxes are the simulation where the vertical and horizontal heights are the magnitude of the error bars.

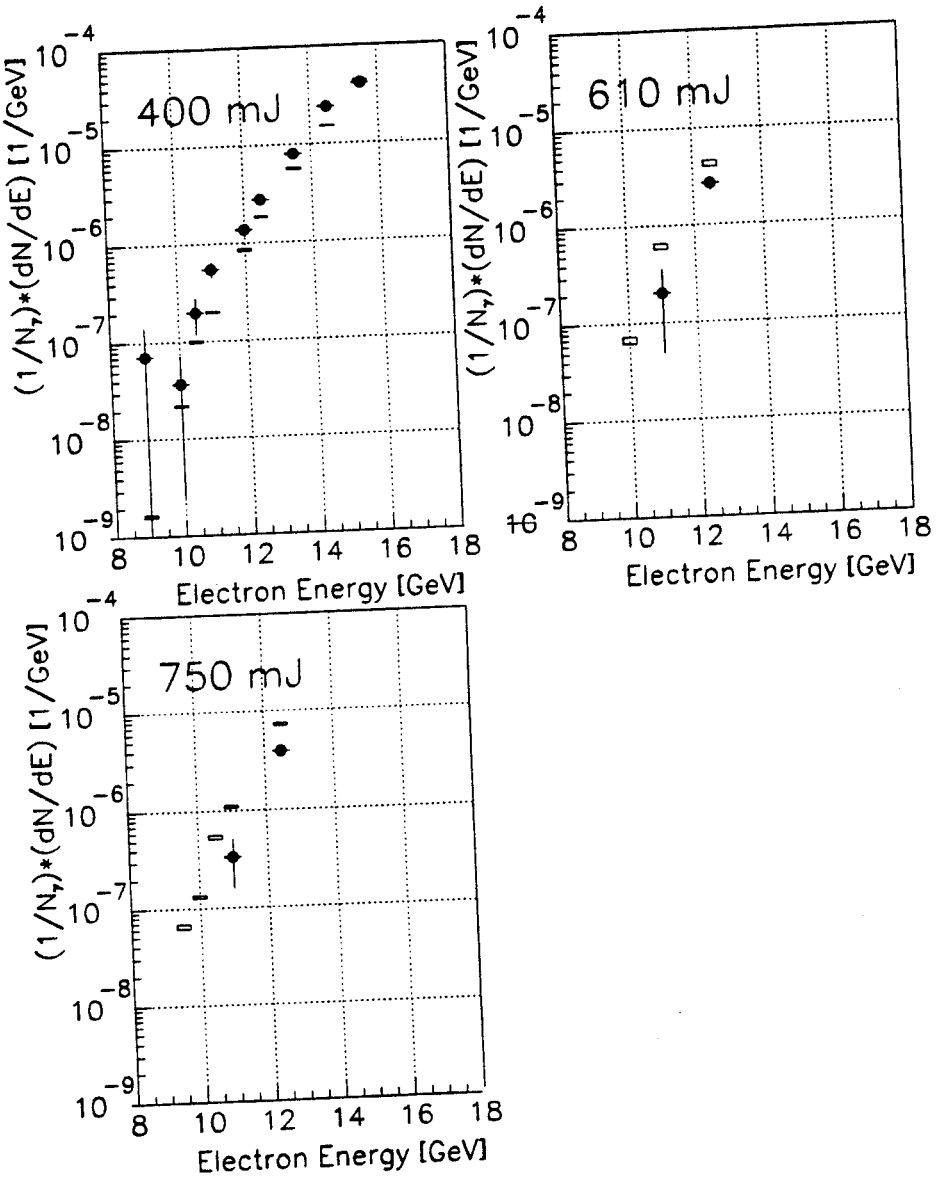

Figure 4.9: Recoil electron yield (reconstructed) vs momentum for fixed IR laser energy (cont'). The data are represented with solid circles with horizontal error bars corresponding to the ECAL row width and vertical error bars corresponding to statistical uncertainties and systematic due to the two methods used for signal reconstruction. The open boxes are the simulation where the vertical and horizontal heights are the magnitude of the error bars.

4.2.2 Scaling to standard electron and laser beam parameters

As we have seen in the last chapter the parameters of the electron beam and of the laser pulses varied during a run and so did the overlap in time and space of the two beams. The effect of jitter has been already discussed and by normalizing to the number of gammas from the linear Compton we become less sensitive to this effect. The data already shown were compared with a point by point simulation because the simulation was done for the parameters of each event and then averaged (as done for the data) in laser energy and momentum bins. This uniform approach of data and simulation showed that data and simulation agree. In order to present the data in a form corresponding to fixed electron beam and laser parameters we create a simulation corresponding to these fixed parameters. Scaling the data to these standard parameters, which is only over a small interval in parameter space, is equivalent with eliminating pulse by pulse variations of the interaction volume.

For this purpose the numerical integration produced lookup tables [91] used to scale the data for each event to fixed parameters of 2 ps pulse-width, 70 μm^2 focal area and 60μm $\times$60 μm $\times$800 μm electron beam size (standard deviation). The data shown in Figures 4.10 to 4.14 have been scaled to these parameters. Now the simulation is a line instead of points. This technique is particularly useful comparing the data with the simulation as a function of laser energy shown later in this chapter; note that from the standard parameters we can calculate the laser intensity for a given laser energy. When the data are scaled the error bars include in addition to the errors discussed for the un-scaled data also the uncertainties in the normalization to standard beam and laser conditions.

In Figures 4.10 - 4.14 the solid circles are the data and the solid line is the simulation that includes both nonlinear Compton scattering and multiple linear Compton scattering. The dashed line is the simulation for multiple linear Compton scattering only.

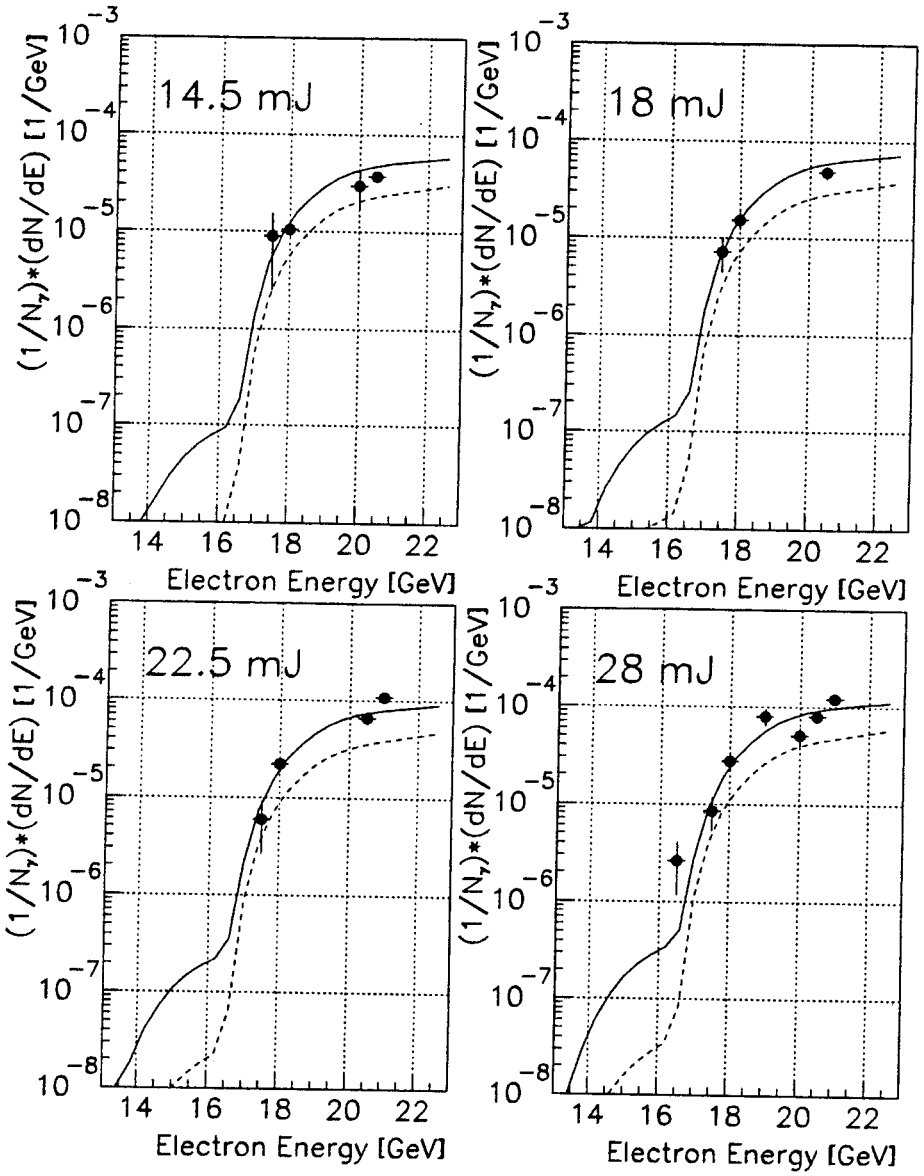

Figure 4.10: Recoil electron yield (scaled and reconstructed) vs momentum for fixed IR laser energy. The solid circles are the data, the solid line is the simulation that includes both nonlinear Compton scattering and multiple linear Compton scattering. The dashed line is the simulation for multiple linear Compton scattering only.

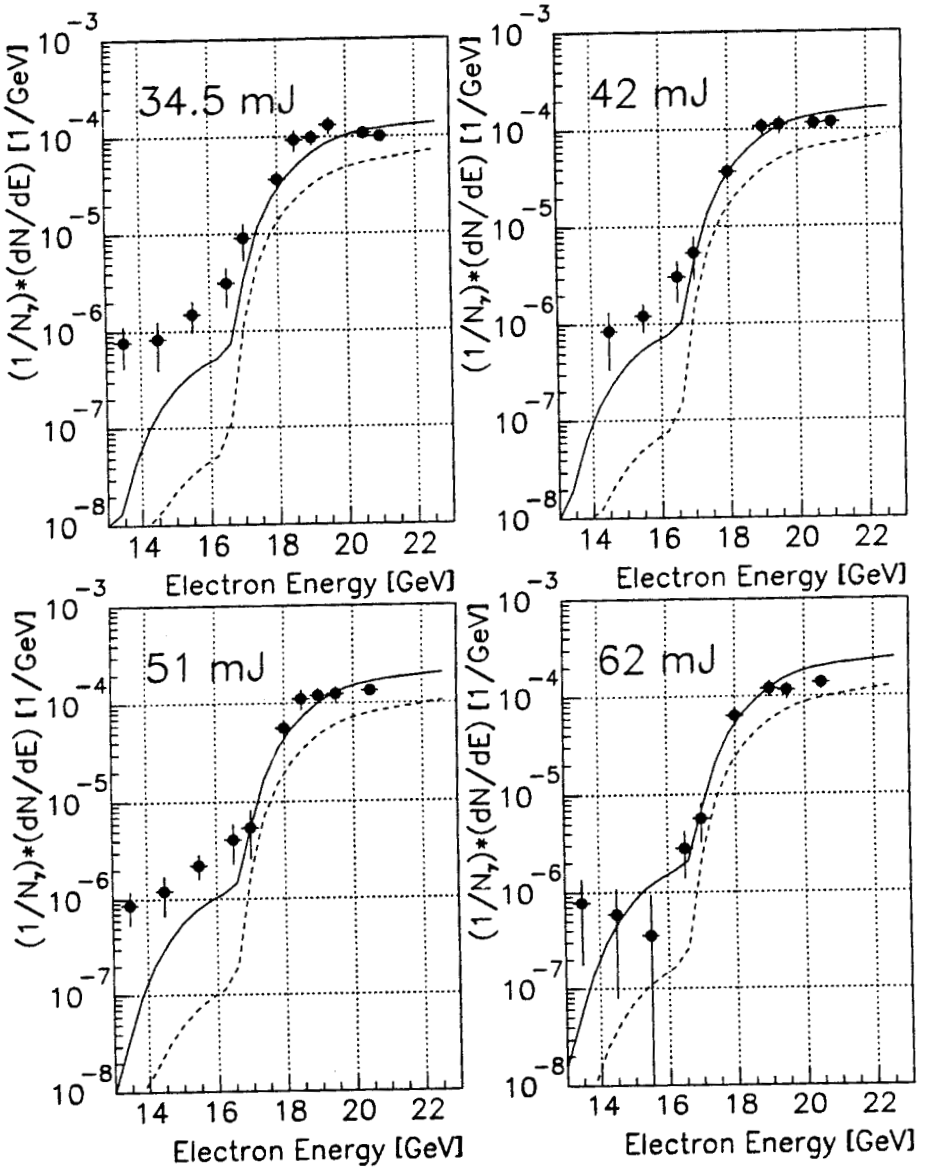

Figure 4.11: Recoil electron yield (scaled and reconstructed) vs momentum for fixed IR laser energy (cont'). The solid circles are the data, the solid line is the simulation that includes both nonlinear Compton scattering and multiple linear Compton scattering. The dashed line is the simulation for multiple linear Compton scattering only.

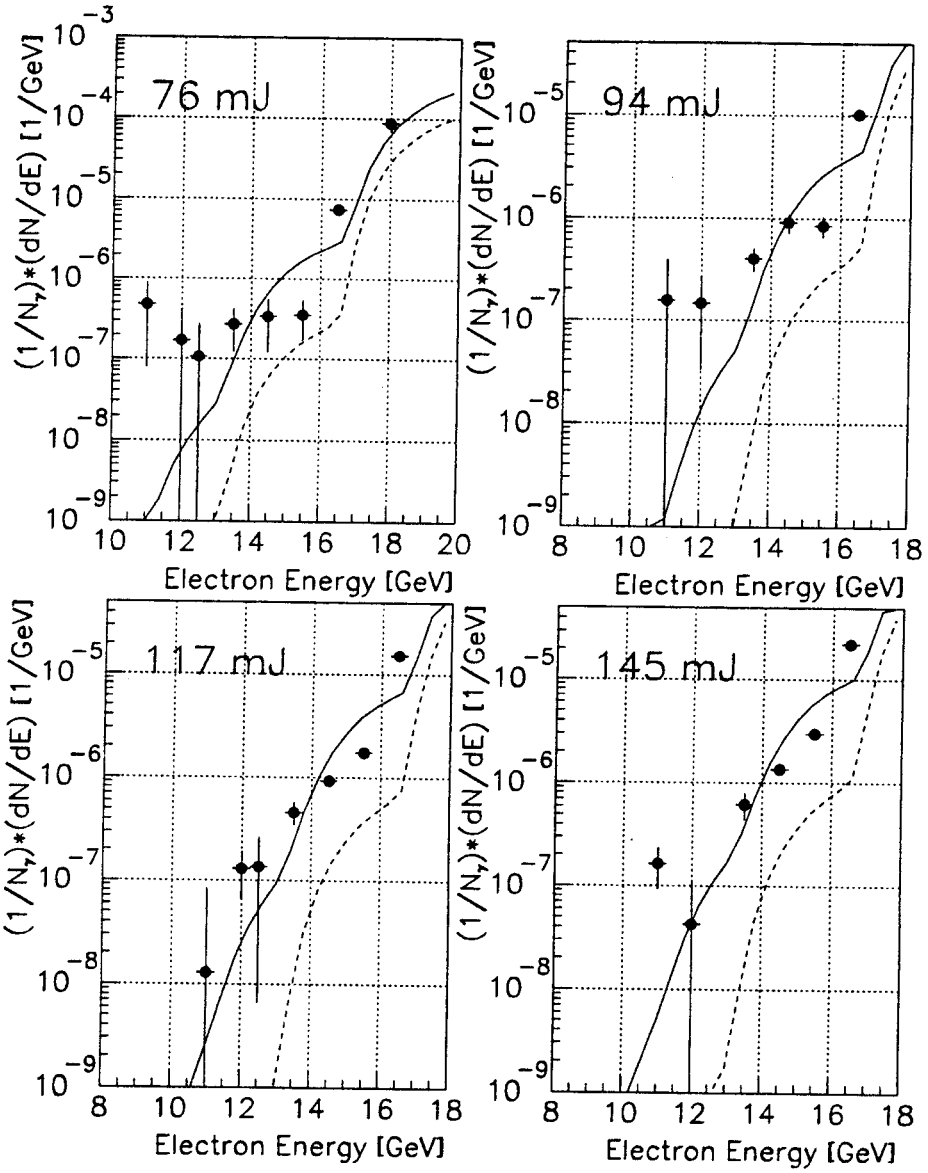

Figure 4.12: Recoil electron yield (scaled and reconstructed) vs momentum for fixed IR laser energy (cont'). The solid circles are the data, the solid line is the simulation that includes both nonlinear Compton scattering and multiple linear Compton scattering. The dashed line is the simulation for multiple linear Compton scattering only.

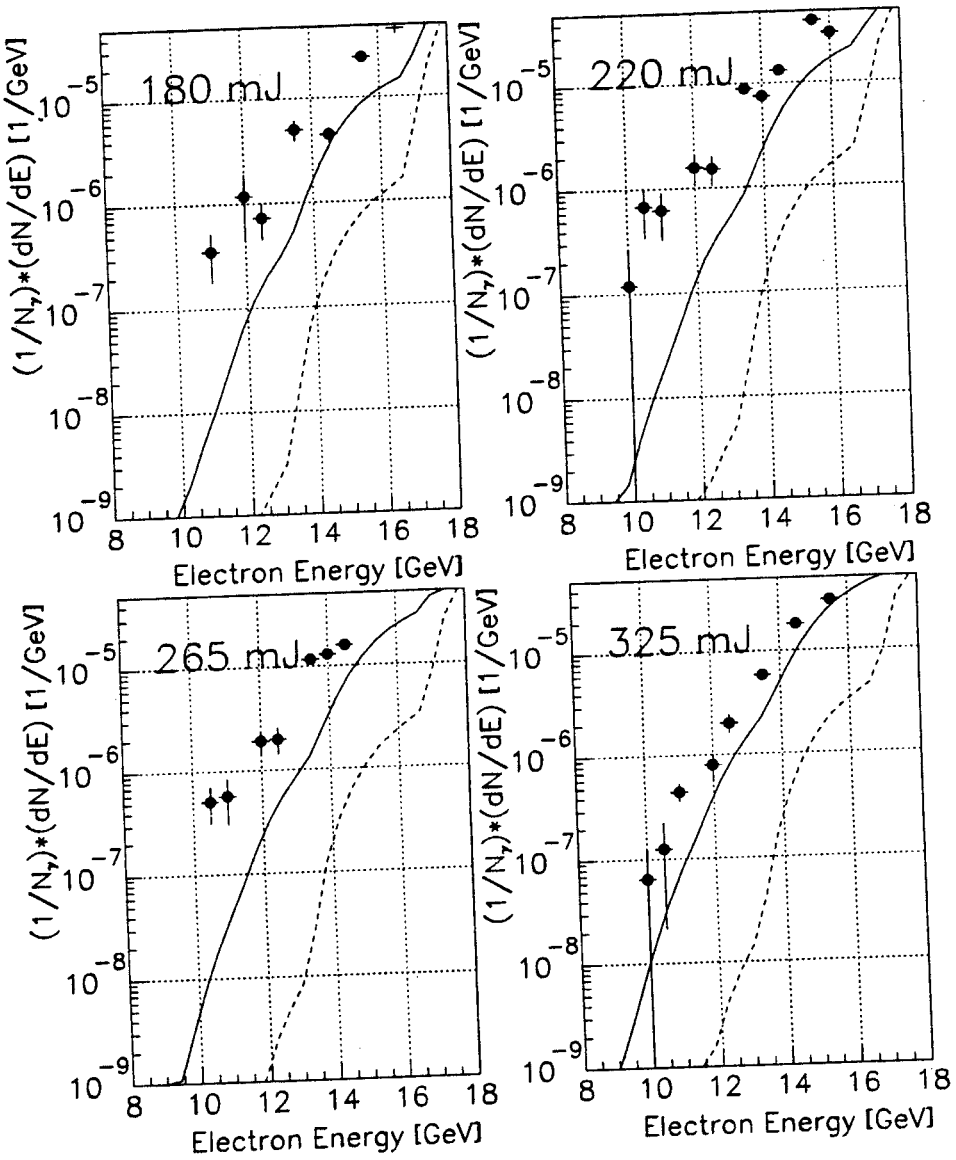

Figure 4.13: Recoil electron yield (scaled and reconstructed) vs momentum for fixed IR laser energy (cont'). The solid circles are the data, the solid line is the simulation that includes both nonlinear Compton scattering and multiple linear Compton scattering. The dashed line is the simulation for multiple linear Compton scattering only.

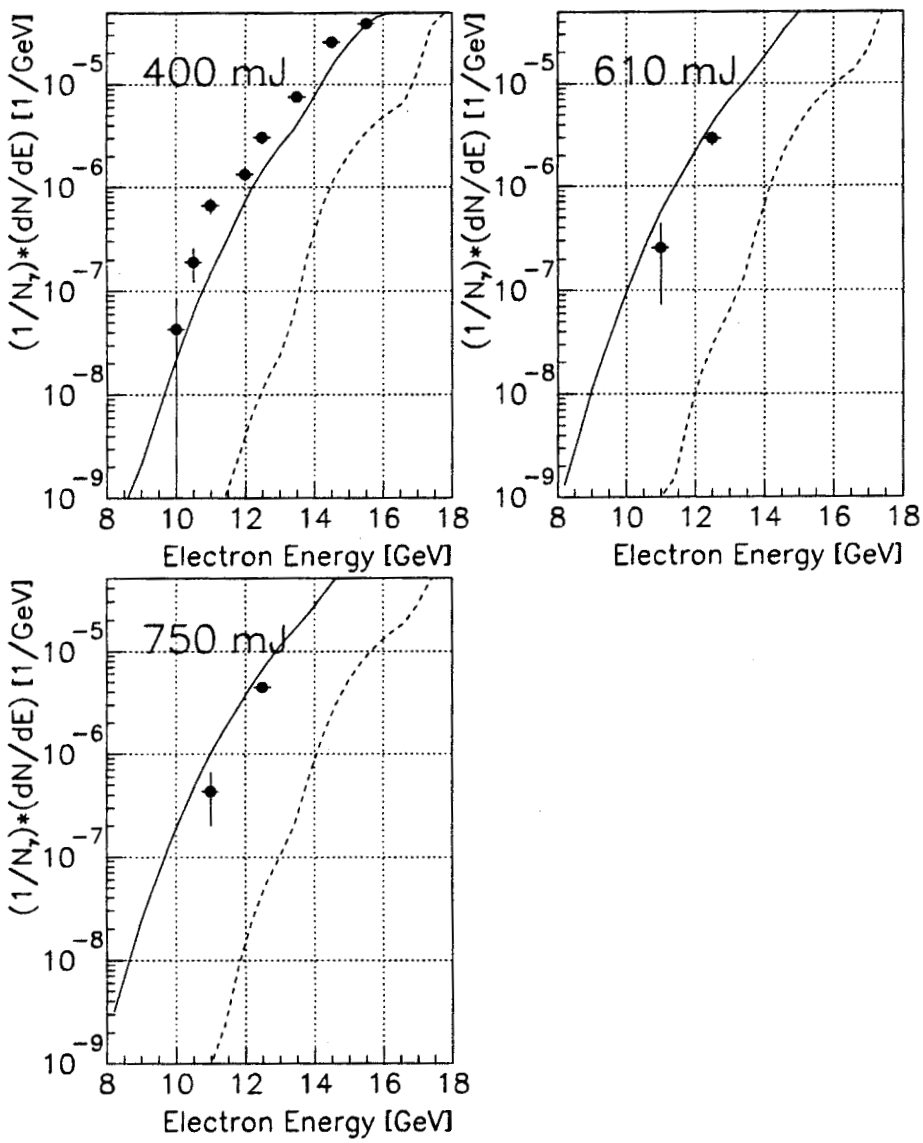

Figure 4.14: Recoil electron yield (scaled and reconstructed) vs momentum for fixed IR laser energy (cont'). The solid circles are the data, the solid line is the simulation that includes both nonlinear Compton scattering and multiple linear Compton scattering. The dashed line is the simulation for multiple linear Compton scattering only.

4.2.3 Scaled recoil electron rates as a function of laser energy for fixed recoil momenta

As described before, due to the nonlinear process the yield for events that are dominated by scattering of an electron with absorption of n photons will scale with η or equivalently with laser intensity as:

$$\frac{dN}{dp} \sim \eta^{2n} \sim I^n \tag{4.12}$$

Therefore the normalized rate will scale as:

$$\frac{1}{N_\gamma}\frac{dN}{dp} \sim \eta^{2(n-1)} \sim I^{n-1} \tag{4.13}$$

Due to the fast drop of the spectrum with recoil electron momenta, for each n a small momentum range need be defined in which the laser intensity is varied. Since data and simulation have been scaled to standard interaction volume parameters as discussed before we can view the yield as a function of laser energy instead of intensity. A log - log plot in laser energy and nonlinear yield is more suitable to view this behavior. Figures 4.15 to 4.19 shows are such plots for various momenta. The momentum range for each such plot was chosen to be 0.5 GeV. The errors on the data are as discussed above in the previous section.

If one could see the simulation line in detail then it would be clear that this line bends as the laser energy increases, since the contribution of higher order scattering increases for the same momentum bin, and as a result the power low changes its slope in the log-log plot. An attempt to choose the 'best' momenta bins and plot for these the yield vs laser energy is shown in Figure 4.39, where the increasing slope of the yield for smaller electron momenta is obvious.

A study of the log-log plots reveals that the agreement of the data with the simulation is better for the two photon process than for the higher order processes. This is due to the 'contamination' of the higher order data by the tail of the energy spectrum of all the lower orders and their combination. One more reason made clear also in the presentation of the yield as a function of momentum is that the yield observed is not reconstructed adequately and energy showering effects contaminate

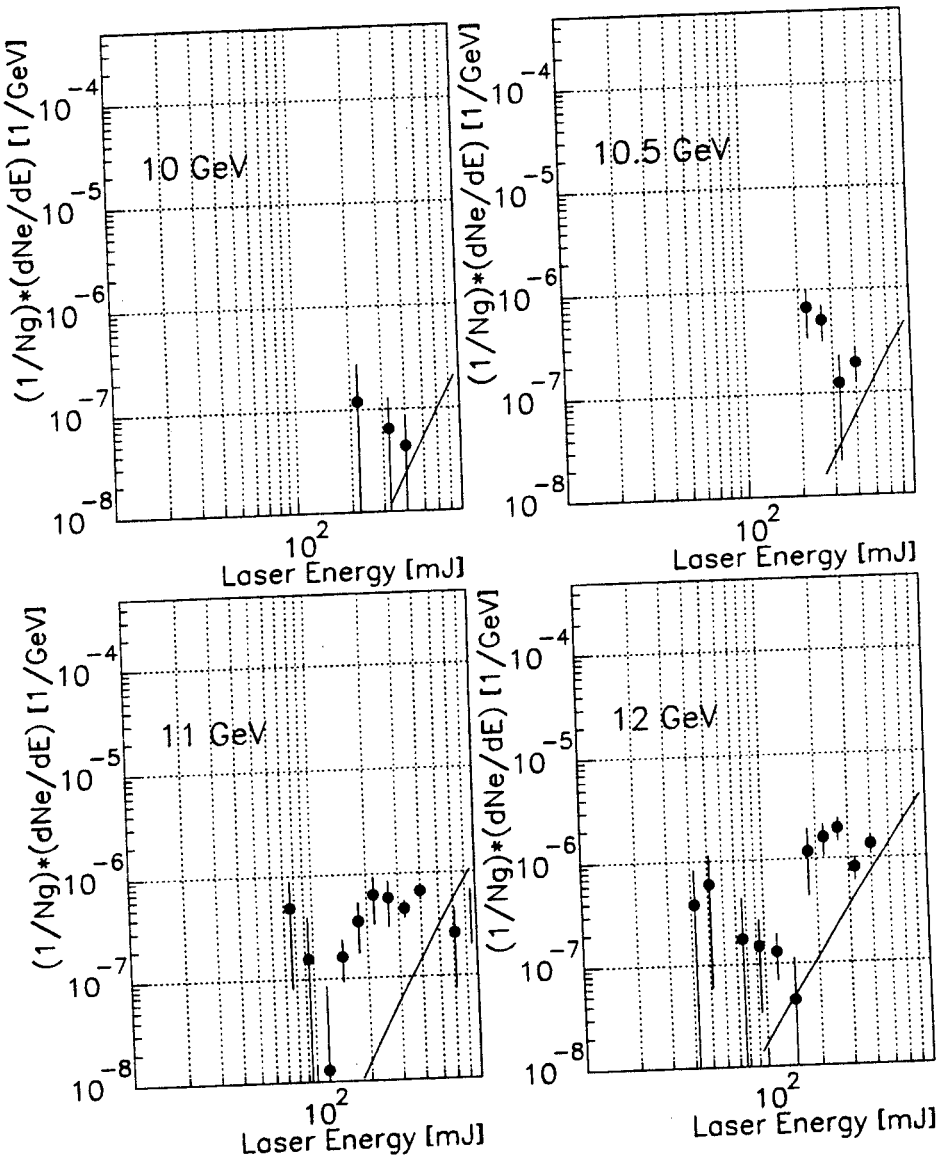

Figure 4.15: Recoil electron yield (reconstructed and scaled) vs IR laser energy for fixed momentum. The solid circles are the data and the solid line is the simulation that includes both nonlinear Compton scattering and multiple linear Compton scattering. The simulation approximates a straight line that follows the characteristic power law for the corresponding order of the nonlinear Compton scattering process.

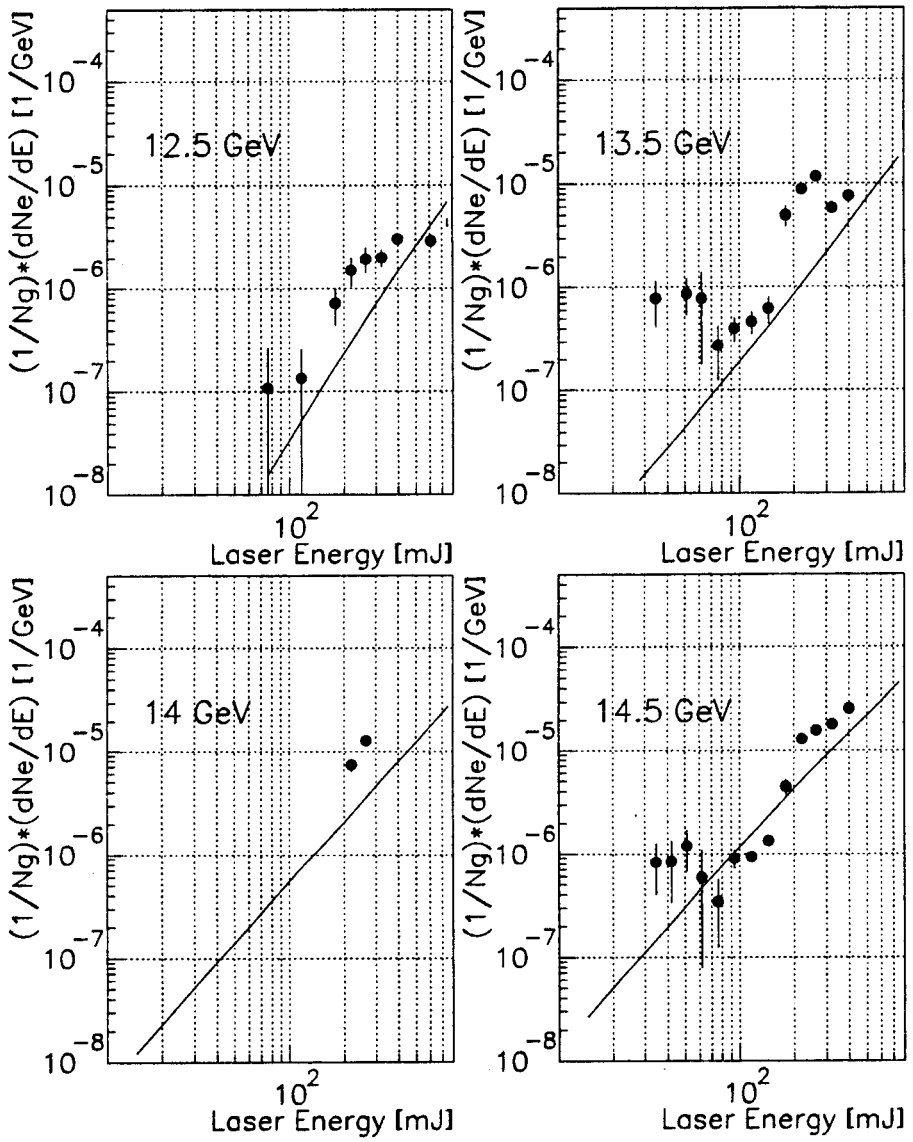

Figure 4.16: Recoil electron yield (reconstructed and scaled) vs IR laser energy for fixed momentum (cont'). The solid circles are the data and the solid line is the simulation that includes both nonlinear Compton scattering and multiple linear Compton scattering. The simulation approximates a straight line that follows the characteristic power law for the corresponding order of the nonlinear Compton scattering process.

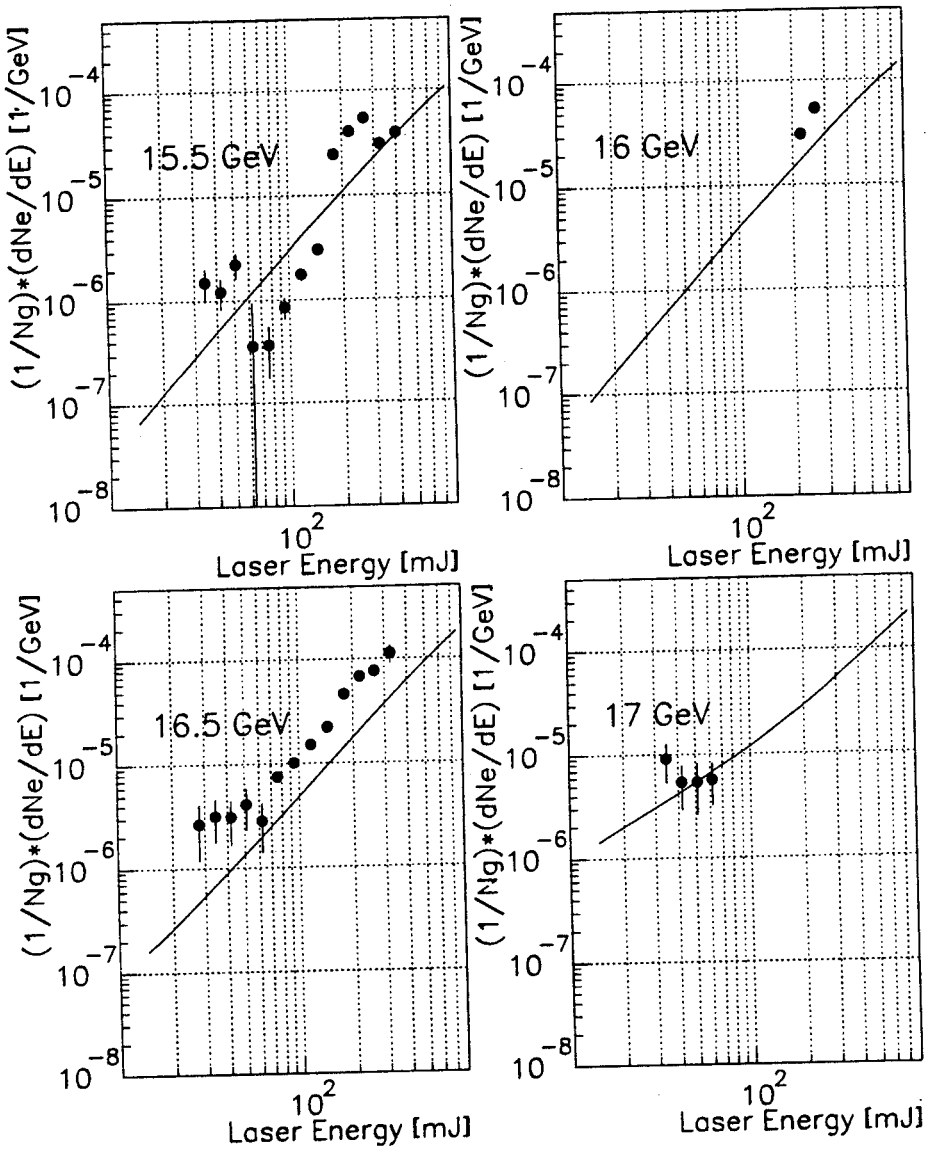

Figure 4.17: Recoil electron yield (reconstructed and scaled) vs IR laser energy for fixed momentum (cont'). The solid circles are the data and the solid line is the simulation that includes both nonlinear Compton scattering and multiple linear Compton scattering. The simulation approximates a straight line that follows the characteristic power law for the corresponding order of the nonlinear Compton scattering process.

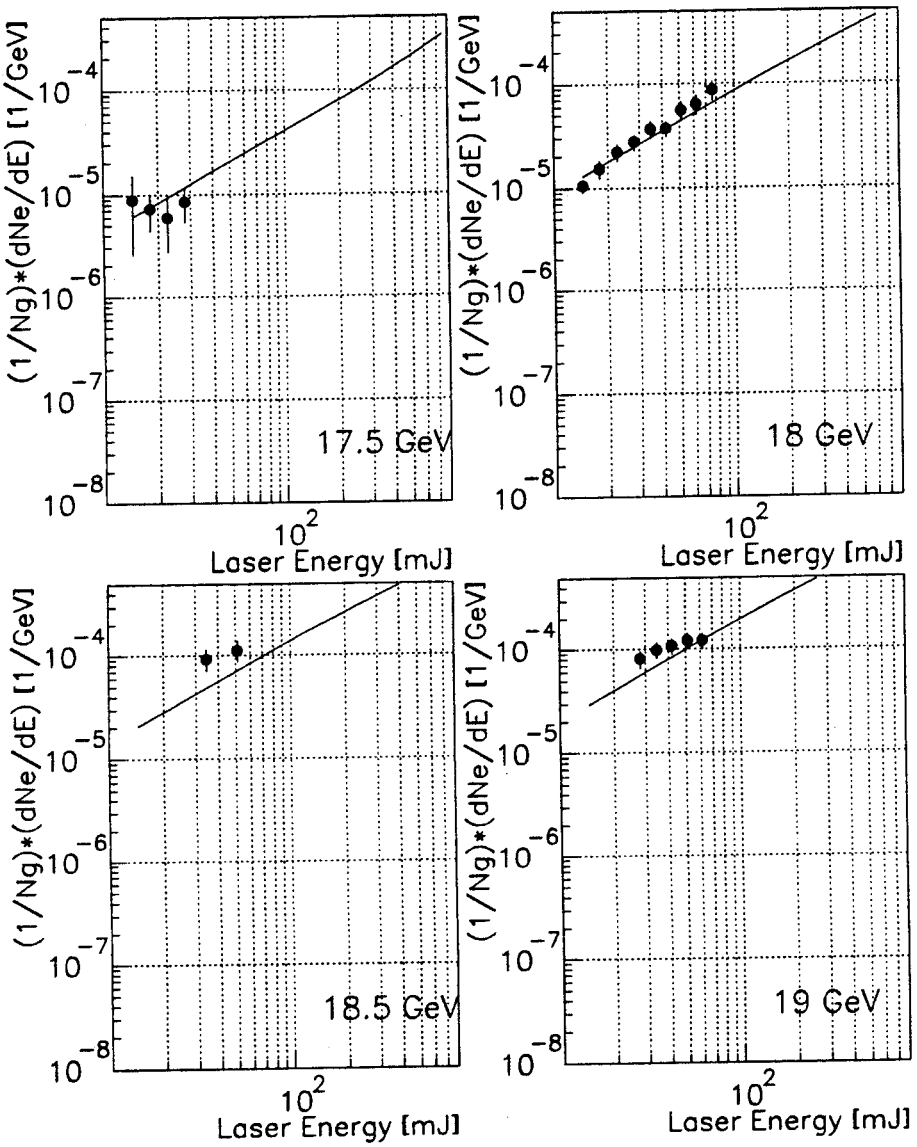

Figure 4.18: Recoil electron yield (reconstructed and scaled) vs IR laser energy for fixed momentum (cont'). The solid circles are the data and the solid line is the simulation that includes both nonlinear Compton scattering and multiple linear Compton scattering. The simulation approximates a straight line that follows the characteristic power law for the corresponding order of the nonlinear Compton scattering process.

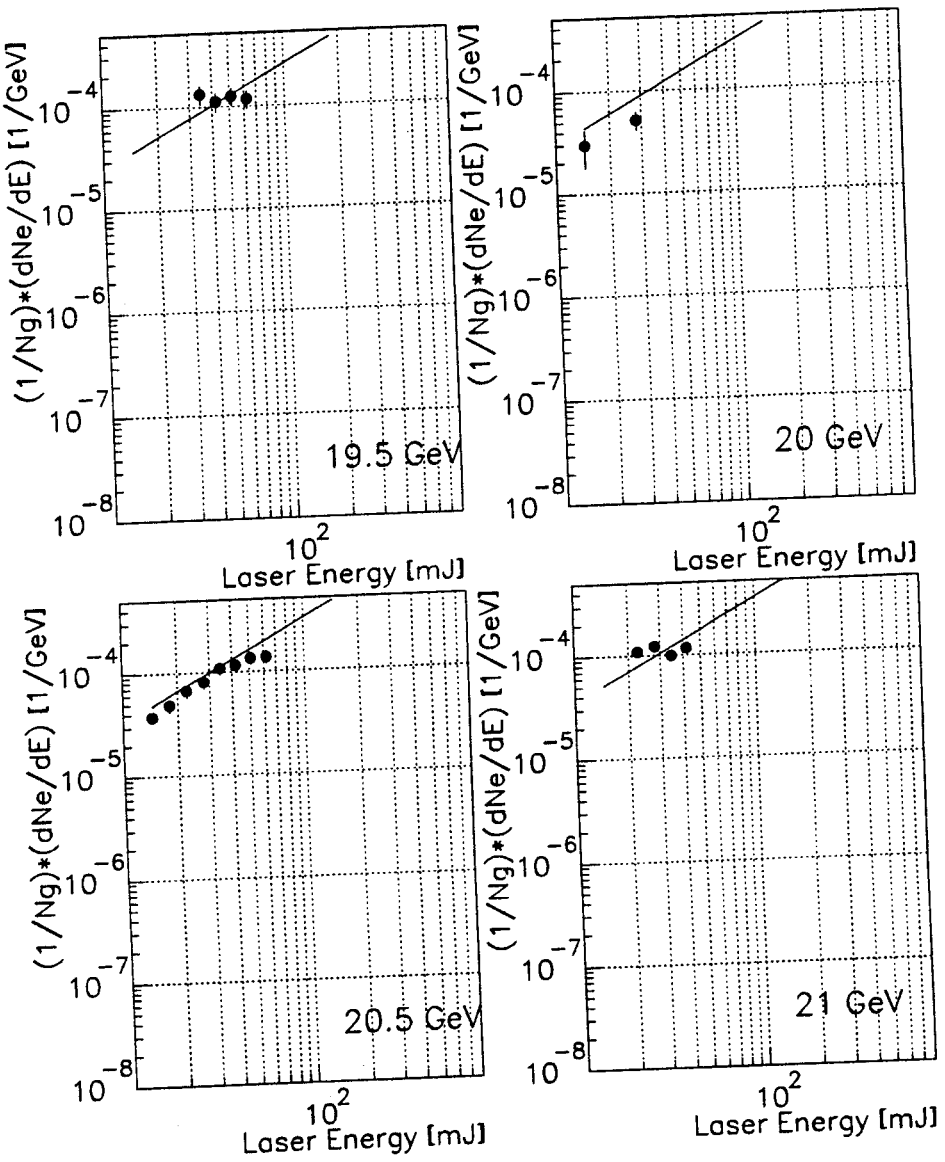

Figure 4.19: Recoil electron yield (reconstructed and scaled) vs IR laser energy for fixed momentum (cont'). The solid circles are the data and the solid line is the simulation that includes both nonlinear Compton scattering and multiple linear Compton scattering. The simulation approximates a straight line that follows the characteristic power law for the corresponding order of the nonlinear Compton scattering process.

4.3 Nonlinear Compton scattering results for green, circularly polarized laser light

4.3.1 Energy spectra of recoil electrons

The results for nonlinear Compton scattering of electrons from green laser light are presented the same way as the IR data. First we show the 'unreconstructed' data. Now the simulation is done for 1.9 ps laser pulse-width, 5 times diffraction limited focal spot area for laser energies up to 200 mJ and 6 times diffraction limited for higher laser energies due to some degradation in the laser focal spot as discussed in the data analysis chapter.

This method produced the plots in Figures 4.20 and 4.21 for the electron yield vs momentum and Figure 4.22 for the dependence of the yield on the laser energy. Unless mentioned otherwise the ECAL signal has been reconstructed as discussed before.

In these Figures we can see the shift of the nonlinear Compton scattering energy spectrum to lower electron energies in the green compared to IR shown before. At the highest laser energies the ECAL was positioned in order to detect electrons with energies as low as 7 GeV.

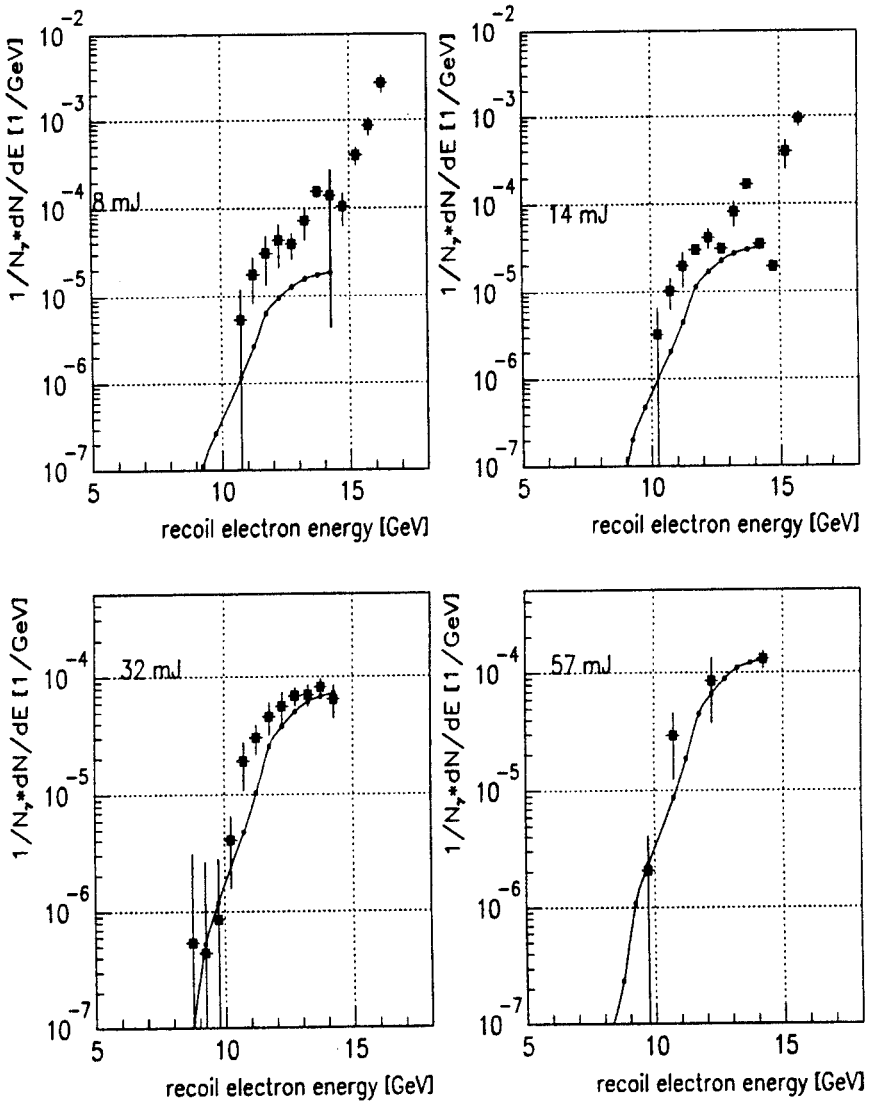

Figure 4.20: Recoil electron yield (unreconstructed) vs momentum for fixed green laser energy. The large, solid squares are the data points while the line connects the simulation points (small solid dots). The errors on the data represent the statistical error of the electron yield distribution for each laser energy - electron momentum bin.

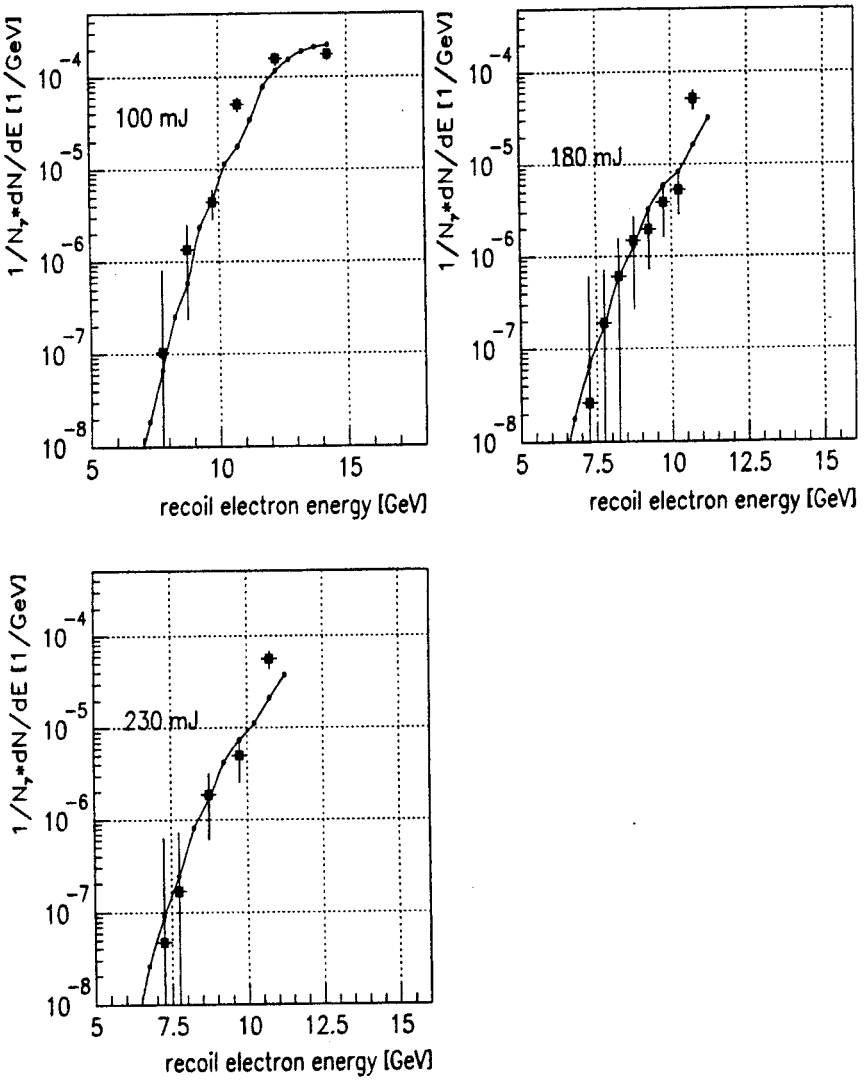

Figure 4.21: Recoil electron yield (unreconstructed) vs momentum for fixed green laser energy (cont'). The large, solid squares are the data points while the line connects the simulation points (small solid dots). The errors on the data represent the statistical error of the electron yield distribution for each laser energy - electron momentum bin.

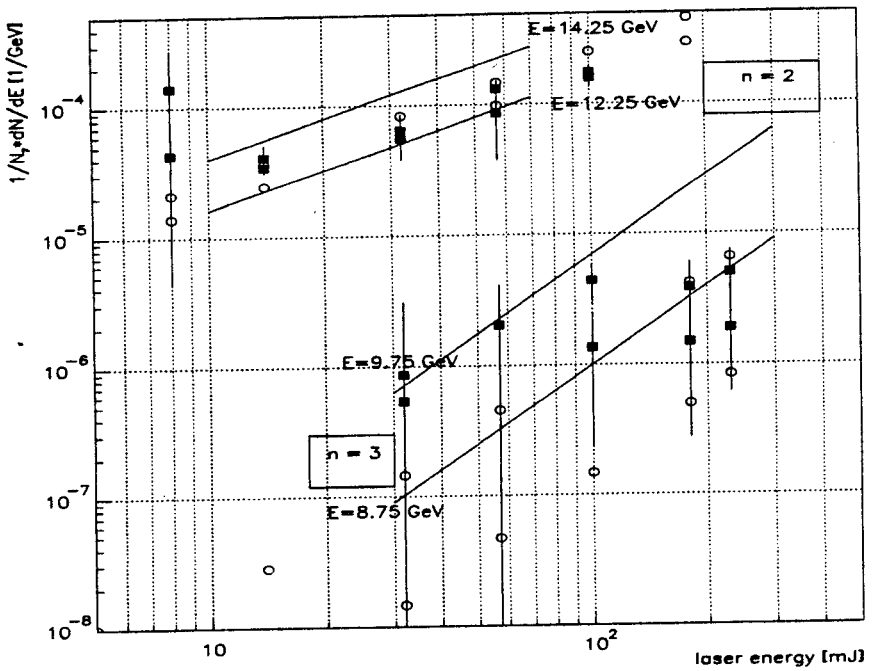

Figure 4.22: Recoil electron yield (unreconstructed) vs green laser energy for representative momentum bands. The solid squares are the data and the open circles the simulation. The straight lines represent the theoretical power low expected for each order of the nonlinear Compton scattering. The error bars reflect the statistical uncertainty on the data.

Similar to the IR case, Figures 4.23 - 4.26 show the electron yield as a function of momentum for various laser energies at green wavelength for reconstructed data using the methods described before. These data have not been scaled. The errors on them are as described for the IR study. Also the same data after scaling is shown in Figures 4.28 - 4.31.

The most convincing data for an n=3 process in the green data is shown in the 180 and 220 mJ data and especially Figures 4.31 and 4.32. The clear plateau from about 10.5 GeV to 8.5 GeV coincides with the theoretical prediction of the n=3 and n=4 kinematic edges. Most of these data were collected by ECAL scans which mapped the details of the kinematic edges in $\simeq$0.1 GeV resolution (1 mm ECAL position steps).

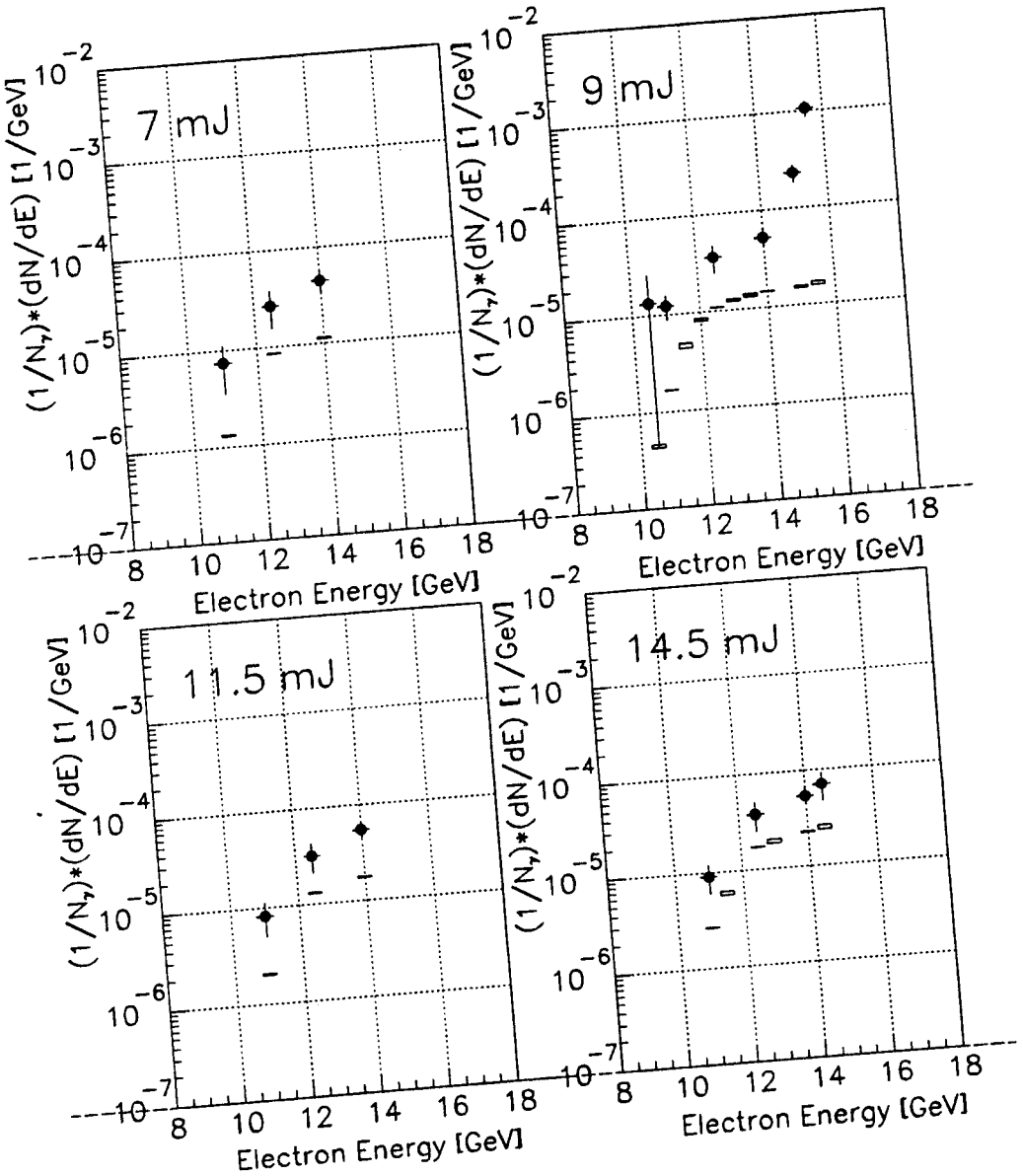

Figure 4.23: Recoil electron yield (reconstructed) vs momentum for fixed green laser energy. The data are represented with solid circles with horizontal error bars corresponding to the ECAL row width and vertical error bars corresponding to statistical uncertainties and systematic due to the two methods used for signal reconstruction . The open boxes are the simulation where the vertical and horizontal heights are the magnitude of the error bars.

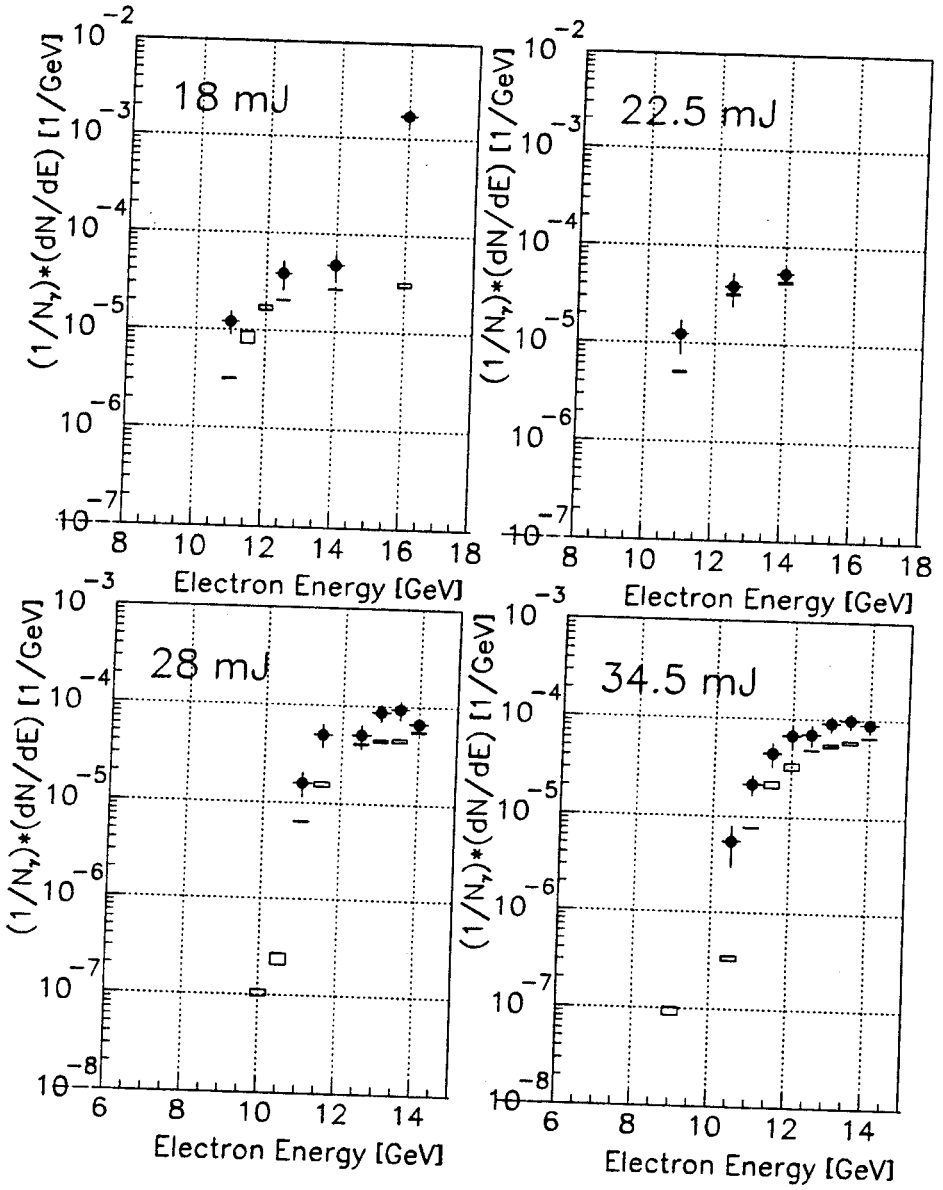

Figure 4.24: Recoil electron yield (reconstructed) vs momentum for fixed green laser energy (cont'). The data are represented with solid circles with horizontal error bars corresponding to the ECAL row width and vertical error bars corresponding to statistical uncertainties and systematic due to the two methods used for signal reconstruction . The open boxes are the simulation where the vertical and horizontal heights are the magnitude of the error bars.

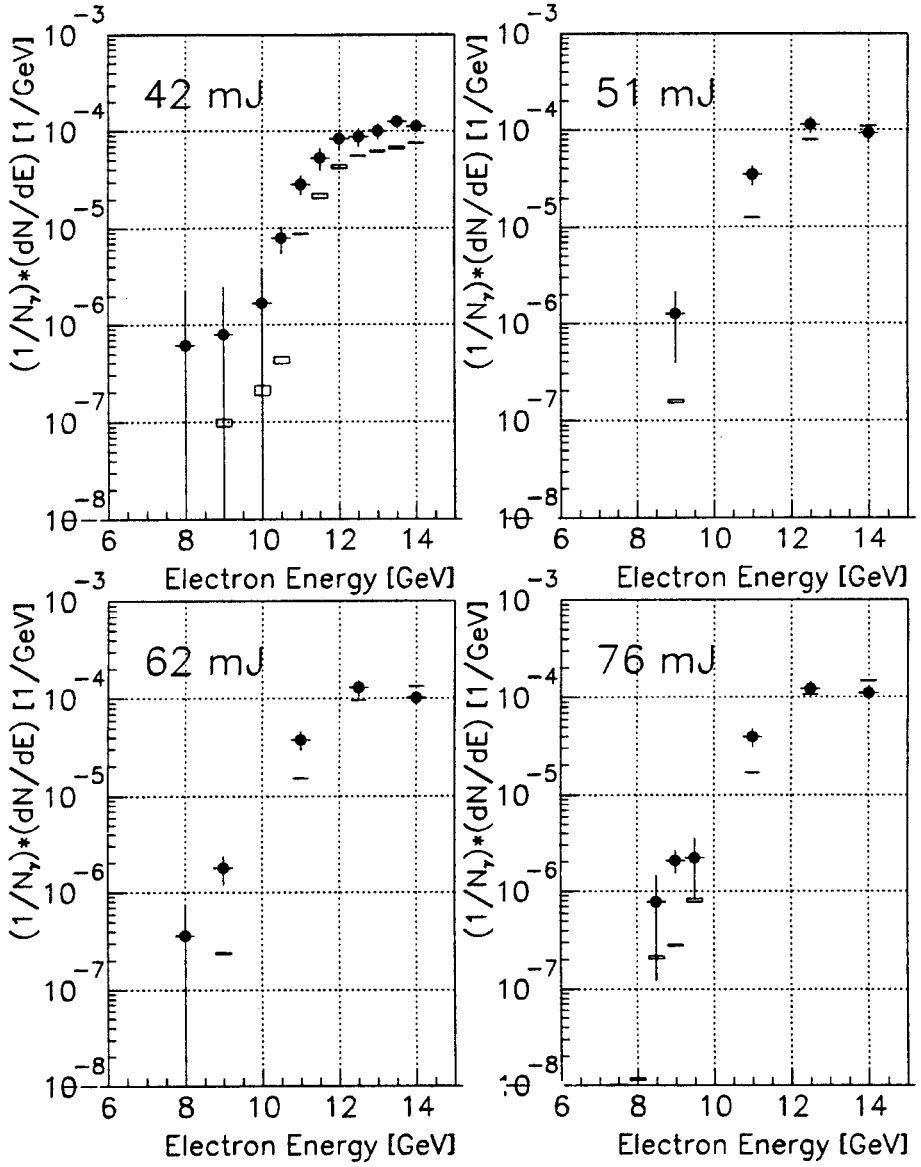

Figure 4.25: Recoil electron yield (reconstructed) vs momentum for fixed green laser energy (cont'). The data are represented with solid circles with horizontal error bars corresponding to the ECAL row width and vertical error bars corresponding to statistical uncertainties and systematic due to the two methods used for signal reconstruction . The open boxes are the simulation where the vertical and horizontal heights are the magnitude of the error bars.

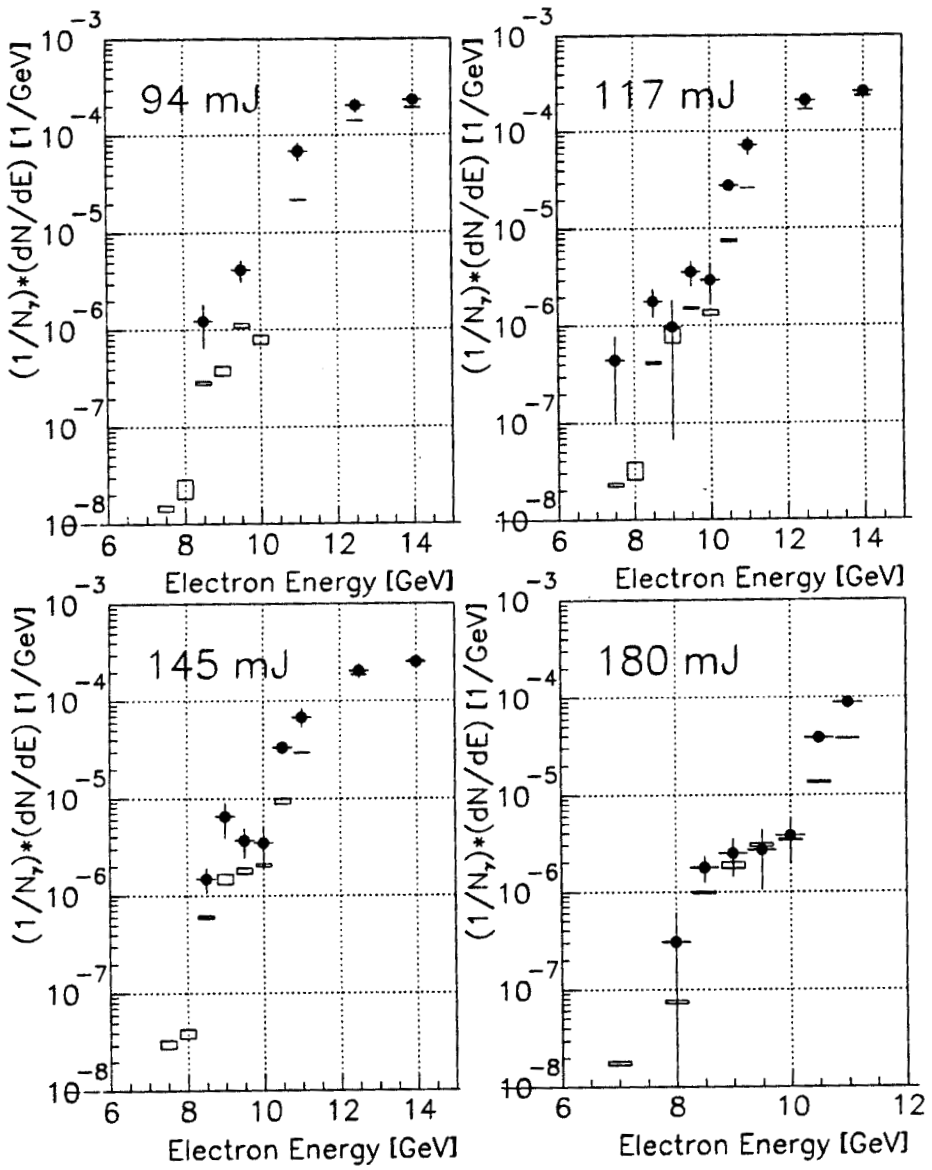

Figure 4.26: Recoil electron yield (reconstructed) vs momentum for fixed green laser energy (cont'). The data are represented with solid circles with horizontal error bars corresponding to the ECAL row width and vertical error bars corresponding to statistical uncertainties and systematic due to the two methods used for signal reconstruction. The open boxes are the simulation where the vertical and horizontal heights are the magnitude of the error bars.

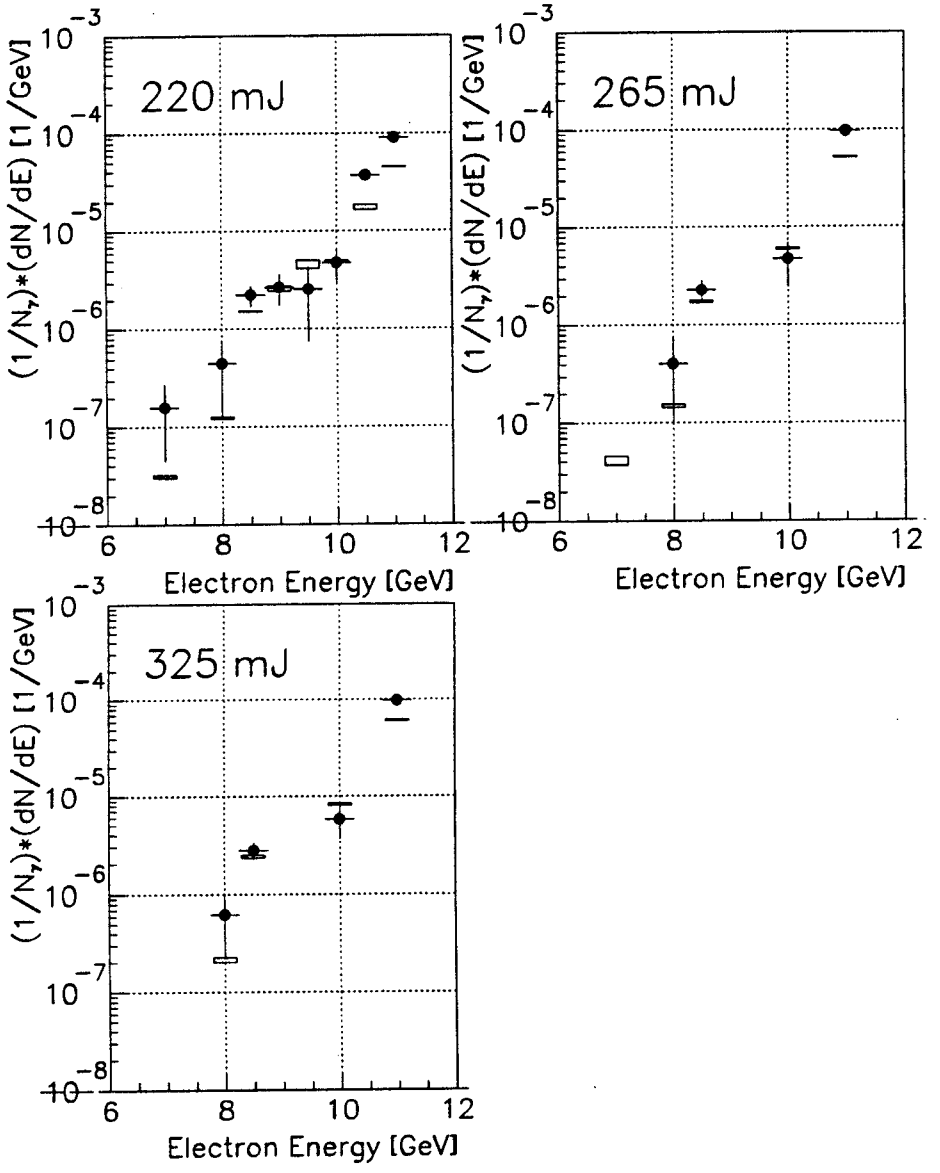

Figure 4.27: Recoil electron yield (reconstructed) vs momentum for fixed green laser energy (cont'). The data are represented with solid circles with horizontal error bars corresponding to the ECAL row width and vertical error bars corresponding to statistical uncertainties and systematic due to the two methods used for signal reconstruction . The open boxes are the simulation where the vertical and horizontal heights are the magnitude of the error bars.

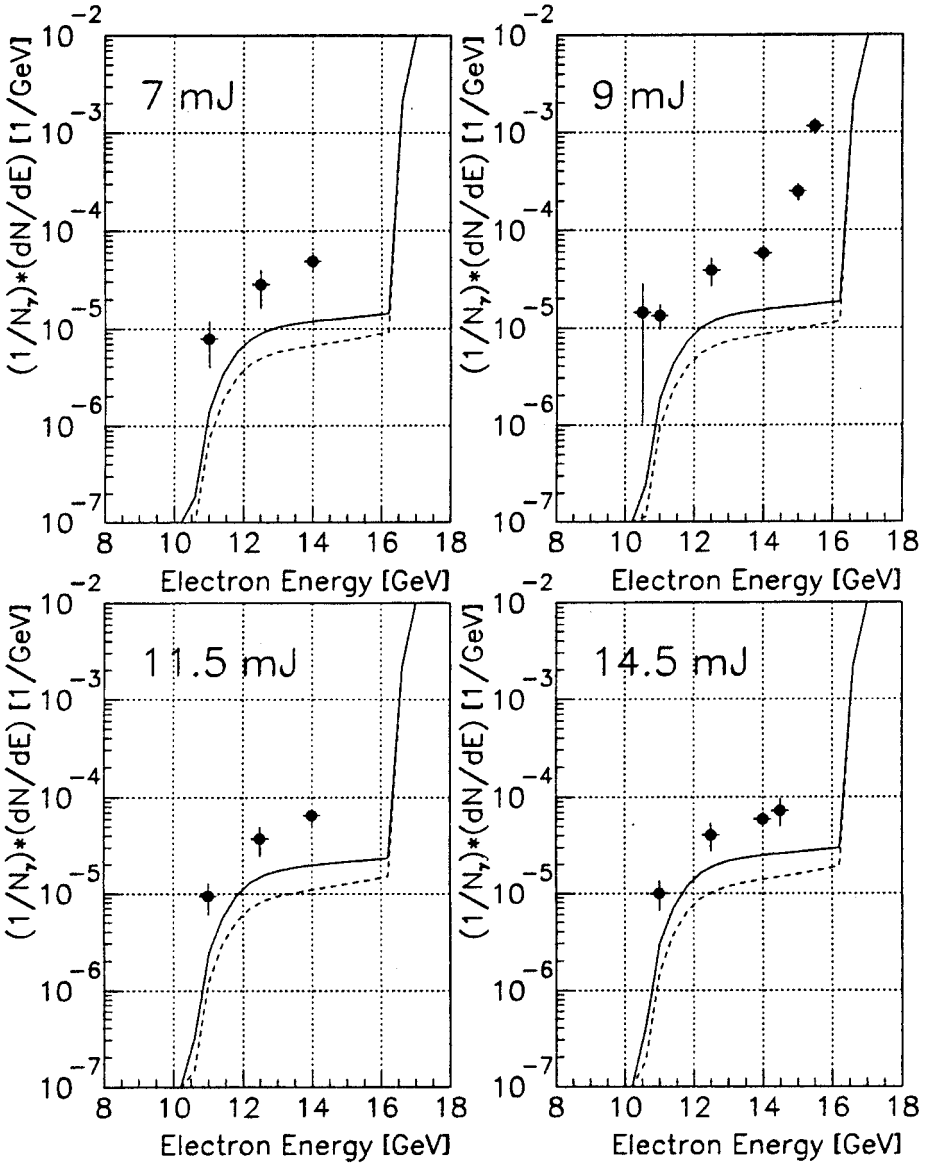

Figure 4.28: Recoil electron yield (reconstructed and scaled) vs momentum for fixed green laser energy. The solid circles are the data, the solid line is the simulation that includes both nonlinear Compton scattering and multiple linear Compton scattering. The dashed line is the simulation for multiple linear Compton scattering only.

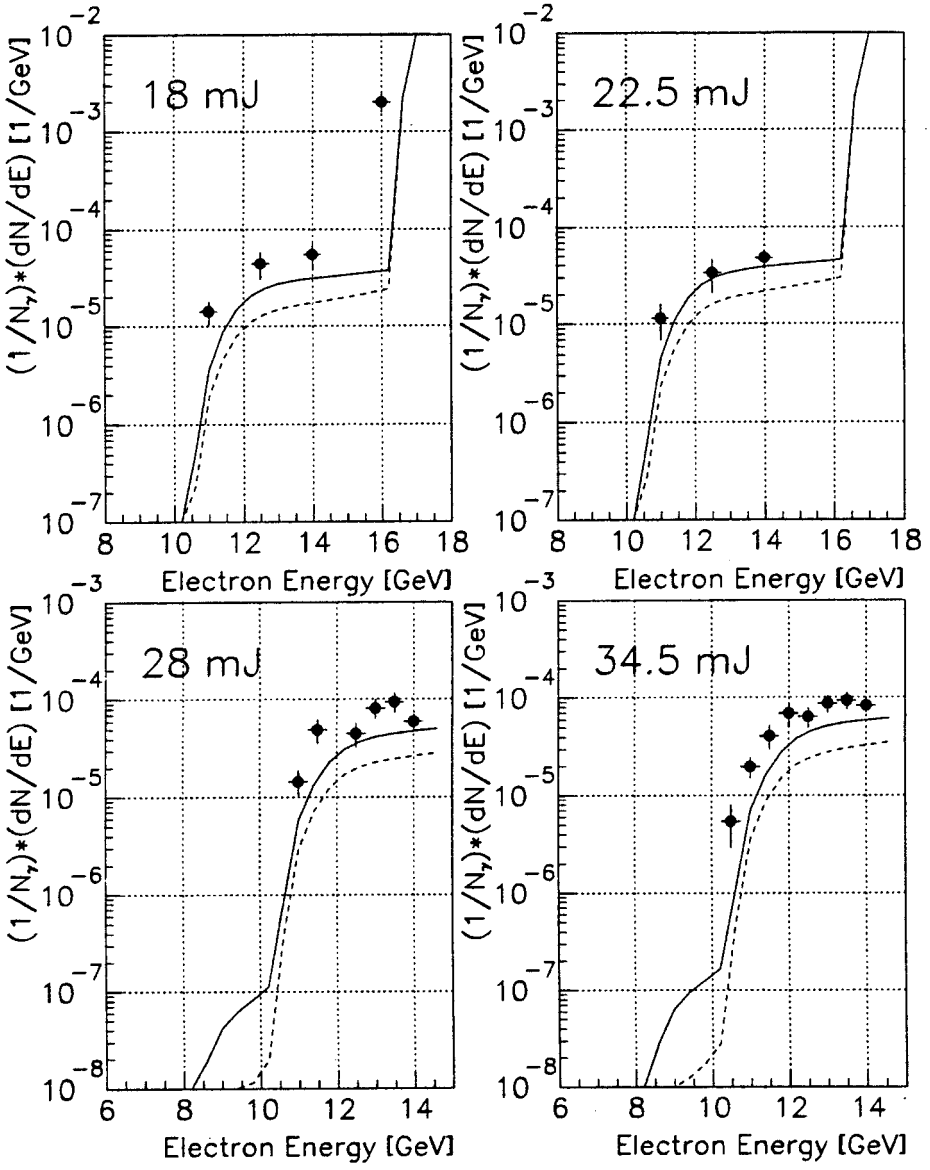

Figure 4.29: Recoil electron yield (reconstructed and scaled) vs momentum for fixed green laser energy (cont'). The solid circles are the data, the solid line is the simulation that includes both nonlinear Compton scattering and multiple linear Compton scattering. The dashed line is the simulation for multiple linear Compton scattering only.

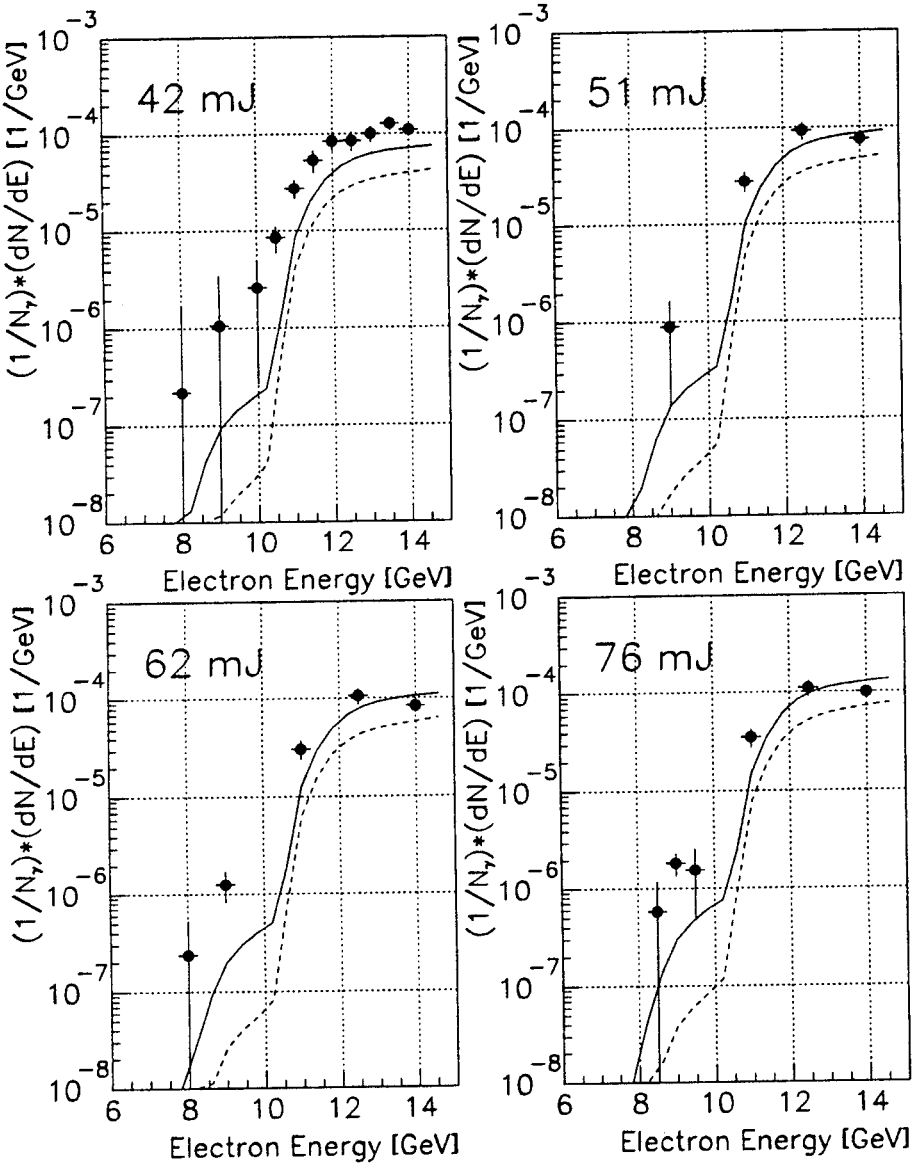

Figure 4.30: Recoil electron yield (reconstructed and scaled) vs momentum for fixed green laser energy (cont'). The solid circles are the data, the solid line is the simulation that includes both nonlinear Compton scattering and multiple linear Compton scattering. The dashed line is the simulation for multiple linear Compton scattering only.

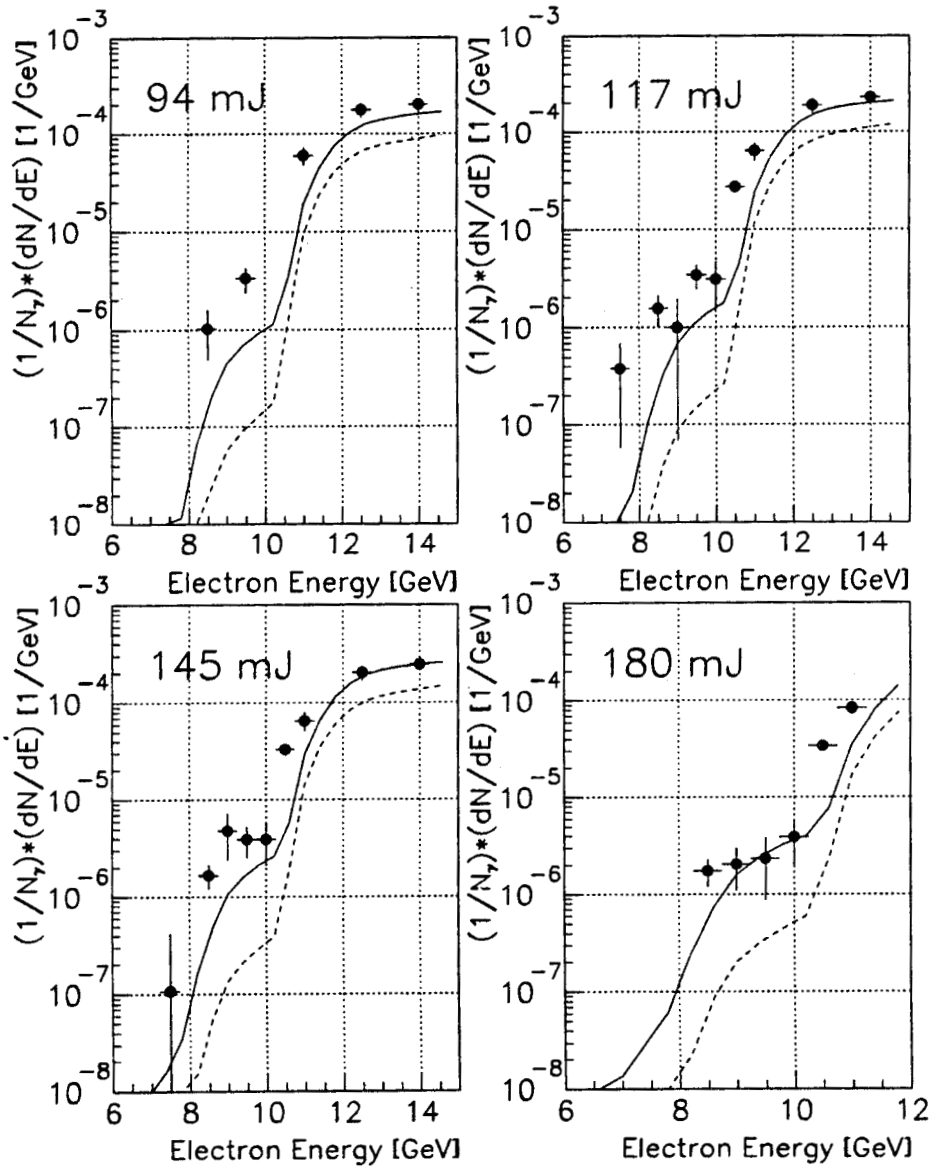

Figure 4.31: Recoil electron yield (reconstructed and scaled) vs momentum for fixed green laser energy (cont'). The solid circles are the data, the solid line is the simulation that includes both nonlinear Compton scattering and multiple linear Compton scattering. The dashed line is the simulation for multiple linear Compton scattering only.

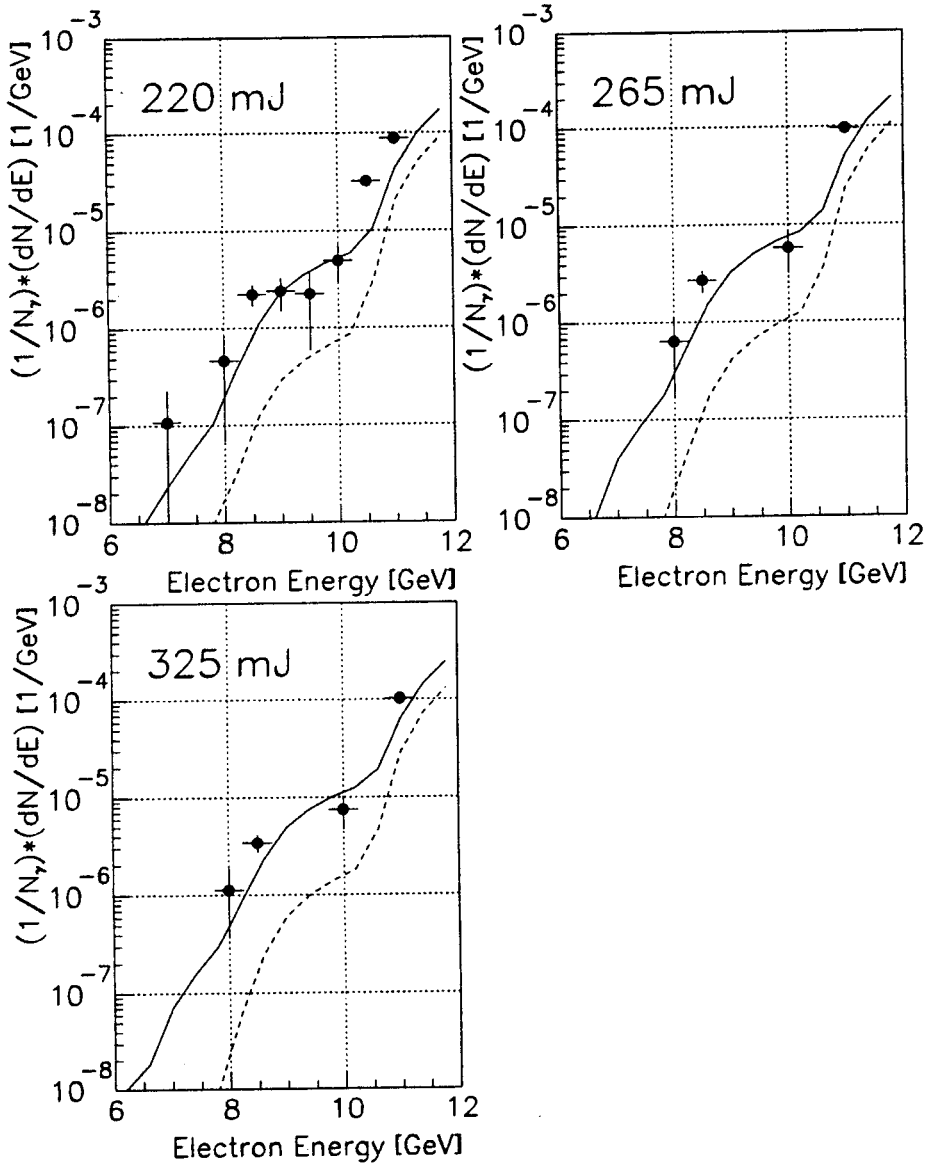

Figure 4.32: Recoil electron yield (reconstructed and scaled) vs momentum for fixed green laser energy (cont'). The solid circles are the data, the solid line is the simulation that includes both nonlinear Compton scattering and multiple linear Compton scattering. The dashed line is the simulation for multiple linear Compton scattering only.

4.3.2 Scaled recoil electron rates as a function of laser energy for fixed recoil momenta.

The recoil electron yield for the green wavelength is scaled to the standard interaction parameters and presented as a function of the laser energy in Figs. 4.33 to 4.36. These 'power low' plots deviate from the simulation more than the IR due to the fact that the kinematic edges for higher order nonlinear Compton scattering are denser in the momentum space for green than from IR and due to the uncertainty in laser intensity.

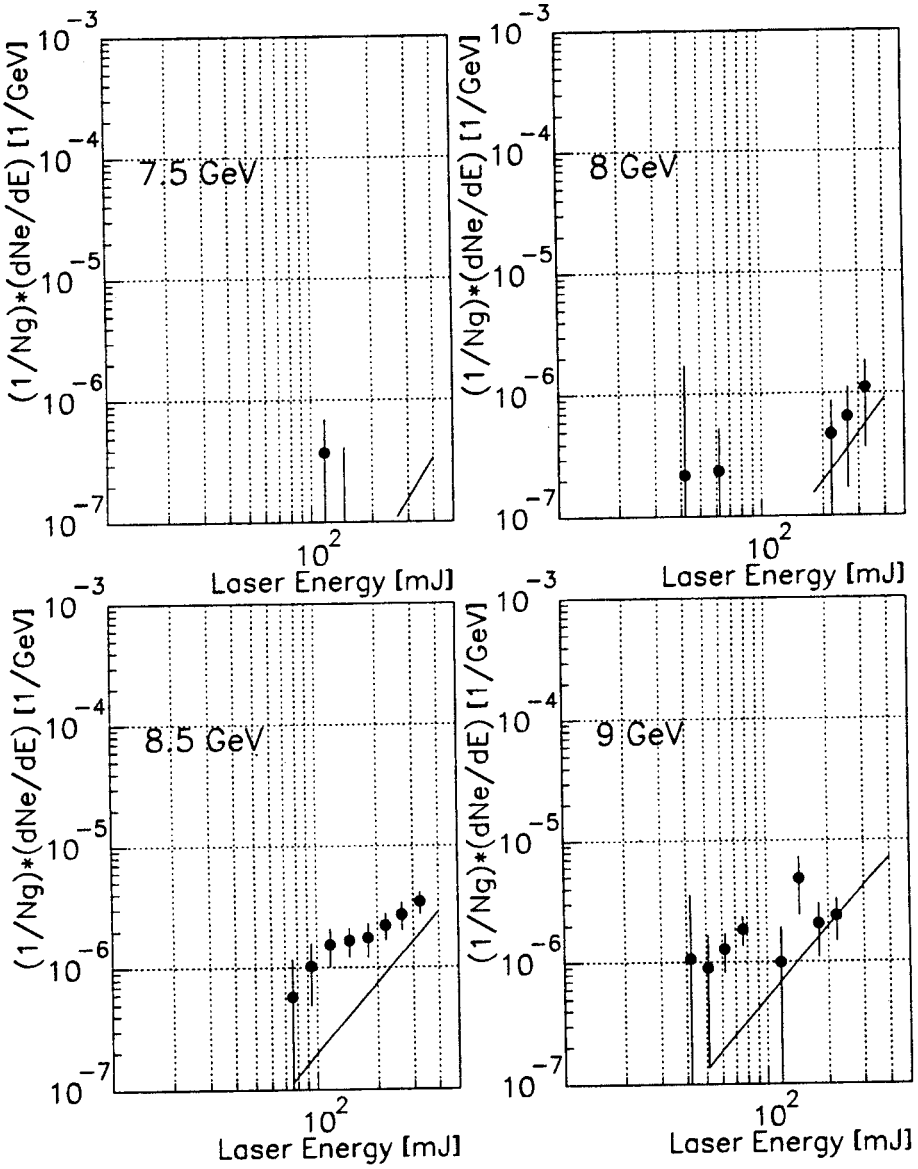

Figure 4.33: Recoil electron yield (reconstructed and scaled) vs green laser energy for fixed momentum. The solid circles are the data and the solid line is the simulation that includes both nonlinear Compton scattering and multiple linear Compton scattering. The simulation approximates a straight line that follows the characteristic power law for the corresponding order of the nonlinear Compton scattering process.

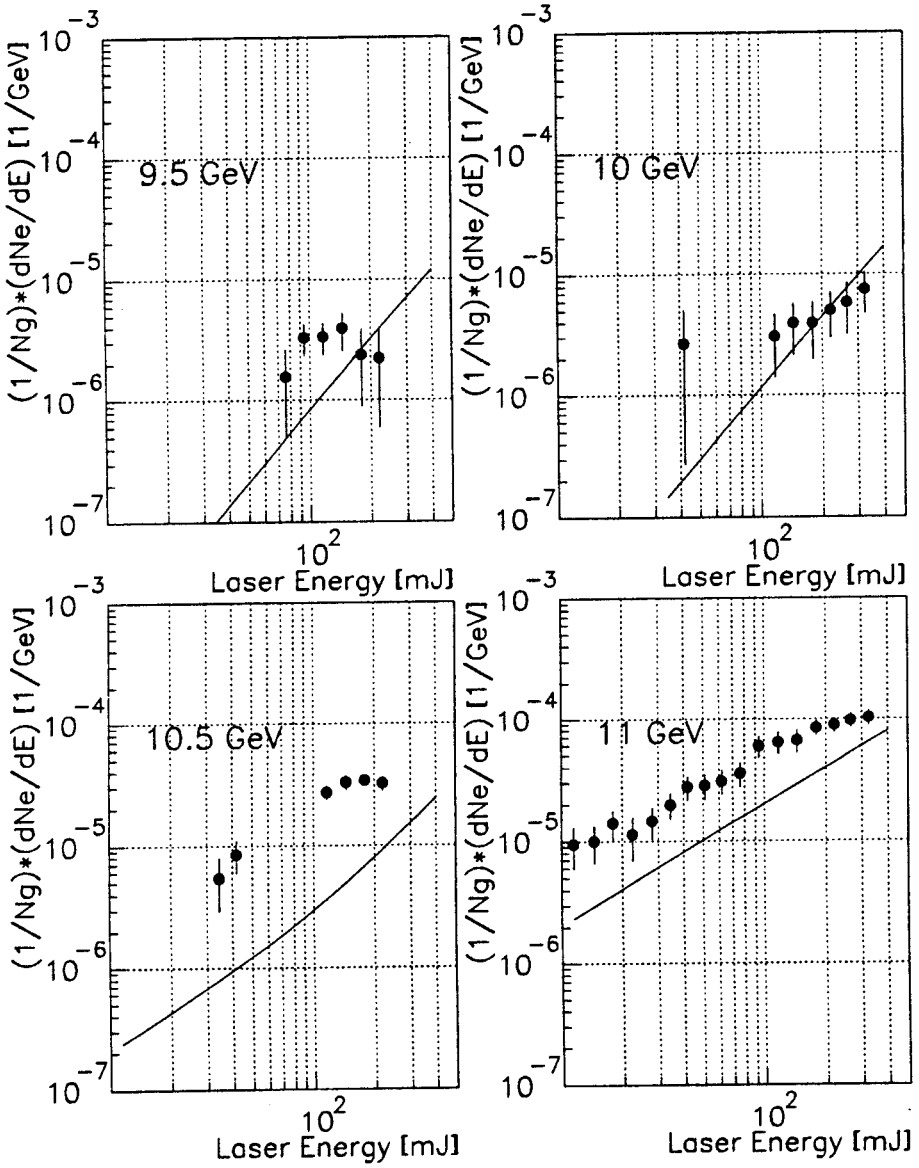

Figure 4.34: Recoil electron yield (reconstructed and scaled) vs green laser energy for fixed momentum (cont'). The solid circles are the data and the solid line is the simulation that includes both nonlinear Compton scattering and multiple linear Compton scattering. The simulation approximates a straight line that follows the characteristic power law for the corresponding order of the nonlinear Compton scattering process.

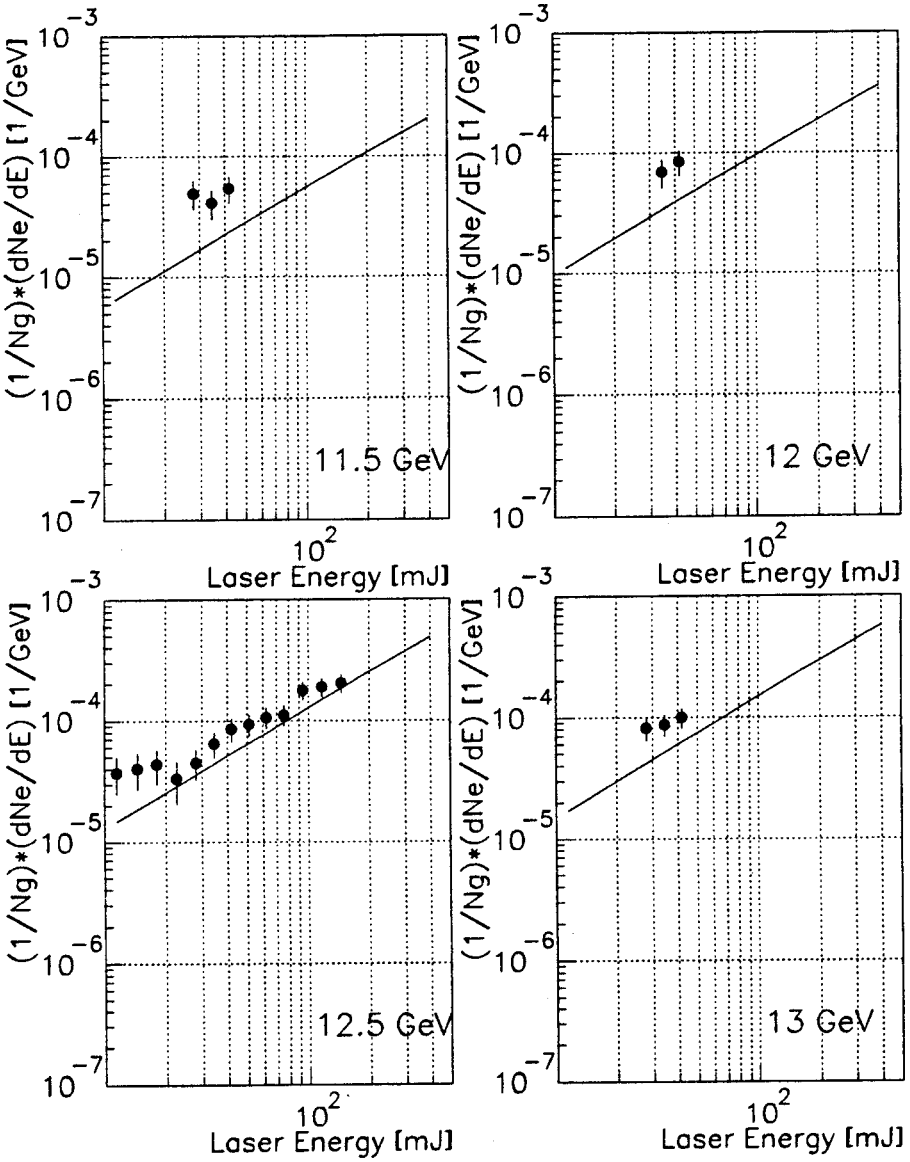

Figure 4.35: Recoil electron yield (reconstructed and scaled) vs green laser energy for fixed momentum (cont'). The solid circles are the data and the solid line is the simulation that includes both nonlinear Compton scattering and multiple linear Compton scattering. The simulation approximates a straight line that follows the characteristic power law for the corresponding order of the nonlinear Compton scattering process.

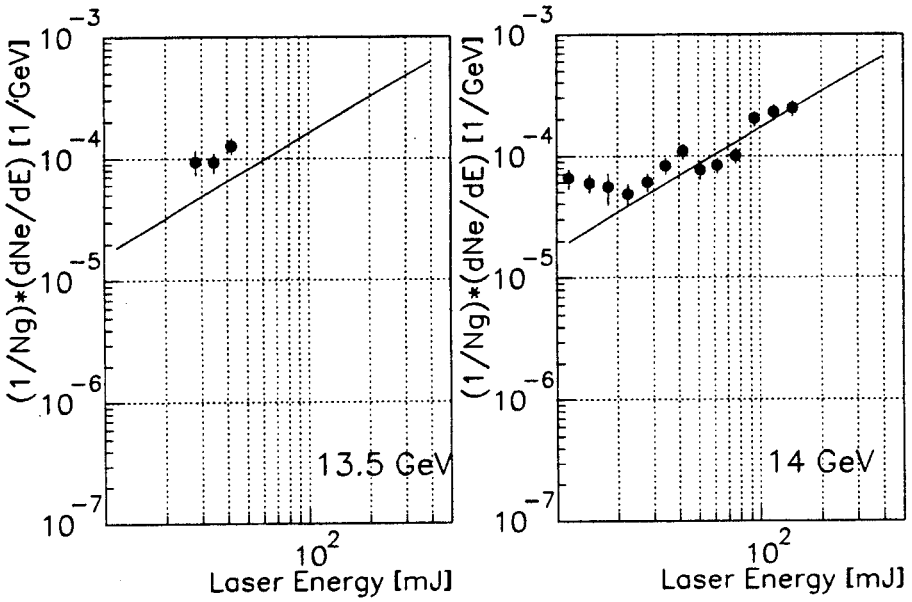

Figure 4.36: Recoil electron yield (reconstructed and scaled) vs green laser energy for fixed momentum (cont'). The solid circles are the data and the solid line is the simulation that includes both nonlinear Compton scattering and multiple linear Compton scattering. The simulation approximates a straight line that follows the characteristic power law for the corresponding order of the nonlinear Compton scattering process.

4.4 Summary of Nonlinear Compton results

From the data presented above a compilation of some of the electron momenta and laser energies leads to a comparison of all observed orders of the nonlinear Compton scattering. For the IR it is easy to see the nonlinear process in comparing the spectra of the electrons produced from 35 mJ and 400 mJ of laser energy (i.e. approximately 10 fold increase in laser energy). The kinematic edges of the spectrum are evidence for observation of up to 4 laser photon absorption in a single scatter.

This is shown in Figure 4.37 where the solid and open circles are the 42 and 400 mJ data, respectively and the solid lines are the simulations that includes both nonlinear Compton scattering and multiple linear Compton scattering for each laser

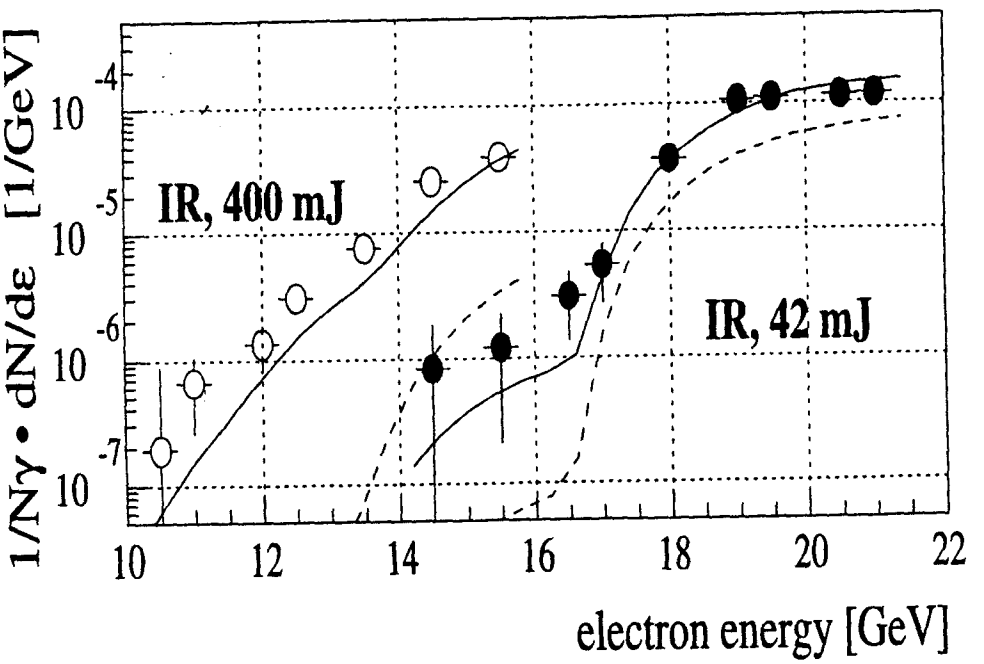

Figure 4.37: Reconstructed and scaled recoil electron yield vs momentum for 2 representative laser energies in the IR. The solid and open circles are the 42 and 400 mJ data, respectively and the solid lines are the simulations that include both nonlinear Compton scattering and multiple linear Compton scattering for each laser energy. The dashed lines are the simulations for multiple linear Compton scattering only.

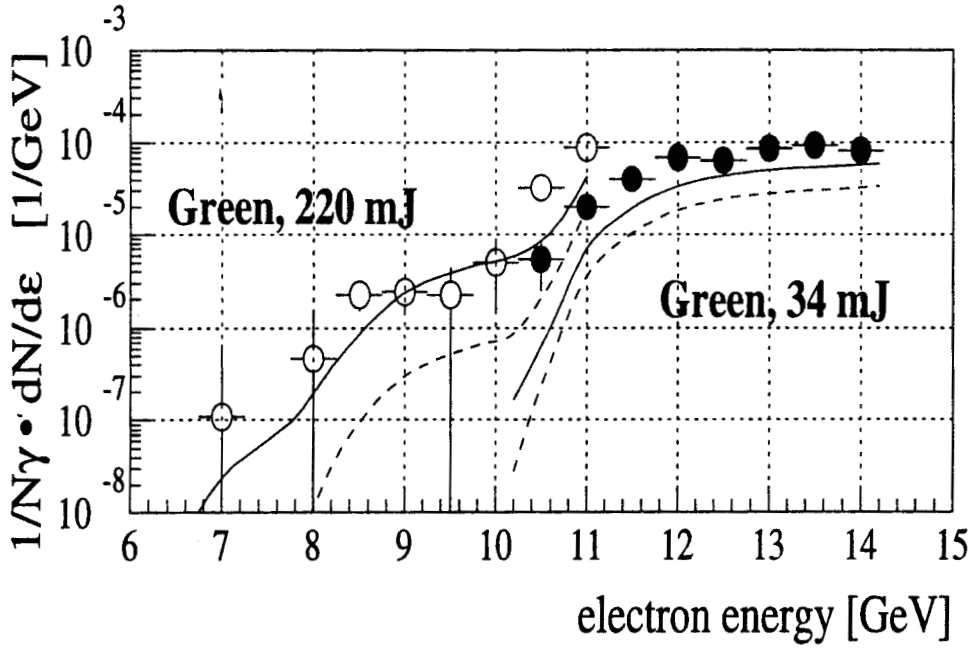

Figure 4.38: Reconstructed and scaled recoil electron yield vs momentum for 2 representative laser energies in the green. The solid and open circles are the 34 and 220 mJ data, respectively and the solid lines are the simulations that includes both nonlinear Compton scattering and multiple linear Compton scattering for each laser energy. The dashed lines are the simulations for multiple linear Compton scattering only

energy. The dashed lines are the simulations for multiple linear Compton scattering only.

The plateau at 19 - 21 GeV corresponds to two-photon scatters, and the fall off at 17-18 GeV is evidence for the two-photon kinematic limit at 17.6 GeV as smeared by the spatial resolution of ECAL. Also in the same figure the shape of the simulation and data agree for a small shoulder in the 42 mJ data which is the n=3 plateau. This agreement for n=3 is even stronger at the 400 mJ data, but the plateau is seen only as a small shoulder as expected. Only a few data points were taken in the n=4 region. But the evidence for n=4 is best in the dependence of the yield with laser intensity shown in Figure 4.39.

For green laser light a similar plot can be done but the difference is not as dramatic although it indeed shows that we observe nonlinear Compton scattering at least of the 3rd order, Figure 4.38. The n=2 plateau at the 34 mJ data and the n=3 kinematic limit at 10.9 GeV can be discerned. Evidence for the n=3 plateau can be seen in the 220 mJ data.

The same compilation can be done for representative momenta bands in order to compare the slopes of the power law of the nonlinear Compton scattering. This is shown in Figure 4.39 for the IR data. As the yields are normalized to the total Compton scattering photon signal, which is primarily linear Compton scattering, data at electron energies dominated by order n should vary with laser pulse intensity as I^{n-1}. The slopes of the four data sets in Figure 4.39 agree reasonably well with this expectation. The data also agree with the simulated yields within the 30% uncertainty in the laser intensity and 10% uncertainty in the measurement of the gammas shown as a band for each electron energy. The signals for the n=2 and 3 processes are strong and for laser intensities above 2×10^{17} W/cm^2 there is good evidence for the n=4 channel.

Figure 4.40 is the same plot for the green data. The larger experimental uncertainties in this case reflect lower statistics and a larger background subtraction.

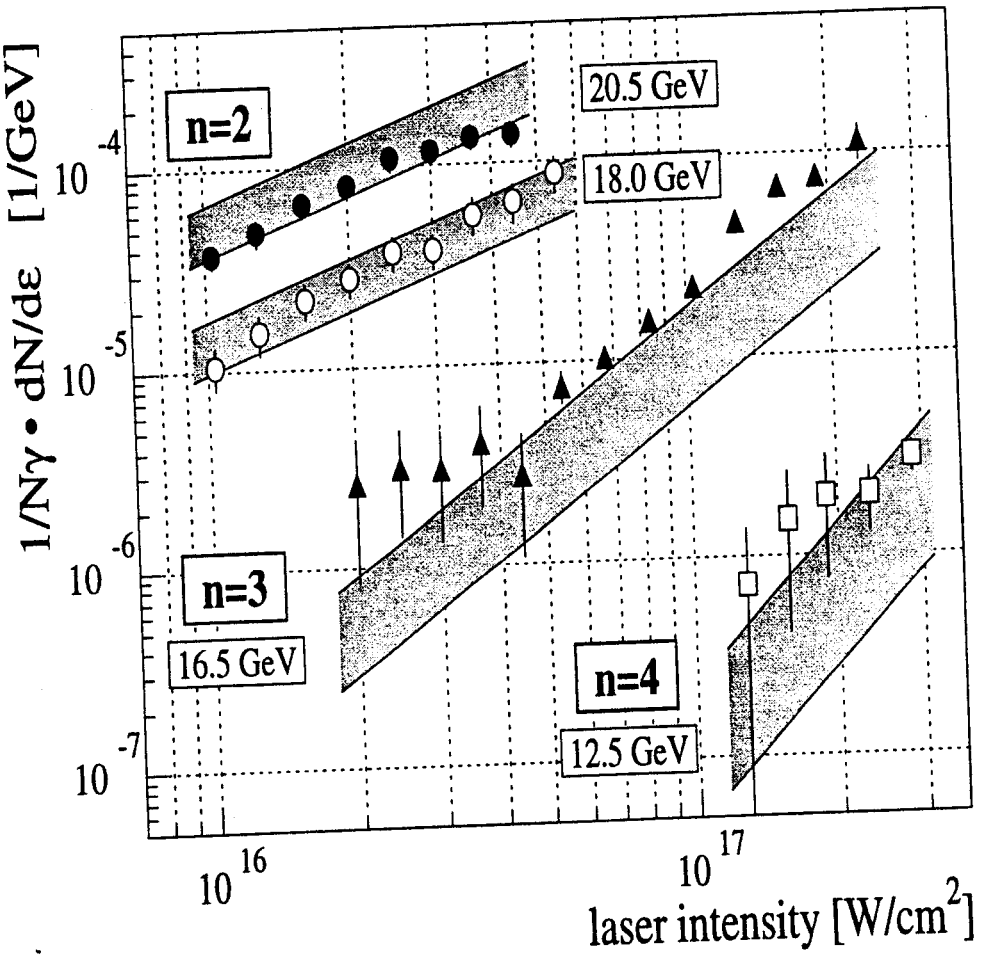

Figure 4.39: Reconstructed and scaled recoil electron yield vs laser intensity for 4 representative momenta in the IR. The solid and open circles are the data for the two photon absorption nonlinear Compton process. The triangles are the data for the n=3 process and the open squares for the n=4. The simulation for each process is shown as bands representing the 30% uncertainty in the laser energy and the 10% uncertainty in the measurement of the gamma flux. The slopes of the bands are characteristic of the order of the nonlinear process

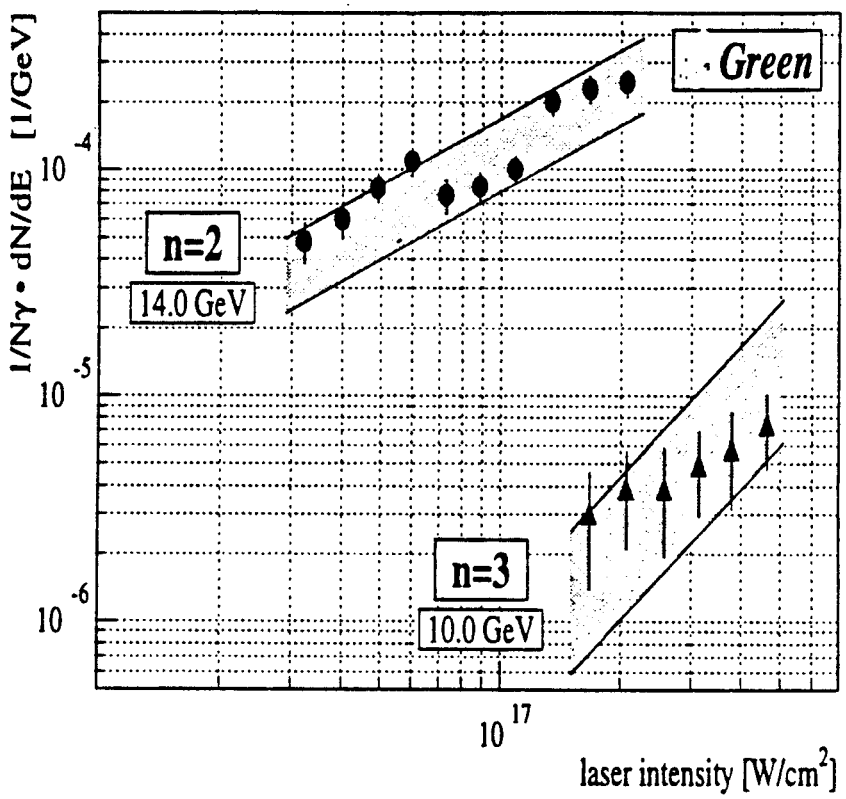

Figure 4.40: Reconstructed and scaled recoil electron yield vs laser intensity for 2 representative momenta in the green. The solid circles are the data for the two photon absorption nonlinear Compton process. The triangles are the data for the n=3 process. The simulation for each process is shown as bands representing the 30% uncertainty in the laser energy and the 10% uncertainty in the measurement of the gamma flux. The slopes of the bands are characteristic of the order of the nonlinear process

Chapter 5

Conclusions

While Quantum Electrodynamics is highly successful in describing the interaction of electrons with weak fields, QED has not been tested in strong electromagnetic fields. In the experiment described here, strong field QED was studied and nonlinear Compton scattering has been observed during the interaction of a 46.6 GeV electron beam with a 10^{18} W/cm^2 laser beam. In this process the electron may absorb n, rather than only one, laser photons to produce a high energy gamma ray:

$$e^- + n\omega_l \longrightarrow e^- + \omega_\gamma$$

This phenomenon depends nonlinearly on the field strength and for strong fields cannot be described by simple perturbative techniques. The strength of the field created by the laser is measured by the parameter η with highest value achieved

$$\eta = 0.6$$

In the rest frame of the electron we approached the critical field of QED as given by the Schwinger parameter Υ with highest value achieved

$$\Upsilon = 0.4$$

A strong signal of electrons that absorbed up to 4 infrared photons (or up to 3 green photons) at the same point in space and time, while emitting a single gamma ray, was observed. The energy spectra of the scattered electrons and the nonlinear dependence

of the electron yield on the field strength agree with the simulation of the experiment based on the cross section calculated by Narozhnyi et al. [14].

This is the first time this process is clearly observed with free electrons in the relativistic regime. The experiment is done in vacuum, i.e. only the strong electric field region is in the vicinity of the interacting electron, in contrast with atomic physics experiments. Evidence of multiphoton Compton scattering exists in the classical (Thomson scattering) regime (keV electron energies and small η values) [3, 4], where the classical radiation spectrum includes the nth harmonic of the frequency of the field (multipole radiation) at relative strength η^{2n}.

The theory of the nonlinear Compton scattering in strong fields was formulated some 30 years ago and this is the first time that it is compared with experimental results. This is mainly due to the advances in the last decade of intense lasers, such as the Table Top Terawatt laser, that allow us to create very strong fields. The laser system for this experiment is state-of-the-art and only one other system using the same techniques is known to us [92]. The high repetition rate, compared with same intensity systems, is particularly favorable for studies of high energy physics phenomena with small cross sections that otherwise would not be accessible with finite accelerator running time.

As discussed in the previous chapters an intense laser itself does not provide the answer to strong field QED phenomena. It has to be probed by an electron beam which also needs to be relativistic in order to tunnel through the ponderomotive forces in the laser focus. The 46.6 GeV electron beam used is also unique in that it can be tuned to a desirable size at the laser - electron interaction point. One of the interesting features of this experiment is that it spans two areas of physics, laser and high energy physics. In order to achieve collisions between the two beams a timing stabilization to σ_{rms}=2 ps between the pulses is necessary. The timing jitter was studied extensively and many cross field technologies applied to decrease it. Regarding this phase of the experiment it is not clear, although desirable, whether further stabilization could be achieved.

The electron spectra that this experiment was called to investigate are falling very steeply with respect to the electron momentum (and of course increase very steeply

with increasing laser intensity because of the nonlinearity of the process) and so the detectors used must have both a fine grain and a large dynamic range. A dynamic range larger than 1:100 was achieved by a sampling calorimeter calibrated by the same electron beam in a test configuration. By providing a degree of motion for the calorimeter we increased the range of the spectra that were mapped by almost a factor of 3.

The main problems of the experiment are reflected in the difficulties in the data analysis. The first problem is the very high laser related background, particularly, the gammas from the linear rate that interact with all the beam-line components in the vicinity of the calorimeter. In order to subtract this background three methods were developed. In the first method the simulation incorporates the calorimeter response in the simulation of the rates and so compares the raw data with a prediction. The results shown in the last chapter confirm the agreement of the theoretical calculations and the experimental data. The other two methods incorporated the calorimeter response in the data by introducing reconstruction matrices on the raw data. Again the experimental data agree with the predictions in the momentum range of 8 - 18 GeV for green and 10 - 25 GeV for infrared laser light. The second problem of the experiment was the timing jitter which was accounted for by the normalization of the nonlinear electron yield by the linear gamma flux; the effects of the time jitter were reduced by using a longer electron bunch. The measured gamma flux agrees with the predictions of the ordinary Compton scattering taking into account the geometry of the laser - electron interaction region. Another problem is the multiple ordinary Compton scattering which produces rates of scattered electrons of the same order of magnitude as the nonlinear Compton scattering. The recoil electrons are insensitive to these two processes but a study of the forward gamma rays does differentiate between the two. For this purpose a CCD pair spectrometer has been constructed and in the future run will be operational. Nevertheless, the simulation has studied this difference and in the last chapter we showed that the rates observed could not be accounted for only by multiple ordinary Compton scattering; nonlinear Compton scattering processes are dominant for $n \geq 3$.

The processes observed in this experiment are directly relevant to other interesting

phenomena of strong field physics such as photon by photon scattering with real photons [17]. The products of this interaction will be low effective mass pairs of electrons and positrons. A study of the invariant mass of the pairs in such processes would reveal new bound systems of electrons and positrons, if they exist. The production rate is expected to be extremely high for large laser intensities; investigations in the use of this process for a possible positron source are underway [34].

In the high energy regime when the colliding photons are in the 100 GeV energy range, even more interesting phenomena can be observed. Lately, such $\gamma - \gamma$ colliders are under consideration; although, the cross section of such processes is low, such collisions are free from the hadronic background. Therefore, high energy photon - photon collisions are favored for a search for a Higgs boson in the intermediate mass range [93]. Precision electroweak tests could also be performed in $\gamma\gamma$ experiments.

Our experiment has looked for production of pairs coming from the interaction of the electron with the laser; this is a two step process due to the interaction of the Compton gammas (already produced by linear or nonlinear Compton scattering in the laser focus) with the laser photons. This last step is what we could present as the first real photon - photon collider at low energies since the laser photon is only 2.35 eV in the green. An increased signal of 13 positron candidates was measured where a background of 4 positrons was expected [22]. In the immediate future the focus of the experiment will be on the positron production. With an expected improvement on the laser intensity by a factor of 2 and of the electron beam focusing of another factor of 15 we have a good chance in probing strong field phenomena even further, giving an answer to the feasibility of some of the proposed research in new QED topics.

Bibliography

[1] V. R. Berestetskii, E. M. Lifshitz and L. P. Pitaevskii, *Quantum Electrodynamics*, 2nd ed., Pergamon Press, 1982.

[2] K. T. McDonald, *Proposal for Experimental Studies of Nonlinear Quantum Electrodynamics*, Princeton U.Report DOE/ER/3072-32 (Sept. 1986).

[3] T. J. Englert and E. A. Rinehart, *Second Harmonic Photons from the Interaction of Free Electrons with Intense Laser Radiation*, Phys. Rev. A **28**, 1539 (1983).

[4] C. I. Moore, J. P. Knauer, and D. D. Meyerhofer, *Observation of the transition from Thomson to Compton Scattering in Multiphoton Interactions with Low-Energy Electrons*, Phys. Rev. Lett. **74** 2439 (1995).

[5] L. S. Brown and T. W. B. Kibble, *Interaction of Intense Laser Beams with Electrons*, Phys. Rev. **133**, A705 (1964).

[6] T. W .B. Kibble, *Refraction of Electron Beams by Intense Electromagnetic Waves*, Phys. Rev. Lett. **16**, 1054 (1966).

[7] T. W. B. Kibble, *Mutual Reflection of Electrons and Photons*, Phys. Rev. **150**, 1060 (1966).

[8] J. Eberly, *Interaction of Very Intense Light with Free Electrons*, Progress in Optics Vol III, ed. E. Wolf, Wiley, NY 1969.

[9] J. Eberly, *Proposed Experiment for Observation of Nonlinear Compton Wavelength Shift*, Phys. Rev. Lett. **15** 91 (1965).

[10] J. H. Eberly and A. Sleeper, *Trajectory and Mass Shift of a Classical Electron in a Radiation Pulse*, Phys. Rev. **176**, 1570 (1968).

[11] E. S. Sarachik and G. T. Shappert, *Classical Theory of the Scattering of Intense Laser Radiation by Free Electrons*, Phys. Rev. D10 2738 (1970).

[12] D.M. Volkov, *Über eine Klasse von Lösungen der Diracschen Gleichung*, Z. Phys. **94**, 250 (1935).

[13] G. V. Shishkin and Yasin Mohammed Ali, *Exact description of a Dirac particle in the presence of wave fields (generalization of the Volkov problem)*, Sov. J. Nucl. Phys. **53**(3) 536 (1991).

[14] N.B. Narozhnyi, A.I. Nikishov and V.I. Ritus, *Quantum Processes in the Field of a Circularly Polarized Electromagnetic Wave*, Soviet Physics JETP **20** 622 (1965).

[15] A.I. Nikishov and V.I. Ritus, *Quantum Processes in the Field of a Plane Electromagnetic Wave and in a Constant Field. I*, Soviet Physics JETP **19** 529 (1964).

[16] A.I. Nikishov and V.I. Ritus, *Nonlinear Effects in Compton Scattering and Pair Production owing to Absorption of Several Photons*, Soviet Physics JETP **20** 757 (1965).

[17] G.Breit and J.A. Wheeler, *Collision of Two Light Quanta*, Phys.Rev. **46** 1087 (1934).

[18] H. R. Reiss, *Absorption of Light by Light*, J. of Math. Phys. **3** 59 (1962).

[19] H. R. Reiss, *Production of Electron Pairs from a Zero-Mass State*, Phys. Rev. Lett. **26** 1072 (1971).

[20] R. Blackenbecler and S. D. Drell, *Quantum Beamstrahlung: Prospects for a Photon -photon Collider*, Phys. Rev Lett. **61** 2324 (1988).

[21] P. Chen and V.I. Telnov, *Coherent Pair Creation in Linear Colliders*, Phys. Rev. Lett. **63** 1796 (1989).

[22] S. Boege, *Evidence for Light by Light Scattering*, PhD thesis on the same experiment, U. of Rochester, Jan 1996.

[23] D-S. Guo and T. Åberg, *Quantum electrodynamical approach to multiphoton ionization in the high intensity H field*, J. Phys. A: Math. Gen. **21** 4577 (1988).

[24] J. Bergou and S. Varro', *Nonlinear scattering processes in the presence of a quantized radiation field: I. Non-relativistic treatment* , J. Phys. A: Math. Gen. **14** 1469 (1981).

[25] J. Bergou and S. Varro', *Nonlinear scattering processes in the presence of a quantized radiation field: II. Relativistic treatment* , J. Phys. A: Math. Gen. **14** 2281 (1981).

[26] W. Greiner and J. Reinhardt, *Quantum Electrodynamics*, Spreinger-Verlag, 1992.

[27] O. Klein and Y. Nishina, Zs. f. Phys. **52**, 853, (1929).

[28] A. C. Melissinos, *Calculation of Event Rate*, E144 Internal Note, July 1994.

[29] C. Bula et al. *Proposal for a Study of QED at Critical Field Strength in Intense Laser - High Energy Electron Collisions at the Stanford Linear Accelerator*, SLAC, Oct. 1990.

[30] P.A. Sturrock, *A Model for Pulsars*, Astro. J. **164**, 529 (1971).

[31] M. Ruderman, *High Energy Radiation from Neutron Stars*, SLAC-PUB-3658 (April 1985).

[32] See for instance T. Cowan and J. Greenberg, in *Physics of Strong Fields*, ed. W. Greiner, Plenum, N.Y., 1987; Also J. Schweppe et al., *Observation of a Peak Structure in Positron Spectra from U + Cm Collisions*, Phys. Rev. Lett. **51**

(1983) 2261; T. Cowan et al., *Observation of Correlated Narrow Peak Structures in Positron and Electron Spectra from Superheavy Collision Systems*, Phys. Rev. Lett. **56** (1986) 444; W. Koenig et al., *On the Momentum Correlation of (e^+e^-) Pairs Observed in U+U and U+Pb Collisions*, Phys. Lett. **B218** (1989) 12.

[33] A. Belkacem et al., *New Channeling Effects in the Radiative Emission of 150 GeV Electrons in a Thin Germanium Crystal*, Phys. Lett. **B177** (1986) 211.

[34] P. Chen and R. Palmer, *'Coherent Pair Production as a Positron Source for Linear Colliders'*, SLAC-PUB-5966, 1992.

[35] J.E. Spencer and S.J. Brodsky, *Breeding New Light into Old Machines (and New)*, SLAC-PUB-3646 (1985).

[36] I.F. Ginzburg et al., *Colliding γe and $\gamma\gamma$ Beams Based on the Single Pass e^+e^- Collider*, Nucl. Inst. and Meth. **205** (1983) 47.

[37] D.D. Meyerhofer, *High Intensity Lasers for gamma - gamma colliders*, Nucl. Instr. and Meth. in Phys. Res. **A355**, 113 (1995).

[38] Final Focus Test Beam Collaboration meetings, Feb. 1992 and Oct. 1993, SLAC.

[39] R.L. Holtzapple, *Measurements of Longitudinal Phase Space in the SLC linac*, SLAC-PUB-95-6841 (1995).

[40] K. Fujii, *Top at Future Linear e^+e^- colliders, SLAC Summer Institute*, July 10 - 21, 1995.

[41] Model OAP 12-017-036Q, Space Optics Research Labs, Chelmsford, MA.

[42] COMP, *Controlled Optics Modeling Package*, Jet Propulsion Lab., Caltech, JPL D-9816, (June 1992).

[43] C. Bamber et. al., *0.5 Hz, Phase-Stabilized Terawatt Laser System with a Nd:Glass Slab Amplifier for Nonlinear QED Experiments*, U.Rochester preprint, UR-1428 (June 1995).

[44] D. Strickland and G. Mourou, *Compression of Amplified-Chirped Optical Pulses*, Opt. Comm. **55**, 447 (1985).

[45] M. Pessot, P. Maine and G. Mourou, *1000 Times Expansion/Compression of Optical Pulses for Chirped Pulse Amplification*, Opt. Commun. **62**, 419 (1987).

[46] Model ML-59.503B1 Acousto-optic mode locker, IntraAction Corp., Bellwood, IL.

[47] Flexcore Single Mode waveguide, Corning Co., Corning, NY.

[48] O. Svelto, *Principles of Lasers*, Plenum Press, pp. 444 - 453, 1989.

[49] Model RC0100 reticon, EG&G, Sunnyvale, CA.

[50] Model no. C3735, Hamamatsu Photonics Systems, Bridgewater, N.J., Model N3373-02.

[51] E.B. Treacy, *Optical Pulse Compression with Diffraction Gratings*, IEEE J. Quan. Elec. **QE-5**, 454 (1969).

[52] O. E. Martinez, *3000 Times Grating Compressor with Positive Group Velocity Dispersion: Application to Fiber Compensation in 1.3 - 1.6 μm Region*, IEEE J. Quan. Elec. **QE-23**, 59 (1987).

[53] Model 1000 Timing Stabilizer Lightwave Electronics Co., Mountain View, CA.

[54] model Q92 Nd:Glass rod, Kigre Co., Hiltonhead, SC.

[55] W. S. Martin and J.P. Chernoch, *Multiple Internal Reflection Face Pumped Laser*, U.S. Patent 3633126 (1972).

[56] M.J. Shoup III and J.H. Kelly, *A High-Energy, Short-Pulse, Multiwavelength, Slab-Geometry Nd:Phosphate Glass Laser Source*, presented at CLEO '89, Baltimore, MD, (April 1989).

[57] Material LG5 from Hoya Co.

[58] W. Koechner, *Solid-State Laser Engineering*, Springer-Verlag, 1992.

[59] D. C. Brown, *High Power Nd: Glass Laser Systems* p.108 -118, Springer - Verlag, 1981.

[60] J - Y Opical Systems, Edison, NJ.

[61] A. Yariv, *Optical Electronics*, p. 238, CBS College Publishing, 1985.

[62] T. Wilson, C. Bamber and R.S. Craxton, *Second and Third Harmonic Generation of 1.054 μm Radiation using Picosecond Pulses* U. of Rochester preprint, UR-1271 (1992).

[63] R.S. Craxton et al., *Basic Properties of KDP Related to the Frequency Conversion of 1 μm laser radiation*, IEEE J. of Quantum Electronics **QE-17** p. 1782, 1981.

[64] A.E. Siegman, *Lasers*, p. 386, University Science Books, 1986.

[65] K. Jobe, *MDL Length Studies, SLAC Memo, Aug. 1988*

[66] RF/Microwave fiber-optic transmitter, Model 3540A and receiver, Model 4510A, Ortel Co.

[67] Optical fiber cable, 6HJ-9336A, Sumitomo Electric Industries Ltd., Yokohama, Japan.

[68] Model DG535, Digital Delay / Pulse Generator, Stanford Research Systems, Sunnyvale, CA.

[69] M. J. W. Rodwell, D. M. Bloom and K. J. Weingarten, *Subpicosecond Laser Timing Stabilization*, IEEE J. of Quantum Electronics **25**, 817 (1989).

[70] M.J.W. Rodwell et al. *Reduction of timing fluctuations in a mode-locked Nd:YAG laser by electronic feedback*, Opt. Lett. **11**, 638 (1986).

[71] R. B. Blackman and J. W. Tukey, *The Measurement of Power Spectra*, Dover, 1959.

[72] Sampling scope, Tektronix CSA803, Communications Signal Analyzer, with an SD-24 TDR Sampling Head.

[73] Model no. HSDPS1, 20 GHz photodiode, Fermionics Corp., Simi Valley, CA.

[74] D. von der Linde, *Characterization of the Noise in Continuously Operating Mode-Locked Lasers*, Appl. Phys. **B39**, 201 (1986).

[75] D.L. Brown, W. Seka, and S. Letzring, *Toward phase noise reduction in a Nd:YLF laser using electro-optic feedback control*, SPIE Vol. 1410 Solid State Lasers II, 209 (1991).

[76] H. Vanherzeele *Optimization of a CW mode-locked frequency-doubled Nd:$LiYF_4$ Laser*, Applied Optics **27** 3608 (1988).

[77] H. A. Haus, *Noise in Mode-Locked Lasers*, IEEE J. Quan. Elec. 29, 3, 984 (1969).

[78] Model 8569B spectrum analyzer, Hewllet Packard

[79] RF/IF Designer's Handbook, Mini-circuits Co. Brooklyn, NY.

[80] Model 3582A spectrum analyzer, Hewllet Packard

[81] S.C. Berridge et al., *Beam Test of the SLD Silicon - Tungsten Luminosity Monitor*, IEEE Trans. Nuc. Sci. **37** (1990) 1191.

[82] E. Prebys, *Possible Readout for the E-144 Calorimetry* E144 Internal Note (Apr. 1992)

[83] S. Iwata, *Calorimeters (Total Absorption Detectors) for High Energy Experiments at Accelerators* A Review for the Tristan Workshop, Nagoya University Preprint DPNU-3-79, (1979).

[84] The Electron - Gamma Shower (EGS4) Code System, SLAC- Report - 265, Dec. 1985.

[85] GEANT, Detector Description and Simulation Tool Software Package, CERN, Geneva, 1993.

[86] K. Shmakov, E144 Collaboration Meeting (July 1995)

[87] C. Bula, *Layout of the E144 Data Acquisition System*, E144 Internal Note (Jan. 1994)

[88] Physics Analysis Workstation (PAW) software package, CERN, Geneva (1989).

[89] G. Horton-Smith, *E144 Ecal 'Best Aperture Reconstruction'*, E144 Internal Note (Sep. 1995)

[90] K. Shmakov, *E144 Ecal Reconstruction*, E144 Internal Note (Sep. 1995)

[91] C. Bula, *LOOKUP: An Interface Program to the Lookup Tables for Compton Scattering*, E144 Internal Note (Oct. 1995)

[92] K. Yamakawa et al., Opt. Commun. **112**, 32 (1994).

[93] D.L. Borden, *Physics at a Photon Linear Collider*, PhD thesis, U.C. Santa Barbara, (July 1994).

[94] F. W. Lipps and H. A. Tolhoek, Physica **20**, 85 and 395 (1954).

[95] M.B. Woods et al. *Measurement of the Longitudinal Polarization of the Final Focus Test Beam* E144 internal report, (Aug. 1994).

[96] M. J. Fero et al., *Measuring the Left-Right Cross Section Asymmetry in Z Boson Production by e^+e^- Collisions at the SLC*, SLAC-PUB-6679, Oct. 1994.

Appendices

Appendix A

E144 collaboration members

This experiment was under number E144 of SLAC. Some of the E144 collaboration members, whose names and institutions are stated below, can be seen in Picture A.1.

In the front row:

Glenn Horton-Smith,[3] Theofilos Kotseroglou,[2] Wolfram Ragg,[2] Steve Boege,[2]

In the back row:

Kostya Shmakov[4], David Meyerhofer[*], Charlie Bamber[2], Bill Bugg[4], Uli Haug[2], Achim Weidemann[4], Dieter Waltz[3], Dave Burke[3], Jim Spencer[3], Christian Bula[1], Kirk McDonald[1] and Adrian Melissinos[2].

Absent from this picture are: Steve Berridge[4], Eric Prebys[1], Thomas Koffas[2] and David Reiss[2].

1: Joseph Henry Laboratories, Princeton University, Princeton, NJ 08544

2: Dept. of Physics and Astronomy, Dept. of Mechanical Engineering[*], University of Rochester

3: Stanford Linear Accelerator Center, Stanford University, Stanford, CA 94309

4: Dept. of Physics and Astronomy, University of Tennessee, Knoxville, TN 37996

APPENDIX A. E144 COLLABORATION MEMBERS

Figure A.1: E144 collaboration members

Appendix B

Critical field of QED

The critical field was first introduced by Sauter as the characteristic field strength at which Klein's paradox becomes important: The solution to the Dirac equation for an electron wave impacting on a potential step of height V_o can give a puzzling result i.e. the current of electrons that is reflected from the barrier is larger than the incident current, if

$$V_o \geq E + mc^2 \tag{B.1}$$

Here E is the kinetic energy of the impacting electrons. The paradox was explained by using the so called hole theory; by attributing the increased flux of the reflected particles to the creation of positrons at the potential barrier. Sauter showed that is the inclination of the potential barrier that matters and pair production occurs if d, the distance in which the potential rises from $V = E$ to $V = V_0$, is less than a Compton wavelength. Since the slope of the potential barrier is the electric field acting on the electron we get:

$$F = -\nabla V \tag{B.2}$$

or

$$e\mathcal{E}_{crit} = \frac{V_o - E}{\lambda_{Compton}} \tag{B.3}$$

and using Eq. B.1, we again obtain the critical field of QED:

$$\mathcal{E}_{crit} = \frac{m^2c^3}{e\hbar} \tag{B.4}$$

The critical field was further interpreted by Heisenberg and Euler as the field strength at which the vacuum 'sparks' into electron-positron pairs.

For an electron of energy E and therefore γ-factor $\gamma = \frac{E}{mc^2}$ in a strong electromagnetic field, a useful dimensionless invariant is :

$$\Upsilon = \frac{\mathcal{E}_{rest}}{\mathcal{E}_{crit}} = 2\frac{\gamma \mathcal{E}_{lab}}{\mathcal{E}_{crit}} \tag{B.5}$$

where $\mathcal{E}_{rest}$ and $\mathcal{E}_{lab}$ are correspondingly the electric fields at the particle's rest and lab frames, γ is the Lorentz boost and for the final equality we assume a head on collision of the particle with the field photons.

Parameter η of the multiphoton Compton process is simply related with the critical field parameter Υ by:

$$\Upsilon = \frac{2\gamma \mathcal{E}}{\mathcal{E}_{crit}} = \frac{2\gamma e \mathcal{E}}{m^2} = \eta \frac{p\omega}{m^2} \tag{B.6}$$

where p is the momentum of the high energy electron. The last eq. shows that Υ varies inversely proportional with the laser wavelength for fixed power and focusing strength, so shorter wavelengths are better in studying the vacuum polarization phenomena. In this experiment the ratio of η to Υ is near unit and so nonlinear effects can be probed due to both multiphoton absorption and vacuum polarization.

Appendix C

The list of runs analyzed

A list of March '95 runs that were analyzed follows. For each run the vertical position of the top of ECAL relative to the electron beam is given, which using the electron tracking map, can translate into momentum information on ECAL. The initial number of events for each run, i.e. before the cuts applied, is also given. Since the rate of collecting data is 3 Hz and the laser fires every 0.5 Hz the duration of each run can be directly calculated. The electron beam sizes for most of these runs were discussed in chapter 2.

Table C.1: Ecal scans with IR, circularly polarized laser

Run no.	no. events	ecal pos.
12167	402	-40
12179	467	-50
12247	777	-63

Table C.2: Data runs with IR, circularly polarized laser

Run no.	no. events	ecal pos.
12170	2001	-39
12172	1715	-39
12177	1021	-39
12180	2545	-46
12192	1801	-38
12200	1801	-54
12201	1801	-62
12203	1801	-70
12204	901	-132
12207	1801	-62
12208	1801	-81
12227	1001	-38
12228	1130	-38
12229	1624	-38
12239	2038	-71
12240	1910	-80
12245	1001	-63
12246	2001	-63
12249	2001	-71
12251	2001	-78
12254	2001	-70
12258	452	-79
12259	1802	-79
12260	1061	-110
12261	901	-161
12262	1801	-94
12264	1801	-78
12269	515	-36
12270	2001	-38
12354	1801	-97
12356	1801	-121
12358	1801	-121

Table C.3: Ecal scans with green, circularly polarized laser

Run no.	no. events	ecal pos.
12382	205	-98
12386	608	-98
12392	738	-82
12428	788	-129

Table C.4: Data runs with green, circularly polarized laser

Run no.	no. events	ecal pos.
12378	3447	-81
12380	3001	-98
12391	4187	-81
12393	1001	-98
12399	3001	-81
12401	1658	-98
12403	3001	-82
12405	2010	-98
12408	3001	-98
12409	1001	-143
12412	3001	-81
12414	3001	-98
12415	3001	-113
12422	3001	-114
12423	1351	-130
12427	2314	-130
12433	3001	-113
12434	3001	-130
12435	601	-151

Table C.5: XT-scans with IR, circularly polarized laser

Run no.	no. events	ecal pos.
12164	3564	-38
12175	3551	-39
12190	3259	-38
12191	1303	-38
12195	717	-54
12197	734	-54
12199	6676	-54
12205	6666	-62
12232	699	-80
12233	5232	-70
12250	6841	-71
12257	6825	-79
12351	3248	-112

Table C.6: XT-scans with green, circularly polarized laser

Run no.	no. events	ecal pos.
12374	3590	-82
12376	2115	-81
12388	6829	-82
12411	6800	-81
12418	539	-114
12419	6813	-114
12430	3601	-113

Appendix D

Timing jitter estimate from the data

The jitter of the laser-electron timing can be estimated with the diagnostics described in the Apparatus chapter, but is also reflected on the data. A study of the jitter in time scans, data runs and xt scans produced the same result of rms jitter 2.0 ps.

A typical timing delay curve is shown in Figure 3.2. Because the timing jitter is of the same order as the width of the curve and due to changes in the laser intensity, several passes are made over the timing curve to reduce fluctuations in statistics. Figure 3.2 is an average over 4 passes. To estimate the timing jitter one can simply equate the width of the timing curve to the quadrature of 3 contributions: the width in time of the laser pulse and of the electron beam and the timing jitter:

$$\sigma_t^2 = \frac{1}{2}(\sigma_{laser}^2 + \sigma_e^2) + \sigma_{jitter}^2 \tag{D.1}$$

where σ_t is the width of the timing curve and the factor $1/2$ stems from the counter-propagation of the two pulses. During the running period we tuned occasionally the pulsewidth of the electron bunch by the bunch compression knob of the accelerator, and in summary we have three data taking configurations of $\sigma_e = 0.67, 0.85$ and 1.08 mm in length or correspondingly $\sigma_e = 2.5, 3.0$ and 3.3 ps in time. Three time scans taken each in one of these running conditions is shown in Figure D.1. The effect of the time jitter is less pronounced, when the electron beam is longer and using Eq.

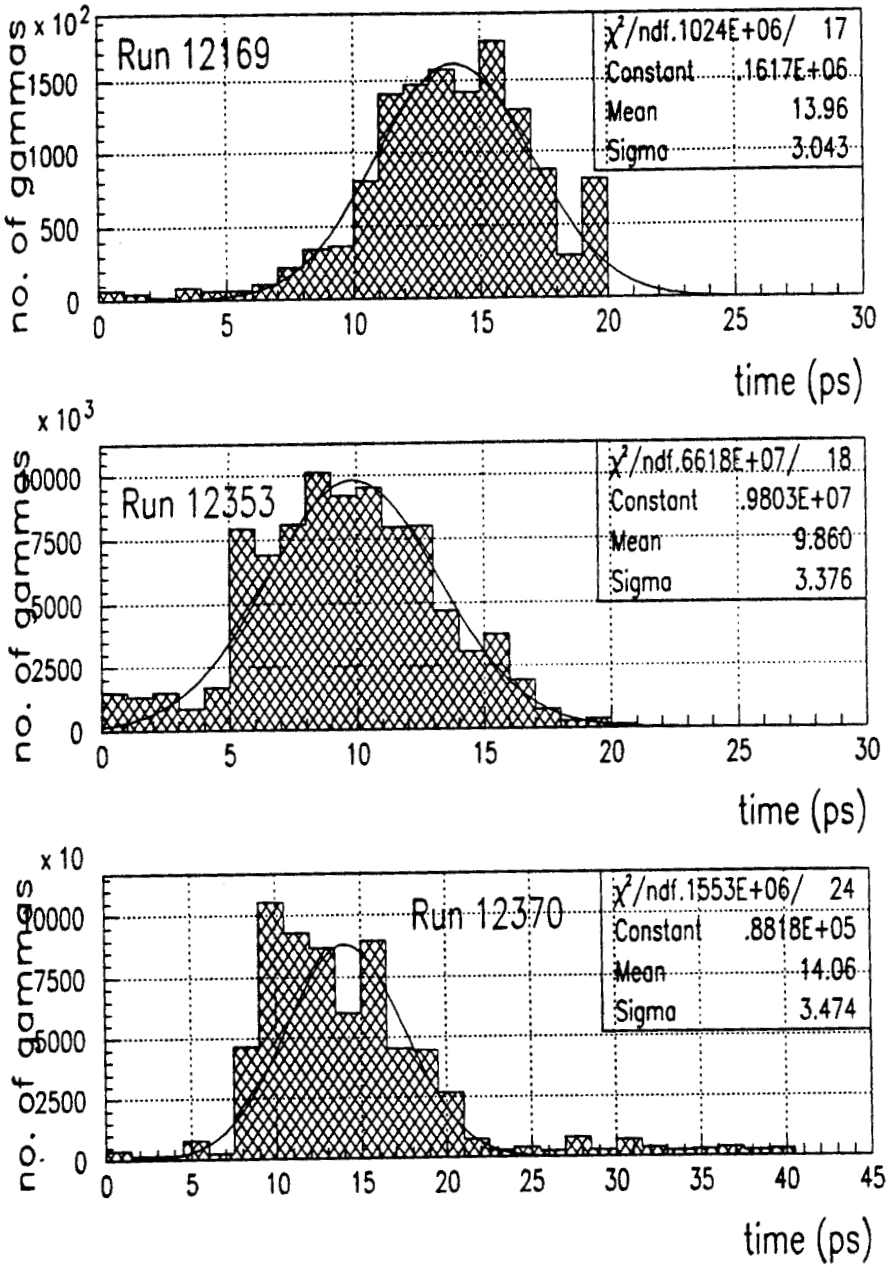

Figure D.1: Time scans taken with various electron beam longitudinal dimensions. The overlap as viewed during time-scans is larger for the longer bunch

D.1 all 3 curves show a consistent value for the timing jitter equal to 1.9 ps.

The most precise measure of the relative timing jitter comes from the analysis of the data runs. Figure D.2 gives the distribution of the ratio of gammas from the linear monitor divided by the laser energy, for a specific data run. In the absence of jitter this ratio should have a fixed value, with a relatively small width corresponding to fluctuations due to measurement error. If the timing jitter is of the same order as the width of the timing overlap curve, the ratio will depart from its maximum tending to lower values. As the jitter increases, the peak is completely washed out. Another way of studying the jitter in data runs is the ratio of the number of gammas from the linear monitor over the number of gammas predicted by the simulation for each event, taking into account not only the laser energy, but also the laser area and pulsewidth and the electron beam configuration for this event. This ratio will peak at 1 for all runs for perfect overlap conditions and will drift to zero if the overlap worsens.

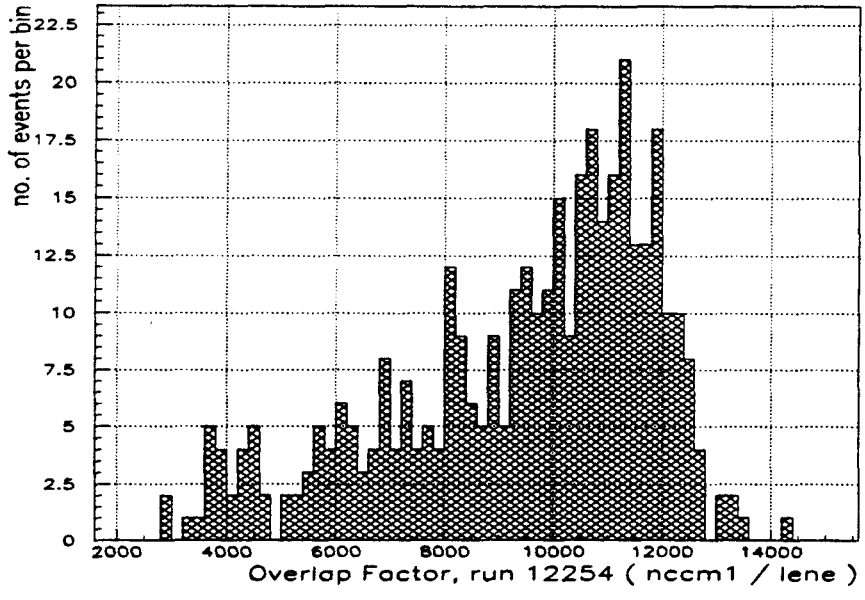

Figure D.2: Ratio of the number of gammas over the laser energy in a data run

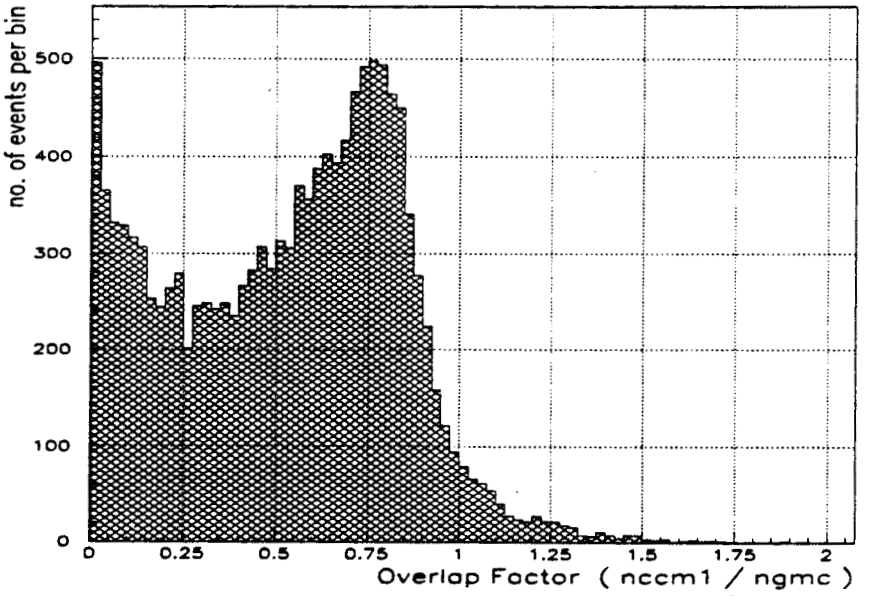

Figure D.3: Overlap Factor estimated from the data: It is defined as the ratio of the number of gammas detected over the gammas predicted by the simulation

This ratio is used in the data analysis as a so called 'overlap factor' (O.F.) of the experiment and can be shown in Figure D.3 for all the IR circular events collected.

Under the assumptions that the timing overlap curve from time scans has a Gaussian shape with dispersion σ_0 the ratio of the events observed over the events with perfect overlap is given as function of time by:

$$N(t) = e^{-\frac{t^2}{2\sigma_0}} \tag{D.2}$$

If we also assume that due to timing jitter, t is distributed as a Gaussian with dispersion σ_j then the frequency function for t is given by:

$$f(t) = \frac{1}{\sqrt{2\pi}} \frac{1}{\sigma_j} e^{-\frac{t^2}{2\sigma_j}} \tag{D.3}$$

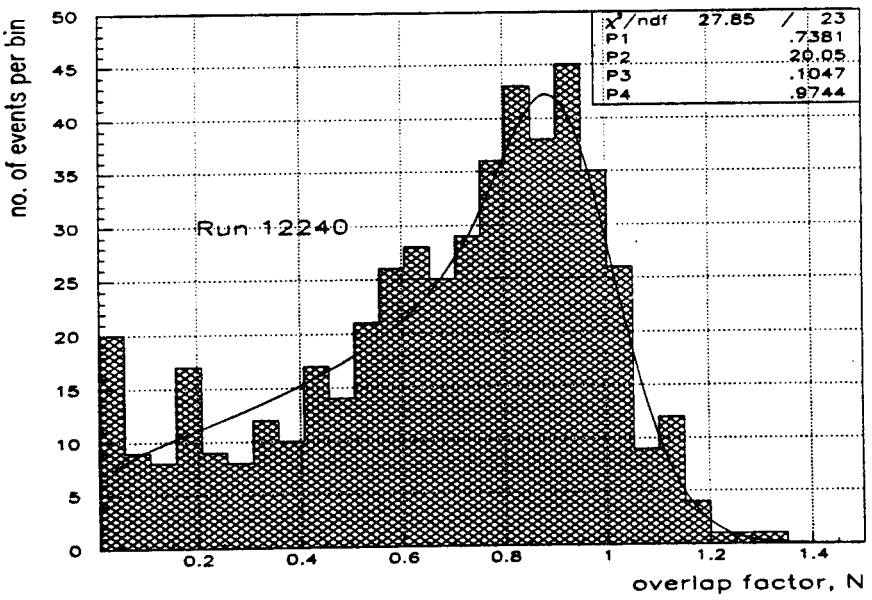

Figure D.4: Timing jitter estimate from data runs. Parameter P(4) is of the fit is the ratio of the rms timing jitter over the rms laser-electron beam overlap

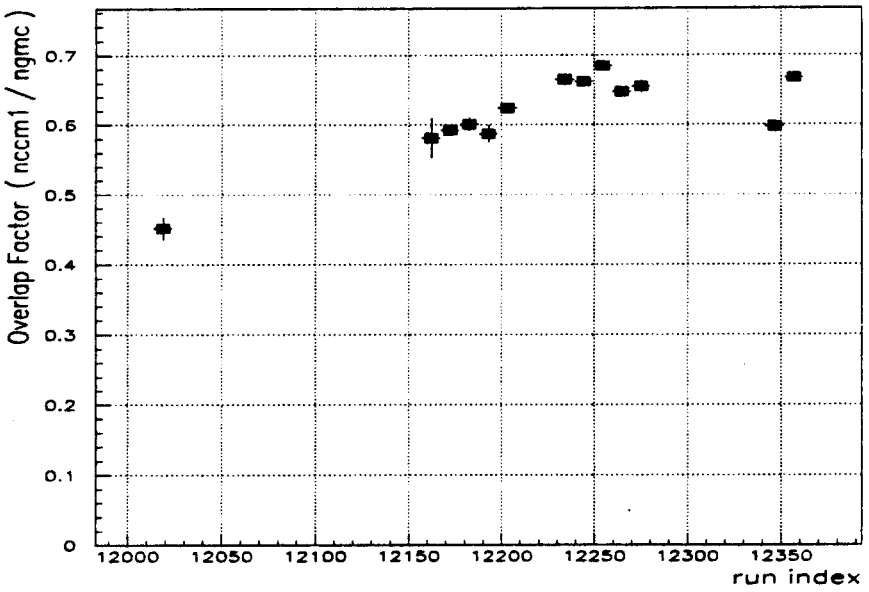

Figure D.5: Drift of the Overlap Factor in the overall IR running period

The distribution of the overlap factor is then given by:

$$f(N) = \frac{R}{\sqrt{\pi}} \cdot \frac{N^{R^2-1}}{\sqrt{\ln 1/N}} \tag{D.4}$$

where N is the ratio of the events observed over the events with perfect overlap and R is the ratio σ_0/σ_j. After integration of the density over finite bins and smearing with a Gaussian of variable width as the respond to experimental conditions, a fit of the data is shown in Figure D.4. The fit gives a ratio σ_0/σ_j= 0.98. By substituting $\sigma_0 \simeq$2.5 ps for the specific run from the timing scan that preceded this run one deduces a timing jitter of $\sigma_j \simeq$2.5 ps. This certainly is an upper limit of the timing jitter since in our model we can not distinguish between jitter and slow drift. The slow drift is revealed in Figure D.5, where the overlap factor is plotted for the whole running period. An increasing run number means a later time and each run is about an hour of data taking, although diversions and breaks may have happened between the runs.

Appendix E

Measurement of the electron beam polarization

In the first running period of March '94, we measured the asymmetry in the recoil electron spectrum from linear Compton scattering of polarized electrons off circularly polarized photons. This experiment was a check for the functionality of the diagnostics, the detectors and the data acquisition system before the nonlinear Compton studies begin.

The asymmetry is defined as :

$$A = \frac{N_+ - N_-}{N_+ + N_-} \tag{E.1}$$

where N_+ and N_- are the electron yield with electron polarizations along and against the electron momentum vector respectively. It can be shown [94, 95] that the asymmetry is proportional to $P_e P_\omega$.

The laser energy recorded for this runs was only 3 mJ, the pulse-length about 100 ps and the wavelength was 527 nm. For this run a different setup of the last stages of the laser system was used, i.e. the slab amplifier was bypassed and a smaller in size compression grating pair was used. The laser was then circularly polarized in better than 96 % . The polarization state of the returned laser pulse was analyzed with the setup in Figure E.1. Both the laser and the electron polarization 'bit' were recorded in every shot. The ECAL was positioned high into the linear Compton scatters and

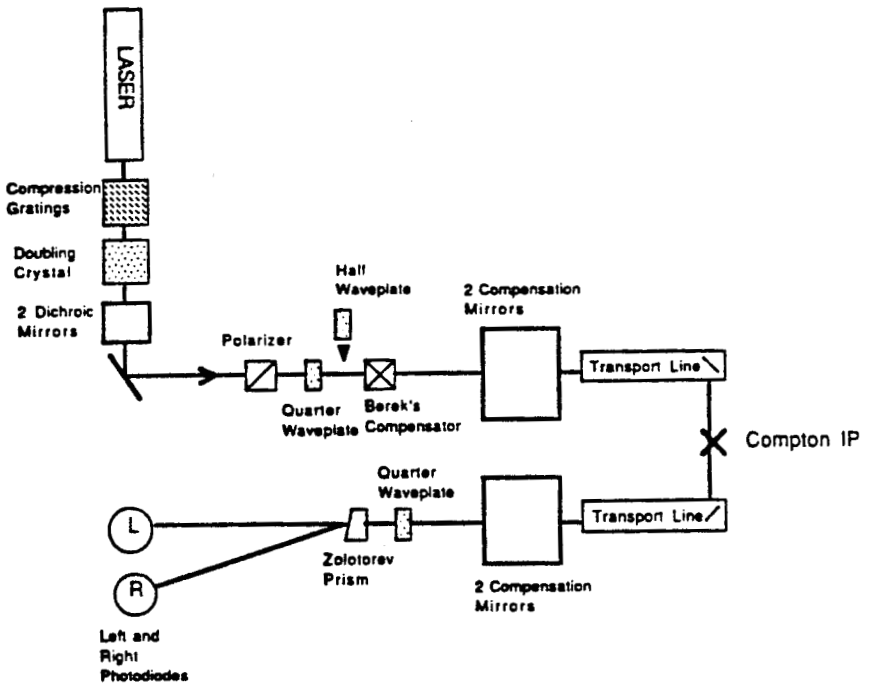

Figure E.1: Setup for measuring the electron beam longitudinal polarization in the FFTB

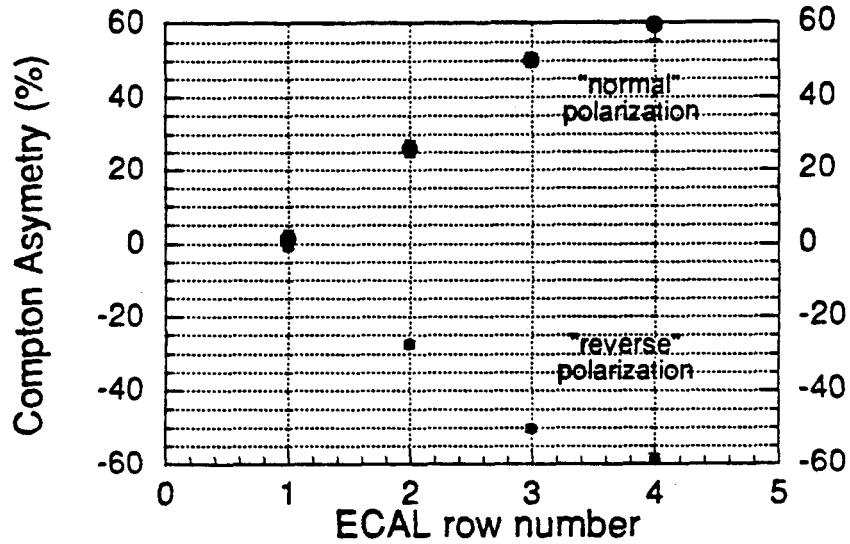

Figure E.2: Compton asymmetry in % for 'normal' and 'reversed' electron longitudinal polarizations.

the momentum map was verified by locating the zero crossing of the asymmetry, i.e. at 25.4 GeV.

Figure E.2 shows the Compton asymmetry for normal and reversed laser polarization. The deduced electron polarization asymmetry [95] was

$$P_e = 0.81^{+0.04}_{-0.01}$$

in good agreement with measurements of the SLD collaboration [96]. The upper error of 0.04 on the polarization is due to the uncertainty in the laser polarization, and could be reduced in a new experiment.

Appendix F

Analysis of XT-scans

The analysis presented in the 3rd and 4th chapters is based on data runs (DR) and ecal scans (ES), but it also agrees with the analysis of xt-scans. Since in the methods that reconstruct the ECAL energy distribution we have implicitly used the information from the xt-scans, it is only appropriate that they are compared with the rest of the runs in the 'raw' or else 'unreconstructed' (UR) method. The following method is used in extracting the normalized electron yield from an xt-scan:

The linear rate and the energy distributions of the top ECAL rows are plotted as 3 dimensional histograms, where one axis is the fast time scans and the other the slower IP box scans, and the entries of the histogram are the average of the gamma flux or of the energy distributions over the number of events collected. This averaging is due to the data collection method, where for each xt scan about 10 events are recorded at each timing stage and IP box offsets, in order to avoid statistical fluctuations of laser intensity and time jitter effects.

These 3 dimensional histograms constructed for xt-scan run 12205 are shown in Figure F.1. Each xt-scan can be viewed as many time scans taken for various IP positions. These time scans are fitted with a Gaussian function as shown in Figures F.2 and F.3 for the gamma flux and the ECAL energy of the top row. From the peak amplitudes of these fits the normalized electron yield is constructed, as was done for data runs, for each IP box position. By fitting these normalized electron yields assuming a Gaussian distribution with linear background, over the IP position,

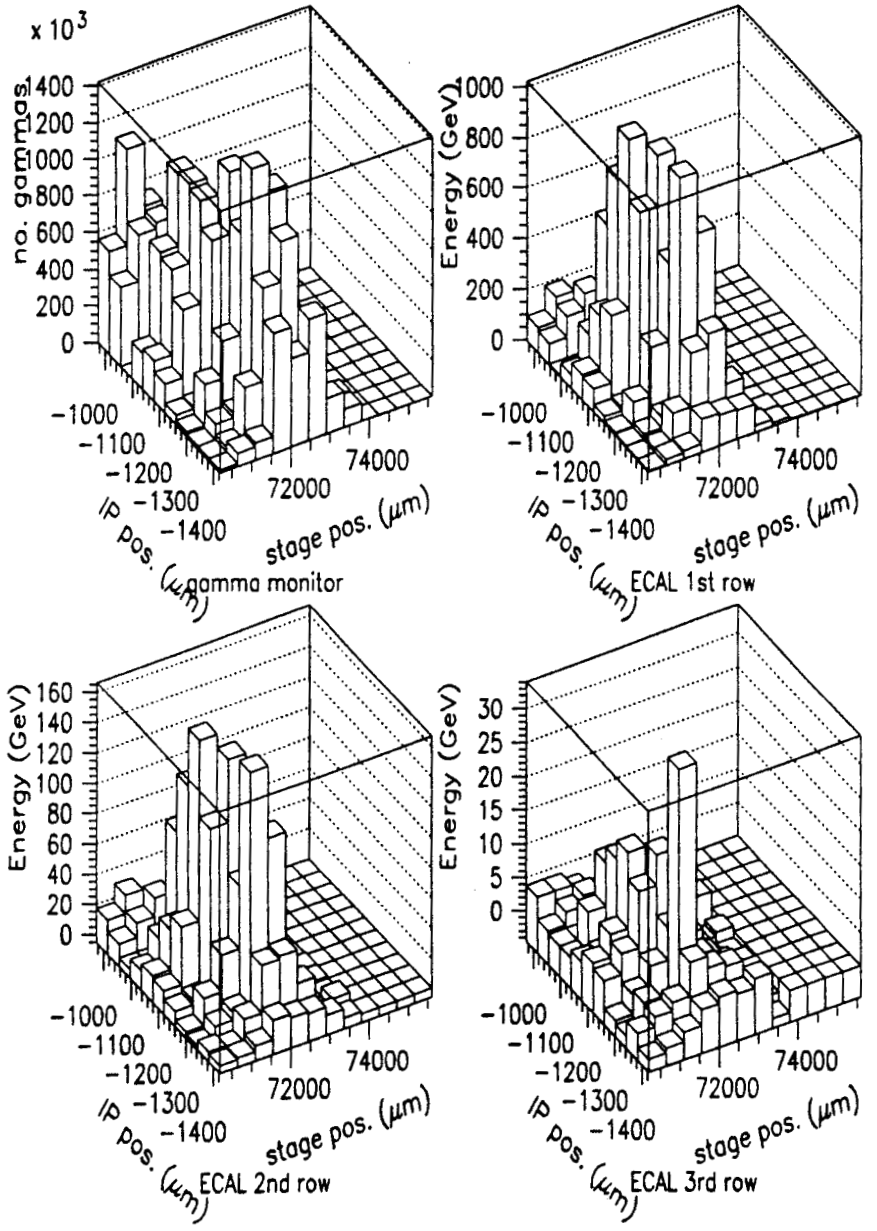

Figure F.1: Three dimensional plots of an xtscan (run 12205). The gamma monitor and the energy detected in the top three rows of ECAL are depicted

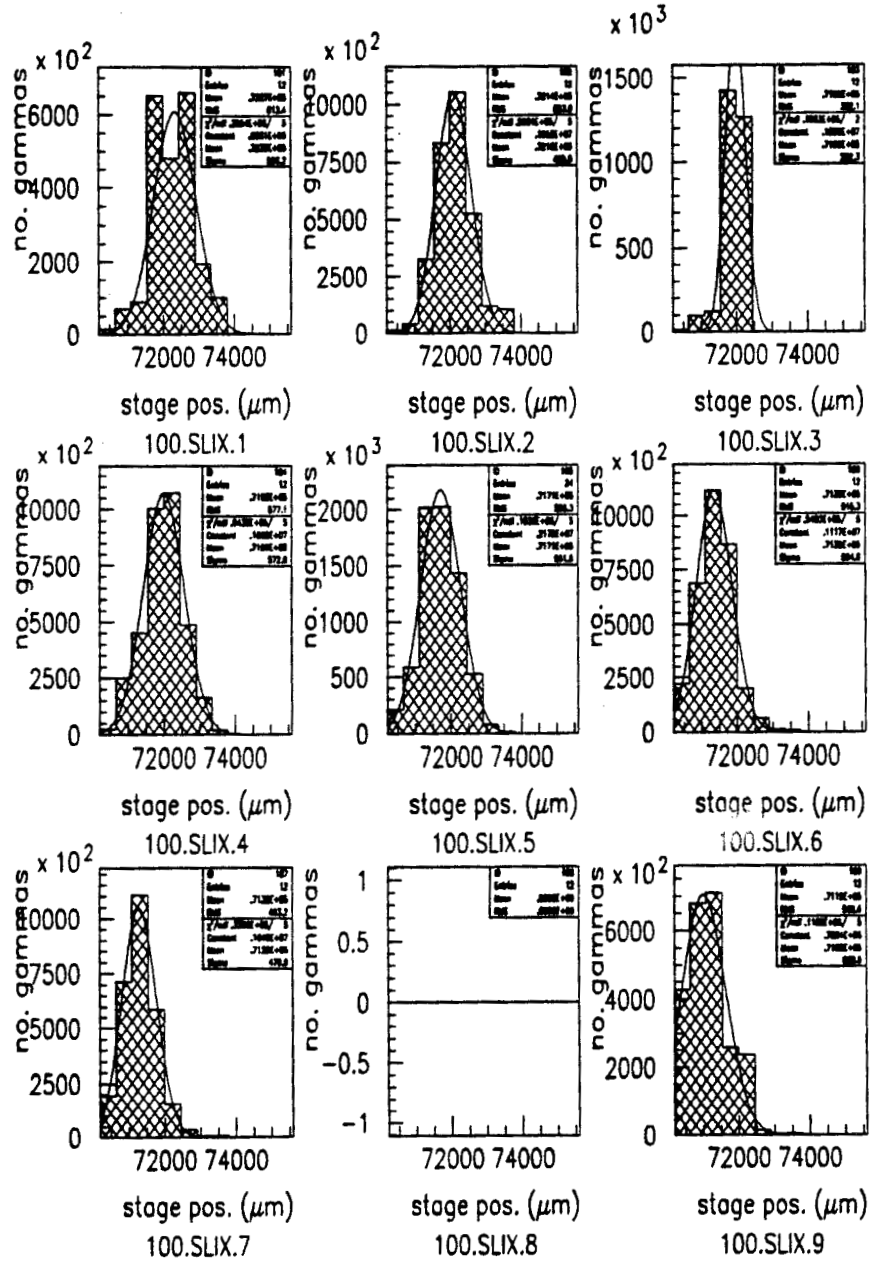

Figure F.2: The gamma flux detected in xtscan 12205 is fitted as if it would have been many timing scans

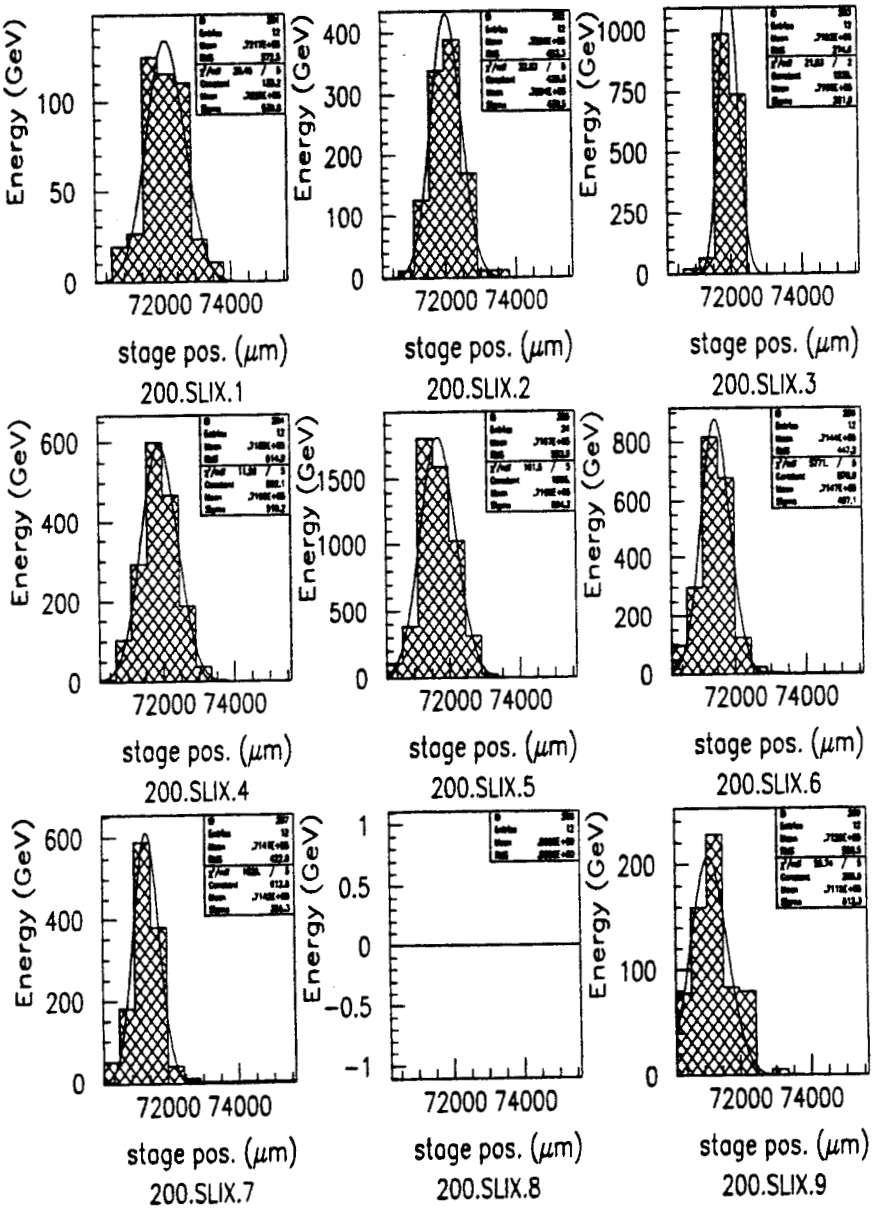

Figure F.3: Fitting the energy distribution in the top row of ECAL in the time axis of xtscan 12205

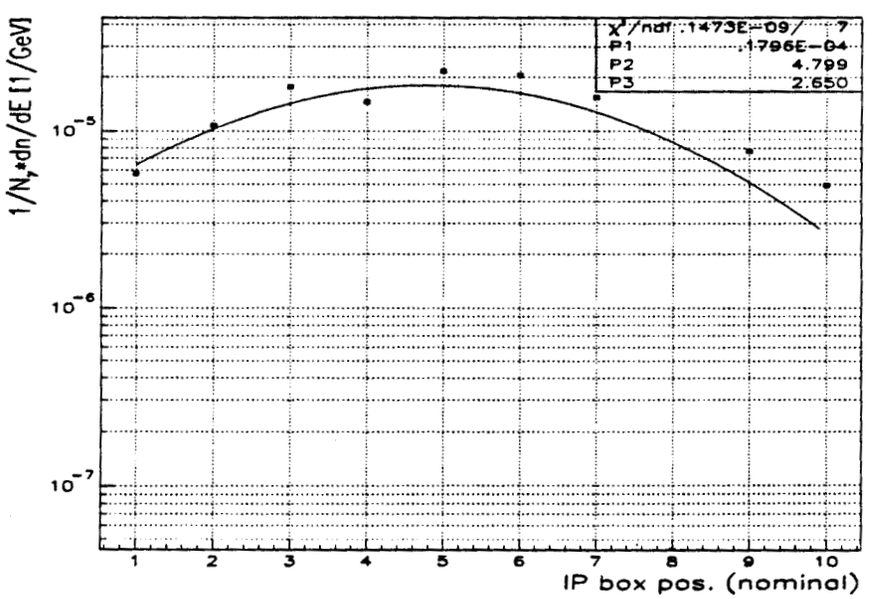

Figure F.4: The electron yield as a function of the IP position from xtscan 12205. The peak of the fit corresponds to the best timing and spatial overlap of the electron beam with the laser pulse.

we extract the maximum normalized electron yield over the course of the run as in Figure F.4.

The normalized recoil electron yields from two xt-scans are compared to that of the data runs under similar laser and electron beam conditions as shown in Figure F.5. This method is robust only for the top 2 rows of ecal, and a more elaborate fit is needed for the lower ECAL rows with weaker signal. Generally an agreement with less than 10 % uncertainty is achieved between data runs and xt-scans.

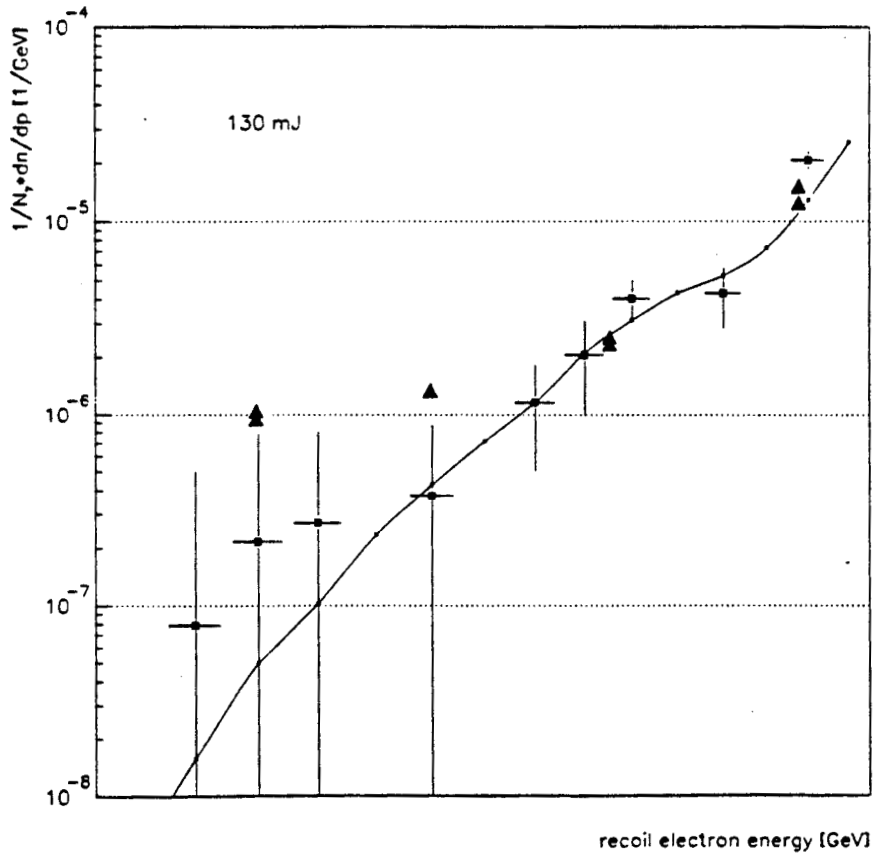

Figure F.5: The electron yield vs momentum from two xt-scans, shown by the solid triangles, agrees with the data run analysis as given by the 'unreconstructed' method.

Appendix G

Index of Abbreviations and Acronyms

ADC: Analog to Digital Converter

BPM: Beam Position Monitor

CCM1: Cherenkov Monitor

DAQ: Data Acquisition System

DBM: Double Balanced Mixer

DFB: Distributed Feedback Laser

ECAL: Electron Calorimeter

ETP: Equivalent Target Plane Technique

F/O: Fiberoptic

FIDO: Fiducial Output

F/T:	Fiberoptic Transmitter
F/R:	Fiberoptic Receiver
FE:	Front End computers
FFTB:	Final Focus Test Beam
GVD:	Group Velocity Dispersion
HPIB:	Hewlett Packard Interface Bus
He-Ne:	Helium Neon laser
IP:	Interaction point or region
LACAMP:	Liquid Argon Calorimeter Amplifiers
LO:	Local Oscillator
MDL:	Main Drive Line
ML:	Modelocker
NLC:	Next Linear Collider
OAP:	Off Axis Paraboloids
PAW:	Physics Analysis Workstation
PDU:	Pulse Delay Unit
PFN:	Pulse Forming Network
PLL:	Phase Locked Loop
PMT:	Photomultiplier
Q:	Quality factor of a cavity
RABBIT:	Redundant Amalog Bus Based Information Transfer system, readout electroni the calorimeter
SCP:	SLC Control Program

SLAC: Stanford Linear Accelerator Center

SLC: Stanford Linear Collider

SPM: Self Phase Modulation

TDR: Time Delay Refractometer

TRLP: Time Reference Laser Pulse

TS: Timing Stabilizer module or Time Scan when refering to data analysis

T-zero: timing of the fiducial pulse

T^3: Table Top Terawatt laser

UD: Upper Deflection Box

XT: Scan of the IP box in the x direction while at the same time the laser pulse is also scanned in time